SISSA
Scuola
Internazionale
Superiore di
Studi Avanzati

Physics Area - PhD course in
Astrophysics and Cosmology

Towards Precision Measurements of the Primordial Power Spectrum of Gravitational Waves: Combining B-mode Cosmic Microwave Background and Direct Gravitational Waves Observations

Candidate:
Paolo Campeti

Advisors:
Davide Poletti
Carlo Baccigalupi

Academic Year 2019-20

Contents

Introduction

The study of the *primordial* (or cosmological) *stochastic gravitational wave background* (SGWB) encompasses two of the most promising and compelling fields of cosmology at the moment: *cosmic microwave background* (CMB) *physics* and *gravitational waves* (GW) *astronomy*. The efforts of these two communities are indeed directed towards a historic goal, that is the first observation of this primordial signal, originating from the first instants of existence of the Universe. A detection of the primordial SGWB would therefore open a unique window on the physics of the early Universe, as this signal contains an unparalleled wealth of information on such processes, and would allow to test some of the predictions of the cosmic inflation paradigm – which at the moment represents the favored scenario – together with other early Universe theories.

At the moment, we are experiencing an extraordinary epoch concerning the progresses associated to both the CMB and GW.

In the last three decades, in fact, CMB data – together with the accurate mapping of the Large Scale Structure of the Universe by means of galaxy surveys – have driven cosmology into its current *precision era*, through measurements of the temperature and polarization fluctuations caused by primordial density perturbations. These observations allowed cosmology to reach full maturity as a branch of physics and to establish the current cosmological model (Planck Collaboration, 2018) – named ΛCDM after the Cosmological Constant Λ e the Cold Dark Matter (CDM) model – which also predicts the production of a primordial SGWB by quantum fluctuations during inflation, a mysterious phase of quasi-exponential expansion in the very early Universe. Such signal is expected to leave its unique imprint in the curl-component – called *B-mode* – of the CMB polarization field: , representing at this moment the most reliable mechanism in order to achieve a convincing detection of primordial GWs.

Given the exceptional importance of such measurements, several CMB B-mode experiments have already been deployed and are currently searching for primordial B-modes, while others have been planned for this and the next decade. The path to B-mode detection,

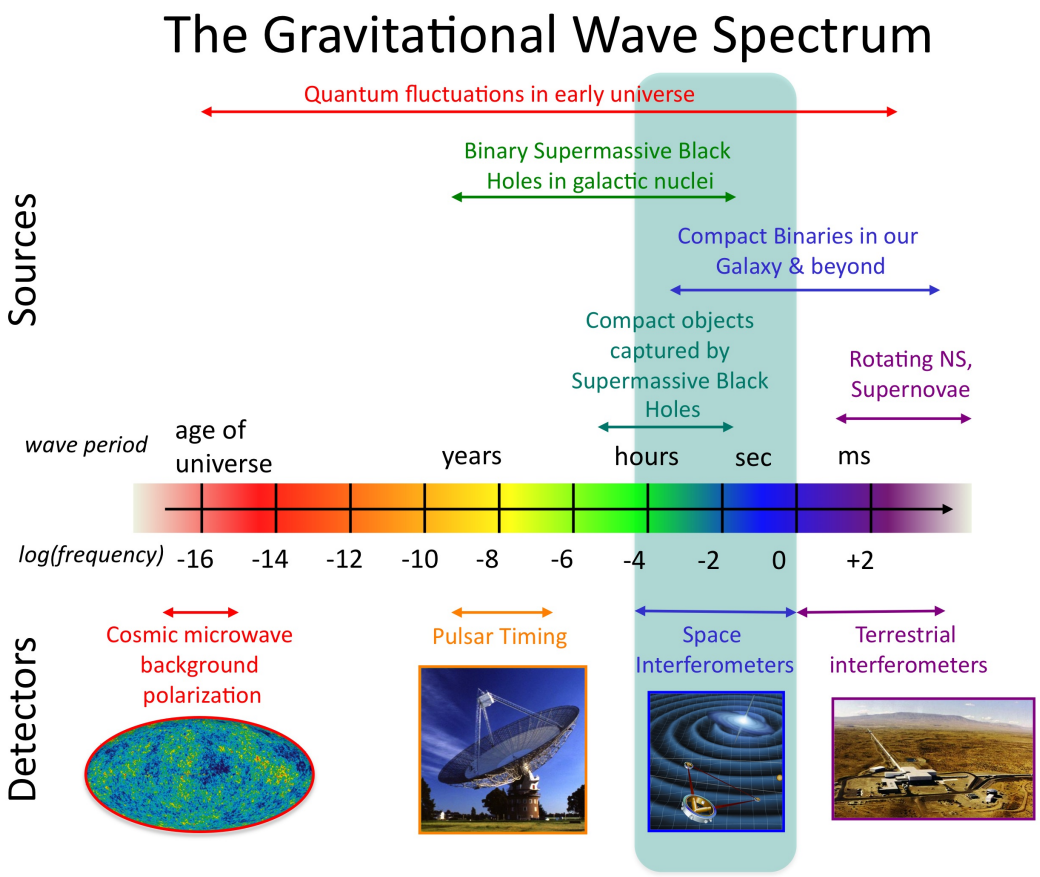

Figure 1: The spectrum of gravitational waves as a function of frequency and wave period, together with some of the available detection methods and some of the relevant sources. Figure credit NASA Goddard Space Flight Center.

however, is full of challenges: this primordial signal, indeed, is very faint, with contaminations by a secondary B-mode signal generated on arcminute scales by curl-free E-modes of the CMB polarization *gravitationally lensed* by the Large Scale Structure of the Universe and on larger scales by the *astrophysical diffuse foregrounds* from our own Galaxy, mainly due to the thermal emission of dust grains and to the synchrotron radiation emitted by cosmic ray electrons spiraling into the Galactic magnetic field.

On the other hand, GW astronomy is undergoing a phase of incredible discoveries. This discipline could be seen, in some sense, as younger with respect to CMB physics: despite the fact that the existence of gravitational radiation had already been confirmed in 1982 by the measurement of the rate of orbital decay due to energy-loss in GWs in a neutron star binary (Taylor and Weisberg, 1982), the date of birth of GW astronomy can coincide with the first direct

observation of the inspiral and merger of a stellar mass black hole binary, that is September 14th, 2015, by the Advanced Laser Interferometer Gravitational-Wave Observatory (LIGO) experiment (Abbott et al., 2016). This observation was followed soon after by the first observation of a binary neutron star merger (Abbott et al., 2017), in collaboration with the Advanced Virgo interferometer (Acernese et al., 2015). These exciting discoveries opened up a new era for fundamental physics investigated through astrophysical and cosmological observations, including the possibility to observe an SGWB of primordial origin, which will be the subject under investigation in this Thesis.

As displayed in Figure 1, the spectrum of an SGWB produced by quantum fluctuations in the early Universe covers a large range of frequencies. This allows for at least other three different detection methods – operating in three different frequency ranges – in addition to the already mentioned CMB B-modes: *Pulsar Timing Arrays*, *space-borne and ground-based laser interferometers*. The search through Pulsar Timing Arrays exploits the correlations induced by the passage of GWs in the arrival times of the radio pulses emitted by an ensemble of Galactic pulsars with rotation period of $\sim 1\,\mathrm{ms}$. Laser interferometers, on the other hand, measure the change – induced by the passage of a GW – in the proper distance between the two test-masses at the ends of one arm of the interferometer, which producies phase-shifts in the laser beams traveling back-and-forth along the arm.

Also in the case of Pulsar Timing and interferometers, an SGWB of primordial origin could be contaminated by the presence of several astrophysical foregrounds components, as exemplified in Figure 1: various populations of unresolved compact objects – including merging binary black holes of both supermassive and of stellar nature, neutron star binaries, Galactic and extra-Galactic binary white dwarfs and others – will also produce a stochastic background of astrophysical origin, which will represent a foreground in the search of primordial SGWB.

Outline of the Thesis

In this Thesis, we will be concerned with the possibility of obtaining precision measurements on the spectrum of a primordial SGWB, using both CMB B-mode experiments and direct detection ones, such as laser interferometers and Pulsar Timing Arrays.

Motivated by the fact that, in addition to the standard prediction of single-field slow-roll inflation models, a multitude of alternative production mechanisms have been proposed in the literature as possible sources of primordial B-modes, we will first explore (Chapter

4) the capabilities of current and future CMB B-mode experiments to characterize the shape of a primordial SGWB spectrum. To this end, we will exploit a *Principal Component Analysis* formalism, in order to maintain a model-independent approach: this will allow us to assess the modulation in sensitivity of an experiment on the different cosmological perturbation scales and to determine where features in the tensor power spectrum can be probed more effectively by each of the considered experiments. We will include in our study – for the first time in the literature on the subject – the contribution from residual diffuse foreground contamination and we will derive robust expectations on the sensitivities of three future B-mode probes, namely the Lite satellite for the studies of B-mode polarization and Inflation from cosmic background Radiation Detection (LiteBIRD) satellite (Hazumi et al., 2019; Sugai et al., 2020), the Simons Observatory (SO) (The Simons Observatory Collaboration et al., 2018; Lee et al., 2019) and the Stage-IV network of ground-based observatories (CMB-S4) (Abazajian et al., 2016; Abazajian et al., 2019b,a).

We will then extend the previous study by including the possibilities offered by measuring the spectrum of a primordial SGWB with laser interferometers and Pulsar Timing Arrays, in addition to CMB B-mode probes (Chapter 5). This allows to constrain the shape of the spectrum across ~ 23 decades in frequencies. The combination experiments probing such different frequency ranges allows to characterize the SGWB beyond the simple detection of primordial tensor modes: this will be extremely important in determining a candidate primordial SGWB originated from quantum vacuum fluctuations in the metric tensor, compatibly with the standard single-field slow-roll scenario, or from alternative scenarios that can also produce the SGWB. In this respect, we perform forecasts also on the promising SU(2)-axion inflation scenario, in addition to the standard single-field slow-roll model.

Concerning CMB and Pulsar Timing Array experiments, we consider the LiteBIRD mission and the Square Kilometre Array (SKA) survey (Weltman et al., 2020), respectively, while for the interferometers we consider space mission proposals including the Laser Interferometer Space Antenna (LISA) (Baker et al., 2019; Smith and Caldwell, 2019), the Big Bang Observer (BBO) (Crowder and Cornish, 2005b; Smith and Caldwell, 2017), the Deci-hertz Interferometer Gravitational wave Observatory (DECIGO) (Seto et al., 2001; Kawamura et al., 2020), μAres (Sesana et al., 2019), the Decihertz Observatory (DO) (Sedda et al., 2019) and the Atomic Experiment for Dark Matter and Gravity Exploration in Space (AEDGE) (El-Neaj et al., 2019), as well as the ground-based Einstein Telescope (ET) (Hild et al., 2011) proposal. In this observational context, we implement the mathemat-

ics needed to compute sensitivities for both CMB and interferometers, and derive the response functions for the latter from the first principles. Furthermore, we provide frequency integrated error bars from the binned sensitivity curves for all the detectors, we include astrophysical foregrounds for all experiments and we use the latest and realistic CMB sensitivity curves for the LiteBIRD mission, including state-of-the-art simulations for the CMB foregrounds.

This Thesis is organized as follows. In Chapter 1 we will briefly review the standard (ΛCDM) cosmological model from its founding principles to the inflationary paradigm and we will summarize its observational successes, predictions and limitations, with a particular focus on the production of a primordial SGWB. Chapter 2, will be dedicated to introducing the CMB as a tool for the detection of primordial GWs. In Chapter 3, we will give an overview on the observational status of current and future experiments that will target the detection and characterization of the primordial SGWB, including CMB *B*-mode probes, interferometers and Pulsar Timing Array surveys. As anticipated above, in Chapter 4 (based on the work Campeti et al., 2019b), we will explore the possibility of constraining the shape of the primordial SGWB with future CMB B-modes in model-independent way, within the framework of Principal Component Analysis. As we also mentioned above, in Chapter 5 (based on the work Campeti et al., 2020) we will extend the analysis of Chapter 4 by including constraints from interferometers and Pulsar Timing Arrays, in addition to CMB B-mode probes. Finally, in Chapter 6, we will summarize our work in this Thesis and outline the conclusions and future work perspectives.

Part I

Primordial Gravitational Waves in the Standard Cosmological Model

1
Standard Cosmology

In this Chapter, we are going to review the current standard cosmological model – named ΛCDM after the Cosmological Constant Λ and the Cold Dark Matter (CDM) model as will be explained later – predicting, among other things, the generation of a primordial *Stochastic Background of Gravitational Waves* (hereafter SGWB), which will be the common thread of this Thesis.

We will start from the cornestones of standard cosmology, i.e. general relativity and the Cosmological Principle (Sections 1.1) and we will use them to justify the introduction of the Friedmann-Lemaître-Robertson-Walker metric of the Universe (Section 1.2). This will lead us to the Einstein field equations, from which we will derive the Friedmann and continuity equations in order to study the dynamics and content of the Universe (Section 1.3). We will then use several observational evidences to introduce the Big Bang model – basis of the current ΛCDM model – and highlight its main features (Sections 1.4 and 1.5): an initial very high temperature state in which matter is ionized and in thermodynamic equilibrium; the expansion; the epochs of radiation, matter and Cosmological Constant domination; a thermal history in which the expansion determines the cooling of the Universe and the consequent decoupling of particle species. Section 1.6 will be dedicated to describe one of the most important predictions of the Big Bang model: the existence of a cosmic microwave background (CMB) of photons of primordial origin. We will then discuss some of the problems of the Big Bang model (Section 1.7). Among them, the fact that we have to postulate the existence of two dark components, dark energy and Dark Matter, the singularity problem, the horizon problem and the flatness problem. In Section 1.8 we will see how cosmic inflation, an early era of accelerated cosmic expansion driven by fundamental quantum fields, can solve some of these issues and we will summarize the main prediction of this paradigm regarding the production of scalar and tensor perturbations primordial power spectra. We will finish this Chapter by discussing a relevant quantity which is used in the current literature for describing the SGWB and which will be useful throughout this Thesis: the gravitational wave energy density (Section 1.9).

This chapter benefited from the reading of the following books Peter and Uzan (2013), Dodelson (2003), Amendola and Tsujikawa (2015), Maggiore (2018), in addition to specific references indicated in the text.

1.1 *Foundations*

Although cosmology as a branch of philosophy may be as old as humankind itself (see Harrison (2000) for an historical review), the root of modern physical cosmology – the effort of understanding the structure, content and evolution of the Universe using methods

belonging to the physical sciences – could arguably be traced back to the formulation of the *Copernican principle* (see for instance Chamcham et al., 2017; Ellis, 2006, and references therein). This principle states that we do not occupy a special place – that is the centre – of the Universe, or, in other words, that we are not privileged observers. Such an apparently simple idea represented a paradigm shift in the history of human thought, and laid the foundations for the modern cosmological model, as we are going to explain in the rest of this Section.

Since modern cosmology, like any other physical science, must pass the test of empirical data, we make a distinction in terminology between the *Observable Universe* – that is the portion of the Universe from which we are able to gather astrophysical and cosmological data – and the *Universe*, which includes unobservable regions lying outside the reach of our experiments. The only way we can infer the properties of the Universe from the Observable Universe is by making several assumptions or hypotheses; in particular, the modern *standard cosmological model* is based on four founding hypotheses:

1. General Relativity (GR) is the theory of gravitation. Einstein's theory describes the mutual dynamical interaction between the space-time structure and its content. GR is well tested on Solar System scales and in the very strong field limit, thanks to the first observations of a binary black hole merger and binary neutron star inspiral by the LIGO collaboration (Abbott et al., 2016, 2017). However, it has not been tested yet neither on cosmological scales nor at early times in the Universe history.

2. Symmetry prescriptions. In order to solve Einstein equations, it is necessary to add to the previous hypotheses a prescription for space-time symmetries. The textbook approach is usually to employ the Copernican principle together with the assumption that the Universe is isotropic, to justify the introduction of the *Cosmological Principle*, stating the statistical homogeneity and isotropy of the Universe on distances larger than its largest structures ($\sim 100\,\mathrm{Mpc}$). However, this formulation of the Cosmological Principle, extends the space-time properties above also to unobservable regions of the Universe, and thus cannot be tested. In this respect, the Cosmological Principle can be regarded as an a priori prescription for the initial conditions of the Universe. A more modern and empirically based approach consists in using the Copernican principle together with the isotropy of Large Scale Structure and CMB observations (see Section 1.6 below) to conclude that the

Observable Universe is statistically homogeneous and isotropic on sufficiently large scales (Ellis et al., 2012). Note also that the Copernican principle does not have to be a philosophical prejudice and can be observationally tested (see for instance Clarkson, 2012; Ellis et al., 2012, and references therein).

3. MATTER CONTENT AND ITS NON-GRAVITATIONAL INTERACTIONS. We will assume that on cosmological scales matter can be modelled as a mixture of a pressureless fluid and radiation, plus a Cosmological Constant (see Section 1.3 below). Moreover, our astrophysical and cosmological observations can probe particular objects (i.e. galaxies, clusters etc.) and not the matter distribution itself. Therefore, it will be necessary to quantify how much individual objects are representative of the true underlying distribution.

4. TOPOLOGY. The three previous hypotheses allow us to determine the local structure of the Universe, that is its *geometry* but not the global structure, i.e. its *topology*. The usual textbook approach, in this case, is to implicitly assume that the local structure coincides with the global one, since most of the predictions of the model are insensitive to this hypothesis. However, it should be noted that cosmic topology can be observationally investigated (especially using CMB data Planck Collaboration, 2016a) and is still subject of inquiry (see for instance Luminet, 2016, for a recent review).

The rest of this Chapter will be dedicated to building the modern cosmological model starting from these four hypotheses. First of all, we will combine the first two hypotheses – GR and and the Cosmological Principle – and introduce the Friedmann-Lemaître-Robertson-Walker (FLRW) metric.

1.2 *The Friedmann-Lemaître-Robertson-Walker Metric*

The properties of homogeneity of space (i.e. that at every moment in time each point of the space is similar to any other) and isotropy (i.e. no preferred direction) of the Universe, as stated by the Cosmological Principle, can be summarized just by saying that every observer sees an isotropic Universe around him. These properties allow to reduce the general form of the space-time metric to the so-called FLRW metric, which reads

$$ds^2 = g_{\mu\nu}dx^\mu dx^\nu = -dt^2 + a^2(t)d\sigma^2 \tag{1.1}$$

and $c = 1$ will be assumed for convenience thoughout this Chapter. Here $g_{\mu\nu}$ is the metric tensor and the scale factor $a(t)$ – which is a function of cosmic time t, that is the time measured by an observer seeing the Universe uniformly expanding around him – encodes the possibility of an expanding Universe (as observed by Hubble in 1929, see Section 1.4 below), and is usually normalized at the present time t_0, $a(t_0) = a_0 = 1$. The term $d\sigma^2$ in Eq. 1.1 represents the metric of the three-dimensional space with constant curvature K, that is

$$d\sigma^2 = \gamma_{ij} dx^i dx^j = \frac{dr^2}{1 - Kr^2} + r^2(d\theta^2 + \sin^2\theta d\phi^2), \tag{1.2}$$

which does not depend on time. Notice that in these last two equations we have chosen *comoving coordinates* (r, θ, ϕ), that is coordinates defined in a reference frame expanding with the Universe and therefore constant in time.

The curvature K will be positive, negative or zero, corresponding to closed, open and flat geometries, respectively. Taking a positive curvature constant produces the metric of a three-sphere: the space in this case is finite but has no boundary. The zero curvature case simply corresponds to the flat Euclidean space, while negative curvature generates a hyperbolic space; both these spaces are usually taken to be infinite although in principle it would be possible to obtain the same local geometry with finite spaces, once one imposes appropriate periodicity conditions (see for instance the textbooks Carroll, 2019; Weinberg, 2008, and references therein). We note incidentally that the spatial metric in Eq. 1.2 is often reported in the literature using the coordinate transformation

$$r = f_K(\chi) = \begin{cases} K^{-1/2} \sin\left(K^{1/2}\chi\right) & \text{if } K > 0, \\ \chi & \text{if } K = 0, \\ (-K)^{-1/2} \sinh\left((-K)^{1/2}\chi\right) & \text{if } K < 0, \end{cases} \tag{1.3}$$

in the form

$$d\sigma^2 = d\chi^2 + f_K^2(\chi)(d\theta^2 + \sin^2\theta d\phi^2). \tag{1.4}$$

We also define here some quantities related to the FLRW metric, and, in particular to the scale factor $a(t)$, that will prove to be useful in the rest of this chapter. We start with the *conformal time* τ, defined as

$$d\tau \equiv \frac{dt}{a(t)}. \tag{1.5}$$

We define then the *Hubble parameter* (where the dot indicates derivative with respect to time), as

$$H = \frac{\dot{a}}{a}; \tag{1.6}$$

its value today is denoted by H_0 and is often expressed in terms of the *reduced Hubble parameter* h, as in

$$H_0 = 100h\,\mathrm{km\,s^{-1}\,Mpc^{-1}}. \tag{1.7}$$

It will be also useful in later Sections to define the characteristic distance and time scale for a FLRW Universe, that is the *Hubble time* and *Hubble radius*

$$t_H = R_H = H^{-1}, \tag{1.8}$$

which are coinciding, since we adopted $c = 1$ in this Chapter. Finally, we quantify the effect cosmic expansion has on the wavelenght λ_{em} of photon emitted at time t_{em} and observed with wavelenght λ_{obs} at time t_{obs}, through the *cosmological redshift* z

$$\frac{a(t_{obs})}{a(t_{em})} = \frac{\lambda_{obs}}{\lambda_{em}} \equiv 1 + z. \tag{1.9}$$

1.3 *Universe Content and Dynamics*

The mutual interaction between the space-time metric and the matter-energy content of the FLRW Universe is expressed in GR by *Einstein field equations*,

$$G_{\mu\nu} = 8\pi G T_{\mu\nu}, \tag{1.10}$$

where the Einstein tensor $G_{\mu\nu} = R_{\mu\nu} - g_{\mu\nu}R/2$ contains derivatives of the metric tensor $g_{\mu\nu}$ through the Ricci scalar R and tensor $R_{\mu\nu}$, and $T_{\mu\nu}$ is the energy-momentum tensor for the matter components of the Universe. The latter is restricted by the FLRW metric to take the perfect fluid form, that is

$$T^{\mu}_{\nu} = (\rho + P)u^{\mu}u_{\nu} + P\delta^{\mu}_{\nu}, \tag{1.11}$$

where ρ and P are the energy density and the pressure of the fluid, respectively, and $u^{\mu} = (-1, 0, 0, 0)$ is the four-velocity of the fluid in comoving coordinates.

We can now use Einstein equations in order to the study the dynamics of a FLRW Universe. First, by taking the (00) and (ii) components of the Einstein equations and eliminating common terms, we get the two *Friedmann equations*

$$H^2 = \left(\frac{\dot{a}}{a}\right)^2 = \frac{8\pi G}{3}\rho - \frac{K}{a^2} \tag{1.12}$$

$$\frac{\ddot{a}}{a} = -\frac{4\pi G}{3}(\rho + 3P). \tag{1.13}$$

Moreover, using the fact that the Einstein tensor satisfies the Bianchi identities (implying $\nabla_{\mu}G^{\mu}_{\nu} = 0$), we get the third fundamental equation describing the Universe dynamics, the *conservation* or *continuity*

equation:

$$\dot{\rho} + 3H(\rho + P) = 0. \tag{1.14}$$

On closer inspection, it is evident that only two of the three equations 1.12, 1.13 and 1.14 are independent, while the unknowns are three: the scale factor, the energy density and the pressure of the cosmological fluid mixture. Therefore we need to provide a third relation in order to solve the system: this is accomplished connecting the energy density and pressure of the fluid through an *Equation of State* (EoS), that is

$$P = w\rho. \tag{1.15}$$

The EoS for radiation is $w = 1/3$, the one for pressureless or "dust-like" matter (modeling for instance the matter in galaxies and gas) will have $w = 0$, the Cosmological Constant Λ will be described by a fluid $w = -1$ (which may be also called *dark energy*), while the curvature term can also be seen as a fluid with $w = -1/3$. We also note that for a component with constant EoS w, the continuity equation gives

$$\rho \propto a^{-3(1+w)}. \tag{1.16}$$

Using also the first Friedmann equation together with the continuity one allows to write the scale factor evolution in time as

$$a(t) \propto \begin{cases} t^{\frac{2}{3(1+w)}} & \text{if } w \neq -1, \\ e^{Ht} & \text{if } w = -1. \end{cases} \tag{1.17}$$

The first Friedmann equation (Eq. 1.12) can also be rewritten as

$$\sum_X \Omega_X + \Omega_K = 1, \tag{1.18}$$

where

$$\Omega_K = -\frac{K}{(aH)^2} \tag{1.19}$$

is the energy density associated to curvature and

$$\Omega_X = \frac{8\pi G \rho_X}{3H^2}, \tag{1.20}$$

called *density parameter*, represents a generic matter-energy component X, such as relativistic particles (including photons, neutrinos and gravitons), non-relativistic matter (including *baryons* and *cold Dark Matter*) and dark energy. We will describe in more detail each of these cosmic components in a moment.

In the following we will also find it useful to define the *critical density of the Universe* ρ_c as the energy density for which $\sum_X \Omega_X = 1$,

$$\rho_c = \frac{3H^2}{8\pi G}. \tag{1.21}$$

Therefore, we get from the first Friedmann equation that if $\rho = \rho_c$ the Universe will be spatially flat ($K = 0$), if $\rho < \rho_c$ it will an open Universe, and if $\rho < \rho_c$ it will be a closed one.

Taking a closer look at Eq. 1.16, we can see that the larger is the factor w in the EoS of a component, the more important such a component becomes as the scale factor a shrinks going back in time towards the birth of the Universe. We can therefore separate the evolution of the Universe in four main regimes, depending on which one of the components is dominating over the others in a specific cosmological era. We list them here in chronological order.

Radiation-dominated era. The term "radiation" indicates any form of matter-energy characterized by having an EoS with $w = 1/3$, which is the case for a gas of relativistic particles. Since this relativistic matter – which includes photons, neutrinos and gravitons produced in the very early Universe – has the largest value of w among all other cosmic components, and therefore

$$\rho \propto a^{-4}, \tag{1.22}$$

from Eq. 1.16, it is the first to dominate in cosmic history. We can understand the behaviour in Eq. 1.22 in a very simple way: the number density of photons, for instance, is inversely proportional to the volume and therefore goes as $\propto a^{-3}$; however the energy density is the product between the number density and the average energy per particle, and the latter goes as $\propto a^{-1}$ due to cosmological redshift (see Section 1.2). Another interesting conclusion that we can draw from Eq. 1.16, is that in the early Universe the temperature was much higher than today. This can be seen for instance by applying the previous argument to the temperature T_{CMB} of the photons of the CMB today, which has been very well constrained to

$$T_{CMB} = 2.7260 \pm 0.0013 \tag{1.23}$$

using FIRAS (Far Infrared Absolute Spectrophotometer) and WMAP (Wilkinson Microwave Anisotropy Probe) data (Fixsen, 2009). In this case, the temperature of the primordial plasma at very early times increases going backwards in time according to the formula

$$T(t) = \frac{T_{CMB}}{a(t)}. \tag{1.24}$$

Matter-dominated era. As time passes the Universe expands and becomes dominated by the matter component, since its energy density goes as

$$\rho \propto a^{-3}. \tag{1.25}$$

We denote by "matter" any form of collisionless matter-energy, that is having pressure much smaller that its energy density ($w = 0$). Such an EoS is typical of a gas of non-relativistic particles, and in the cosmic budget includes baryonic matter and Dark Matter. The term baryonic matter comprises all particles included in the standard model of particle physics that can interact electromagnetically, mostly protons, neutron and electrons.

Dark matter is a form of matter invisible through electromagnetic observations, and its existence can be inferred by observing its gravitational effect on the visible matter and radiation. There are several observational indications of the existence (or the necessity) of Dark Matter, among others, the rotational speeds of galaxies, gravitational lensing, the temperature distribution of hot gas in galaxies and clusters of galaxies, the angular power spectrum of CMB anisotropies (see for instance the recent review by Di Paolo and Salucci, 2020, and references therein).

In the standard cosmological model, the Dark Matter component is modelled as a CDM component and consists in an additional collisionless fluid (with $w = 0$) coupled to matter (almost) only by gravity. Currently, the most suitable candidate for CDM is represented by massive particles – named *Weakly Interacting Massive Particles* (WIMPS) – very weakly interacting with each other and with other cosmic components.

Dark matter is thought to be a fundamental ingredient for the formation of the cosmic large scale structure that we observe today, in particular by providing deep initial potential wells.

Despite the efforts of the astroparticle physics community, the DM particle has not been detected yet (apart from an announcement by the DAMA experiment Bernabei et al., 2018, on which there is at the moment no consensus in the community) but remains one of the major focuses of current research (Arcadi et al., 2018).

Current observations suggest that baryonic matter represents only $\sim 5\%$ of the total energy budget, while Dark Matter constitutes the $\sim 27\%$ of the matter-energy content of the Universe (Planck Collaboration, 2018).

Curvature-dominated era. As we anticipated, curvature appears in the first Friedmann equation with a term $-K/a^2$ but can be regarded equivalently as a cosmological fluid with $w = -1/3$ and energy-density evolving with the scale factor as

$$\rho \propto a^{-2}. \tag{1.26}$$

However, we will see in Section 1.4.2 that the curvature of the Universe is compatible with zero according to current observations.

Dark energy-dominated era. As we will study in more detail in Sections 1.4.2 and 1.7.6, current observations point out that the Universe is currently subject to an accelerated expansion. In the standard cosmological model a fluid component with constant EoS $w = -1$, named dark energy, is conventionally held responsible for this phenomenon, although other candidates exist and are constantly scrutinized as observations improve. Note that the effect of this fluid is completely equivalent to that of a Cosmological Constant Λ, therefore including dark energy in the Einstein field equations inside the matter-energy budget in the right-hand-side or in the left-hand-side as a Cosmological Constant term, (that is $G_{\mu\nu} + \Lambda g_{\mu\nu} = 8\pi G T_{\mu\nu}$) gives the same results. The standard cosmological model takes the name of ΛCDM after this dark energy or Cosmological Constant term and after the CDM model for Dark Matter.

The energy density resulting from Eq. 1.16 for this component is constant

$$\rho \propto const. \tag{1.27}$$

and is the last one to dominate the Universe.

Dark energy, according to latest observations, constitutes a striking $\sim 68\%$ of the whole cosmic energy budget and its mysterious nature constitutes one of the greatest challenges for current research.

We close this Section stating one of the most important predictions of the standard cosmological model: an inevitable consequence of extrapolating the expanding FLRW cosmological solution to the initial time is that the scale factor becomes zero at this time $a(t) = 0$, creating a singularity in space-time which is usually called *Big Bang*. We will see in Section 1.7.1 that this represents a limit for the model and that this conclusion is likely to be challenged by quantum gravity theories.

1.4 *Expansion History*

Cosmologists have been accumulating observational evidences of the expansion of the Universe for more than ninety years, starting with Hubble's work in 1929 (Hubble, 1929). Moreover, around twenty-two years ago, simultaneous astronomical observations of distant Type Ia Supernovæ by the two groups HSST (High-Redshift Supernova Research Team, Riess et al., 1998) and SCP (Supernova Cosmology Project, Perlmutter et al., 1999) pointed out that the cosmic expansion is accelerating today, a fact that currently seems to be understandable only postulating the existence of a dark energy component.

1.4.1 *Cosmological distance measurements*

First of all we must stress that cosmological distances cannot be measured directly, and the purely geometrical parallax method can be used only for the closest stars to our Galaxy. One method is to use the *intrinsic luminosity* L of a *standard candle* – that is a class of objects for which it is known to be constant (or correlated to another parameter independent of the distance) – and measure the flux F coming from the same object, to compute the so-called *luminosity distance*

$$D_L = \sqrt{\frac{L}{4\pi F}} = (1+z) f_K(\chi), \tag{1.28}$$

where

$$\chi = \frac{1}{H_0} \int_0^z dz' \frac{H_0}{H(z')}. \tag{1.29}$$

The dependence of the Hubble rate from the redshift, obtained from the first Friedmann equation and Eq. 1.16, can then be expressed as

$$H^2(z) = H_0^2 \left[\Omega_r^{(0)} (1+z)^4 + \Omega_m^{(0)} (1+z)^3 + \Omega_K^{(0)} (1+z)^2 + \Omega_\Lambda^{(0)} \right], \tag{1.30}$$

where $\Omega_X^{(0)}$ indicates the density parameter for each component at present time and the index $X = r, m, K, \Lambda$ stands for radiation, non-relativistic matter (which includes baryons and CDM $\Omega_m = \Omega_b + \Omega_c$), curvature and dark energy, respectively. One can then measure the redshift z (Eq. 1.9) of the object via spectroscopic observations and extract the value of the Hubble parameter today H_0 from Eq. 1.28.

The equivalent of standard candles for the angular size are called *standard rulers*: the principle is completely similar to the previous one, but this time we know the transverse physical size of an object dS_{source}, we measure the solid angle under which it is observed $d\Omega^2_{obs}$ and compute the *angular distance*:

$$D_A = \sqrt{\frac{dS_{source}}{d\Omega^2_{obs}}} = \frac{f_K(\chi)}{(1+z)}. \tag{1.31}$$

Hubble's measurement, although plagued by large systematic errors due to the calibration of the standard candles he was using (Cepheid variables in particular), can be regarded as the first attempt at measuring the expansion rate. In particular, the relations 1.28 and 1.31, in the hypothesis of small redshift $z \ll 1$, reduce to the *Hubble Law*

$$D_A \sim D_L \sim \frac{z}{H_0} \sim \frac{v}{H_0}, \tag{1.32}$$

where v is the recession velocity with which galaxies in an expanding Universe are moving away from each other. In this low redshift case, the slope of the curve in the plane v vs D_L gives the Hubble

parameter (Figure 1.1) today, however to extend the measurement to larger redshifts, we need to use other kinds of standard candles or distance indicators.

At the moment, the two most precise methods to measure H_0 are, on one hand, astronomical observations using Type Ia supernovæ (SN Ia) as standard candles[1] (for instance Riess et al., 2019) calibrated using Cepheid variables[2] or other local distance indicators, and, on the other hand, CMB observations, by assuming the ΛCDM model and and inferring the expansion rate from the sound horizon at recombination, which represents a standard ruler (Planck Collaboration, 2018). In a similar way, H_0 can be determined also without CMB observations, by putting together Baryon Acoustic Oscillation (BAO), big bang nucleosynthesis (BBN), and weak lensing data (Abbott et al., 2018). Unfortunately, there exists a 4.4σ tension between the values of H_0 determined by the SH_0ES experiment – obtained using SN Ia and Cepheids in the Large Magellanic Cloud for calibration – that is (Riess et al., 2019)

$$H_0 = 74.03 \pm 1.42\,\mathrm{km\,s^{-1}\,Mpc^{-1}}, \tag{1.33}$$

and the Planck measurement (Planck Collaboration, 2018)

$$H_0 = 67.4 \pm 0.50\,\mathrm{km\,s^{-1}\,Mpc^{-1}}. \tag{1.34}$$

The remarkable tension between these two measurements – which refer to two extremely different epochs of cosmic history – has stimulated discussion within the cosmology community, with multiple attempts of experimental and theoretical explanation (see for instance Knox and Millea, 2020), development of alternative ways of measuring H_0, for instance using GWs as standard sirens (The LIGO Scientific Collaboration et al., 2019), real-time cosmology observations of the Hubble cooling of the CMB monopole temperature (Abitbol et al., 2019), the strong gravitational lensing of quasars (Wong et al., 2020; Shajib et al., 2020), alternative candles like Mira variables stars (Huang et al., 2019), the tip of the Red Giant Branch of stellar evolution (Freedman et al., 2019), or new data analysis techniques (Kozmanyan et al., 2019; Reid et al., 2013; Jimenez et al., 2019). Despite this effort, the H_0-tension still remains an open and central issue in modern cosmology.

1.4.2 *Cosmic acceleration*

In 1998, two groups independently reported evidences for a late-time acceleration in the cosmic expansion, using observations of SN Ia up to redshift $z \sim 1$ (Riess et al., 1998; Perlmutter et al., 1999). For such redshifts, the Hubble law (Eq. 1.32) does not hold anymore and

[1] Type Ia supernovæ are produced when one of the stars in a binary system is a white dwarf accreting matter from the other companion star. The white dwarf will eventually reach the Chandrasekhar limit, collapse and explode in a supernova. It has been observed in local ($z \ll 1$) SN Ia samples that the absolute magnitude can be correlated with the width of the luminosity curve, and by measuring simultaneously the apparent magnitude and the luminosity curve it is possible to predict the absolute magnitude. They are therefore considered to be good standard candles, and they can be used up to redshift $z \sim 1$.

[2] Cepheids are variable stars which emit pulses with a period between 2 and 100 days. The theory behind their pulsation mechanism is very well understood and therefore they can be used as standard candles. However, their detection extends only to about 20 Mpc and their most precise calibration is currently performed on the Large Magellanic Cloud, and for larger distances we need to use other types of standard candles.

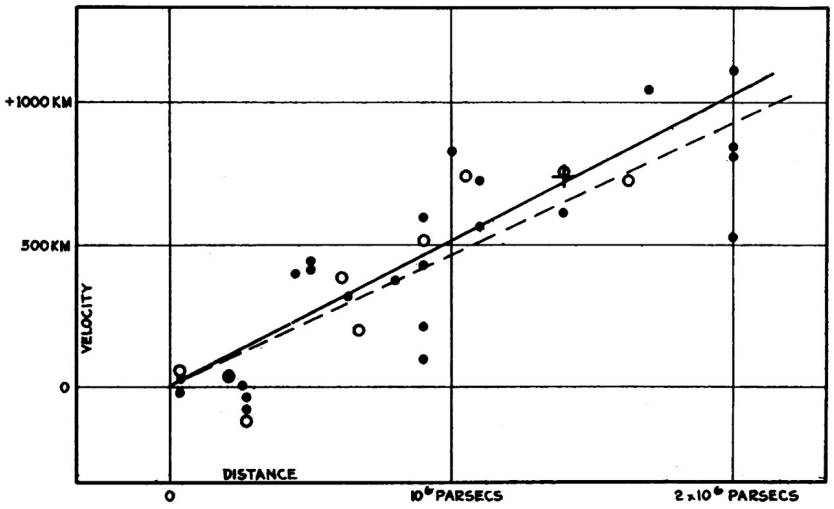

Figure 1.1: Original observations of the recession velocity and distance of galaxies by Hubble in 1929 (From Hubble (1929)). Hubble was the first to measure the expansion of the Universe, proposing a value $H_0 = 500\,\mathrm{km\,s^{-1}\,Mpc^{-1}}$, much higher than today's accepted value.

the appropriate expression for the distance luminosity is the one in Eq. 1.28, which depends on the cosmological density parameters. This last relation can be used to infer that, assuming the ΛCDM model, SN Ia data clearly favors a dark energy-dominated Universe, and current Planck satellite CMB and BAO observations, which indicate that the Universe is flat[3] (Planck Collaboration, 2018), report indeed a dark energy density[4]

$$\Omega_\Lambda = 0.6847 \pm 0073. \tag{1.35}$$

Combining recent SN Ia data from the Pantheon survey with CMB data from the Planck experiment and BAO data (Planck Collaboration, 2018) the EoS of dark energy is tightly constrained to be

$$w_{de} = -1.03 \pm 0.03, \tag{1.36}$$

compatible with a Cosmological Constant.

Note that the hypothesis that SN Ia are actually good standard candles has been repeatedly tested, for instance by exploring the possibility of observational biases, variation of their properties with cosmic time, dimming effect of interstellar medium and gravitational lensing. However, the evidences are confirming the cosmic acceleration explanation and new observations have been added, further improving the robustness of the result.

As we will discuss in more detail in Section 1.7.6, the existence of dark energy (and of Dark Matter as well) has to be postulated in the ΛCDM model, and currently we have no deep understanding of this component. A plethora of models – both theoretical and phenomenological – has been considered for explaining dark energy beyond the

[3] In Planck Collaboration (2018) the constraint on the curvature density parameter is found to be $\Omega_K = 0.0007 \pm 0.0019$, adopting the data combination *TT,TE,EE+lowE+lensing+BAO* to break the degeneracy. As we will explain in detail in Chapter 2, here *TT* indicates the CMB temperature power spectrum, while *EE* indicates the *E*-type polarization one and *TE* the cross-correlation between the two. Lensing data will also be discussed later in Chapter 2.

[4] This result adopts the *TT,TE,EE+lowE+lensing* data combination (see discussion in footnote 3).

standard Cosmological Constant scenario, including modifications of GR (see Planck Collaboration, 2016b; Ishak, 2019, and references therein). However, further testing is needed and useful indications on the nature of dark energy (and also Dark Matter) are likely to come from the future Euclid mission (Laureijs et al., 2011; Amendola et al., 2018), which will reconstruct the clustering of galaxies up to $z \sim 2$ and weak lensing up to $z \sim 3$.s

1.5 *Thermal History of the Universe*

As we anticipated in Section 1.3 (and in particular in Eq. 1.24), we can expect the Universe to increase its temperature as we go backwards in time and towards the big bang singularity, until we reach an initial extremely hot and dense plasma state in which radiation (photons) and matter where in thermodynamic equilibrium. In particular, we can compute the temperature above which radiation start to become important, that is the temperature at matter-radiation equivalence,

$$T_{eq} = T_{CMB}(1 + z_{eq}) \simeq 6.56 \times 10^4 \Omega_m^{(0)} h^2 \,\mathrm{K}, \tag{1.37}$$

where T_{CMB} is the CMB temperature today and z_{eq} is the redshift of matter-radiation equivalence.

The cosmic thermal history will be characterized by the competition between two quantities: on one side the *reaction rate* Γ of particle interactions, on the other the Hubble *expansion rate* H. The *thermodynamic equilibrium* at a temperature T is achieved if $\Gamma \gg H$, and in this case the particle species can be treated according to a *Fermi-Dirac* or *Bose-Einstein* distribution

$$F_i(E,T) = \frac{g_i}{(2\pi)^3} \frac{1}{\exp\left[(E-\mu_i)/T_i(t)\right] \pm 1} = \frac{g_i}{(2\pi)^3} f_i(E,T), \tag{1.38}$$

where, for each particle species i of mass m and momentum p at temperature T_i, g_i represents the degeneracy factor, μ_i the chemical potential and its energy is given by $E^2 = p^2 + m^2$.

The *temperature of the Universe* T at a certain cosmic epoch will be equal to the photon temperature T_γ, since the interacting particle species at equilibrium will have all the same temperature. If the temperature of the Universe, because of the expansion, goes below a certain threshold set by the cross-section of each interaction, the equilibrium is broken, the particle *decouples* and the interaction is *frozen*.

Another important concept governing the cosmic thermal history is that particle-antiparticle pairs are produced when the photons energy is large enough, that is $T > 2m$ for a particle species of mass m.

Let us now consider what happens when the reaction rate of a particle species, that was before in thermodynamic equilibrium with the primordial plasma, drops below the expansion rate. The form of its distribution function at decoupling time t_D is given by the function $f_i[\mathbf{p}, t_D]$, defined in Eq. 1.38; after decoupling the particles will propagate freely, conserving the form of f, while the momentum $\mathbf{p}$ will be redshifted, according to $\mathbf{p} \to [a(t)/a(t_D)]\mathbf{p}$. Particle species can decouple either when they are relativistic ($T \gg m$) or when they are non-relativistic ($T \ll m$); in the former case the temperature of the species will decrease in time as $T_i = T(t_D)[a_D/a(t)]$ and its distribution function becomes

$$f_i(\mathbf{p}, t > t_D) = \frac{1}{\exp\left[E/T_i(t)\right] \pm 1}, \tag{1.39}$$

while in the latter case we have $T_i = T(t_D)[a_D/a(t)]^2$ and

$$f_i(\mathbf{p}, t > t_D) = e^{-(m-\mu)/T(t_D) - p^2/(2mT_i(t))}. \tag{1.40}$$

The last fundamental concept in order to understand the thermal evolution of the Universe can be derived from the conservation of entropy s, that is

$$s = \frac{2\pi^2}{45} g_{s*}(T) T^3, \tag{1.41}$$

with

$$g_{s*}(T) = \sum_{i=bosons} g_{s*i} \left(\frac{T_i}{T}\right)^3 + \frac{7}{8} \sum_{i=fermions} g_{s*i} \left(\frac{T_i}{T}\right)^3, \tag{1.42}$$

being the *effective number of relativistic degrees of freedom* contributing to the entropy. When a particle species becomes non-relativistic, the temperature of the remaining relativistic particles is boosted according to

$$T_{(+)} = \left[\frac{g^{(-)}_{s*\gamma}}{g^{(+)}_{s*\gamma}}\right]^{1/3} T_{(-)}, \tag{1.43}$$

where $g_{s*\gamma}$ is given by 1.42 summing only over relativistic particles in equilibrium with the photons and $(+)$ and $(-)$ indicate values after and before decoupling, respectively. Armed with these tools, we can now describe – in chronological order – some of the most relevant events during the cosmic thermal history.

Planck epoch and radiation-dominated regime. For temperature above 10^{16}GeV, the physics is not still well understood: the matter composition of the Universe represents the main uncertainty as the particle species present at this time may not be evident today. Moreover, GR may break down and quantum gravity effects may

become very important for energies equal or above the Planck mass $m_{Pl} = 1/\sqrt{G} \approx 1.22 \times 10^{19}$GeV, in the so-called *Planck epoch*.

In the energy range comprised between 10^{16}GeV $\approx$ 10^{29}K and 1GeV $\approx$ 10^{13}K there are not unique theoretical predictions at the moment, and several models describing the physics of the Universe have been developed. Moreover, terrestrial particle accelerators allow us to understand the range between $\sim$ 10 TeV and $\sim$ 1GeV, but only below 1GeV we can currently trace back the cosmic evolution with a relatively good accuracy. At about 100GeV the *electroweak phase transition* happens, and particles receive their masses via the Higgs mechanism; somewhere before sthere has to be some dynamical mechanism producing an asymmetry in the number of baryons and antibaryons, with the latter being much less than the former in our Universe. This process is called *baryogenesis* and we will give more details in Section 1.7.4. At temperatures below $\sim$ 200MeV the *QCD phase transition* takes place: free quarks and gluons form baryons and mesons.

At temperature $T \sim 10^{12}$ K, as we anticipated in Section 1.3, the Universe is in thermodynamic equilibrium and is dominated by relativistic particles. In this regime, the radiation energy density can be computed as

$$\rho_r = g_*(T) \left(\frac{\pi^2}{30}\right) T^4, \tag{1.44}$$

where the index i runs over the particle species and g_* is the *effective number of relativistic degrees of freedom* contributing to the energy density

$$g_* = \sum_{i=bosons} g_{*i} \left(\frac{T_i}{T}\right)^4 + \frac{7}{8} \sum_{i=fermions} g_{*i} \left(\frac{T_i}{T}\right)^4. \tag{1.45}$$

At this temperature, the primordial plasma is composed of ultra-relativistic electrons and positrons (since the temperature is higher than the electron rest mass, $T > m_e \approx 0.5$MeV $\approx 6 \times 10^9$K), neutrinos, neutrons and protons and of course photons. The chemical potential of photons is $\mu_\gamma = 0$, since the number of photons in the interactions is not conserved, therefore they must follow a blackbody distribution. The equilibrium between electrons and positrons is mantained by the reaction

$$e + \bar{e} \longleftrightarrow \gamma + \gamma. \tag{1.46}$$

Using the chemical potential conservation for this reaction and the electrical neutrality of the Universe (the number of electrons and protons is equal and we can use therefore the constraint on the

baryon to photon ratio today $n_b/n_\gamma \sim 5 \times 10^{-10}$), it is possible to infer that, after *electron-positron annihilation* ($T \sim m_e$), the ratio of the excess of electrons over positrons and the photon density will be

$$\frac{n_e - n_{\bar{e}}}{n_\gamma} \simeq 1.33 \frac{\mu}{T} \simeq 10^{-8}, \tag{1.47}$$

and therefore the chemical potential for electrons and positrons can be neglected as well.

Cold Dark Matter relics. If we assume that Dark Matter is produced in the early Universe in the form of weakly interacting massive particles (WIMPs) and initially was in thermodynamic equilibrium with the cosmic plasma (see Section 1.3), we can reproduce pretty well the observed Dark Matter density, though a caveat is represented by the fact that for a proper treatment of the Dark Matter evolution the equilibrium description adopted until now is not sufficient anymore, and the introduction of the Boltzmann equation is required (see Section 1.6). We will present here the main results concerning the WIMP hypothesis without any derivation; a detailed treatment can be found for instance in Arcadi et al. (2018). We assume that a heavy Dark Matter particle X and its antiparticle $\bar{X}$ can remain in thermodynamic equilibrium annihilating into two light particles l and $\bar{l}$ via the interaction

$$X + \bar{X} \longleftrightarrow l + \bar{l}, \tag{1.48}$$

as long as the T is larger than its mass. If this particle decouples while it is non-relativistic, it produces a so-called *cold relic*: in this case the density parameter for a cold relic (Arcadi et al., 2018) can be expressed as

$$\Omega_c h^2 \approx 8.76 \times 10^{11} \mathrm{GeV}^{-2} \left[\int_{T_0}^{T_f} g_*^{1/2} \langle \sigma v \rangle \frac{dT}{m} \right]^{-1} \tag{1.49}$$

where T_0 is the temperature of the Universe at present time and T_f indicates the one at the *freeze-out* time, that is when the reaction in Eq. 1.48 cannot keep the particle in equilibrium anymore. From this last equation, we can see that the density of a cold relic (produced at electroweak mass scales $m \sim 200\,\mathrm{GeV}$) matches the observed Dark Matter density today ($\Omega_c h^2 \sim 0.12$) for a cross-section $\langle \sigma v \rangle \sim 10^{-26} \mathrm{cm}^3 s^{-1}$. This is called the *WIMP miracle*: this cross-section is typical of the weak interaction and there are several theoretical models predicting such a particle.

Neutrinos decoupling. Neutrinos are kept into thermodynamic equilibrium above temperatures $T_D \gtrsim 1\,\mathrm{MeV}$ only by the weak interaction, via the reactions

$$\nu + e \longleftrightarrow \nu + e \quad \text{and} \quad \nu + \bar{\nu} \longleftrightarrow e + \bar{e}. \tag{1.50}$$

For $T < T_D$, the reaction time scale for these reactions drop below the expansion rate, determining the decoupling of neutrinos from the rest of the matter. Neutrinos decouple when they are relativistic, therefore, from decoupling time on, their temperature will decrease a a^{-1}. Note however that while the temperature of the photons increases after electron-positron annihilation, the one of neutrinos stays the same, since they are already decoupled. The increase in temperature with respect to T_ν can be computed using Eq. 1.41 as

$$T_\gamma = \left(\frac{11}{4}\right)^{1/3} T_\nu. \tag{1.51}$$

An interesting consequence of neutrino decoupling is that, very much alike what happens for photons, there exists also a *cosmic neutrino background* (CνB) with temperature today $\sim 1.95\,\mathrm{K}$, however current technology is not sufficient to detect it yet.

Primordial nucleosynthesis. Within the first three minutes, deuterium, helium and other light elements are synthesized in what we call *primordial* or *big bang nucleosynthesis* (BBN) (Figure 1.2). Before that, at temperatures $T \gtrsim 100\,\mathrm{MeV}$, the Universe is radiation-dominated and electron and positrons are kept in equilibrium with the primordial plasma by the interaction in Eq. 1.48. Nucleons (that is neutrons and protons), on the other hand are maintained in equilibrium by the weak interactions

$$\nu_e + n \longleftrightarrow p + e, \tag{1.52}$$

$$\bar{e} + n \longleftrightarrow p + \bar{\nu}_e, \tag{1.53}$$

$$n \longleftrightarrow p + e + \bar{\nu}_e. \tag{1.54}$$

The neutron-to-proton ratio in these conditions can be computed from the assumption of thermodynamic equilibrium, as

$$\left(\frac{n}{p}\right)_{eq} = \left(\frac{n_n}{n_p}\right)_{eq} \sim e^{-Q/T} \sim 1, \tag{1.55}$$

where n_n (n_p) is the number density of neutrons (protons) and $Q = m_n - m_p = 1.293\,\mathrm{MeV}$ is the mass difference between the two nucleons. As the temperature of the Universe drops below the freeze-out temperature for weak interactions ($T_f \sim 0.8\,\mathrm{MeV}$), neutrinos decouple – as we just discussed – and the reactions 1.52- 1.54 fail to maintain neutrons and protons in equilibrium. Neutrons, whose mass is larger, decouple before protons, disrupting the balance between the two nucleons in Eq. 1.55

$$\left(\frac{n}{p}\right)_f \sim e^{-Q/T_f} \sim \frac{1}{5}, \tag{1.56}$$

and then start to decay into protons (according to Eq. 1.54), with their abundance decreasing in time as

$$n_n(t) \approx n_n(t_f) e^{-t/\tau_n}, \tag{1.57}$$

where τ_n is the neutron lifetime.

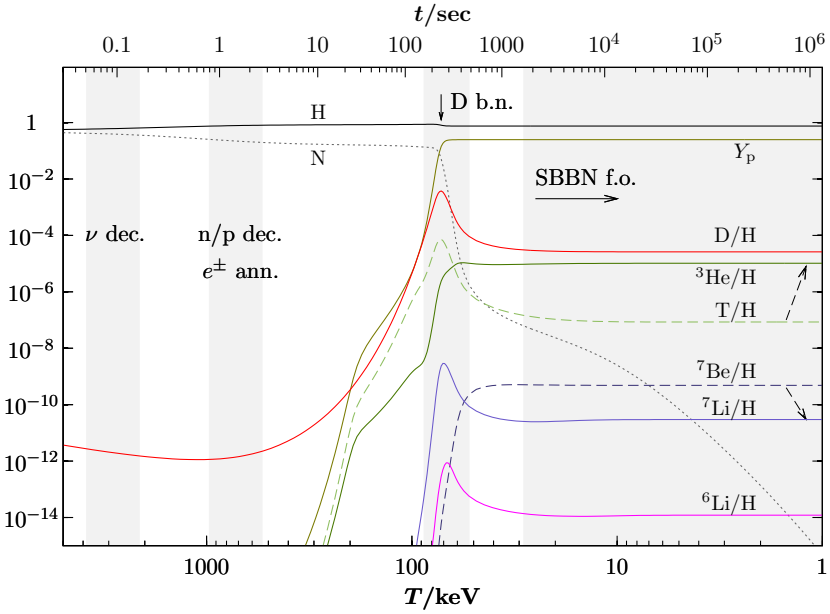

Figure 1.2: Evolution in time and temperature of the abundances for primordial elements. Protons are indicated as H and neutrons as N. Relevant events in the cosmic history re also indicated, such as neutrino decoupling, electron-positron annihilation and the starting of BBN ("SBBN" in the figure). From Pospelov and Pradler (2010).

As the temperature falls below 0.7 MeV, atomic nuclei cannot be kept in thermodynamic equilibrium anymore and light elements (deuterium, ^{3}He, ^{4}He, ^{7}Li) finally be produced in a network of two-body nuclear reactions. A key ingredient to achieve significant abundances is the formation of a sufficient amount of deuterium: light elements cannot be synthesized until the temperature drops below $T_{Nuc} \sim 0.086$ MeV, so that the production of deuterium takes place according to the reaction

$$p + n \longrightarrow D + \gamma, \tag{1.58}$$

overcomes the photodissociation of deuterium. This is usually referred to as the *deuterium bottleneck*. Around the temperature T_{Nuc}, the neutron-to-proton ratio can be computed from Eq. 1.57 to be $(n/p)_{Nuc} \sim 0.133$, and all neutrons are bound in ^{4}He nuclei, which have an abundance

$$Y_P \sim \frac{2\left(\frac{n}{p}\right)_{Nuc}}{1+\left(\frac{n}{p}\right)_{Nuc}} \sim 0.238. \tag{1.59}$$

Finally, BBN does not produce significant abundances of elements heavier than ^{4}He for two reasons: first, there are no stable isotopes with atomic mass number $A = 5$ or $A = 8$, so that the reactions $n + {}^4\mathrm{He}$, $p + {}^4\mathrm{He}$ or ${}^4\mathrm{He} + {}^4\mathrm{He}$ cannot take place; second, reactions such as ${}^3\mathrm{H} + {}^4\mathrm{He} \longrightarrow {}^7\mathrm{Li} + \gamma$ or ${}^3\mathrm{He} + {}^4\mathrm{He} \longrightarrow {}^7\mathrm{Be} + \gamma$ present a significant Coulomb barrier. Nucleosynthesis stops as the temperature drops below $\sim 0.05\,\mathrm{MeV}$.

Recombination and photons decoupling. For temperature above $T \sim 1\,\mathrm{eV}$, the thermodynamic equilibrium between baryons and photons is achieved through electromagnetic interactions, such as the photoionization reaction:

$$p + e \longleftrightarrow H + \gamma. \tag{1.60}$$

The behaviour of the ionization fraction $X_e = n_e/(n_p + n_H)$ can be approximately understood using the *Saha equation*

$$\left(\frac{1 - X_e}{X_e^2}\right)_{eq} = \frac{2\zeta(3)}{\pi^2}\frac{n_b}{n_\gamma}\left(\frac{2\pi T}{m_e}\right)^{3/2} e^{B_H/T}, \tag{1.61}$$

where $B_H = m_e + m_p - m_H = 13.6\,\mathrm{eV}$ is the ionization energy for the hydrogen atom. We can use this equation to give a rough estimate[5] of the recombination temperature $T_{rec} \sim 0.3\,\mathrm{eV} \sim 3600\,\mathrm{K}$, that is the temperature at which 90% of the electrons have recombined with protons to form hydrogen. Note that recombination happens at a temperature much lower than the hydrogen binding energy B_H because of the high number of photons per baryon present in the Universe ($n_b/n_\gamma \sim 5 \times 10^{-10}$). From the temperature we can also compute the recombination redshift, using Eq. 1.24, $z_{rec} \sim 1320$ and the cosmic time of recombination $t_{rec} \sim 290\,000\,\mathrm{yr}$.

[5] A more careful and detailed treatment, exploiting a Boltzmann approach, can be found for instance in Jones and Wyse (1985); Peebles (1968).

Photons have been, up to this moment, tightly coupled to the primordial plasma through Compton scattering

$$e + \gamma \longleftrightarrow e + \gamma, \tag{1.62}$$

with an interaction rate $\Gamma = n_e \sigma_T$ and σ_T is the Thomson cross-section. We can find the *decoupling* (or *last scattering*) temperature for photons by equating the interaction and the expansion rates and using again Saha equation. In this case, the decoupling energy scale is found to be $T_{dec} \sim 0.27\,\mathrm{eV}$, corresponding to a redshift $z_{dec} \sim 1100$ and cosmic time $t_{dec} \sim 380\,000\,\mathrm{yr}$. However, the *last scattering surface* (LSS) is not infinetesimally thin: defining its width as the redshift range in which the visibility function

$$g(\tau) = e^{-\eta_{opt}}\frac{d\eta_{opt}}{d\tau}, \tag{1.63}$$

where η_{opt} is the *optical depth*

$$\eta_{opt} = \int_{\tau}^{\tau_0} n_e \sigma_T a d\tau, \tag{1.64}$$

is halved, we can find its thickness to be $\Delta z_{dec} \sim 185$. After the last scattering, photons can propagate freely throughout the Universe, forming the *cosmic microwave background* (CMB), whose main properties we are going to describe in the next Section.

Reionization. After the emission of the CMB, the Universe enters the so-called *dark ages*. This period of darkness ends when the first sources of ultraviolet photons are produced and the *reionization* of the Universe can begin: current models trace back the origin of these ultraviolet photons to first massive stars in relatively low mass early galaxies, reionizing hydrogen between redshift $12 \gtrsim z \gtrsim 6$, and to quasars reionizing helium between $6 \gtrsim z \gtrsim 2$ (Planck Collaboration, 2018d). However, we must stress that the uncertainties on this process are still significant. In Section 2.1, we will study in more detail the imprint of reionization on the CMB observables.

1.6 The Cosmic Microwave Background

The CMB, discovered in 1965 (Penzias and Wilson, 1965; Dicke et al., 1965), represents one of the cornestones of our current understanding of the Universe, and will likely continue to be at the center of the cosmological research at least for the next decade, as we are going to discuss in this Thesis (in particular Sections 5 and 4). As we will describe in detail in Section 2.1, the greatest impact on cosmology was arguably given by the discovery and detailed characterization of the *CMB anisotropies* – small variations in intensity and polarization across the sky – but also the absence of *spectral distortions* in the CMB (Fixsen et al., 1996b; Chluba and Sunyaev, 2012) represents a remarkable achievement, as we will explain later in this Section. The CMB is, in fact, the best-measured blackbody in nature, with a Planck spectrum

$$B_\nu(\nu, T) = 2h\nu^3 \frac{1}{e^{h\nu/k_B T} - 1}, \tag{1.65}$$

which, in the current cosmological picture, is a manifestation of the fact that photons were once thermalized with the primordial plasma. The temperature of the CMB today, defined as the average across the full sky, has been measured with very high precision up to $\sim 1\,\mathrm{mK}$, (see Eq. 1.23) using the FIRAS and WMAP data (Fixsen, 2009) (Figure 1.3).

If some exotic physics mechanism – such as decaying or annihilating particles, primordial black holes, topological defects, primordial

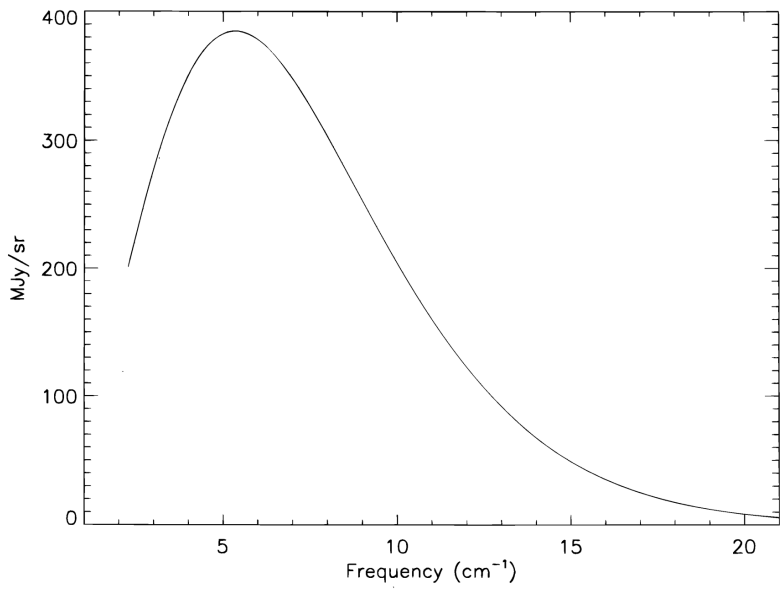

Figure 1.3: The original FIRAS measurement of the intensity CMB blackbody spectrum as a function of frequency, from Fixsen et al. (1996a). Note that error bars are invisible because they are a small fraction of the line thickness.

magnetic fields to name a few – injects energy in the Universe at $z \gtrsim 2 \times 10^6$, we should be able to see some distortion in the blackbody spectrum. These spectral distortions can be classified into two main categories: *μ-type distortions*, *Compton or y- type distortions* (see Tashiro, 2014, for a recent review).

μ-type distortions. Distortions of the μ-type arise from energy injections between $2 \times 10^6 \gtrsim z \gtrsim 10^5$: in this case the CMB can be thermalized via Compton scattering but double Compton scattering and bremsstrahlung are inefficient at high frequencies and cannot change the photon number, leaving a non-vanishing an frequency-dependent chemical potential μ in the Bose-Einstein spectrum (Eq. 1.38).

y-type distortions. On the other hand, y-type distortions are generated when the energy injection happens at $z < z_{dec}$ and therefore the injected energy cannot be thermalized with photons. However, if the exotic physics event occurs at $z > 500$, the electron temperature can increase because of the energy injection. Despite the fact that the event occurs after decoupling, some interaction between electrons and photons due to Compton scattering still happens, causing a distortion in the spectrum whose exact shape can be predict using a Boltzmann approach. The parameter governing the effect is the integrated Compton optical depth

$$y = \int \sigma_T n_e \frac{T_e - T_\gamma}{m_e} dt, \tag{1.66}$$

with n_e the number density of free electrons, m_e the electron mass and the difference between electron and photon temperature is clearly highlighted as the cause of the effect.

The FIRAS instrument onboard the COBE (COsmic Background Explorer) satellite experiment put very tight constraints on the two distortions parameter (Fixsen et al., 1996a): $|y| < 15 \times 0^{-6}$ and $|\mu| < 9 \times 10^{-5}$ at 95% C.L.

We conclude this chapter by reporting another remarkable achievement of the COBE satellite (Smoot et al., 1992): the detection of fluctuations in the temperature of the CMB with characteristic amplitude

$$\left\langle \left(\frac{\delta T}{T} \right)^2 \right\rangle^{1/2} \sim 1.1 \times 10^{-5}, \tag{1.67}$$

varyung across the sky. These are the so-called CMB anisotropies, which were present in the CMB at the recombination time and were redshifted by the cosmic expansion. We will return on them in Section 2.1.

1.7 *Shortcomings of The Big Bang Model*

In this Section we review the main problems associated to the picture above, which required the construction of a new phase of expansion, based on early Universe processes, to be described in Section 1.8.

1.7.1 *Singularity Problem*

We already anticipated in Section 1.3, that the prediction of a big bang singularity of the standard cosmological model, obtained by extrapolating the FLRW cosmological solution to the initial time. We remark here that the big bang is in fact not a physical event but a limit of our standard model: the classic description of space-time is likely to fail and quantum gravity effects are likely to become significant.

1.7.2 *Horizon Problem*

In order to study the causality structure of the Universe, we need to define the so-called *particle horizon*, that is the surface of the hypersurface $t = t_0$, for an observer O at t_0, that divides all particles in the Universe in two sets: the ones that have already been observed at t_0 or before and the ones that have not yet been observed. For a Universe obeying the Cosmological Principle, the particle horizon is

simply a sphere of centre O and comoving radius χ given by

$$\chi = \int_0^{t_0} \frac{dt}{a(t)}. \tag{1.68}$$

If we take the scale factor to evolve in time as $a(t) = t^n$, the integral in Eq. 1.68 will converge only if $n < 1$. We know from Eq. 1.17 that for a flat Universe $n = 2/(3(1+w))$, therefore the particle horizon will exist only if the cosmological fluid dominating the early Universe has EoS $w > -1/3$. For two events at times t_1 and t_2 during an era dominated by radiation – having constant EoS $w = 1/3$ – in the early Universe, such particle horizon is well defined, and we can write the physical diameter at time t_2 for an event occurred at time $t_1 < t_2$

$$D_{phys}(t_1, t_2) = 2a(t_2) \int_{t_1}^{t_2} \frac{dt}{a(t)} \simeq 2R_H = 2H^{-1} \tag{1.69}$$

where R_H is the Hubble radius define in Eq. 1.8 and the last two equalities hold for $t_1 \ll t_2$.

We can now enunciate the so-called *horizon problem* of the HBB model. At decoupling time the size of the causally-connected regions (defined by the particle horizon) was smaller than the size of the Observable Universe at that time, and the LSS comprised as many as $\sim 10^5 - 10^6$ different causally connected regions. One of these causally connected regions occupies today an angular dimension on the sky of about 1°, therefore it is very difficult to explain the remarkable isotropy of the CMB on the entire sky, down to the level of $\sim 10^{-5}$ (see Eq.1.67), without any causal contact between separate regions.

1.7.3 *Flatness Problem*

If we rewrite the Friedmann equations 1.12 and 1.13 as a dynamical system for the density parameters, we can find

$$\frac{\dot{H}}{H^2} = -(1+q), \tag{1.70}$$

where $q = (3(w+1) - 2)(1 - \Omega_K) - 3(w+1)\Omega_\Lambda$. From this last equation we can express the evolution of Ω_K with the scale factor – neglecting the late Universe Ω_Λ contribution – as

$$\frac{d\Omega_K}{d\ln a} = (3w+1)(1-\Omega_K)\Omega_K, \tag{1.71}$$

which can in turn be integrated assuming a constant w to give

$$\Omega_K(a) = \frac{\Omega_K^{(0)}}{(1-\Omega_K^{(0)})(1+z)^{1+3w} + \Omega_K^{(0)}}. \tag{1.72}$$

Current observations indicate a very small present value for the curvature (see note 3), we are justified therefore to assume $|\Omega_K^{(0)}| =$

$|\Omega_0 - 1| < 0.1$. In this case, Eq. 1.72 will predict an extremely small curvature density parameter value at the Planck epoch of the order

$$|\Omega(z_{Pl}) - 1| < 10^{-60}. \tag{1.73}$$

This the so-called *flatness problem*: the big bang model alone does not provide any explanation for such a small curvature at the Planck epoch, giving rise to a fine-tuning issue, or alternatively, why we should have strictly $\Omega_K = 0$ at all times.

1.7.4 *Baryogenesis Problem*

Current observations highlight a strong asymmetry between baryons and antibaryons $(n_b - n\bar{b})/n_\gamma \sim 5 \times 10^{-10}$, which is just what we need to explain the primordial nucleosynthesis abundances (and the CMB anisotropies observations as we will see in Section 2.1). While antimatter is produced in terrestrial particle accelerators and cosmic rays, concentrations on cosmological scales, which would necessarily produce intense X and γ rays because of the baryon-antibaryon annihilation, have never been observed.

An attempt at explaining the baryon-antibaryon asymmetry with an asymmetry in the initial conditions of the Universe fails if we accept the inflation paradigm (as we will see in Section 1.8), since an inflationary stage erases any pre-existing asymmetry.

Sakharov (Sakharov, 1991) identified three conditions that every succesful theory must satisfy in order to produce a baryon-antibaryon asymmetry: the violation of the baryon number, the C and CP violation and the out-of-equilibrium state. Despite the fact the standard model already contains all three ingredients, it cannot explain the observed asymmetry, and therefore the baryogenesis problem requires solutions beyond the standard model, such as Grand Unified Theories (GUTs) or Supersymmetry (see Mukhanov (2005) and references therein).

1.7.5 *Magnetic monopole Problem*

While topological defects, such as magnetic monopoles, are not predicted by standard model of particle physics, they are in general predicted by theories beyond the standard model. One famous example is represented by GUTs: if a phase transition takes place at the GUT energy scale $T_{GUT} \sim 10^{16}$GeV as the temperature of the Universe is dropping, magnetic monopoles with mass $M_{monopole} \sim T_{GUT}$ are copiously produced with a density

$$\Omega_{Monopole} h^2 \sim 10^{17} \left(\frac{T_{GUT}}{10^{16}\text{GeV}}\right)^3 \left(\frac{M_{monopole}}{10^{16}\text{GeV}}\right) \tag{1.74}$$

and therefore can dominate the energy budget of the Universe. This is known as the *magnetic monopole problem*, since these magnetic monopoles have never been observed.

1.7.6 *Dark-sector, Cosmological Constant and coincidence problems*

As we already pointed out in Sections 1.3, current cosmological observations indicate that only around 5% of the total matter-energy content of the Universe is in the form of baryonic matter, and that we need to postulate that the remaining 95% is split between Dark Matter and dark energy.

Dark matter, which according to recent observations is of non-relativistic nature and constitutes around $\sim 27\%$ of the total matter-energy budget (Planck Collaboration, 2018), could be produced in the primordial Universe and remain as a relic, as we have shown in Section 1.5. There are many candidates for Dark Matter as a particle beyond the standard model, but no convincing detection has been achieved until now (see Section 1.3).

As we discussed in Section 1.4.2, current observations indicate that dark energy is the cosmic component dominating the Universe today and producing the observed accelerated expansion. Its behaviour has been found to be very close to that of a Cosmological Constant (see Section 1.4.2), with an energy density given approximately by

$$\rho_\Lambda \approx \frac{\Lambda m_{Pl}^2}{8\pi} \approx 10^{-47}\text{GeV}^4 \tag{1.75}$$

where $m_{Pl} \approx 1.22 \times 10^{19}$GeV is the Planck mass, $\Lambda \approx H_0^2 = (2.1332\,h \times 10^{-42}\text{GeV})^2$ and $h = 0.674$.

We can explore the possibility that the energy density of the Cosmological Constant is a manifestation of the vacuum energy of an empty space; assuming that GR is valid up to the Planck scale, the vacuum energy density is found to be

$$\rho_{vac} \approx \frac{m_{Pl}^4}{16\pi^2} \approx 10^{74}\text{GeV}^4, \tag{1.76}$$

which is factor 10^{121} larger than the observed value for the Cosmological Constant energy density (Eq. 1.75). Note that even if we consider other plausible energy scales the discrepancy is still extremely large: in order to be consistent with the standard model of particle physics, the vacuum energy scale must be at least of the order of the electroweak symmetry-breaking scale $\rho_{vac} \sim 10^{12}\text{GeV}^4$. This is known as the *Cosmological Constant problem*.

Many attempts have been made to explain cosmic acceleration beyond the mere Cosmological Constant (see for instance the recent review Ishak, 2019, and references therein); as we anticipated in

Section 1.3, one possibility is to introduce a a uniformly distributed cosmic fluid with EoS $w = -1$ that we named dark energy. We could also change the background parametrization, having for instance a *dynamical dark energy* with EoS w_{de} and energy density going as

$$\rho_{de} = \rho_{de}^{(0)} a^{-3(1+w_{de})}, \tag{1.77}$$

or also using the *CPL parametrization* (Chevallier and Polarski, 2001; Linder, 2003) that lets the EoS vary with the scale factor according to $w(a) = w_0 + w_a(1-a)$. An EoS with w very close to -1 can be obtained introducing a canonical scalar field ϕ with a potential $V(\phi)$ interacting only gravitationally with other components: this is called a *quintessence* model. Other possibilities include changing the perturbation parametrization, for instance through a phenomenological approach (Planck Collaboration, 2016b).

Another path that has been (and currently is) explored to explain cosmic acceleration is the one contemplating modifications of GR: as we stated in Section 1.1 GR has been thoroughly tested, until now, only on solar system scales and in the strong field limit, therefore there could be room for modifications on cosmological scales. A compilation of specific modified gravity models can be found for instance in Ishak (2019) and also an attempt of "unified" approach to dark energy and modified gravity has been developed, the Effective Field Theory of dark energy, in which the gravitational action includes a wide range of models (Creminelli et al., 2009).

Finally, a general problem of the standard cosmological model involving the dark sector is the so-called *coincidence problem*: the baryonic matter density , the Dark Matter density and the dark energy density today coincide apart from a small multiplicative factor

$$\Omega_b^{(0)} : \Omega_c^{(0)} : \Omega_\Lambda^{(0)} \sim 1 : 5 : 14, \tag{1.78}$$

for no obvious reason, despite the fact that these three components originate from very different mechanisms. In particular, we could ask why the Cosmological Constant, in addition to have a very different value from all known fundamental energy scales and therefore requiring fine-tuning, only starts to dominate the Universe today. This coincidence problem can be used as a guide for selecting interesting directions of research, since it is difficult to imagine a satisfying explanation of the nature of dark energy that does not solve also the coincidence problem.

1.7.7 *Origin of Structure Problem*

The big bang model, being based on a perfectly homogeneous and isotropic FLRW metric, is not capable of explaining the formation of

cosmic structures that we observe today. In order to reproduce the Universe as we observe, we need to introduce by hand in this framework some small density fluctuations in the initial conditions, which will then collapse under the action of gravity and form structures. As we mentioned in Section 1.6, these fluctuations have indeed been detected for the first time by the COBE satellite, so what we need in an extension to the standard framework is a mechanism explaining their presence.

1.8 The Inflationary Paradigm

As we discussed in the previous Section, the ΛCDM model – despite its successes in predicting the existence and the spectrum of the CMB and the abundance of primordial elements – presents several issues, which generally require a fine-tuning of the initial conditions, and evidently provide an incomplete explanation for cosmological observations. This is where the inflationary paradigm comes to our rescue: as we will discuss in this Section, inflation – that is a period of accelerated expansion occurring before the radiation-dominated era – provides a simple explanation for the homogeneity and isotropy of the Universe, for its flatness and predicts the origin of the density fluctuations that are the seeds for cosmological structure formation. Moreover, inflation not only solves many of the problems of the standard model, but provide also falsifiable predictions regarding the statistics and the spectrum of density perturbations and primordial gravitational waves.

Although the idea of a phase of initial exponential expansion had been circulating quite some time before, the first to introduce a realistic idea of cosmic inflation justified by quantum gravity ideas were Starobinsky in 1979 (Starobinsky, 1979) and Guth in 1981 (Guth, 1987).

In this Section, we will first describe how the inflationary paradigm, regardless of the specific model considered, solves some of the big bang theory problems, then we wil review the predictions of the simplest single-field scenario and the slow-roll approximation and summarize its predictions regarding scalar and tensor perturbations.

1.8.1 Inflation and the solution of the big bang problems

Flatness Problem. From the first Friedmann equation, we can easily infer that the quantity $(1-\Omega^{-1})\rho a^2 = 3K/8\pi G$ is constant during the evolution of the Universe, and therefore

$$(1-\Omega_i^{-1})\rho_i a_i^2 = (1-\Omega_f^{-1})\rho_f a_f^2 \tag{1.79}$$

where t_i and t_f are the initial and final time of inflation. From Eq. 1.73, we get

$$(1-\Omega_i^{-1})\rho_i a_i^2 \sim 10^{-60}(1-\Omega_0^{-1})\rho_f a_f^2, \tag{1.80}$$

which indicates that the flatness problem could be solved if $\rho_f a_f^2 \gg \rho_i a_i^2$, implying $\dot{a}_f > \dot{a}_i$. In other words, the cosmic expansion during inflation must accelerate

$$\ddot{a}(t) > 0, \tag{1.81}$$

Moreover, this last condition, when inserted in the second Friedmann equation, implies that the Universe during inflation is dominated by a fluid with

$$\rho + 3P < 0. \tag{1.82}$$

The usual way to quantify the duration of inflation is through the number of *e-folds*

$$N = \ln\left(\frac{a_f}{a_i}\right), \tag{1.83}$$

We can therefore estimate the number of e-folds needed to obtain the curvature density in Eq. 1.73 at the end of inflation, from the equation

$$\left|\frac{\Omega_K(t_f)}{\Omega_K(t_i)}\right| = \left(\frac{a_f}{a_i}\right)^{-2} = e^{-2N}, \tag{1.84}$$

to be $N \gtrsim 70$. In conclusion, inflation solves the fine-tuning issue of the flatness problem by explaining in a natural way an extremely small number $\sim 10^{-60}$ with a number of e-folds $N \sim 70$.

Horizon Problem. A period of accelerated expansion solves also the horizon problem, since the condition in Eq. 1.81 can be expressed in terms of the comoving Hubble radius $\mathcal{H}^{-1} = (aH)^{-1}$, as

$$\frac{d}{dt}(aH)^{-1} < 0. \tag{1.85}$$

This implies that the comoving Hubble radius decreases in time – contrary to what happens in a radiation or matter dominated era – thus solving the horizon problem: after inflation, the regions appear to be separated by a distance larger than the Hubble radius, but before inflation the entire Observable Universe was indeed in causal contact (Figure 1.4). The number of e-folds needed to solve the horizon problem today can be computed imposing that a causal region of size a_i corresponds today to the size of the Observable Universe

$$\frac{a_f R_H(t_0)}{a_0 R_H(t_f)} \sim \frac{T_0 R_H(t_0)}{T_f R_H(t_f)} \sim e^N, \tag{1.86}$$

which gives, assuming $T_f \sim T_{GUT}$, $N \gtrsim 57$.

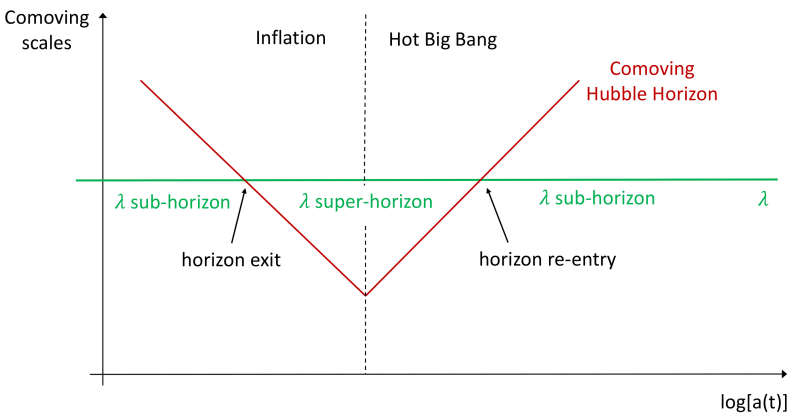

Figure 1.4: Solution of the horizon problem within the inflationary paradigm, from Guzzetti et al. (2016). The plot shows the time evolution of the comoving Hubble radius during inflation and during a radiation or matter dominated era (here indicated as "Hot Big Bang"). The behaviour of a comoving scale λ, initially "sub-horizon", is also shown: during inflation the λ exits the comoving Hubble radius (becoming "super-horizon") and later re-enters in a radiation or matter- dominated era.

Magnetic Monopole and Perturbations production Problem. Inflation solves also the monopole problem: if monopoles are produced before inflation, the accelerated expansion would severely dilute their number density, until we have less than one monopole per horizon scale. For what concerns the production of primordial density perturbations, inflation provides a mechanism based again on the accelerated expansion: quantum vacuum fuctuations generated around the Planck epoch are stretched to cosmological scales by the inflationary expansion. We will formalize this statement in the rest of this Section and we will provide predictions on the spectrum of these fluctuations.

1.8.2 *Single scalar field scenario*

The simplest inflationary models only require – in order to get the sought-after accelerated expansion – the introduction of the *inflaton*, a scalar field φ, with action

$$\mathcal{S} = -\int \sqrt{-g}\left[\frac{1}{2}\partial_\mu\varphi\partial^\mu\varphi + V(\varphi)\right] d^4x, \tag{1.87}$$

and energy-momentum tensor

$$T_{\mu\nu} = \partial_\mu\varphi\partial_\nu\varphi - \left(\frac{1}{2}\partial_\alpha\varphi\partial^\alpha\varphi + V\right) g_{\mu\nu}, \tag{1.88}$$

and from its (00) and (ii) components we can extract, respectively, the energy density and pressure of the inflaton

$$\rho_\varphi = \frac{\dot{\varphi}^2}{2} + V(\varphi) \tag{1.89}$$

$$P_\varphi = \frac{\dot{\varphi}^2}{2} - V(\varphi). \tag{1.90}$$

Using this last equation together with both the Friedmann equations, we can derive the evolution equation for the inflaton, that is the *Klein-Gordon equation*

$$\ddot{\varphi} + 3H\dot{\varphi} + V_{,\varphi} = 0, \tag{1.91}$$

which can also be seen as a the equation of motion of a particle rolling down its potential V, with $V_{,\varphi}$ acting as a force and the expansion of the Universe in the term $H\dot{\varphi}$ acting as a friction term.

The second Friedmann equation can be recast, for a inflaton-dominated Universe, in the form

$$\frac{\ddot{a}}{a} = \frac{8\pi G}{3}(V - \dot{\varphi}^2), \tag{1.92}$$

from which it is evident that, in order to realize an accelerated expansion, we must have $\dot{\varphi}^2 < V$. Furthermore, if $\dot{\varphi}^2 \ll V$, the EoS associated with the inflaton will be $w_\varphi = -1$ and so we can use Eq. 1.17 to infer that the expansion will be quasi-exponential. If we also make a further assumption on the smallness of the field "acceleration" $\ddot{\varphi} \ll 3H\dot{\varphi}$ in order to make the condition $\dot{\varphi}^2 \ll V$ last for enough time, we realize the so-called *slow-roll regime*, in which the inflaton field varies very little during inflation (Figure 1.5).

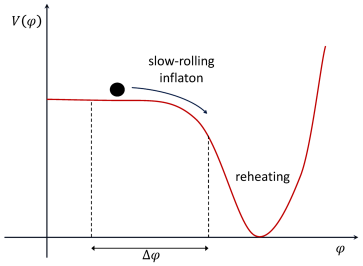

Figure 1.5: An example of inflationary potential $V(\varphi)$, having a flatter region in which the slow-roll of the scalar field φ can be realized (see Section 1.8.2). After the slow-roll phase, the reheating starts and the field oscillates around the potential minimum and decays in other particles. From Guzzetti et al. (2016).

In this regime, we can formulate most models in terms of the *slow-roll parameters*

$$\epsilon = -\frac{\dot{H}}{H^2}, \tag{1.93}$$

$$\eta = \epsilon - \frac{\dot{\epsilon}}{2H\epsilon} \tag{1.94}$$

and their predictions will be independent of the actual shape of the potential $V(\varphi)$. Note that, in terms of this two slow-roll parameters, the conditions 1.81 and 1.82 reduce to $\epsilon < 1$ and the slow-roll conditions translate into $\{\epsilon, |\eta|\} \ll 1$. It is possible to introduce a second set of slow-roll parameters, the *potential slow-roll parameters* in terms of derivatives of the inflaton potential

$$\epsilon_V = \frac{1}{16\pi G}\left(\frac{V_{,\varphi}}{V}\right)^2,$$

$$\eta_V = \frac{1}{8\pi G}\left(\frac{V_{,\varphi\varphi}}{V}\right), \tag{1.95}$$

which is useful to assess if a given potential can satisfy the slow-roll conditions $\{\epsilon_V, |\eta_V|\} \ll 1$.

In order to be consistent with the big bang model predictions of a radiation dominated era followed by a matter dominated one, inflation must end at a certain point. In this single field slow-roll scenario the end of inflation coincides with the end of the slow-roll

regime, that is when $\{\epsilon, |\eta|\} \simeq 1$ and the field starts to rolls fast along its potential. The inflaton will then reach the minimum of the potential (see for instance Figure 1.5) and start to oscillate around it. Up to this point, the Universe has been completely dominated by the inflaton energy density, however the hot big bang paradigm requires that the Universe is radiation-dominated and in a state of thermodynamic equilibrium at a temperature $T_{reheat} \sim 1\,\mathrm{MeV}$: there must be therefore a phase of *reheating*, in which the inflaton energy is exploited to reach such a state. Typical mechanisms for achieving reheating are the perturbative decay of the inflaton field and the parametric resonance, the latter leading to an initial rapid and violent phase called *preheating* (for more details see for instance Lozanov (2019); Allahverdi et al. (2010) and references therein).

1.8.3 *Cosmological perturbation theory and Scalar Vector Tensor (SVT) decomposition*

As we anticipated in Section 1.8.1, inflation is capable of explaining through microphysics – that is through quantum fluctuations in the early Universe – the macrophysics in today cosmological observations, and, in particular, the origin of the temperature fluctuations observed in the CMB and of the cosmic large scale structure.

Before attacking the study of inflationary quantum fluctuations, we need to briefly summarize the general theory of cosmological perturbations, first introduced by Lifshitz in 1946 (Lifshitz, 1946). A comprehensive review of the theory can be found for instance in Kodama and Sasaki (1984).

The perturbed metric can be written at linear order as

$$ds^2 = a^2(\tau)[-(1+2A)d\tau^2 + 2B_i dx^i d\tau + (\delta_{ij} + h_{ij})dx^i dx^j], \qquad (1.96)$$

while the metric tensor is composed of an unperturbed flat FLRW part (that we will call *background* space-time) plus perturbations at first order:

$$g_{\mu\nu} = \bar{g}_{\mu\nu} + \delta g_{\mu\nu}. \qquad (1.97)$$

We can then perfom the so-called *SVT decomposition*, completely analogous to the decomposition of a vector in a *longitudinal* and *transverse* part according to the *Helmholtz theorem*:

$$B_i = B_i^{||} + B_i^{\perp} = \partial_i B + B_i^{\perp}. \qquad (1.98)$$

Here the longitudinal part $B_i^{||}$ is curl-free and can therefore be written as the gradient of a generic scalar function, while the transverse part $B_i^{\perp}$ is divergence-free $\partial^i B_i^{\perp} = 0$. The equivalent SVT decomposition for a rank-2 tensor reads

$$h_{ij} = 2C\delta_{ij} + 2E_{ij}^{||} + 2E_{ij}^{\perp} + 2E_{ij}^{t}, \qquad (1.99)$$

where

$$E_{ij}^{||} = \left(\partial_i\partial_j - \frac{1}{3}\delta_{ij}\nabla^2\right) E, \tag{1.100}$$

$$E_{ij}^{\perp} = \frac{1}{2}\left(\partial_i E_j^{\perp} + \partial_j E_i^{\perp}\right) \tag{1.101}$$

and $E_i^{\perp}$ and E_{ij}^t (also called *transverse-traceless* part) are divergence-free quantities. The scalar modes in this decomposition represent density perturbations, while transverse vector modes represent vector perturbations (vorticity) and tensor modes represents gravitational waves. Scalar modes represent the seed for cosmic structures, which grow thanks to gravitational instability, while tensor modes are a most important prediction of inflation and will be the main focus of this Thesis. We will not be concerned further about vector modes, since independently from the specific single-field inflation model they are quickly suppressed by the cosmic expansion and disappear before the end of inflation. The main advantage of the SVT theorem is that it allows to decouple – at linear order – the perturbation equations for the three types of modes, and this translates into an independent evolution of each mode.

The perturbation in a certain quantity $Q(\mathbf{x}, t)$ is defined as the difference between the value at a point in the perturbed space-time and that at the corresponding point in the background space-time

$$\delta Q(\mathbf{x}, t) = Q(\mathbf{x}, t) - \bar{Q}(\mathbf{x}, t). \tag{1.102}$$

Notice that the perturbations in the metric 1.96 are *gauge-dependent*, that is they change according to our coordinate choice. In order to compare meaningful quantities in defining the perturbations as in 1.102, we must make a *gauge-choice*, prescribing a one-to-one correspondence between points in the background space-time and points in the perturbed space-time, keeping the background coordinates fixed. It is therefore useful to introduce *gauge-invariant variables*, such as the two *Bardeen's potentials* (Bardeen, 1980)

$$\Phi \equiv -C - \mathcal{H}(B - E') + \frac{1}{3}\nabla^2 E \quad \text{and} \quad \Psi \equiv A + \mathcal{H}(B - E') + (B - E')' \tag{1.103}$$

where a $'$ indicates derivative with respect to conformal time Note also that this gauge-dependency does not affect the intrinsically tensor components E_{ij}^t.

We introduce here another gauge-independent quantity – which will turn out to be useful later in this Section, when treating the scalar perturbations produced by inflation – the *comoving curvature perturbation*

$$\mathcal{R} = C - \frac{1}{3}\nabla^2 E + \mathcal{H}(B + v) \tag{1.104}$$

where v is the scalar part of the 3-velocity v_i appearing in the perturbed energy-momentum tensor.

1.8.4 *Generation of primordial scalar perturbations*

Any fluctuation in the inflaton field will generate metric perturbations, so, in order to study the evolution of scalar and tensor modes, we apply the gauge-invariant perturbations theory and write the perturbed Einstein equations

$$\delta G_{\mu\nu} = 8\pi G \delta T_{\mu\nu}. \tag{1.105}$$

In particular, this last equation allows us to derive the so-called *perturbed Klein-Gordon equation*, describing the evolution of the inflaton fluctuations

$$Q'' + 2\mathcal{H}Q' - \nabla^2 Q + a^2 \frac{d^2V}{d\varphi^2} Q = \varphi' \left(X' - \frac{1}{\mathcal{H}} \nabla^2 \Psi \right), \tag{1.106}$$

where we introduced another gauge-invariant variable, the *Mukhanov-Sasaki variable*

$$Q = \delta\varphi - \frac{\varphi' C}{\mathcal{H}'}. \tag{1.107}$$

and $X = \Psi + \Phi + (\Psi/\phi)'$. The Klein-Gordon 1.106 equation is equivalent to the equation of motion obtained from the variation of the action for a scalar field v with a time-dependent mass in a Minkowski space-time, expanded to second-order

$$\delta^{(2)}\mathcal{S} = \frac{1}{2} \int d\tau d^3\mathbf{x} \left[(v')^2 - \delta^{ij} \partial_i v \partial_j v + \frac{z''}{z} v^2 \right] \tag{1.108}$$

where $v = aQ = -z\mathcal{R}$ and $z = a\varphi'/\mathcal{H}$. We can therefore promote the field v to a quantum operator $\hat{v}$ and perform the quantization of a scalar field evolving in a time-dependent exterior field, where the time-dependence is due to the space-time dynamics. The field equation for $\hat{v}$ is usually called the *Mukhanov-Sasaki equation*

$$\hat{v}'' - \left(\nabla^2 + \frac{z''}{z} \right) \hat{v} = 0. \tag{1.109}$$

We can then solve this equation in Fourier space and compute the *power spectrum* of the comoving curvature perturbation $\mathcal{R}$

$$\mathcal{P}_\mathcal{R} = \frac{k^3}{2\pi^2} \left| \frac{v_k}{z} \right|^2, \tag{1.110}$$

which reduces in the slow-roll regime, after expanding the solution and keeping leading and next-order terms for super-horizon modes, to

$$\mathcal{P}_\mathcal{R} = \frac{1}{\pi} \frac{H^2}{m_{Pl}^2 \epsilon} \left[1 - 2(2c_e + 1)\epsilon + 2c_e \eta + (2\eta - 4\epsilon) \ln \left(\frac{k}{aH} \right) \right], \tag{1.111}$$

where $c_e = \gamma_e + \ln 2 - 2$ and γ_e is the Euler constant. We can also define a *scalar spectral index* n_s, as

$$n_s - 1 = \frac{d \ln \mathcal{P}_\mathcal{R}}{d \ln k} = 2\eta - 4\epsilon. \tag{1.112}$$

The scalar perturbations power spectrum can also be re-parametrized in a phenomenological way as a power-law, in order to compare it more easily with observational data

$$\mathcal{P}_\mathcal{R} = A_S \left(\frac{k}{k_0} \right)^{n_s - 1}, \tag{1.113}$$

where A_S is the amplitude of perturbations at a given pivot scale k_0.

1.8.5 *Generation of primordial tensor perturbations*

The perturbed Einstein equation 1.105 gives also the evolution equation for tensor perturbations, which reads, in the flat $K = 0$ case,

$$E_{ij}^{t''} + 2\mathcal{H} E_{ij}^{t'} - \nabla^2 E_{ij}^t = 8\pi G a^2 \Pi_{ij}^t, \tag{1.114}$$

where Π_{ij}^t is the purely tensor part of the *anisotropic stress tensor*, quantifying the difference between a perfect and a non-perfect fluid. In this case, anisotropic stress represents a damping term and is mainly due to free-streaming neutrinos[6] (see Section 1.3). Therefore, moving to Fourier space, Eq. 1.114 becomes

$$h''_{P,\mathbf{k}} + 2\mathcal{H} h'_{P,\mathbf{k}} + k^2 h_{P,\mathbf{k}} = 16\pi G a^2 \Pi^t_{P,\mathbf{k}}, \tag{1.115}$$

where we expanded gravitational waves into the two polarization states $P = +, \times$,

$$E_{ij}^t(\mathbf{k}, \tau) = \sum_{P=+,\times} E_P^t(\mathbf{k}, \tau) \epsilon_{ij}^P(\mathbf{k}) \tag{1.116}$$

using the polarization tensor

$$\epsilon_{ij}^+ = \begin{pmatrix} 1 & 0 & 0 \\ 0 & -1 & 0 \\ 0 & 0 & 0 \end{pmatrix} \qquad \epsilon_{ij}^\times = \begin{pmatrix} 0 & 1 & 0 \\ 1 & 0 & 0 \\ 0 & 0 & 0 \end{pmatrix}, \tag{1.117}$$

and we defined $E_P^t(\mathbf{k}, \tau) = h_{P,\mathbf{k}}(\tau)/2$ to make contact with the conventional notation in the literature. The source term in the right-hand side of 1.115, being given by causal mechanisms which cannot act outside the horizon, can be neglected for super-horizon modes ($k \ll \mathcal{H}$), together with the third term on the left-hand side: in this situation, the solution is simply given by $h_{P,\mathbf{k}} \propto const$. The modes will re-enter the horizon at a later time and evolve according to the

[6] See for instance Watanabe and Komatsu (2006) for a detailed discussion on the effect of neutrino free-streaming on the evolution of gravitational waves. Also free streaming photons have a damping effect, although smaller than the neutrino's one: for a detailed account see Saikawa and Shirai (2018).

full equation 1.115: we can therefore write a general solution solution in terms of a *tensor transfer function* $\mathcal{T}(\tau, \mathbf{k})$

$$h_P(\mathbf{k}, \tau) = h_P^{prim}(\mathbf{k})\mathcal{T}(\tau, \mathbf{k}), \tag{1.118}$$

and a primordial amplitude $h_P^{prim}(\mathbf{k})$, which is determined when the gravitational wave is well outside the horizon. Note also that the transfer function is normalized as $\lim_{k\to 0} \mathcal{T}(\tau, \mathbf{k}) = 1$.

Numerical solutions to the tensor evolution equation 1.115 are shown in Figure 1.6 for three different wavenumbers: modes remain constant as long as they are super-horizon and their amplitude start to decay ad oscillate as soon as they enter the horizon; modes with higher wavenumber enter the horizon earlier and are damped by the expansion of the Universe.

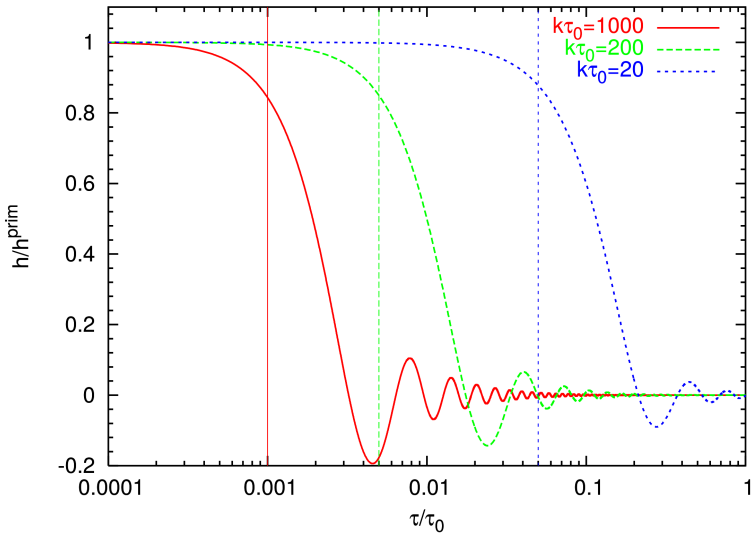

Figure 1.6: Tensor modes amplitude from the numerical solution of the perturbation equation 1.115 as a function of conformal time, from Watanabe and Komatsu (2006). Three different modes with high, medium and low wavenumbers are shown as solid red, dashed green and short-dashed blue lines, respectively. Vertical lines indicate the horizon crossing time for each mode.

We come back now to the production mechanism of gravitational waves during inflation. If we use the variable

$$\mu_P(\mathbf{k}, \tau) = \sqrt{\frac{m_{Pl}^2}{32\pi}} a(\tau) h_P(\mathbf{k}, \tau) \tag{1.119}$$

and vary the action for tensor perturbations at second order, we arrive at the expression (assuming $K = 0$)

$$\delta^{(2)}\mathcal{S} = \frac{1}{2} \sum_{P=+,\times} \int \left[(\mu_P')^2 - \gamma^{ij} \partial_i \mu_P \partial_j \mu_P + \frac{a''}{a} \mu_P^2 \right] \sqrt{\gamma} d^3\mathbf{x} d\tau, \tag{1.120}$$

from which we can obtain the tensor evolution equation 1.115. The last equation is actually the action for two independent scalar

fields u_P (corresponding to the two polarization state of a gravitational wave), with a time-dependent mass and evolving in a static Minkowski space-time. The quantization of this theory is then straightforward, once we promote μ_P to a quantum operator. Similarly to the scalar case, the field equation in Fourier space is

$$\mu_P''(k) + \left(k^2 - \frac{a''}{a}\right)\mu_P(k) = 0. \tag{1.121}$$

As in the scalar case, we can solve this last equation and write the power spectrum of tensor perturbations

$$\mathcal{P}_T = \frac{k^3}{2\pi^2}\frac{64\pi}{m_{Pl}^2}\left|\frac{\mu_k}{a}\right|^2, \tag{1.122}$$

which, in the slow-roll regime, becomes

$$\mathcal{P}_T = \frac{16}{\pi}\frac{H^2}{m_{Pl}^2}\left[1 - 2(c_e+1)\epsilon - 2\epsilon\ln\left(\frac{k}{aH}\right)\right]. \tag{1.123}$$

We can also define then the *tensor spectral index* n_T

$$n_T = \frac{d\ln\mathcal{P}_T}{d\ln k} = -2\epsilon, \tag{1.124}$$

use it to parametrize the tensor perturbations power spectrum as a power-law

$$\mathcal{P}_T = A_T\left(\frac{k}{k_0}\right)^{n_T}, \tag{1.125}$$

where A_T is the amplitude of tensor perturbations at a given pivot scale k_0. Another quantity very commonly used in the primordial gravitational waves literature is the *tensor-to-scalar ratio*

$$r = \frac{A_T}{A_S} = 16\epsilon \tag{1.126}$$

Finally, it is possible to connect the tensor-to-scalar ratio and the spectral index n_T in the *consistency relation*

$$n_T = -\frac{r}{8}, \tag{1.127}$$

which is valid at lowest order for every single-field slow-roll inflation model. An observational confirmation of this relation would represent a remarkable confirmation of the simplest model of inflation; we will provide more details on this issue in Sections 5.5.3 and 4.4.3. However, many alternative models to the single-field slow-roll predict deviations from this consistency relation: some examples are multifield inflation (Bartolo et al., 2001; Wands et al., 2002; Byrnes and Wands, 2006), models with generalized lagrangians such as k-inflation (Garriga and Mukhanov, 1999) or inflation with Galileon

fields (G-inflation) (Kobayashi et al., 2010), inflation with gauge fields (Maleknejad et al., 2013) or alternative to inflation, such as in string cosmology (Gasperini and Veneziano, 1993; Brandenberger et al., 2007) or in a cyclic Universe (Boyle et al., 2004).

We conclude this section with an important remark: an observational confirmation of the existence of primordial gravitational waves through a measurement of the r parameter is currently one of the main targets of the research in cosmology, since, in the context of single field slow-roll models r is directly connected to the energy scale of inflation. This can be seen recalling that the Friedmann equation connects the inflationary potential and the Hubble parameter during inflation ($V \simeq 3H^2 M_{Pl}^2$ with $M_{Pl} = 1/\sqrt{8\pi G}$ being the *reduced Planck mass*), therefore we have (Abazajian et al., 2016)

$$V^{1/4} = 1.04 \times 10^{16} \text{GeV} \left(\frac{r_*}{0.01} \right)^{1/4}, \tag{1.128}$$

where r_* is the value of r at the pivot scale, that we chose as $k_0 = 0.05\,\text{Mpc}^{-1}$ in this last equation.

1.8.6 *Observational constraints on inflation*

Currently the best observational constraints on the physics of inflation come from CMB and Large Scale Structure experiments. However, as we will describe in more detail in Chapter 5, extremely interesting constraints could be put in the future using other probes, such as direct detection gravitational wave experiments.

The most recent observations – especially by the Planck satellite's data (Planck Collaboration, 2018c) (often in combination with other experiments datasets to obtain tighter constraints or to break degeneracies in the parameters) – are consistent with the simplest inflationary scenario (single field slow-roll), according to the following evidences:

1. *The Universe is spatially flat.* The constraint on curvature from the Planck measurement (see note 3 for more details) reads $\Omega_K = 0.0007 \pm 0.0019$, compatible with the $K = 0$ hypothesis.

2. *Density fluctuations have a nearly scale-invariant, red-tilted, almost power-law spectrum*. Again, from Planck's results we get a spectral index $n_s = 0.967 \pm 0.004$ not compatible with scale-invariance (that is $n_s = 1$) and without any evidence of a running of the scalar spectral index ($dn_s/d\ln k = -0.0042 \pm 0.0067$ at 1σ), consistently with the inflationary predictions.

3. *Scalar perturbations dominate over tensor ones*. Currently no detection of r exists and the best upper limit available is $r < 0.06$ at

$k_0 = 0.05\,\mathrm{Mpc}^{-1}$ at 95% CL from the combination of CMB B-mode polarization[7] data from the Background Imaging of Cosmic Extragalactic Polarization 2 (BICEP2) - Keck (BICEP2 Collaboration, 2018) and Planck 2018 data (Planck Collaboration, 2018). Figure 1.7 shows the constraints from these combined datasets in the plane r-n_s for several models in the slow-roll approximation[8] and including an uncertainty in the number of e-folds $50 < N_* < 60$. This figure shows results for several inflationary models, among which R^2 inflation[9], natural inflation[10], hilltop quartic models[11], α-attractors[12], power-law inflation[13], spontaneously broken supersymmetry (SB SUSY)[14] and several different monomial potentials; for a detailed description of each model and of the corresponding results, we refer the reader to Planck Collaboration (2018c) and references therein. Note in particular that R^2 inflation, also called the Starobinsky model, is the one favored by current data.

4. *Scalar perturbations are Gaussian and adiabatic.* Scalar fluctuations – due to the fact that, within the framework of the standard single-field slow-roll model, they are produced from the quantum vacuum fluctuations of a scalar field – they must have a Gaussian statistics. The Planck satellite has put tight constraints on primordial non-Gaussianity (Planck Collaboration, 2019), limiting the number of alternative models to be explored. Also the adiabatic nature of the scalar fluctuations (i.e. the fact that the relative number densities of the various particle species are spatially constant) has been confirmed (Planck Collaboration, 2018c).

In conclusion, the inflationary paradigm solves many of the problems of the big bang models and provides several falsifiable predictions, which are all consistent with current observations. In the rest of this Thesis, we will be particularly concerned in providing forecasts for future experiments capable of testing the existence of inflationary gravitational waves, an extremely important prediction of this theory that would allow us to directly probe the energy scale of inflation if the simplest models hold true and would give us an invaluable information on early Universe physics.

1.9 *Evolution of the SGWB after inflation: the gravitational waves energy density*

As this Thesis will be dealing mostly with the tensor perturbations, we give here some of the basic quantities describing the background properties of the SGWB, and in particular we focus in this Section on the time evolution of the inflationary SGWB after inflation.

Note that in the following we will often find useful to pass from

[7] As we will discuss in detail in Chapter 2, we anticipate here that the SGWB is known to excite the divergenceless component of the CMB polarization anisotropies, the so-called polarization B-modes.

[8] See also our forecasts in Section 5.5.3 including future B-mode probes and gravitational wave interferometers.

[9] In the Starobinsky or R^2 model, a term quadratic in the Ricci scalar R is added to the gravitational action, in addition to the usual linear term in the Einstein-Hilbert action. This model predicts $r = 3(n_s - 1)^2$, that is $r \simeq 0.003$ for the Planck central value $n_s \simeq 0.968$ (Kamionkowski and Kovetz, 2016).

[10] Natural inflation (Freese et al., 1990) is characterized by the periodic potential

$$V(\phi) = \Lambda^4 \left[1 + \cos\left(\frac{\phi}{f}\right)\right],$$

with f being the scale which determines the curvature of the potential.

[11] Hilltop quartic models have a potential of the form (Boubekeur and Lyth, 2005)

$$V(\phi) \approx \Lambda^4 \left(1 - \frac{\phi^p}{\mu^p} + ...\right).$$

In these models, the inflaton rolls away from an unstable equilibrium.

[12] These models, described in Ferrara et al. (2013); Kallosh et al. (2013) are motivated by conformal symmetry and supergravity. See Planck Collaboration (2016) for a detailed description of the potential for these models.

[13] Power-law k-inflation models (Armendariz-Picon et al., 1999) are currently ruled out (see Planck Collaboration (2014)).

[14] In these models, slow-roll inflation is driven by loop corrections in spontaneously broken supersymmetric (SUSY) grand unified theories (Dvali et al., 1994).

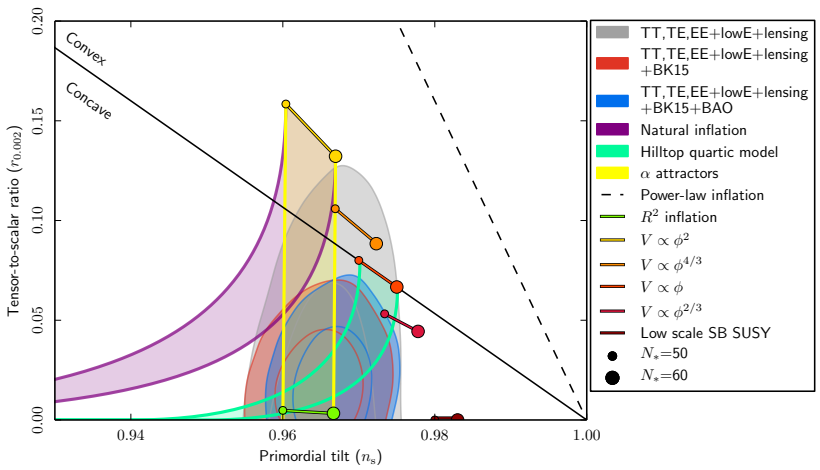

Figure 1.7: Constraints at 68% and 95% C.L. in the plane r-n_s obtained using Planck 2018 data alone (grey contours) and in combination with the B-mode polarization data of BICEP2-Keck (red contours) and BAO data (blue contours), from Planck Collaboration (2018c) (see also footnote 3 and 7). The predictions for several theoretical models of inflation are also shown, including an uncertainty in the number of e-folds $50 < N_* < 60$, as indicated by circles.

the GW wavenumber k to the frequency f of the GW today, which are connected by the relation[15] $k = 2\pi f/c$, can be expressed making explicit the units of measure as $\frac{k}{\text{Mpc}^{-1}} = 6.5 \times 10^{14} \frac{f}{\text{Hz}}$.

A quantity commonly used in the gravitational wave literature to compare the sensitivities of different experiments[16] is the *fractional energy density in GWs* at present (conformal) time τ_0

$$\Omega_{GW}(k, \tau_0) = \frac{1}{\rho_c(\tau_0)} \frac{\partial \rho_{GW}(k, \tau_0)}{\partial \ln k}. \tag{1.129}$$

In the equation above, ρ_c is the critical density of the universe (see Eq. 1.21) and ρ_{GW} the energy density of GWs, given by the (00) component of the energy-momentum tensor of gravitational waves[17]

$$\rho_{GW} = \frac{1}{32\pi^2 a^2(\tau) G} \langle h'_{ij} h'^{ij} \rangle, \tag{1.130}$$

where the tensor h_{ij} represents the GW metric perturbation. Expressing the time evolution of the primordial GW amplitude in terms of the GW transfer function $\mathcal{T}(k, \tau)$ (see Eq. 1.118), we can write the tensor power spectrum at conformal time τ as

$$\mathcal{P}_T(k, \tau) = \mathcal{P}_T^{prim}(k) \left[\mathcal{T}'(k, \tau)\right]^2. \tag{1.131}$$

Substituting the last two equalities in Eq. 1.129, we obtain the following expression for the energy density of gravitational waves at conformal time τ (see Watanabe and Komatsu, 2006, and references therein).

$$\Omega_{GW}(k, \tau) = \frac{\mathcal{P}_T^{prim}(k)}{12 a^2(\tau) H^2(\tau)} \cdot \left[\mathcal{T}'(k, \tau)\right]^2. \tag{1.132}$$

In Chapter 5, we will find useful to compute Ω_{GW} at present time in an approximate analytical form. To this end, simple solution to

[15] We reinstate only in this formula the factor c, which is set to 1 elsewhere in this Section and Thesis.

[16] This quantity will come in particularly handy in Chapter 5, when we will compare forecasts on the sensitivities of future CMB B-mode experiments and direct experiments, such as space and ground laser interferometers.

[17] The energy-momentum tensor of gravitational waves can be defined starting from the variation of the action for tensor perturbations with respect to the metric, and assumes the form $t_{\mu\nu} = \frac{1}{16\pi G} \sum_{P=+,\times} (\partial_\mu E_P^t \partial_\nu E_P^t - \bar{g}_{\mu\nu} \partial_\alpha E_P^t \partial^\alpha E_P^t)$.

the wave equation 1.115 can be analytically derived – neglecting the anisotropic stress term for the moment – for a mode that re-enters the horizon in a radiation-dominated

$$h_P^{RD}(k,\tau) = h_P^{prim}(k) j_0(k\tau) \tag{1.133}$$

or a matter-dominated Universe,

$$h_P^{MD}(k,\tau) = h_P^{prim}(k) \frac{3j_1(k\tau)}{k\tau}. \tag{1.134}$$

Exploiting the transfer function we defined in Eq. 1.118, and assuming an instantaneous transition between matter- and radiation-dominated eras, we can express the time evolution of the gravitational waves amplitude in the following three regimes

$$\mathcal{T}(k,\tau) = \begin{cases} j_0(k\tau), & \text{if } \tau < \tau_* \text{ and } k > k_*, \\ \dfrac{\tau_*}{\tau}\left[A(k) j_1(k\tau) + B(k) y_1(k\tau)\right], & \text{if } \tau > \tau_* \text{ and } k > k_*, \\ \dfrac{3j_1(k\tau)}{k\tau}, & \text{if } \tau > \tau_* \text{ and } k < k_*, \end{cases} \tag{1.135}$$

where the first two expressions represent the evolution of modes that entered the horizon during the radiation-dominated era, while the third one describes modes which entered the horizon during matter-dominated era. Here τ_* is the conformal time at the epoch of matter-radiation equality and k_* is the comoving wavenumber of the modes that entered the horizon at that time, j_x, and y_x with integer x are the spherical Bessel functions of first and second kind, respectively. The functions $A(k)$ and $B(k)$ are computed matching the first two expressions of Eq. 1.135 and their first derivatives at matter-radiation equality, and read

$$A(k) = \frac{3}{2k\tau_*} - \frac{\cos(2k\tau_*)}{2k\tau_*} + \frac{\sin(2k\tau_*)}{(2k\tau_*)^2}, \tag{1.136}$$

$$B(k) = -1 + \frac{1}{(k\tau_*)^2} - \frac{\cos(2k\tau_*)}{(k\tau_*)^2} - \frac{\sin(2k\tau_*)}{2k\tau_*}. \tag{1.137}$$

In conclusion, the resulting Ω_{GW} can be written as a piecewise function for the three different regimes (Watanabe and Komatsu, 2006)

$$\Omega_{GW}(k,\tau) = \frac{k^2 \mathcal{P}_T^{prim}(k)}{12} \cdot \begin{cases} \dfrac{a^2(\tau)}{a^4(\tau_*) H^2(\tau_*)} \left[j_1(k\tau)\right]^2, & \text{if } \tau < \tau_* \text{ and } k > k_*, \\ \dfrac{a(\tau)}{a^3(\tau_0) H_0^2} \dfrac{\tau_*^2}{\tau^2} \left[A(k) j_2(k\tau) + B(k) y_2(k\tau)\right]^2, & \text{if } \tau > \tau_* \text{ and } k > k_*, \\ \dfrac{a(\tau)}{a^3(\tau_0) H_0^2} \left[\dfrac{3j_2(k\tau)}{k\tau}\right]^2, & \text{if } \tau > \tau_* \text{ and } k < k_*. \end{cases} \tag{1.138}$$

We need now to choose an appropriate conformal time to match the first two expressions in Eq. 1.135. A possibility is to choose $\tau_* = \tau_{eq}$, where τ_{eq} is computed by equating the scale factor at matter-radiation equality a_{eq} with the analytical expression for the scale factor for a mixed matter-radiation Universe (that is $a(\tau) = H_0^2\Omega_m a_0^3\tau^2/4 + H_0\sqrt{\Omega_r}a_0^2\tau$) (Caprini and Figueroa, 2018)

$$a_{eq} = a_0\left(\frac{\Omega_r}{\Omega_m}\right) = \frac{H_0^2}{4}\Omega_m a_0^3\tau_{eq}^2 + H_0\sqrt{\Omega_r}a_0^2\tau_{eq}. \tag{1.139}$$

The resulting τ_{eq} is

$$\tau_{eq} = \frac{2\left(\sqrt{2}-1\right)\sqrt{\Omega_r}}{a_0 H_0\Omega_m} \simeq 86\,\mathrm{Mpc}, \tag{1.140}$$

corresponding to a wavenumber

$$k_{eq} = \frac{\sqrt{2}a_0 H_0\Omega_m}{\sqrt{\Omega_r}} \simeq 1.3\times10^{-2}\mathrm{Mpc}^{-1}. \tag{1.141}$$

However, as noted by Caprini and Figueroa (2018), the gravitational waves transfer function obtained using $\tau_* = \tau_{eq}$ does not reproduce very well the actual numerical solution of Eq. 1.115. In fact, a better choice of the matching time is represented by $\tau_* = \tau_{cross}$, where τ_{cross} is the time at which the scale factors $a_m = H_0^2\Omega_m a_0^3\tau^2/4$ and $a_r = H_0\sqrt{\Omega_r}a_0^2\tau$ cross. Setting $a_m(\tau_{cross}) = a_r(\tau_{cross})$ gives

$$\tau_{cross} = \frac{4\sqrt{\Omega_r}}{a_0 H_0\Omega_m} \simeq 420\,\mathrm{Mpc}, \tag{1.142}$$

corresponding to $k_{cross} = 1/\tau_{cross} \simeq 2.38\times10^{-3}\mathrm{Mpc}^{-1}$. As can be inferred from Figure 1.8, matching the two solutions at τ_{cross} better reproduces the behaviour of the actual background and gives an analytical solution which better approximates the numerical one (Figure 1.9). We adopt therefore this latter choice for the matching time in the following.

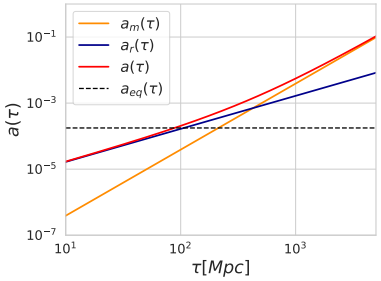

Figure 1.8: Scale factor evolution as a function of conformal time τ: the one for a matter-dominated Universe a_m (see tect for details) is shown in orange, a_r for a radiation-dominated one is shown in blue, while the mixed matter + radiation one is in red. We also show the scale factor at matter-radiation equality a_{eq} as a dashed black line. Adapted from Caprini and Figueroa (2018).

1.9.1 *Damping due to changes in the effective degrees of freedom*

As we discussed extensively in Section 1.5, because of the cosmic expansion and the consequent temperature decrease, a certain particle species will not be able to maintain its equilibrium anymore with the cosmic plasma. Therefore, the effective number of relativistic particle species contributing to the energy density g_* and entropy g_{s*} of the Universe will decrease in time. A detailed calculation of this two functions can be found in Saikawa and Shirai (2018) in the context of the Standard Model of particle physics (see Figure 1.10).

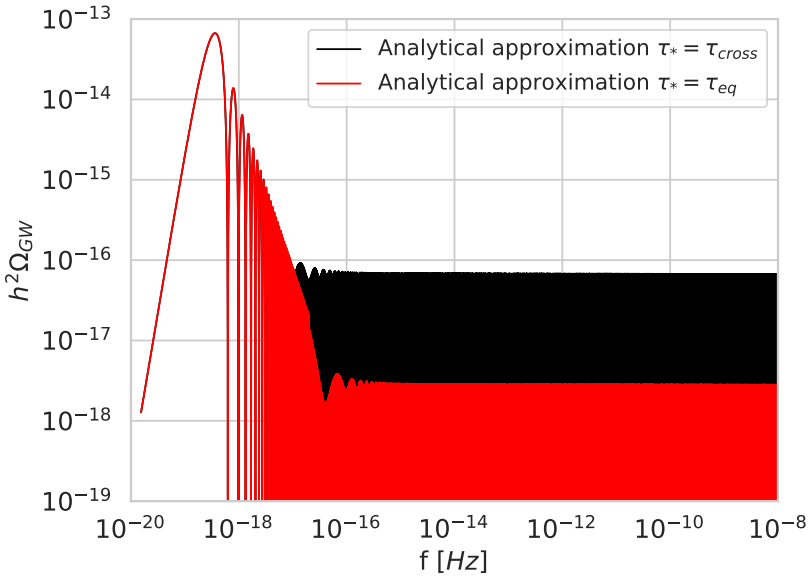

Figure 1.9: Comparison between the Ω_{GW} today obtained from the analytical approximation in Eq. 1.138, assuming $\tau_* = \tau_{eq}$ (in red) and $\tau_* = \tau_{cross}$ (in black). We chose for both curves a value $r = 0.01$ for the tensor-to-scalar ratio and we neglected the neutrino damping and the damping due to the change in effective degrees of freedom in the early Universe (see Section 1.9.1).

Using the conservation of entropy and Eqs. 1.41 and 1.44, it can be shown that the energy density of the Universe in the radiation dominated era evolves according to $\rho \propto g_* g_{s*}^{-4/3} a^{-4}$. This will affect the evolution of scale factor, through the Friedmann equation 1.12 and, in turn, the evolution of the SGWB through the Eq. 1.115.

We can approximately quantify the suppression effect on $\Omega_{GW}(k, \tau_0)$ due to the change in effective relativistic degrees of freedom, noting that the ratio between the GW amplitude when taking into account the change in g_* (and g_{s*}) and the one neglecting it, is (Caprini and Figueroa, 2018)

$$\frac{h(k,\tau_0)|_{with\, g_*}}{h(k,\tau_0)|_{without\, g_*}} = \left(\frac{g_*}{g_{*0}}\right)^{1/2} \left(\frac{g_{s*}}{g_{s*0}}\right)^{-2/3}, \tag{1.143}$$

where g_{*0} and g_{s*0} are the values of the functions g_* and g_{s*} at present time. The SGWB energy density at present time will be suppressed accordingly:

$$\frac{\Omega_{GW}(k,\tau_0)|_{with\, g_*}}{\Omega_{GW}(k,\tau_0)|_{without\, g_*}} = \left(\frac{g_*}{g_{*0}}\right) \left(\frac{g_{s*}}{g_{s*0}}\right)^{-4/3}. \tag{1.144}$$

This damping effect is evident at frequencies $> 10^{-12}$ Hz, as we show in Figure 1.11 and it is particularly important at laser interferometers frequencies ($f > 10^{-6}$ Hz), as we will discuss in Chapter 5. Figure 1.11 also shows a good agreement between the analytical and the numerical solutions obtained from the Boltzmann code CLASS (Cosmic

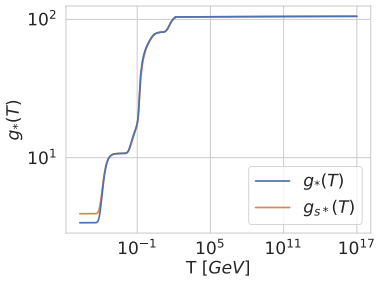

Figure 1.10: Number of effective degrees of freedom contributing to energy density (g_*, blue curve) and entropy (g_{s*}, orange curve) of the Universe in the context of the Standard Model of particle physics. These two functions have been computed and made available by Saikawa and Shirai (2018).

Linear Anisotropy Solving System, Blas et al., 2011) and by Saikawa and Shirai (2018), except from the region between $\sim 10^{-16}$ Hz and $\sim 10^{-10}$ Hz, where the effect of neutrinos damping is taken into account in the numerical solutions but not in the analytical one. Both numerical solutions take also into account the damping from free-streaming photons, which, according to Saikawa and Shirai (2018), can cause up to a factor ~ 0.85 decrease around $\sim 10^{-17}$ Hz. Furthermore, the small differences in height between the peaks in the range $10^{-18}\,\text{Hz} \lesssim f \lesssim 10^{-16}\,\text{Hz}$ of the numerical and analytical solutions, are also due to differences between the actual (numerical) scale factor and the approximated one (see discussion around Eq. 1.139). However, as we will discuss in Chapter 5, neglecting both the neutrinos and photons damping effects and the small scale factor differences does not represent a problem for our purposes, for two reasons: (i) we will be only interested in experiments probing frequencies above $\sim 10^{-10}$ Hz, where the effect of neutrinos damping is negligible; (ii) we will use for our forecasts on the SGWB at CMB frequencies ($\sim 10^{-18} - 10^{-16}$ Hz) the angular power spectra computed by Boltzmann codes (such as `CLASS` (Blas et al., 2011; Dahal et al., 2020) and `CAMB` (Code for Anisotropies in the Microwave Background, Lewis et al., 2000)), which include the neutrino and photon damping terms.

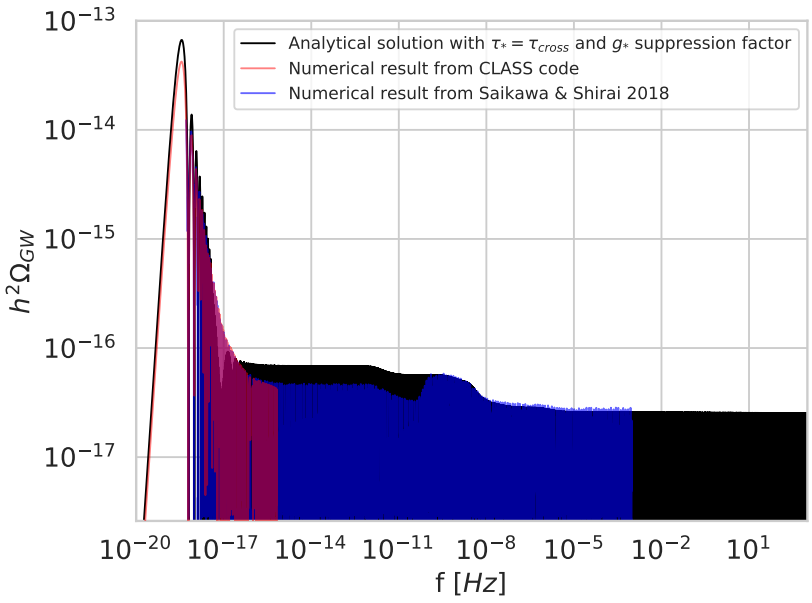

Figure 1.11: Comparison between the Ω_{GW} today obtained from the analytical approximation in Eq. 1.138, assuming $\tau_* = \tau_{cross}$, including the suppression factor 1.144 due to the change in the effective degrees of freedom in the early Universe (in black), the Ω_{GW} obtained from the numerical solution to Eq.1.115 using the `CLASS` code, including the free-streaming neutrinos and photons damping (in red) and the numerical solution to Eq.1.115 shown in Saikawa and Shirai (2018), which also includes the neutrinos and photons damping term and the suppression due to the change in the effective degrees of freedom. We chose for all curves a value $r = 0.01$ for the tensor-to-scalar ratio.

2
Imprint of gravitational waves in the CMB

As we will discuss in detail in Chapters 3 and 5, the detection of the primordial SGWB can be pursued in a direct way – through ground and space based laser interferometers or other techniques – or in a more "indirect" way, by observing its effect on the CMB, and in particular on its polarization. The latter option, represents at the moment our best near future opportunity to probe the primordial SGWB, if the correct model for inflation is the standard single-field slow-roll.

This Chapter will be dedicated to the study of the imprints that primordial gravitational radiation leaves on the CMB. We will need to introduce the theory of CMB anisotropies, starting from the rich phenomenology of the *temperature anisotropies* (Section 2.1) and gathering the main mathematical and statistical tools useful for this study. Sections 2.1.7 of this Chapter will be dedicated to the description of other physical mechanisms producing *secondary CMB anisotropies*, such as the Sunyaev-Zeldov'ich effect and the reionization. Section 2.2 will introduce the anisotropies in the *polarization* pattern of the CMB and their splitting – according to their parity – into *E and B-modes*, with particular attention to the way the scalar and tensor perturbations of the metric (Section 2.3). We will then explore the *gravitational lensing* mechanism of the CMB anisotropies (Section 2.4), with a special focus on its contamination to primordial *B*-modes observations (Section 2.4.1) and the possibility of "cleaning" the signal in a procedure called *delensing*.

This chapter is built upon the reading of the following books and reviews Dodelson (2003), Hu (1995), Hu and Dodelson (2002) and Bucher (2015) in addition to specific references indicated in the text.

2.1 *Theory of CMB anisotropies: Temperature*

This Section will be dedicated to the understanding of CMB temperature anisotropies: we will first introduce the necessary Boltzmann equations formalism to treat the evolution of a perturbed multi-component Universe made of photons, baryons, neutrinos, Dark Matter and Dark Energy (Section 2.1.1). We will then study the behaviour of perturbations on large, intermediate and small scales (Sections 2.1.2, 2.1.3 and 2.1.4). We will then connect the Boltzmann perturbed equations with the observed temperature anisotropies (Section 2.1.5) and introduce their angular power spectrum (Section 2.1.6), explaining the origin of the various contributions to the observed temperature anisotropie. Finally, we will consider some of the major

secondary sources of anisotropy.

2.1.1 *Boltzmann equations*

In order to study the evolution of perturbations in the primordial plasma of photons and matter, we have to take into account the mutual interactions between the matter-energy components themselves (for instance the Compton interactions which couple photons to electrons) and between the matter content and the space-time metric (Figure 2.1).

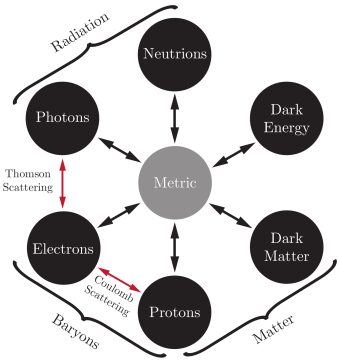

Figure 2.1: Mutual interactions between the cosmic matter-energy components and the space-time metric, as encoded in the Boltzmann equation 2.1. From Baumann (2018).

This is achieved through the *Boltzmann equation*, describing the time evolution of the distribution function f (see Eq.1.38) of a certain species. Therefore, each of the species $\alpha = \gamma, \nu, e, b, c...$ will satisfy a Boltzmann equation of the kind

$$\frac{df_\alpha}{dt} = C[f_\beta], \tag{2.1}$$

where C is the *collision term*, describing the interactions of the species α and can depend on the distribution functions of other species β. In particular, the absence of a collision term implies the *free-streaming* of a certain species

$$\frac{df_\alpha}{dt} = 0, \tag{2.2}$$

which corresponds to Liouville's theorem, i.e. the number of particles in a phase space element does not change in time.

In the following, we will be concerned with studying the effect of linear order perturbations in the Boltzmann equation for photons, therefore we expand the photon distribution function (which for convenience will be denoted simply as f) at first order around its zero-order Bose-Einstein value

$$f(\mathbf{x}, \mathbf{p}, t) = \left[\exp\left(\frac{p}{T(t)[1 + \Theta(\mathbf{x}, \mathbf{p}, t)]}\right) - 1\right]^{-1}, \tag{2.3}$$

where $\mathbf{p}$ is the photon momentum and we introduced the perturbation to the photon distribution function $\Theta = \delta T/T$. If we define the zero-order distribution function as

$$\bar{f} = \left[\exp\left(\frac{p}{T(t)}\right) - 1\right]^{-1}, \tag{2.4}$$

we can rewrite Eq. 2.3 as

$$f = \bar{f} - p\frac{\partial \bar{f}}{\partial p}\Theta, \tag{2.5}$$

at first order.

Now, the left-hand side of Eq. 2.1 for photons can be rewritten expanding the full time derivative in partial derivatives and using the

geodesic equation obtained from the perturbed metric[1] 1.96, while the collision term in the right-hand side can be computed accounting for the Compton interaction between photons and electrons (Eq. 1.62). The final Boltzmann equation for photons in terms of conformal time and neglecting polarization, reads (Dodelson, 2003)

$$\Theta' + ik\mu\Theta + \Phi' + ik\mu\Psi = -\eta'_{opt}\left[\Theta_0 - \Theta + \mu v_b\right], \tag{2.6}$$

in Fourier space[2], where we defined the cosine between the wavenumber $\mathbf{k}$ and the photon direction $\hat{p}$ as

$$\mu = \frac{\mathbf{k}\cdot\hat{p}}{k}, \tag{2.7}$$

the ℓth *multipole moment* Θ_ℓ of the temperature field is defined as

$$\Theta_\ell = \frac{1}{(-i)^\ell}\int_{-1}^{1}\frac{d\mu}{2}\mathcal{P}_\ell(\mu)\Theta(\mu), \tag{2.8}$$

and $\mathbf{v}_b$ is the baryon velocity. Note that in the Boltzmann equation above, all ℓ multipoles are in Θ, and only the monopole, Θ_0, appears explicitely. In order to understand the physical mechanism leading to CMB temperature anisotropies – which involves the coupling of baryons and photons in a single *photon-baryon fluid* before recombination – we will need also evolution equations for baryons. These can be derived considering Compton and Coulomb ($e + p \longrightarrow e + p$) collision terms and noting that electrons and protons are tightly-coupled because of the latter interaction, and therefore their fractional overdensities are equal,

$$\delta_b \equiv \frac{\delta\rho_e}{\rho_e} = \frac{\delta\rho_p}{\rho_p}, \tag{2.9}$$

and also their velocities $\mathbf{v}_b \equiv \mathbf{v}_e = \mathbf{v}_p$. The Boltzmann equations for the baryons in Fourier space will then read

$$\begin{aligned} &\delta_b^{'} + ikv_b + 3\Phi^{'} = 0, \\ &v_b^{'} + \frac{a'}{a}v_b + ik\Psi = \eta_{opt}^{'}\frac{1}{R}\left[3\Theta_1 + v_b\right], \end{aligned} \tag{2.10}$$

where we defined the ratio of photon to baryon density as

$$\frac{1}{R} = \frac{4\bar{\rho}_\gamma}{3\bar{\rho}_b}. \tag{2.11}$$

We can now study the dynamics of the photon-baryon fluid before recombination, when the *tight-coupling approximation* holds true.

2.1.2 *Tight-coupling regime: small and intermediate scales*

As we have outlined above, before recombination photons were tightly-coupled to the baryons through Compton scattering. In

[1] Note that in this Chapter we have chosen the *conformal Newtonian gauge* to express the perturbed metric. This amounts to saying that Eq. 1.96 will have $E = B = B_i^{\perp} = 0$, and therefore, from Eq. 1.103 for the two Bardeen potentials, we get that $A = \Psi$ and $C = -\Phi$.

[2] Following the notation common in the literature, we are neglecting a ˜over all quantities computed in Fourier space throughout this Chapter.

particular, recalling the mantra of Section 1.5, the tight-coupling is a regime in which the expansion rate is much smaller than the reaction rate ($\Gamma \gg \mathcal{H}$), or, in other words, the optical depth is $\eta_{opt} \gg 1$. In this approximation, it can be shown (using Eqs. 2.6 and 2.8) that the only non-negligible moments of the temperature fluctation (the multipoles Θ_ℓ) are the *monopole* $\ell = 0$ and the *dipole* $\ell = 1$: photons, therefore, behave as a fluid and can be described by just density and pressure.

The Boltzmann equations for photons and baryons (Eqs. 2.6 and 2.10) can be recast into a single second order differential equation, describing the the *acoustic oscillations* of the photon-baryon fluid in the tightly-coupled limit, that is

$$\Theta_0'' + \frac{a'}{a}\frac{R}{1+R}\Theta_0' + k^2 c_s^2 \Theta_0 = \underbrace{-\frac{k^2}{3}\Psi - \frac{a'}{a}\frac{R}{1+R}\Phi' - \Phi''}_{F(\tau)}, \tag{2.12}$$

where we defined the fluid *sound speed* as

$$c_s = \sqrt{\frac{1}{3(1+R)}}. \tag{2.13}$$

This equation can be generally regarded as that of a *forced harmonic oscillator*, with the right-hand-side representing the forcing term $F(\tau)$: it describes a system in which compression and rarefaction phases, accompanied by heating and cooling of the fluid, alternates due to the action of the radiation pressure against the gravitational attraction. While on super-horizon scales the perturbations show hardly any evolution (see Section 2.1.4 below), smaller scales enter the horizon at a certain point and oscillate in time: in particular, modes that arrive at recombination in state of maximum compression (rarefaction) generate odd (even) peaks in the temperature fluctuations (see Eq. 2.14 below).

From the definition in Eq. 2.13, we can notice immediately that the sound speed decreases as R increases, that is when the baryon density becomes larger: this produces acoustic oscillations with lower frequency. Baryons have also another important effect in the acoustic peaks phenomenology: they shift the equilibrium point of the forced harmonic oscillator (Eq. 2.12) with respect to radiation, enhancing only oscillations in the compression phase (i.e. the odd peaks) because of their additional mass. This is commonly called *baryon drag* or *baryon loading* in the literature (Figure 2.3). Furthermore, an increase in baryon density influences the *diffusion damping* scale (described in Section 2.1.3 below).

The gravitational potentials,known also as Bardeen potential (Bardeen, 1980), in the forcing term $F(\tau)$ are mainly determined by Dark Matter in a matter-dominated Universe, therefore this component influences the oscillation peaks structure too: an increase in

$\Omega_c h^2$ determines an increased asymmetry between the amplitudes of even and odd peaks, similarly to what happens with an increase in the baryon density. Other effects of variations of the Dark Matter density – including its impact on the *early integrated Sachs-Wolfe* effect – will be explored in Section 2.1.6.

An analytical solution to Eq. 2.12 for the monopole was obtained by Hu and Sugiyama (1995)

$$\Theta_0(\tau) + \Phi(\tau) = (\Theta_0(0) + \Phi(0)) \cos kr_s + \frac{k}{\sqrt{3}} \int_0^\tau (\Phi(x) - \Psi(x)) \sin\left[k(r_s(\tau) - r_s(x))\right] dx, \tag{2.14}$$

where we defined the *sound horizon* r_s as

$$r_s(\tau) \equiv \int_0^\tau c_s(x) dx. \tag{2.15}$$

This solution, sometimes called the *Sachs-Wolfe term*[3] (SW), describes the dynamics of the photon-baryon fluid and gives the position of the *acoustic peaks* as the extrema of the cosine in the first term[4], that is $k_{peak} = n\pi/r_s$ with $n = 1, 2, ...$

We can arrive also at an analytical solution for the dipole moment by taking the time derivative of Eq. 2.14,

$$\Theta_1(\tau) = \frac{1}{\sqrt{3}} (\Theta_0(0) + \Phi(0)) \sin kr_s - \frac{k}{3} \int_0^\tau (\Phi(x) - \Psi(x)) \cos\left[k(r_s(\tau) - r_s(x))\right] dx, \tag{2.16}$$

which produces peaks $\pi/2$ out of phase with the monopole solution 2.14, since it is dominated by the term $\sin kr_s$. This dipole contribution is sometimes called the *Doppler term*, and will be of utmost importance in Section 2.1.6, where we will study its impact on the angular spectrum of temperature anisotropies.

Let us now go beyond the strict tight-coupling approximation and the simplified acoustic oscillations we have been treating up to now, considering other physical mechanisms that act on the photon baryon fluid for smaller scale perturbations. We start with the diffusion damping of the oscillations.

[3] Not to be confused with the *Sachs-Wolfe plateau* (described in Section 2.1.6) and the *integrated Sachs-Wolfe effect* (Section 2.1.5).

[4] We are assuming here that the first term $\propto \cos kr_s$ dominates over the integral term. This approximation gives a reasonably accurate position of the first peaks, when compared to the exact solution (Hu and Sugiyama, 1995)

2.1.3 *Diffusion damping*

Perturbations with larger wavenumber k (that is smaller scales) are affected by the diffusion damping[5], due to the fact that the tight-coupling approximation in which photons and baryons constitute an ideal single fluid is valid only if the Compton interaction is perfectly efficient. This is not actually the case as photons travel a finite

[5] Sometimes also called *Silk damping* in the literature.

distance between scatterings λ_D, determined by the expansion of the Universe and the by the Compton mean free path

$$\lambda_D \sim \lambda_C \sqrt{N} = \frac{1}{n_e a \sigma_T} \frac{1}{a}, \tag{2.17}$$

where $N = \sqrt{n_e \sigma_T H^{-1}}$ is the number of scatterings in a Hubble time. Every perturbation with $\lambda < \lambda_D$ will thus be erased by the mixing of hot and cold spots due to the traveling of the photons, causing an exponential damping of smaller scales modes. In this scenario, diffusion will generate heat conduction and shear viscosity π_γ in the photon-baryon fluid (Figure 2.2), leading to a non-negligible quadrupole moment[6] Θ_2. Therefore, we will keep moments up to the quadrupole $\ell = 2$ in the hierarchy of Boltzmann equations for photon perturbations, while, for what concerns the baryons, the second of Eqs. 2.10 will suffice for our purposes. The time dependence of the solutions will be in this case (Dodelson, 2003)

$$\Theta_0, \Theta_1 \sim e^{ik \int d\tau c_s(\tau)} e^{-k^2/k_D^2}, \tag{2.18}$$

$$\Theta_2 = -\frac{4k}{9\eta'_{opt}} \Theta_1, \tag{2.19}$$

where the *damping scale* is given by

$$\frac{1}{k_D^2} = \int_0^\tau \frac{1}{6(1+R) n_e \sigma_T a(x)} \left(\frac{R^2}{1+R} + \frac{8}{9} \right) dx, \tag{2.20}$$

and can be connected to Eq. (2.17), as $\lambda_D \sim 1/k_D$.

[6] We shall see in Section 2.2 the importance of the quadrupole moment in producing polarization.

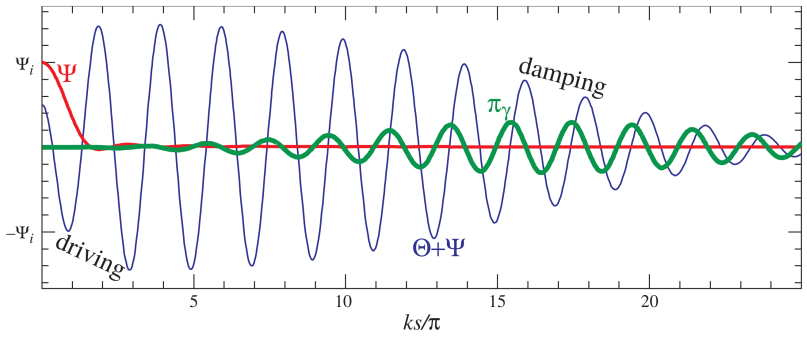

Figure 2.2: The temperature acoustic oscillations in the photon-baryon fluid are damped by photon diffusion, which produces anisotropic stress π_γ. The potential Ψ drives the oscillations (a phase indicated as "driving" in the plot) by decaying and leaving the photon-baryon fluid in the phase of maximum compression without a gravitational force to counteract the pressure. From Hu and Dodelson (2002).

A very important physical effect connected to the damping scale, is the the one due to the baryon density: an increase in $\Omega_b h^2$ determines a larger k_D and therefore a shift of the the diffusion damping effect to smaller scales[7]. This latter effect can be used in combination with the fact that a an increase in baryon density enhances odd peaks and suppresses even peaks, to break the degeneracies with other cosmological parameters and put tight constraints on $\Omega_b h^2$.

[7] It can be shown (Dodelson, 2003), that $k_D \propto (\Omega_b h^2)^{1/2}$.

2.1.4 *Super-horizon modes*

Having described the main phenomenology at smaller and intermediate scales, we now pass to large-scale modes. As anticipated in Section 2.1.2, fluctuations on scales larger than the Hubble horizon remain almost constant during the Universe evolution. This can be seen by taking the super-horizon limit of the Boltzmann equations for photons and by using the appropriate adiabatic initial conditions: the effective temperature observed at recombination time will be given by (Dodelson, 2003)

$$(\Theta_0 + \Psi)(\tau_{rec}) = -\frac{1}{3}\Phi(\tau_{rec}) = -\frac{1}{5}\mathcal{R} = -\frac{1}{6}\delta_c(\tau_{rec}), \tag{2.21}$$

in terms of the curvature perturbation $\mathcal{R}$ (Eq. 1.104) and the Dark Matter density perturbation δ_c. This equation can derived considering that for super-horizon scales $\Phi \simeq -\Psi$, $\Phi = 3\mathcal{R}/5$. The last equality in 2.21, in particular, tells us that super-horizon Dark Matter positive perturbations (overdensities) at recombination corresponds to negative temperature fluctuations ("cold spots") in the CMB, since photons have to climb up the potential well. The redshift they experience in this situation is enough to cancel the initial positive temperature fluctuation due to the overdensity.

2.1.5 *Connecting recombination to observed CMB: Free-streaming and line-of-sight integration*

We will now be concerned with deriving an expression for the multipole moment observed today in the CMB anisotropy pattern in terms of the temperature fluctuations at recombination. Through manipulations and integration over conformal time of the Boltzmann equation for photons 2.6, we can arrive at an analytical expression connecting the monopole and dipole at recombination with temperature fluctuations at τ_0

$$\begin{aligned}\Theta_\ell(k,\tau_0) = &\int_0^{\tau_0} g(\tau)\left[\Theta_0(k,\tau) + \Psi(k,\tau)\right] j_\ell[k(\tau_0-\tau)]d\tau \\ &- \frac{i}{k}\int_0^{\tau_0} g(\tau) v_b(k,\tau)\frac{d}{d\tau} j_\ell[k(\tau_0-\tau)]d\tau \\ &+ \int_0^{\tau_0} e^{-\tau}\left[\Psi'(k,\tau) + \Phi'(k,\tau)\right] j_\ell[k(\tau_0-\tau)]d\tau,\end{aligned} \tag{2.22}$$

where $g(\tau)$ is the visibility function defined in 1.63. This relation can be recast in a more interpretable manner by noting that, since the visibility function is sharply peaked at recombination, the first two integrals in 2.22 can be substituted with the value of their integrands

at recombination:

$$\Theta_\ell(k,\tau_0) = \underbrace{[\Theta_0(k,\tau_{rec}) + \Psi(k,\tau_{rec})]\, j_\ell[k(\tau_0-\tau_{rec})]}_{\text{SW term}} + \underbrace{3\Theta_1(k,\tau_{rec})\left(j_{\ell-1}[k(\tau_0-\tau_{rec})] - (\ell+1)\frac{j_\ell[k(\tau_0-\tau_{rec})]}{k(\tau_0-\tau_{rec})}\right)}_{\text{Doppler term}} + \underbrace{\int_0^{\tau_0} e^{-\tau}\left[\Psi'(k,\tau)+\Phi'(k,\tau)\right] j_\ell[k(\tau_0-\tau)]d\tau}_{\text{ISW term}}. \tag{2.23}$$

The last integral, which is not zero only if the gravitational potentials are time-dependent, represents the contribution of the *integrated Sachs-Wolfe effect* (ISW). We will give more details on this important effect in a dedicated Section (2.1.6). Another important information that we can draw from this last expression is that, due to the characteristic shape of spherical Bessel functions, the contribution of a mode k manifest itself mainly on angular scales $\ell \sim k\tau_0$.

2.1.6 *Angular power spectrum of temperature anisotropies*

To make contact with observations, it is customary to expand the temperature fluctuation $\Theta(\mathbf{x},\hat{\mathbf{p}},\tau)$ in spherical harmonics $Y_{\ell m}$, according to

$$\Theta(\mathbf{x},\hat{\mathbf{p}},\tau) = \sum_{\ell=1}^{\infty}\sum_{m=-\ell}^{\ell} a^T_{\ell m}(\mathbf{x},\tau)Y_{\ell m}(\hat{\mathbf{p}}). \tag{2.24}$$

Using the orthogonality of spherical harmonics allows to relate the observables $a^T_{\ell m}$ to the multipole moments

$$a^T_{\ell m}(\mathbf{x},\tau) = \int \frac{d^3k}{(2\pi)^3} e^{i\mathbf{k}\cdot\mathbf{x}} \int d\omega Y^*_{\ell m}(\hat{\mathbf{p}})\Theta(\mathbf{k},\hat{\mathbf{p}},\tau). \tag{2.25}$$

The distribution of the $a^T_{\ell m}$ is expected to be Gaussian due to the Gaussianity of inflationary quantum fluctuations: this implies a zero mean $\langle a^T_{\ell m}\rangle = 0$ and variance

$$\langle a^T_{\ell m} a^{*T}_{\ell' m'}\rangle = \delta_{\ell\ell'}\delta_{mm'}C^{TT}_\ell. \tag{2.26}$$

Here C_ℓ is the *angular power spectrum* of temperature anisotropies: it cannot be observed directly, but one can obtain an estimator in the form

$$\hat{C}^{TT}_\ell = \frac{1}{2\ell+1}\sum_m a^T_{\ell m} a^{*T}_{\ell m}. \tag{2.27}$$

Furthermore, there is a fundamental statistical limitation to the estimator effciency, the so-called *cosmic variance*

$$\frac{\langle \hat{C}^{TT\,2}_\ell\rangle - \langle \hat{C}^T_\ell\rangle^2}{C^{TT\,2}_\ell} = \frac{2}{2\ell+1}, \tag{2.28}$$

predominantly affecting larger scales.

It is possible to obtain an expression for the temperature spectrum produced by scalar perturbations only – which we indicate as $C_{\ell,s}^{TT}$ with a subscript s standing for scalar – in terms of the multipoles Θ_ℓ, that is

$$C_{\ell,s}^{TT} = \frac{2}{\pi}\int_0^\infty k^2 \mathcal{P}_\mathcal{R}(k)\left|T_{\ell,s}^{TT}(k)\right|^2 dk. \tag{2.29}$$

In order to derive the expression above, we have separated the temperature fluctuation in a part depending on the initial amplitude and phase of the perturbation ($\mathcal{R}(\mathbf{k})$) and a scalar modes transfer function $T_{\ell,s}^{TT}(\mathbf{k}, \hat{\mathbf{k}}\cdot\hat{\mathbf{p}})$, describing its evolution

$$T_{\ell,s}^{TT}(k) = \frac{\Theta_\ell(k,\tau_0)}{\mathcal{R}(k)}, \tag{2.30}$$

and we have expanded $T_s^{TT}(\mathbf{k},\hat{\mathbf{p}})$ in Legendre polynomials. Equivalent expressions for the angular spectrum and transfer function for tensor modes can be obtained; the total C_ℓ^{TT} will be the sum of the scalar and tensor part in this case (see Section 4.1).

Note that completely analogous expressions to the TT angular power spectra 2.29 and the transfer function 2.30 can be derived as well for the E and B polarization spectra (which will be introduced later in Section 2.2) and their cross-correlations (see for instance Dodelson, 2003).

Large scales: Sachs-Wolfe plateau

We can now use Eq. 2.29 in conjunction with the solutions to the Boltzmann equations at different scales – discussed in Sections 2.1.2 - 2.1.4 – to provide some insight in the structure of the temperature power spectrum. We start with the simplest one to interpret, the super-horizon solution 2.21: in this case the angular power spectrum at large scales is expected to be a constant (for a scale-invariant scalar spectrum) , the so-called *Sachs-Wolfe plateau* (SWP) (Hu, 1995) (Figure 2.3)

$$\ell(\ell+1)C_\ell^{TT,SWP} = \frac{8}{25}A_S, \tag{2.31}$$

and this last expression can be derived using the consideration that the gravitational potential is constant in the matter-dominated epoch. From Eq. 2.23, there are other effects that can produce deviations from the SW constant plateau, in particular the dipole (Doppler) term and the ISW effect (see Section 2.1.6 below).

Intermediate and small scales: acoustic oscillations

On intermediate and small scales there are several effects contributing: the monopole, the dipole, the ISW effect and the diffusion

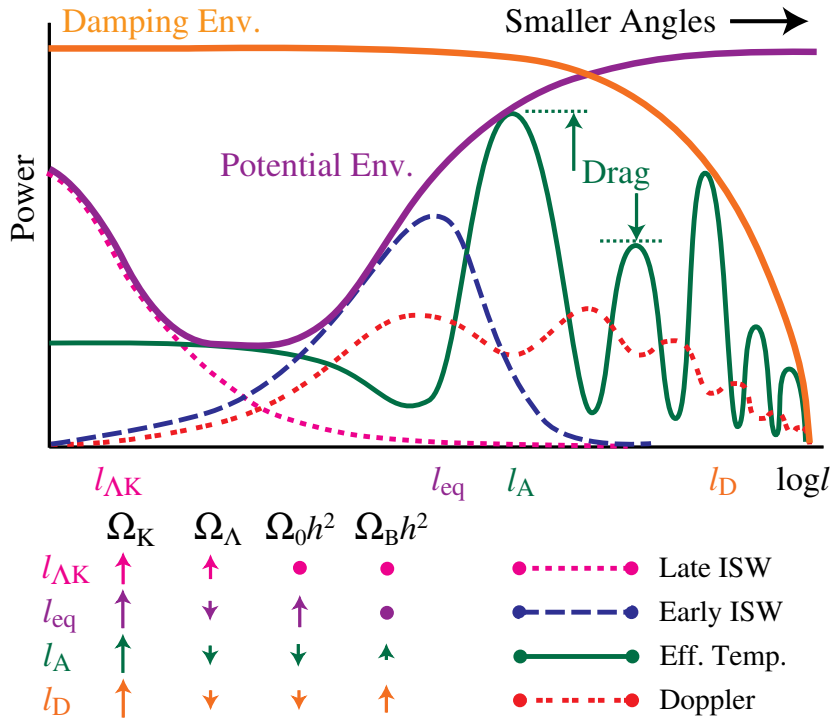

Figure 2.3: A visual summary of the physical mechanisms, described in Section 2.1, affecting the spectrum of temperature anisotropies, from Hu (1995). The solid green line represents the effective temperature $\Theta(\tau) + \Psi(\tau)$, with the effect of baryons on the asymmetry of odd and even peaks indicated as "drag" and the SW plateau clearly evident at large scales. The Doppler term is indicated as the dotted red curve. The diffusion damping affecting smaller scales is represented as the solid orange curve. The Early ISW and Late ISW effects are represented as dashed blue and dotted pink curves, respectively. Below the plot, a scheme representing the shift in the ℓ-axis (beginning with $\ell = 2$), due to a change in the cosmological parameters.

damping. The first thing to notice is that, due to the free-streaming, the monopole term shows peaks slightly shifted to smaller ℓ with respect to the approximated prediction in Section 2.1.2, that is $k_{peak} \sim 0.75\pi/r_s$. The dipole term, as we observed before, is out-of-phase with the monopole, therefore its addition will mainly impact the trough regions, raising their level with respect to the peaks.

Integrated Sachs-Wolfe effect

The ISW effect is due to the time-variation of the Bardeen potentials Ψ and Φ in Eq. 2.23 during the time in which a photon is falling down and climbing up a potential well, determining a net change in the photon temperature. It can be separated in two different contributions:

Early ISW effect (EISW). This term is due to the variation of gravitational potentials at the transition between a matter- and a radiation-dominated Universe, and is particularly important for modes corresponding to the horizon scale around recombination time (around the first peak, see Figure 2.3), due to the Bessel function behaviour in the ISW integral in 2.23. The EISW contribution

can be approximated therefore by

$$\Theta_\ell(k,\tau_0)^{EISW} = [\Psi(k,\tau_0) - \Psi(k,\tau_{rec}) - \Phi(k,\tau_0) + \Phi(k,\tau_{rec})]j_\ell[k(\tau_0 - \tau_{rec})], \tag{2.32}$$

which adds constructively to the monopole, raising the amplitude of the first peak.

Late ISW effect (LISW). This effect is due to the variation of the potentials in the late Universe, when dark energy or curvature are dominating. The main contribution is at very large scales $\ell \lesssim 30$ (Figure 2.3), affecting the SW plateau, since the potentials are already very small for sub-horizon scales at decoupling. LISW is an important probe of the nature of dark energy, and can be cross-correlated with other cosmological observables – for instance large scale structure (Corasaniti et al., 2005) or radio galaxies surveys (Vielva et al., 2006) – to constrain the EoS or the sound speed of dark energy.

Effect of the cosmological parameters

We consider now the impact that a variation of a selection of the ΛCDM model cosmological parameters can have on the angular power spectrum of temperature anisotropies.

We start from the effect of curvature Ω_K: in an open (closed) Universe the peaks get shifted to higher (lower) ℓ with respect to the flat case, due to the different projection of the anisotropies.

Dark energy has two main effects: on one side it enhances the spectrum at very large scales due to the LISW effect, while on the other side has a similar effect to curvature, since it changes the angular diameter distance to the LSS, thus shifting the peaks location to lower ℓ for higher Ω_Λ.

Varying the amplitude A_S and tilt n_S of the scalar spectrum changes the overall normalization of the spectrum and the relative importance of large and small scales, pivoting around the reference scale k_0. This effect is similar to the one of the optical depth to reionization[8] η_{reion}. The rescattering of photons on newly freed electrons only affects modes which are sub-horizon at the time of reionization: an increase in η_{reion} determines a suppression in the spectrum at $\ell \gtrsim 100$, while larger scale modes are unaffected.

We already discussed at lenght the effect of variation in the baryon density (see also Figure 2.4), so we refer the reader to Sections 2.1.2 and 2.1.3 for details.

For what concerns the CDM density, we also anticipated in Section 2.1.2 that it affects the temperature spectrum in a similar way to baryon density, exacerbating the height asymmetry between even and

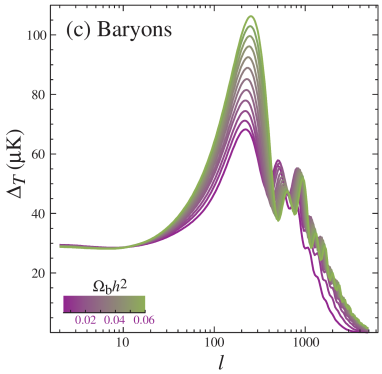

Figure 2.4: Effect of the variation of the baryon density $\Omega_b h^2$ on the temperature angular power spectrum of CMB anisotropies. From Hu and Dodelson (2002).

[8] A description of reionization can be found in Section 1.5

odd peaks (if we keep baryon fixed). Notice also that variations in the Dark Matter density affect also the Bardeen's potential decay: for an increase in $\Omega_c h^2$ the potentials decay less and therefore the EISW effect is less pronounced, with a corresponding suppresion of the first peak.

2.1.7 *Other secondary sources of anisotropy*

We gather in this Section some of the most important secondary sources of anisotropy that we neglected in the previous Section. Also the ISW effect and the gravitational lensing of the CMB can be considered secondary sources. We described the former in Section 2.1.6, while the latter will be discussed in a separate Section (2.4).

Reionization

During reionization, electrons are freed by the first sources of ultraviolet photons, with consequent rescattering of the CMB photons after decoupling. The consequence of this phenomenon are threefold: (i) the production of new secondary anisotropies; (ii) the suppression of the already formed temperature anisotropies on small scales, due to the averaging of many lines of sight converging at the scattering event (leaving anisotropies only in the unscattered fraction $e^{-\tau_{reion}}$); (iii) the generation of additional polarization on large scales (see Section 2.3.2 for details). The anisotropy observed today (neglecting the ISW effect) will be given therefore by (Peter and Uzan, 2013)

$$\begin{aligned}\Theta(\tau_0) \simeq (1 - e^{-\eta_{reion}})[\Theta(\tau_{reion}) + \hat{\mathbf{p}} \cdot v_b(\tau_{reion})] \\ + e^{-\eta_{reion}}[\Theta(\tau_{rec}) + \hat{\mathbf{p}} \cdot v_b(\tau_{rec})],\end{aligned} \tag{2.33}$$

where η_{reion} is the optical depth to reionization and we have approximated the visibility function as a sum of two Dirac deltas at recombination and reionization time. Note also that the first term in Eq. 2.33 represents both the averaging over many lines of sight and the new secondary anisotropies, while the second term depicts the temperature of the unscattered fraction of photons.

Sunyaev-Zel'dovich effect

CMB photons, during their free-streaming, can encounter the regions of hot plasma ($\sim 10^7 - 10^8$K) found in galaxy clusters, and this can give rise to variations of their temperature through the inverse Compton scattering with free electrons in the cluster. This effect is called *thermal Sunyaev-Zel'dovich effect* (tSZ)[9]. The starting point is the Kompaneets equation (see for instance Rybicki and Lightman, 1986, and references therein), describing the Compton interaction

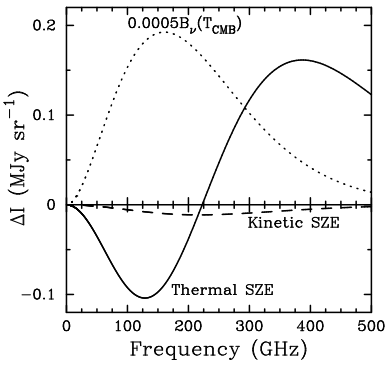

Figure 2.5: A comparison of intensity variation for the tSZ (solid line) and the kSZ (dashed line), for a cluster with Compton y paramter 10^{-4}, $T_e = 10\,\mathrm{keV}$ and peculiar velocity $v_r = 500\,\mathrm{km\,s^{-1}}$. Also shown for reference is the CMB original spectrum multiplied by a factor 0.0005. From Carlstrom et al. (2002).

[9] See Carlstrom et al. (2002) for a review.

of an isotropic and unpolarized radiation with an optically thick gas of non-relativistic electrons at temperature T_e. Specializing the Kompaneets equation to the case of an incident blackbody spectrum with intensity I_ν and temperature $T_\gamma \ll T_e$, we get a temperature variation

$$\frac{\Delta T_\gamma}{T_\gamma} = \frac{\Delta I_\nu}{I_\nu} = -2\frac{k_B}{m_e c^2}\int n_e \sigma_T T_e dl. \tag{2.34}$$

The tSZ introduces therefore spectral distortions of the y-type (Section 1.6), with a net effect of an increase in temperature (or intensity) at high frequencies and a decrease in temperature at low frequencies (Figure 2.6).

The tSZ effect has interesting astrophysical and cosmological applications: the temperature variation is proportional to n_e, thus providing a measurement for the mass of the gas in the cluster; moreover, ΔT_γ is independent of the redshift of the galaxy cluster, allowing to detect them at high redshift.

The peculiar velocity of a cluster can also induce a distortion in the CMB spectrum: this is called *kinetic Sunyaev-Zeldovich effect* (kSZ) and is governed by the equation

$$\frac{\Delta T_\gamma}{T_\gamma} = -\frac{v_r}{c}\int n_e \sigma_T dl. \tag{2.35}$$

where v_r is the radial component of the cluster velocity.

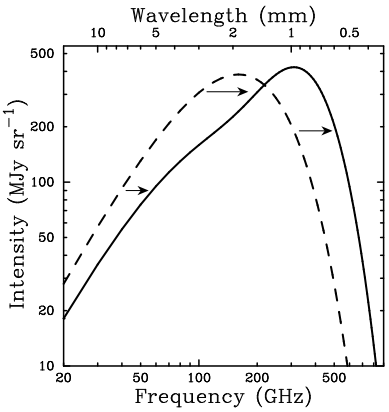

Figure 2.6: tSZ effect for a galaxy cluster with mass exaggerated by a factor 1000 with respect to a typical one. The dashed line represents the original blackbody spectrum, while the solid line the spectrum distorted by the SZ effect. From Carlstrom et al. (2002).

Gravitational waves signature in the temperature spectrum

Also tensor perturbations contribute to the temperature anisotropies: they affect almost exclusively the large scale part of the temperature power spectrum (see Figure 2.8), since on smaller scales gravitational waves have entered the horizon and decayed (see Section 1.8.5). This tensor contribution to the temperature at very large scales is roughly scale-invariant, similarly to scalars.

The effect on the temperature spectrum is too weak – consistently with current CMB upper limits from polarization spectra (see Section 1.8.6) – and too limited by cosmic variance to be detected using the current state-of-the-art CMB technology, therefore, as we will see in Section 2.3, primordial GWs detection is best attempted through their imprint on the B-modes of the polarization.

2.2 *Theory of CMB anisotropies: Polarization*

Up to now we have considered only the physics behind intensity (temperature) of the CMB and neglected the possibility of having a polarized radiation. The CMB is indeed polarized by Thomson scattering [10] (Eq. 1.62), as we will explore in the following. In order

[10] Compton scattering reduces to Thomson one since the energy of CMB photons is much smaller than the electrons rest mass.

to treat properly polarization, we need to introduce some of the necessary formalism, starting from the *Stokes parameters*.

2.2.1 Stokes parameters

A monochromatic electromagnetic plane wave of frequency ω propagating along the $\hat{z}$-axis in Cartesian coordinates, has an electric field vector, evolving in time as

$$\mathbf{E}(\mathbf{x}, t) = \mathcal{E} \exp\left[i(\omega t - \mathbf{k} \cdot \mathbf{x})\right] \tag{2.36}$$

with $\mathcal{E}$ is given by

$$\mathcal{E} = \begin{pmatrix} a_x \exp\left(i\xi_x\right) \\ a_y \exp\left(i\xi_y\right) \\ 0 \end{pmatrix} \tag{2.37}$$

and ξ_x and ξ_y are phase angles. The wave can also be described using the four Stokes parameters, that is the *total intensity*

$$I = \langle a_x^2 \rangle + \langle a_y^2 \rangle = I_x + I_y, \tag{2.38}$$

and the Q, U and V parameters, characterizing its polarization state

$$Q = \langle a_x^2 \rangle - \langle a_y^2 \rangle = I_x - I_y, \tag{2.39}$$

$$U = 2\langle a_x a_y \cos(\xi_x - \xi_y) \rangle, \tag{2.40}$$

$$V = 2\langle a_x a_y \sin(\xi_x - \xi_y) \rangle, \tag{2.41}$$

where the $\langle ... \rangle$ represent averages over several periods, with the assumption that $a_{x,y}$ and $\xi_{x,y}$ are slowly varying with respect to the period of the wave. Furthermore, only three of the four Stokes parameters are independent, being connected by the relation

$$I^2 = Q^2 + U^2 + V^2. \tag{2.42}$$

We are interested now in the way the Stokes parameters transform under a rotation of the $\hat{x} - \hat{y}$ plane by an angle α around the propagation direction $\hat{z}$, that is under the coordinate transformation

$$\begin{pmatrix} x' \\ y' \end{pmatrix} = \begin{pmatrix} \cos\alpha & \sin\alpha \\ -\sin\alpha & \cos\alpha \end{pmatrix} \begin{pmatrix} x \\ y \end{pmatrix}. \tag{2.43}$$

The Q and U parameters transform under this rotation as

$$\begin{pmatrix} Q' \\ U' \end{pmatrix} = \begin{pmatrix} \cos 2\alpha & \sin 2\alpha \\ -\sin 2\alpha & \cos 2\alpha \end{pmatrix} \begin{pmatrix} Q \\ U \end{pmatrix}, \tag{2.44}$$

while I and V are invariant. This means that (Q, U) transforms, under a coordinate transformation of the kind

$$x_i' = A_i^k x_k \tag{2.45}$$

as

$$P_{ij}' = A_i^k A_j^l P_{kl} \tag{2.46}$$

or, in other words, Q and U transform under rotation as the components of a symmetric traceless 2×2 tensor,

$$\begin{pmatrix} Q & U \\ U & -Q \end{pmatrix} \to \begin{pmatrix} \cos\alpha & \sin\alpha \\ -\sin\alpha & \cos\alpha \end{pmatrix} \begin{pmatrix} Q & U \\ U & -Q \end{pmatrix} \begin{pmatrix} \cos\alpha & -\sin\alpha \\ \sin\alpha & \cos\alpha \end{pmatrix}. \tag{2.47}$$

Therefore, we can build two quantities from Q and U transforming as a spin-2 field under rotation, that is

$$(Q \pm iU)'(\hat{z}) = e^{\mp 2i\alpha}(Q \pm iU)(\hat{z}). \tag{2.48}$$

2.2.2 *Spin-s spherical harmonics*

We now introduce a basis of spin-s spherical harmonics (Goldberg et al., 1967), which will be relevant in the next Subsection, where we will expand the polarization field on the sphere, just like what we did for the temperature field in Section 2.1.6.

First of all, we define as a spin-s function on the sphere a function ${}_sf(\theta, \phi)$ that transforms under a rotation of angle α about the $\hat{z}$-axis, as

$${}_sf'(\theta, \phi) = e_s^{-is\alpha} f(\theta, \phi). \tag{2.49}$$

Such a function can be expanded in the basis ${}_sY_{\ell m}$ of spin-s spherical harmonics satisfying the completeness and orthogonality relations:

$$\int_0^{2\pi} d\phi \int_{-1}^{1} d\cos\theta \, {}_sY^*_{\ell' m'}(\theta, \phi) \, {}_sY_{\ell m}(\theta, \phi) = \delta_{\ell\ell'}\delta_{mm'}, \tag{2.50}$$

$$\sum_{\ell m} {}_sY^*_{\ell m}(\theta, \phi) \, {}_sY_{\ell m}(\theta', \phi') = \delta(\phi - \phi')\delta(\cos\theta - \cos\theta'). \tag{2.51}$$

This basis allows for the construction of the so-called *spin-raising* and *spin-lowering* operators $\partial^{\pm}$, capable of increasing and decreasing the spin of a function, respectively:

$$\partial^{\pm} \, {}_sf(\theta, \phi) = -\sin^s\theta \left(\partial_\theta \pm \frac{i}{\sin\theta} \partial_\phi \right) \sin^{\mp s}\theta \, {}_sf(\theta, \phi). \tag{2.52}$$

These operators can be then used to define the spin-s spherical harmonics in terms of the spherical harmonics $Y_{\ell s}$:

$${}_sY_{\ell m} = \sqrt{\frac{(\ell - s)!}{(\ell + s)!}} (\partial^+)^s Y_{\ell m} \quad \text{and} \quad {}_sY_{\ell m} = (-1)^s \sqrt{\frac{(\ell + s)!}{(\ell - s)!}} (\partial^-)^{-s} Y_{\ell m}, \tag{2.53}$$

where the expression on the right holds for $0 \leq s \leq \ell$ and the one on the left for $-\ell \leq s \leq 0$.

2.2.3 *E and B modes*

Having defined the appropriate basis, we are now in the position to expand the polarization field just as we did for the temperature one:

$$(Q \pm iU)(\hat{n}) = \sum_{\ell m} {}_{\pm 2}a_{\ell m}\, {}_{\pm 2}Y_{\ell m}(\hat{n}), \tag{2.54}$$

with expansion coefficients

$${}_{\pm 2}a_{\ell m} = \int d^2\hat{n}\, {}_{\pm 2}Y^*_{\ell m}(Q \pm iU). \tag{2.55}$$

We can now solve the inconvenience of having Stokes parameters Q and U which are not invariant under rotation: in a similar way to the Helmholtz theorem (Section 1.8.3), which allows the decomposition of a vector into gradient and curl components, the spin-2 polarization field can be decomposed in gradient and curl components, the so-called polarization $E-modes$ and $B-modes$, respectively, which are invariant under rotations just like the temperature. The polarization field is thus decomposed in terms of these two quantities, as

$$(Q \pm iU)(\tau, \mathbf{x}, \hat{n}) = -\sum_{\ell m} (a^E_{\ell m} \pm i a^B_{\ell m})\, {}_{\pm 2}Y_{\ell m}(\hat{n}), \tag{2.56}$$

with expansion coefficients given by

$$a^E_{\ell m} = -\frac{1}{2}\left[{}_2a_{\ell m} + {}_{-2}a_{\ell m}\right] \quad \text{and} \quad a^B_{\ell m} = -\frac{1}{2i}\left[{}_2a_{\ell m} - {}_{-2}a_{\ell m}\right], \tag{2.57}$$

and the newly defined E- and B- modes

$$E(\hat{n}) = \sum_{\ell m} a^E_{\ell m} Y_{\ell m}, \tag{2.58}$$

$$B(\hat{n}) = \sum_{\ell m} a^B_{\ell m} Y_{\ell m}. \tag{2.59}$$

The analogy of polarization E- and B-modes with the electric and magnetic fields appears evident once we consider their behaviour under a parity transformation, that is a reflection with respect to the plane perpendicular to $\mathbf{k}$: $a^E_{\ell m}$ takes a factor $(-1)^\ell$, while $a^B_{\ell m}$ transforms as $(-1)^{\ell+1} a^B_{\ell m}$. Therefore, E is the scalar or *electric* component of the polarization, while B is the pseudo-scalar or *magnetic* component.

The angular power spectra can be defined similarly to temperature fluctuations ones (Eq. 2.26) also for E- and B-modes. Taking into account temperature and polarization, the CMB will therefore be

described by the correlations

$$\langle a^{T*}_{\ell m} a^{T}_{\ell' m'} \rangle = C^{TT}_{\ell} \delta_{\ell\ell'} \delta_{mm'}, \tag{2.60}$$
$$\langle a^{E*}_{\ell m} a^{E}_{\ell' m'} \rangle = C^{EE}_{\ell} \delta_{\ell\ell'} \delta_{mm'}, \tag{2.61}$$
$$\langle a^{T*}_{\ell m} a^{E}_{\ell' m'} \rangle = C^{TE}_{\ell} \delta_{\ell\ell'} \delta_{mm'}, \tag{2.62}$$
$$\langle a^{B*}_{\ell m} a^{B}_{\ell' m'} \rangle = C^{BB}_{\ell} \delta_{\ell\ell'} \delta_{mm'}. \tag{2.63}$$

Note that the TB and EB cross-spectra vanish if the physics behind the production of temperature and polarization fluctuations is not parity-violating.

2.2.4 *The generation of CMB polarization*

We now turn to the physical mechanism generating polarizations in the CMB, that is the Thomson scattering between CMB photons and electrons, and we show that polarization is produced only if the radiation incoming on electrons possesses a quadrupolar intensity distribution.

The angular dependence of the differential cross-section for Thomson scattering is (Chandrasekhar, 1960)

$$\frac{d\sigma}{d\Omega} = \frac{3\sigma_T}{8\pi} |\hat{\epsilon}' \cdot \epsilon|^2, \tag{2.64}$$

where $\hat{\epsilon}'$ and $\hat{\epsilon}$ are the polarization directions of the incident and scattered radiation, respectively, and σ_T is the Thomson cross-section.

Following the discussion by Kosowsky (1996), we choose our coordinate system so that the outgoing scattered radiation is along the $\hat{z}$-axis and is characterized by the Stokes parameters I, Q, U and V[11]. On the other hand, incident radiation has intensity $I'(\theta, \phi)$ and is assumed to be completely unpolarized.

[11] We will not consider further the V Stokes parameter in this derivation, since it can be shown that it remains zero after scattering, if it was zero initially.

Now, an unpolarized light beam can be represented as the independent superposition of two linearly polarized beams with perpendicular linear polarization vectors. Moreover, we can choose the polarization vectors for the scattered beam so that $\hat{\epsilon}_y$ is in the scattering plane and $\hat{\epsilon}_x$ is perpendicular to the scattering plane. Similarly, the incident beam will have $\hat{\epsilon}'_y$ in the scattering plane and $\hat{\epsilon}'_x$ perpendicular to the scattering plane (Figure 2.7).

Form Eqs. 2.38 and 2.40, intensities along the $\hat{x}$- and $\hat{y}$-axes will be given by $I_x = (I + Q)/2$ and $I_y = (I - Q)/2$. Furthermore, the condition that incident radiation is unpolarized corresponds to $I'_x = I'_y \equiv I'/2$.

The scattered intensities are

$$I_x = \frac{3\sigma_T}{8\pi} \left[I'_x (\hat{\epsilon}'_x \cdot \hat{\epsilon}_x)^2 + I'_y (\hat{\epsilon}'_y \cdot \hat{\epsilon}_x)^2 \right] = \frac{3\sigma_T}{16\pi} I', \tag{2.65}$$
$$I_y = \frac{3\sigma_T}{8\pi} \left[I'_x (\hat{\epsilon}'_x \cdot \hat{\epsilon}_y)^2 + I'_y (\hat{\epsilon}'_y \cdot \hat{\epsilon}_y)^2 \right] = \frac{3\sigma_T}{16\pi} I' \cos^2\theta, \tag{2.66}$$

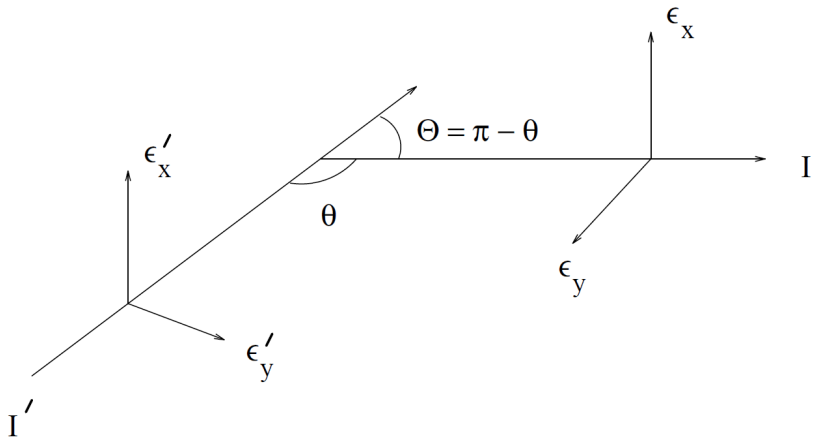

Figure 2.7: Definitions of quantities involved in the description of polarization generated by Thomson scattering. Primed quantities refer to the incident beam, while unprimed one to the scattered beam. From Kosowsky (1996).

from which we can compute the Stokes parameters for the scattered wave, that is

$$\begin{aligned} I &= I_x + I_y = \frac{3\sigma_T}{16\pi} I'(1+\cos^2\theta) \\ Q &= I_x - I_y = \frac{3\sigma_T}{16\pi} I' \sin^2\theta \\ U &= 0 \end{aligned} \tag{2.67}$$

Integrating over all incident intensities, we get the total Stokes parameters, which, depend only on the intensity of the incident radiation, (having assumed unpolarized incident radiation):

$$\begin{aligned} I_{tot} &= \frac{3\sigma_T}{16\pi} \int d\Omega (1+\cos^2\theta) I'(\theta,\phi), \\ Q_{tot} &= \frac{3\sigma_T}{16\pi} \int d\Omega \sin^2\theta \cos 2\phi I'(\theta,\phi), \\ U_{tot} &= \frac{3\sigma_T}{16\pi} \int d\Omega \sin^2\theta \sin 2\phi I'(\theta,\phi). \end{aligned} \tag{2.68}$$

If we now expand the incident intensity in spherical harmonics (see Eq. 2.24),

$$I'(\theta,\phi) = \sum_{l,m} a_{lm} Y_{lm}(\theta,\phi), \tag{2.69}$$

we can rewrite the scattered wave Stokes parameters as

$$\begin{aligned} I &= \frac{3\sigma_T}{16\pi} \left[\frac{8}{3}\sqrt{\pi} a_{00} + \frac{4}{3}\sqrt{\frac{\pi}{5}} a_{20} \right], \\ Q &= \frac{3\sigma_T}{4\pi} \sqrt{\frac{2\pi}{15}} \Re(a_{22}), \\ U &= -\frac{3\sigma_T}{4\pi} \sqrt{\frac{2\pi}{15}} \Im(a_{22}), \end{aligned} \tag{2.70}$$

from which we can infer that the polarization of the scattered radiation into the $\hat{z}$ direction is

$$Q - iU = \sqrt{\frac{3}{40\pi}}\sigma_T a_{22}. \tag{2.71}$$

In conclusion, Thomson scattering will generate polarization in the CMB – from incoming unpolarized radiation[12] – only if the incident radiation possesses a quadrupolar anisotropy pattern (Y_{22} in terms of spherical harmonics).

[12] This is an approximation, as radiation incoming on electrons could in general be already polarized because of previous Thomson scatterings. In this case, a Boltzmann treatment is needed (see for instance Maggiore (2018) and references therein).

2.3 *Primordial gravitational waves and B-modes*

An important property of the CMB polarization is that *scalar perturbations can only generate E-mode polarization*, while *tensor perturbations can produce both E- and B-modes*. Therefore, in an ideal setting in which no contamination from foregrounds and gravitational lensing is present, observing the primordial B-modes would therefore correspond to directly observing primordial gravitational waves. As we will discuss in detail in Sections 2.4 and 3.1.3, this is not the case unfortunately, as a secondary B-mode signal is generated by Galactic diffuse foregrounds and by the leaking of E-mode polarization into B-modes due to gravitational lensing by the cosmological Large Scale Structure. However, there are several strategies to disentangle the primordial SGWB signal from the contaminants and subtract the latter, and even though this procedures leave in general a residual contribution limiting our observational power, it certainly allows the exploitation of CMB B-modes for the exploration of an SGWB produced in the early Universe.

2.3.1 *GW records in the polarized CMB*

In order to show that B-modes are actually produced – in an ideal situation, as explained above – only by primordial tensor perturbations, we follow the calculation by Polnarev (1985)[13] and consider a simplified situation in which we have a single monochromatic plane-wave gravitational wave (propagating along the $\hat{z}$-axis) which is perturbing the flat FRLW metric:

[13] See also Kamionkowski and Kovetz (2016) and references therein.

$$h_+(\mathbf{x}, \tau) = h(\tau)e^{ik\tau - ikz}. \tag{2.72}$$

Note that we chose a $+$-polarized wave, although the following calculation can be easily repeated for a $\times$-polarized wave.

Now, the geodesic equation allows us to write the frequency shift experienced by freely-propagating photons, due to the single gravitational wave:

$$\frac{1}{\nu}\frac{d\nu}{d\tau} = -\frac{1}{2}(1-\mu^2)\cos 2\phi\, e^{-ikz}\frac{d}{d\tau}(he^{ik\tau}). \tag{2.73}$$

The next step will be to compute the polarization produced by this anisotropic radiation field because of Thomson scattering; to this end we introduce the distribution functions $f_i(\mathbf{p}, \mathbf{x}, \tau)$ with $i = I, Q, U, V$ and $\mathbf{p}$ is the photon momentum. The unperturbed distribution for intensity (see also discussion around Eq. 2.4) is

$$\bar{f}_I = \left[e^{h\nu/kT(\tau)} - 1\right]^{-1}, \tag{2.74}$$

while the other Stokes parameters have zero unperturbed distributions $\bar{f}_Q = \bar{f}_U = \bar{f}_V = 0$. Perturbations to these distribution functions are defined according to $\Delta_i e^{i\mathbf{k}\cdot\mathbf{x}} = 4\delta f_i / (\partial \bar{f} / \partial \ln T)$. Since Thomson scattering does not generate circular polarization, we will just set $\Delta_V = 0$ in the rest of the derivation.

Defining the new variables $\tilde{\Delta}_i$ through the relations

$$\Delta_I = \tilde{\Delta}_I (1 - \mu^2) \cos 2\phi, \tag{2.75}$$
$$\Delta_Q = \tilde{\Delta}_Q (1 + \mu^2) \cos 2\phi, \tag{2.76}$$
$$\Delta_U = \tilde{\Delta}_U 2\mu \sin 2\phi, \tag{2.77}$$

we can finally write the Boltzmann equations for the polarization distributions functions

$$\tilde{\Delta}_I' + ik\mu\tilde{\Delta}_I = -h' - \eta'[\tilde{\Delta}_I - \tilde{\Lambda}], \tag{2.78}$$
$$\tilde{\Delta}_Q' + ik\mu\tilde{\Delta}_Q = -\eta'[\tilde{\Delta}_Q + \tilde{\Lambda}], \tag{2.79}$$
$$\tilde{\Delta}_U = -\tilde{\Delta}_Q \tag{2.80}$$

where η is the Thomson optical depth and $\tilde{\Lambda}$ is given in terms of the Legendre moments $\tilde{\Delta}_{i\ell}$ of $\tilde{\Delta}_i$

$$\tilde{\Lambda} = \left[\frac{1}{10}\tilde{\Delta}_{I0} + \frac{1}{7}\tilde{\Delta}_{I2} + \frac{3}{70}\tilde{\Delta}_{I4} - \frac{3}{5}\tilde{\Delta}_{Q0} + \frac{6}{7}\tilde{\Delta}_{Q2} - \frac{3}{70}\tilde{\Delta}_{Q4}\right]. \tag{2.81}$$

We can then use the formalism developed in Section 2.2.2 to compute the expansion coefficients for E- and B-modes ($a^E_{\ell m}$ and $a^B_{\ell m}$) and finally, the angular power spectra

$$C_l^{EE} = \frac{1}{16\pi}\int dk\, k^2 \left[\frac{(l+2)(l+1)\tilde{\Delta}_{Q\,l-2}}{(2l-1)(2l+1)} + \frac{6l(l+1)\tilde{\Delta}_{Q\,l}}{(2l+3)(2l-1)} + \frac{l(l-1)\tilde{\Delta}_{Q\,l+2}}{(2l+3)(2l+1)}\right]^2,$$
$$C_l^{BB} = \frac{1}{4\pi}\int dk\, k^2 \left[\frac{l+2}{2l+1}\tilde{\Delta}_{Q\,l-1} + \frac{l-1}{2l+1}\tilde{\Delta}_{Q\,l-1}\right]^2, \tag{2.82}$$

from which we can conclude that tensor perturbations produce both E and B non-zero angular power spectra.

In a completely analogous way, it can be shown that a single scalar mode with wavenumber $\mathbf{k}$ along the $\hat{z}$-axis does not produce B-mode

polarization. The frequency shift experienced by the photons (named Sachs-Wolfe effect, see Section 2.1.2) due to this scalar perturbation, will have a different dependence proportional to $\propto (\cos^2\theta - 1/3)$ with respect to the tensor perturbation case. In this case, only the $a^E_{\ell m}$, and, consequently, the C_ℓ^{EE} will be non-zero.

2.3.2 *Physical interpretation of the polarization spectra*

We show in Figure 2.8 the separate scalars and tensors contribution to the temperature and polarization $C_\ell^{XX'}$s, with $X, X' = T, E, B$, evaluated using the Boltzmann code `CLASS`. The cosmological parameters have been chosen to match the Planck 2018 Planck Collaboration (2018) ones and we chose a value $r = 0.01$ for the tensor-to-scalar ratio, below the current upper limits.

We discuss now some of the relevant physical mechanisms at work in the polarization spectra (see Cabella and Kamionkowski, 2004, and references therein). Polarization spectra due to scalar (density) perturbations show acoustic peaks (left panel of Figure 2.8), out-of-phase with respect to the peaks in the TT scalar power spectrum. This happens because, before recombination, electrons and photons are in the tight-coupling regime and no polarization is produced, since no quadrupolar anisotropy pattern in the radiation incident on the electrons can be generated. However, as recombination approaches, photons start decouple and to have longer free paths lenghts, a process which depends on the time derivative of the baryon density. Therefore, polarization will have acoustic oscillations governed by Eq. 2.12 and will be out-of-phase with the temperature peaks produced by density perturbations at the LSS, and in phase with the peculiar velocity at the LSS (Cabella and Kamionkowski, 2004).

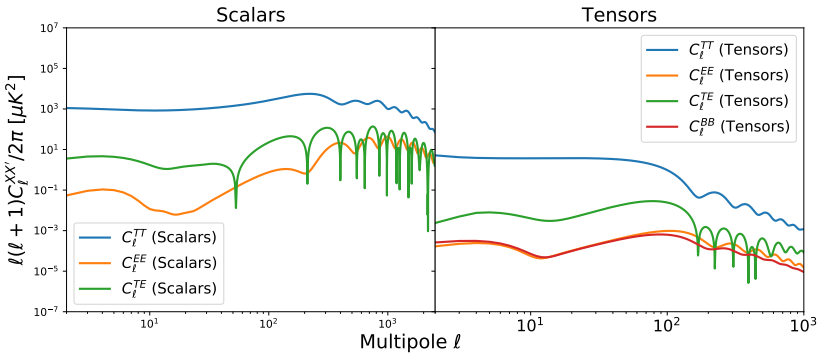

Figure 2.8: Separate scalar and tensor perturbations contribution to the temperature and polarization CMB angular power spectra, evaluated using the Boltzmann code `CLASS`. The cosmological parameters have been chosen to match the Planck 2018 Planck Collaboration (2018) ones and we chose a value $r = 0.01$ for the tensor-to-scalar ratio.

As the right panel of Figure 2.8 shows, the power spectra due to tensor perturbations have all a dramatic decrease for $\ell \gtrsim 100$, due to the fact that smaller scale gravitational waves enter the horizon ear-

lier and therefore have more time to decay (see Discussion in Section 1.8.5). In particular, the peak at $\ell \sim 100$ – named *recombination bump*– will arise from gravitational waves entering the horizon around the time of recombination. Focusing on C_ℓ^{BB} (see also Figure 2.9), we see that larger-scale modes – which were superhorizon at recombination time – will have a suppressed effect on subhorizon physics: this causes the decrease in the spectra towards smaller ℓ.

As we anticipated in Section 2.1.7, also reionization has a remarkable effect on polarization spectra: it produces bumps at $\ell \lesssim 10$ thanks to the scattering of the quadrupole – which has been growing since the time of decoupling due to the free-streaming of photons – by the newly freed electrons. In the following, we will call this feature of the C_ℓ^{BB} spectrum *reionization bump* (see also Figure 2.9). Another effect of reionization is to lower the heights of the acoustic peaks in temperature and polarization spectra, as we already discussed in Section 2.1.7.

The recombination and the reionization bumps represent the most prominent features in the C_ℓ^{BB} spectrum, and will be subject of further analysis and forecasts for future detection in Chapters 4 and 5.

2.4 *Weak gravitational lensing of the CMB*

We have shown in Section 2.3 that scalar perturbations are not capable of producing B-modes, while tensor ones can both generate E- and B-type polarization. However, we also anticipated that this is true only in absence of secondary effects and mentioned diffuse Galactic foregrounds and the E-to-B leakage due to gravitational lensing by the cosmological Large Scale Structure as the most prominent contaminants to the primordial SGWB signal.

The application of gravitational lensing to CMB anisotropies constitutes a subject with a vast literature; in this Section we will introduce only the very basics of the topic, with a focus on the contaminating effect on B-modes.

Lensing – due to the density perturbation pattern intervening between the LSS and us – is a nonlinear effect that remaps the primordial temperature and polarization of the CMB, displacing each field from a direction $\boldsymbol{\theta}$ at the LSS to a new direction $\boldsymbol{\theta} + \delta\boldsymbol{\theta}$ (Bartelmann and Schneider, 2001):

$$\begin{pmatrix} T \\ Q \\ U \end{pmatrix}_{lensed} (\boldsymbol{\theta}) \simeq \begin{pmatrix} T \\ Q \\ U \end{pmatrix}_{unlensed} (\boldsymbol{\theta}) + \delta\boldsymbol{\theta} \cdot \nabla \begin{pmatrix} T \\ Q \\ U \end{pmatrix}_{unlensed} (\boldsymbol{\theta}), \tag{2.83}$$

where $\delta\boldsymbol{\theta} = \nabla\varphi$ is the *deflection angle* and φ is *lensing potential*, that is the projection on the sphere of the integrated 3-dimensional gravitational potential $\boldsymbol{\Phi}(\mathbf{x})$ along the line of sight $\hat{n}$ between us and the LSS. Restricting for simplicity to the flat-sky limit (Hu, 2000) [14], assuming the Born approximation holds true[15] and defining the *convergence field* in terms of the lensing potential $\kappa = -\nabla^2\phi/2$, it can be shown that the lensing of E-modes produces a B-mode component, according to

$$C_\ell^{BB,lens} = \int \frac{d^2\mathbf{l}'}{(2\pi)^2} W^2(\mathbf{l},\mathbf{l}') C_{l'}^{EE} C_{|\boldsymbol{l}-\boldsymbol{l}'|}^{\kappa\kappa}, \tag{2.84}$$

even if no $B-mode$ component is initially present. Here the weight with which different Fourier modes $\mathbf{l},\mathbf{l}'$ contribute is defined as

$$W(\mathbf{l},\mathbf{l}') = \frac{2\mathbf{l}'\cdot(\mathbf{l}-\mathbf{l}')}{|\mathbf{l}-\mathbf{l}'|^2}\sin(2\phi_{\mathbf{l},\mathbf{l}'}), \tag{2.85}$$

with $\phi_{\mathbf{l},\mathbf{l}'}$ being the angle between the modes $\mathbf{l}$ and $\mathbf{l}'$ and $C_{|\boldsymbol{l}-\boldsymbol{l}'|}^{\kappa\kappa}$ is the convergence power spectrum.

A quick numerical evaluation of $C_\ell^{BB,lens}$ in the full-sky is achievable using the `CLASS` or `CAMB` Boltzmann codes, and is shown in Figure 2.9 as a red dot-dashed line, for the Planck 2018 cosmological parameters (Planck Collaboration, 2018).

As evident from this Figure, the lensing B-mode contribution is particularly important at smaller scales, and its amplitude is similar or even greater than the primordial signal one, even at the recombination peak, for interesting values of r. Even though this lensing signal has a well-understood amplitude which has already been measured by current experiments (as we will mention later in this Section), its the sample-variance associated to the lensed B-modes in the maps that increases the noise when trying to measure primordial B-modes. An efficient subtraction strategy appears therefore necessary: as we will see in the next Subsection, the lensing contamination can be cleaned adopting a *delensing* technique, that is by estimating at the map level both the primordial E-mode contribution and the lensing potential.

The B-modes from gravitational lensing have been detected by Planck (Planck Collaboration, 2016), BICEP2 (The BICEP/Keck Collaboration et al., 2018), POLARBEAR (POLARBEAR Collaboration et al., 2017), the ACT (Louis et al., 2017) and the SPT experiments (Hanson et al., 2013), while no detection exists yet for primordial B-modes; we will delve more deeply into the current observational status of CMB B-mode measurements in the next Chapter (in particular in Section 3.1).

[14] For the extension to the full-sky is also presented in Hu (2000) and Challinor and Lewis (2005).

[15] That is, we can take the integral along the unperturbed line of sight.

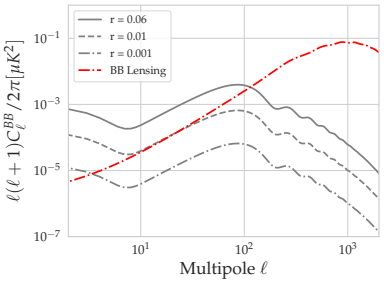

Figure 2.9: Numerical evaluation of the primordial C_ℓ^{BB} for the three values of tensor-to-scalar ratio $r = 0.06, 0.01, 0.001$ (solid, dashed and dot-dashed grey curves, respectively) and of $C_\ell^{BB,lens}$ (red dot-dashed curve) using the `CLASS` Boltzmann codes. We adopted the Planck 2018 cosmological parameters (Planck Collaboration, 2018).

2.4.1 *Lensing reconstruction and delensing*

Several ways to reconstruct the lensing potential have been explored in the literature (see for instance Diego-Palazuelos et al., 2020, for a recent work comparing different techniques).

One possibility is represented by the exploitation of Large Scale Structure tracers correlated with CMB lensing (Manzotti, 2018), such as galaxy surveys (Namikawa et al., 2016), the Cosmic Infrared Background (CIB) (Manzotti et al., 2017; Planck Collaboration, 2018e) or through tomographic line intensity mapping (Karkare, 2019).

Another possibility is represented by reconstructing directly the lensing potential from the CMB itself – which we will call *internal lensing reconstruction* – taking advantage of the higher order statistics introduced by lensing. One of the most common tool to achieve this are the optimal quadratic estimators introduced in Hu and Okamoto (2002b), which exploit the information stored in off-diagonal mode-coupling in spherical harmonics space induced by lensing. Averaging over pairs of harmonic space modes separated by a given scale allows to estimate the amount of lensing on that scale: the accuracy of this reconstruction procedure tipically increases as we increase the angular resolution and sensitivity of a CMB experiment simply because this increases the number of smaller-scale modes it is possible to measure.

Besides quadratic estimators, other techniques for internal lensing reconstruction are represented by maximum likelihood (Hirata and Seljak, 2003) and by optimal maximum a posteriori methods (Carron and Lewis, 2017).

It is important to mention that the internal lensing reconstruction – and therefore the *internal delensing* of B-modes – can be improved in a significant way using an *iterative approach* (Hirata and Seljak, 2003; Smith et al., 2012): this technique can be intuitively understood considering that, since the lensed B-mode represents a source of noise for the lensing reconstruction estimator, the delensed B-mode (having less power than the initial lensed B-mode) can be used in an iterative way as input for a further round of delensing with lower statistical errors.

A comparison of the delensing efficiency between the quadratic estimators and the iterative delensing for the CMB-S4 experiment (Abazajian et al., 2016) is also shown in Figure 2.10. In particular this Figure shows the B-mode noise on scales $\ell \lesssim 300$ as a function of the noise level used in polarization-based lensing reconstruction for the CMB-S4 experiment (Abazajian et al., 2016), which will be discussed in more detail in Section 3.1.2. The case without any delensing (purple line) is equivalent to an effective $\sim 5\,\mu\mathrm{K} - \mathrm{arcmin}$ white

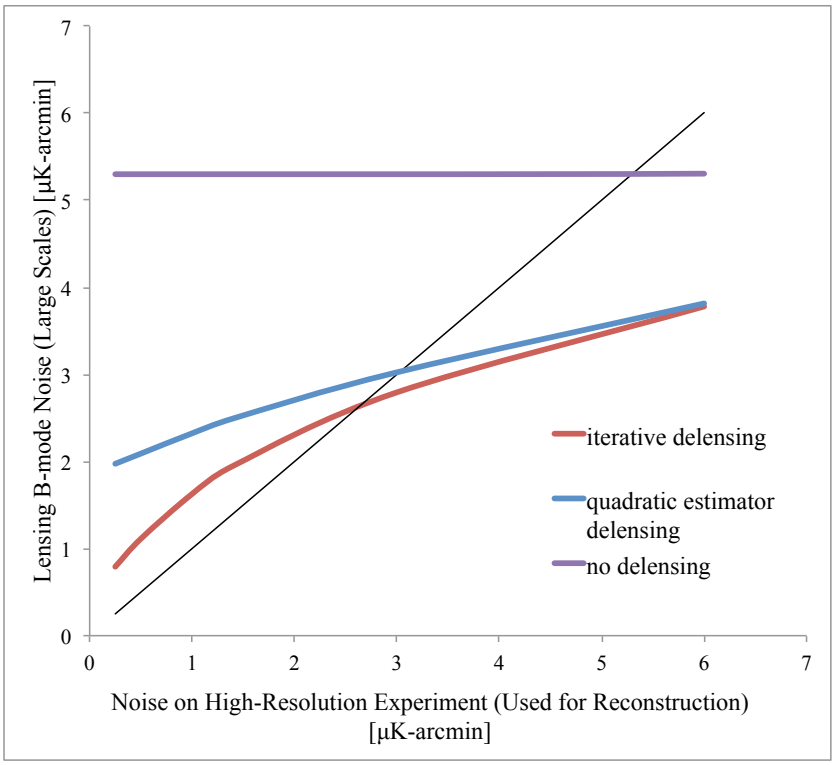

Figure 2.10: The B-mode noise on scales $\ell \lesssim 300$ as a function of the noise level used in polarization-based lensing reconstruction for the CMB-S4 experiment (Abazajian et al., 2016). The case without any delensing (purple line) is equivalent to an effective $\sim 5\,\mu\mathrm{K} - \mathrm{arcmin}$ white noise level. The blue and red curves represent the case with delensing using quadratic estimators and the one using an iterative procedure (Hirata and Seljak, 2003), respectively. From Abazajian et al. (2016).

noise level. The blue and red curves represent instead the case with delensing using quadratic estimators and the one using an iterative procedure (Hirata and Seljak, 2003), respectively: from the slopes of the curves we can see that, especially for lower levels of noise used during reconstruction, the iterative strategy produces significantly better results than the simple quadratic estimators.

3
Observations of the primordial gravitational wave background: where do we stand?

The production of a primordial SGWB is predicted by the inflationary paradigm (Section 1.8.5): this scenario predicts indeed the generation of tensor and scalar perturbations by vacuum quantum fluctuations. Scalar modes are known to be the seeds for the cosmic Large Scale Structure formation and have been subject to thorough measurements, while *primordial tensor modes still remain undetected*. The importance of their detection cannot be overestimated, since this primordial SGWB contains an unparalleled amount of information on the very early Universe physics (see Section 1.8.5). Furthermore, if the standard single-field slow-roll inflationary scenario is confirmed, a detection of the tensor-to-scalar ratio r would allow to directly infer the energy scale of inflation (Eq. 1.128), allowing us to probe ultra-high energy scales, not accessible by terrestrial particle colliders.

In this Chapter, we will give an overview of the current and future landscape of experiments that will target the detection and characterization of the primordial SGWB. As we will discuss in much more depth in Chapter 5, there are at least three methods – in three separate frequency ranges – to search a primordial SGWB:

- the *CMB B-mode experiments*, at frequencies $f \approx 10^{-18} - 10^{-16}$ Hz,
- *Pulsar Timing Arrays (PTA)* at $f \approx 10^{-9} - 10^{-7}$ Hz,
- *Laser and atomic interferometers* at $f \approx 10^{-7} - 10^{3}$ Hz.

In the following we are going to describe each of these three observational methods, and establish their status at present time and their future perspectives, starting with the CMB B-mode experiments (Section 3.1). This Section will also introduce one of the major challenges – together with lensing (see Section 2.4.1) – for detection of the primordial signal by CMB experiments, that is the contamination due to Galactic diffuse foregrounds, the most prominent ones being the thermal emission of dust grains and the synchrotron radiation from cosmic ray electrons spiraling in the magnetic fied of our Galaxy (Section 3.1.3). We will then describe in Section 3.2 the possibilities offered by some of the already operating or planned PTA experiments and laser (and atomic) interferometers. Similarly to what happens in the CMB case, also direct detection experiments can suffer from the presence of an astrophysical foreground: in this case, the contamination of the primordial SGWB signal is due to the astrophysical SGWB emitted by populations of compact objects, such as *black-hole binaries* (BBH), *neutron-star binaries* (BNS), *Galactic and Extragalactic white dwarfs* (GWD and EGWD), *massive black hole binaries* (MBHB) and others. Section 3.2.6 will be dedicated

to a brief description of the contribution of these astrophysical foreground sources for each of the direct detection experiments we consider.

This Chapter is based on the following reviews Christensen (2019); Caprini and Figueroa (2018); Romano and Cornish (2017), to which we refer the reader for a more detailed and comprehensive treatment.

3.1 *Status of CMB B-mode experiments*

In this Section, we will discuss the current status of CMB measurements, starting with a concise summary of the status of temperature anisotropies, E-type polarization and lensing (Section 3.1.1), presenting also the current upper limits available on the primordial B-modes. We will then introduce some representatives of the current and next-generation B-mode probes (Section 3.1.2), which will be the subject of further analysis in Chapters 4 and 5. Finally, we will outline the situation concerning the astrophysical foregrounds contamination, which represent a formidable antagonist in all B-mode searches (Section 3.1.3).

3.1.1 *CMB constraints on temperature, E- and B-modes and lensing*

Temperature anisotropies, as we anticipated in Section 1.6, were first detected by the COBE satellite experiment (Smoot et al., 1992); currently the best measurements on the their power spectrum come from the data from the the SPT (Calabrese et al., 2013), the ACT (Louis et al., 2017; Choi et al., 2020) and the Planck satellite (Planck Collaboration, 2018) experiments (Figure 3.1).

For what concerns the EE and TE polarization spectra, the current constraints are given by data from Planck (Planck Collaboration, 2018), BICEP2-Keck (Ade et al., 2016a), ACTPol (Louis et al., 2017; Choi et al., 2020), SPTPol (Henning et al., 2018) and WMAP (Hinshaw et al., 2013), (Figures 3.2 and 3.3).

The gravitational lensing potential power spectrum has also been measured by several CMB experiments, including the Planck satellite (Planck Collaboration, 2018e), the BICEP2 (Ade et al., 2016b), POLARBEAR (POLARBEAR Collaboration, 2020, 2014), ACT (Das et al., 2014; Sherwin et al., 2017) and SPT (van Engelen et al., 2012; Simard et al., 2018; Wu et al., 2019) experiments (Figure 3.4).

As we mentioned earlier, no detection exists yet of B-type polarization associated to primordial tensor modes; however, B-modes from lensing (Section 2.4) have been already measured by Planck (Planck Collaboration, 2016), BICEP2 (The BICEP/Keck Collaboration et al., 2018), POLARBEAR (POLARBEAR Collaboration et al., 2017), ACT (Louis et al., 2017) and SPT (Hanson et al., 2013) (Figure 3.5). Furthermore, the joint analysis of Planck and BICEP2-Keck data allowed to

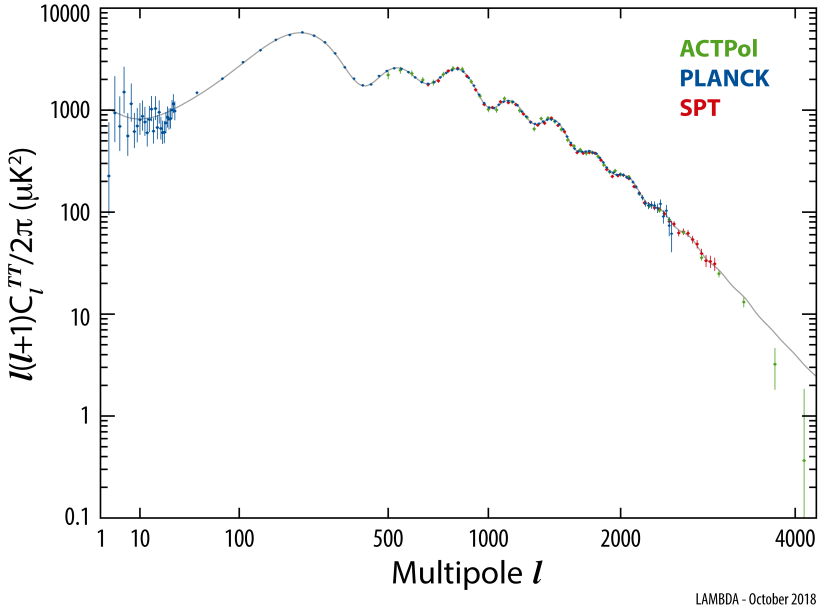

Figure 3.1: Current constraints on the TT spectrum from the SPT, ACT and Planck experiments. Also shown is the theoretical spectrum computed from Planck best-fit ΛCDM cosmology. From https://lambda.gsfc.nasa.gov/.

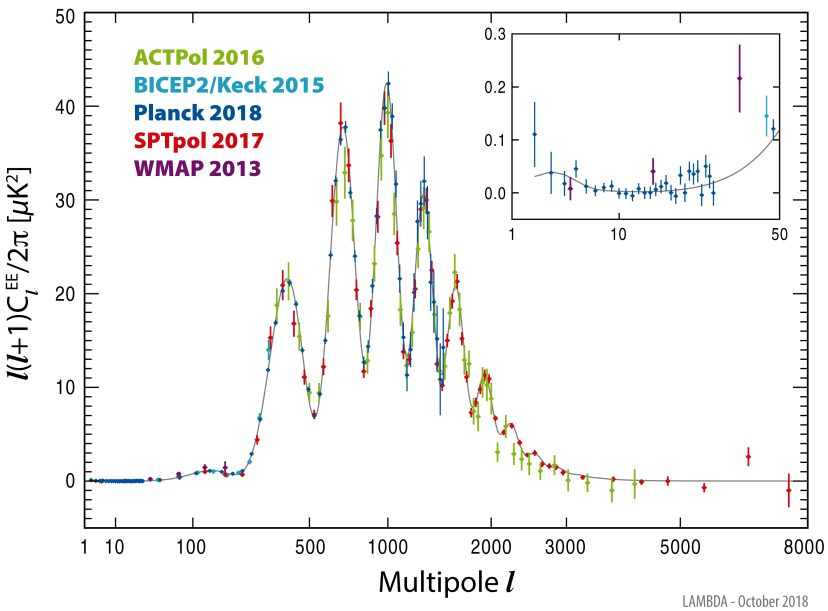

Figure 3.2: Current constraints on the EE spectrum from the SPTPol, ACTPOl, WMAP, BICEP2-Keck and Planck experiments. From https://lambda.gsfc.nasa.gov/.

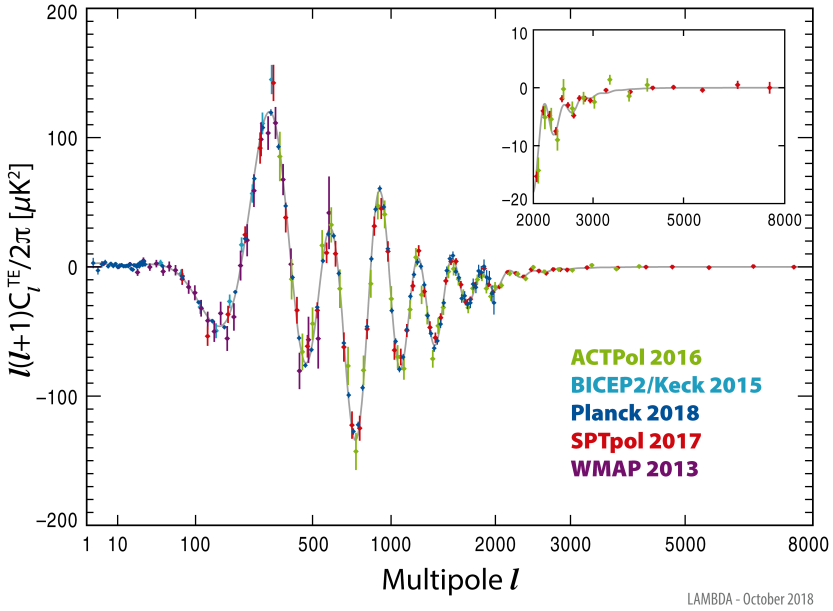

Figure 3.3: Current constraints on the TE spectrum from the SPTPol, ACTPOl, WMAP, BICEP2-Keck and Planck experiments. From https://lambda.gsfc.nasa.gov/.

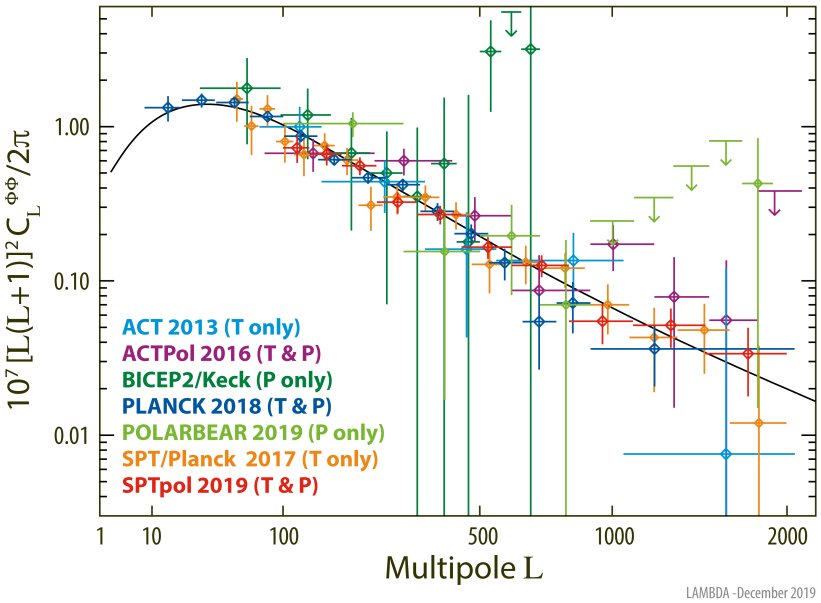

Figure 3.4: Current constraints on the gravitational lensing power spectrum from the SPT, SPTPol, ACT, ACTPOl, BICEP2-Keck, POLARBEAR and Planck experiments. From https://lambda.gsfc.nasa.gov/.

put upper limits on the amplitude of primordial tensor perturbations at the pivot-scale $k_0 = 0.05\,\mathrm{Mpc}^{-1}$, that is $r_{0.05} < 0.06$ at 95% C.L. (BICEP2 and Planck Collaborations).

A detection of primordial B-modes was initially claimed by the BICEP2 experiment (Ade et al., 2014), but – after further analysis – the detection was not confirmed due to possible contamination from diffuse Galactic foregrounds (BICEP2 and Planck Collaborations). The impact of CMB foregrounds on primordial B-modes estimates can indeed be very significant, as we will later discuss in Section 3.1.3.

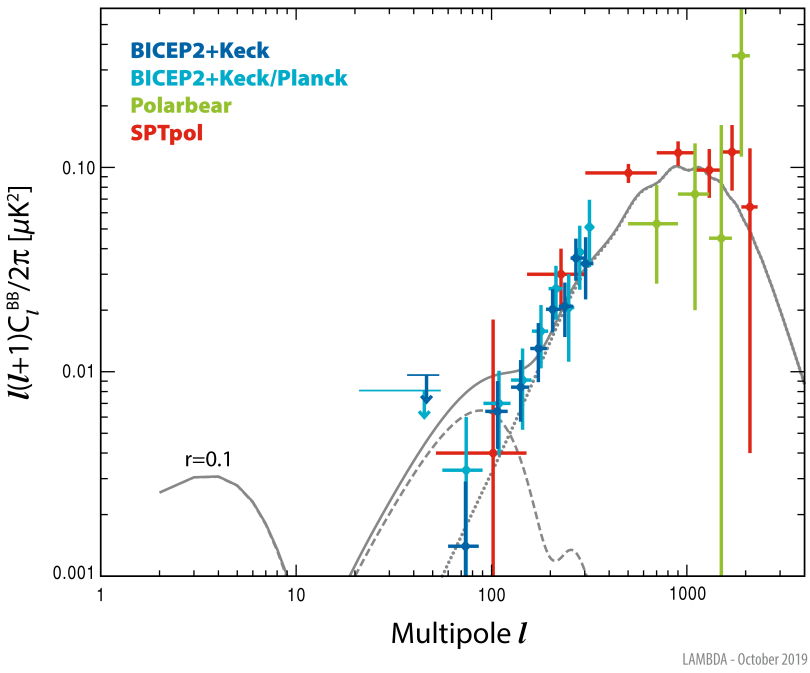

Figure 3.5: Current constraints on the BB spectrum from the from the POLARBEAR, SPTPol, BICEP2-Keck, Planck experiments and from the combined BICEP2-Keck and Planck data. See text for references. From https://lambda.gsfc.nasa.gov/.

3.1.2 *B-mode probes*

The primordial SGWB is known to imprint its unique signature in the B-mode polarization of the CMB (see Section 2.3), and this represents currently the most promising channel for a near future detection. Driven by these motivations, numerous CMB B-mode experiments are currently scanning the microwave sky in search of primordial B-modes, among them the the BICEP2/Keck Array (The BICEP/Keck Collaboration et al., 2018), POLARBEAR/Simons Array (POLARBEAR Collaboration et al., 2017; Suzuki et al., 2016), the Atacama Cosmology Telescope (ACT) (Louis et al., 2017), the South Pole Telescope (SPT) (Hanson et al., 2013), the Cosmology

Large Angular Scale Surveyor (CLASS) (Dahal et al., 2020), the Q and U Bolometric Interferometer for Cosmology (QUBIC) (Tartari et al., 2016) and the Large Scale Polarization Explorer (LSPE) (Addamo et al., 2020).

Furthermore, the next decade will see a great increase in the efforts for detection with a new generation of experiments from the ground, including the Simons Observatory (SO) (The Simons Observatory Collaboration et al., 2018; Lee et al., 2019), the South Pole Observatory (SPO) and the Stage-IV network of ground-based observatories (CMB-S4) (Abazajian et al., 2016; Abazajian et al., 2019b,a). The other very promising strategy for detection is represented by space-borne experiments: recently, the Japan Aerospace Exploration Agency has selected the LiteBIRD[1] (Hazumi et al., 2019; Sugai et al., 2020) as the second Strategic Large-class mission.

[1] See also the link https://ntrs.nasa.gov/search.jsp?R=20190032161.

In the following, we will briefly describe the design of the LiteBIRD, SO and CMB-S4 experiments, since in Chapters 4 and 5 we will perform forecasts based on the specifications for these experiments. Note that, since these three experiments are under current development, the design and specifications reported here may be subject to rapid change in the near future.

The LiteBIRD satellite

One of the main advantage of space missions over ground-based telescopes is represented by their access to the largest angular scales (multipoles $\ell \approx 2 - 30$). In fact, those scales are in general outside the reach of ground-based experiments due to the presence of $1/f$ noise due to the *atmospheric contamination* (see Section 4.1.2).

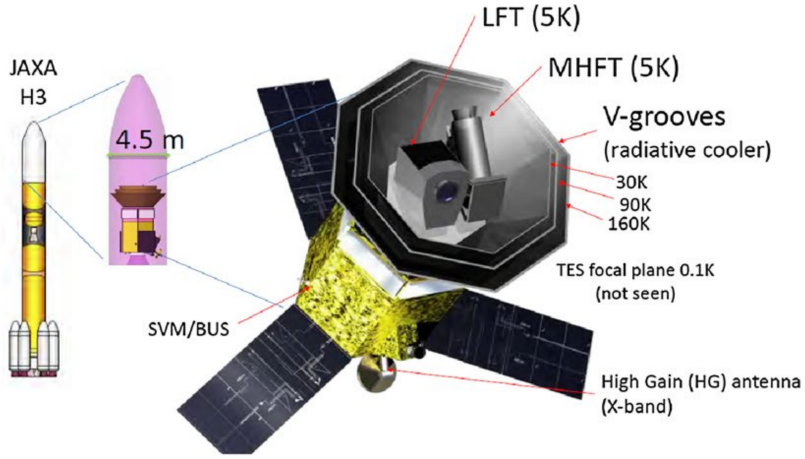

Figure 3.6: Schematic design for the LiteBIRD satellite. From Sugai et al. (2020).

The LiteBIRD satellite is indeed designed in order to target not

only the scales where the *recombination bump* lies (in the range $\ell \approx 11 - 200$, with a maximum around $\ell \sim 80$), but also the very large scales ($\ell \approx 2 - 11$), where a peak in the B-mode primordial signal – the *reionization bump* – is expected due to cosmic reionization physics (see Section 2.3.2).

In this respect, the full-sky measurement of LiteBIRD – including these largest of scales – will be complementary to the measurements of ground-based experiments such as SO, SPO and CMB-S4. In fact, the latter will focus on deep observations of low-foregrounds sky patches, reaching smaller scales with respect to the LiteBIRD satellite.

This space mission – which will observe the full-sky from the second Sun-Earth Lagrangian point L2 – will feature more than 4000 transition-edge sensor bolometers (TES), divided between three 5 K-cooled telescopes: the Low-, Medium- and High-Frequency Telescopes (LFT, MFT and HFT respectively). Each telescope will also be supplied with rotating half-wave plates as the first optical element, in order to separate the CMB and the instrumental polarization components and to suppress the instrumental $1/f$ noise. LiteBIRD will have in total fifteen frequency channels (from 40 to 402 GHz), distributed among these three telescopes: as we will see in Section 4.3.1, this wide frequency coverage increases the capability of LiteBIRD to separate the Galactic foreground contamination from the primordial CMB signal. We report in Table 5.1, the sensitivities and angular resolution for each of these 15 frequency channels, for the most updated design configuration under study at the moment of writing.

The primary objective of the LiteBIRD mission – among other scientific objectives, such as measuring the optical depth to reionization to cosmic variance-limited error and others (see Hazumi et al. (2019)) – will be to the detection of the tensor-to-scalar ratio with an uncertainty $sigma_r < 0.001$ (Sugai et al., 2020), which is the condition defining the full success of the mission. Even in absence of a detection, the upper limit set by LiteBIRD will have important consequences in terms of disfavoring several well-motivated inflation models.

It is worth mentioning here again the complementarity between the ground experiments and LiteBIRD: this satellite will indeed provide a full-sky and multi-frequency measurement of the foreground sky, which could be very useful for the foreground-cleaning of ground-based observations. On the other hand, the high-resolution lensing measurements by ground-based probes could be useful to delens LiteBIRD data (Diego-Palazuelos et al., 2020) (see also Section 2.4.1).

The Simons Observatory

The ground-based SO is currently being built in the Atacama Desert at an altitude of about 5200 m. It will feature about 60000 detectors, divided among its four telescopes, that is one Large Aperture Telescope (LAT) with a 6 m-aperture primary mirror and three refracting 0.4 m Small Aperture Telescopes (SATs). Both LAT and SATs will provide multifrequency measurements of the CMB sky in six bands, from 27 to 280 GHz.

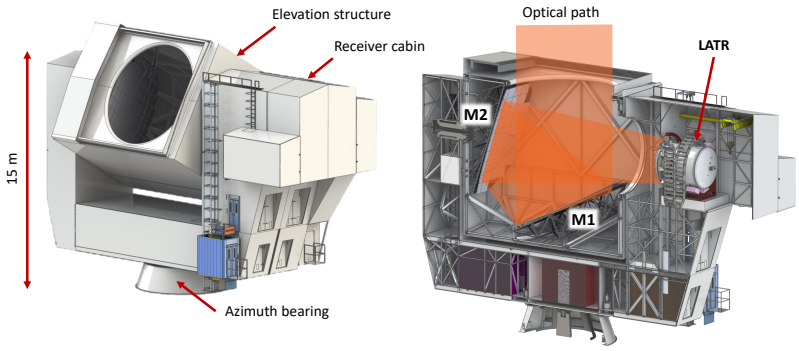

Figure 3.7: Schematic design for the SO LAT telescope. From Galitzki et al. (2018).

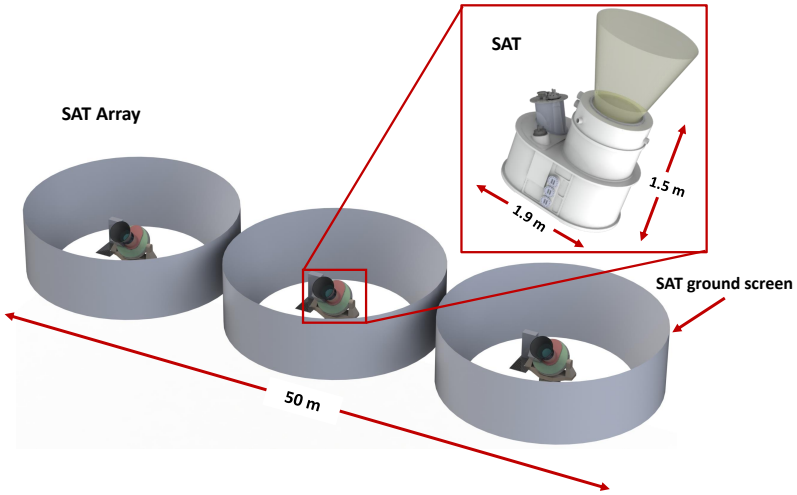

Figure 3.8: Schematic design for the SO SAT telescope. From Galitzki et al. (2018).

The SATs are optimized for a deep survey of larger angular scales (about $\sim 1°$) polarization over $\sim$ 10% of the sky: they will be employed therefore to search for primordial B-modes (see Table 4.1 for the specifications used in this Thesis).

The LAT will provide instead high angular resolution measurements (up to $\sim$ 1 arcmin) over $\sim$ 40% of the sky: it will target the

smaller angular scale of temperature and polarization spectra, the lensing, the SZ effects, the primordial bispectrum and extragalactic sources. Notably, the lensing measurement obtained from the LAT could also be used to delens the SATs (see Section 2.4.1).

SO will target, among many other scientific objectives (including measurements of the scalar perturbations spectrum, non-Gaussianity, the neutrino mass and others, see Lee et al., 2019), a value of $\sigma_r = 0.003$ for the baseline configuration (or $\sigma_r = 0.002$ for the goal configuration) for an $r = 0$ model. Such a sensitivity would allow a measurement at least 3σ for a model with $r \geq 0.01$.

CMB-S4

CMB-S4 will be composed of a collection of large and small telescopes situated at the South Pole and in the Atacama Desert. The South Pole is characterized by a particularly stable atmosphere, a location ideal for deep observations using small telescopes, in order to search for primordial B-modes. On the other hand, the Atacama site is – thanks to its height and its very dry atmosphere – the preferred location for conducting an $\sim 70 - 80\%$ fraction of the sky necessary for one of the other science cases of the experiment, that is measuring the contribution of light relic particles to the effective number of relativistic species in the early Universe (N_{eff}).

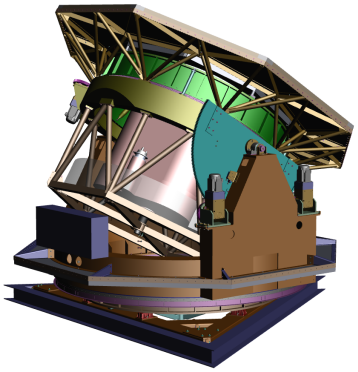

Figure 3.9: Schematic design for the CMB-S4 SAT telescopes. From Abazajian et al. (2019b).

Considering the peculiarities of each of the two sites, the CMB-S4 experiment will perform two different surveys: a low-resolution *ultra-deep* one (with noise level $\leq 1\,\mu\text{K} - \text{arcmin}$) dedicated to B-mode searches and a *deep and wide* (with noise $\sim 1\,\mu\text{K} - \text{arcmin}$ and resolution $\leq 1.5\,\text{arcmin}$) one dedicated to measuring N_{eff}. The former survey will observe a low-foreground $\sim 3\%$ patch of the sky (extensible to a larger fraction if the primordial SGWB is discovered) from the South pole, using fourteen 0.55 m refractor SATs observing frequencies $\leq 155\,\text{GHz}$, other four 0.55 m SATs at $220 - 270\text{GHz}$ and a 6-m LAT observing seven frequency bands from 20 to 278 GHz devoted to low-resolution B-mode measurements for systematics contamination control and high-resolution ($\sim 1.5\,\text{arcmin}$) measurements for delensing. On the other hand, the deep and wide survey will be conducted from the Atacama site and will feature two 6-m LATs covering eight frequency bands from 30 to 278 GHz. In total, the number of TES detectors used in CMB-S4 will be one order of magnitude greater than SO, reaching about 511000 units.

Concerning the target sensitivity of CMB-S4 to primordial GWs, this experiment will aim at detecting $r \geq 0.003$ at more than 5σ. In absence of a detection, this experiment will be able to push the upper limit to $r \leq 0.001$ at 95% C.L. (Abazajian et al., 2019b),

3.1.3 *The foregrounds challenge for B-mode experiments*

As we mentioned frequently above, astrophysical foregrounds constitute one of the main challenges for the primordial SGWB detection using CMB *B*-modes, and represent one of the major limiting factors for achieving the $r \sim 0.001$ level. These foregrounds produce a *B*-mode signal of secondary origin, which contaminates the sought-after primordial one, making it necessary to resort to component separation strategies in order to separate the two contributions or to marginalise over them at the power spectrum or cosmological parameters estimation stage. Such strategies require some previous knowledge on the spectral shape of the foregrounds, on their spatial fluctuations and on their intensity and polarization maps.

Concerning, component separation algorithms – as we will detail in Section 4.3 for the specific case of a *maximum-likelihood parametric component separation approach* – they allow in general to subtract the foreground and estimate the primordial contribution, at the price of a residual noise contribution limiting the sensitivity of the experiment.

In this Section, we will briefly review the main mechanisms producing astrophysical foregrounds, whose impact will be relevant for the *B*-mode probes will we consider later in this Thesis (Chapters 4 and 5). We will start with the two most important foregrounds sources, namely synchrotron and thermal dust emissions, and then we will move to secondary contaminants, such as spinning and magnetic dust, carbon monoxide and others, see for a review Dickinson (2016).

Synchrotron

One of the two strongest contributions to polarized foregrounds is represented by the synchrotron radiation emitted by cosmic ray electrons accelerated by the Galactic magnetic field. The emission law is thus governed by the strength of the magnetic field, the number and the energy spectrum of the cosmic ray electrons and can therefore vary across the sky. At first approximation, the Spectral Energy Distribution (SED) of synchrotron radiation is given by a (curved) power-law (see Farsian et al., 2020, and references therein)

$$I_{sync}(\hat{n}, \nu) = A_{sync}(\hat{n}) \left(\frac{\nu}{\nu_s}\right)^{\beta_s(\hat{n}) + C_s(\hat{n}) \ln(\nu/\nu_s)} , \tag{3.1}$$

where ν_s is the pivot frequency, A_{sync} the amplitude, β_s the spectral index, C_s the curvature and $\hat{n}$ the direction of observation.

The spectral index for synchrotron has been found to vary in the range $-2.5 \leq \beta_s \leq -4.4$ with an average value $\beta_s \simeq -3.25 \pm 0.15$, combining polarization observations from the S-band Polarization

All Sky Survey (S-PASS), Planck and WMAP (Krachmalnicoff et al., 2018). Concerning the synchrotron curvature, no evidence as been found yet within current precision (see Krachmalnicoff et al., 2018, and references therein).

The polarization fraction of synchrotron at high Galactic latitude is between 10% and 40% (see Dickinson, 2016, and references therein), and therefore this foreground has an important impact on B-mode searches. This is also highligthed from Figure 3.10, comparing the power spectrum of synchrotron at 95 GHz (orange band) with the one of primordial B-modes with $r = 0.1, 0.01$ and 0.001 (grey curves) and lensing B-modes (blue curve). The upper edge of the synchrotron band has been obtained from power-law fits of Planck data on the largest sky fraction considered in the analysis ($\sim$ 70%), while the lower edge comes from the smallest sky fraction analyzed in Krachmalnicoff et al. (2018).

Thermal dust

The other main contribution to B-mode foregrounds comes from the thermal emission of interstellar dust grains (with sizes ranging from a fraction of µm to 1 nm) heated by stellar radiation, with a temperature tipically around $\sim$ 20 K. Their emission depends on the density, temperature, size and chemical composition of the dust grains, and thus it is spatially variable across the sky.

The thermal dust SED is tipically approximated by the one-component modified black-body (or *grey body*) (see Farsian et al., 2020, and references therein)

$$I_{dust}(\hat{n}, \nu) = A_{dust}(\hat{n}) \left(\frac{\nu}{\nu_d}\right)^{\beta_d(\hat{n})+1} \frac{e^{\frac{h\nu_d}{kT_d(\hat{n})}} - 1}{e^{\frac{h\nu}{kT_d(\hat{n})}} - 1}, \tag{3.2}$$

where β_d is the spectral index, T_d is the dust temperature and A_{dust} the amplitude.

As we anticipated above, the emission from thermal dust can represent a significant contamination for CMB polarization: the mean polarization fraction at high Galactic latitude can reach up to 20%. Again Figure 3.10 highlights the importance of the dust foreground with respect to the primordial B-mode signal.

Recent observations by the Planck satellite (Planck Collaboration, 2018b) show that the dust SED is well-fitted by the modified blackbody in Eq. 3.2, and point towards a value of $T_d \approx 19.6$ K and $\beta_d = 1.53 \pm 0.02$.

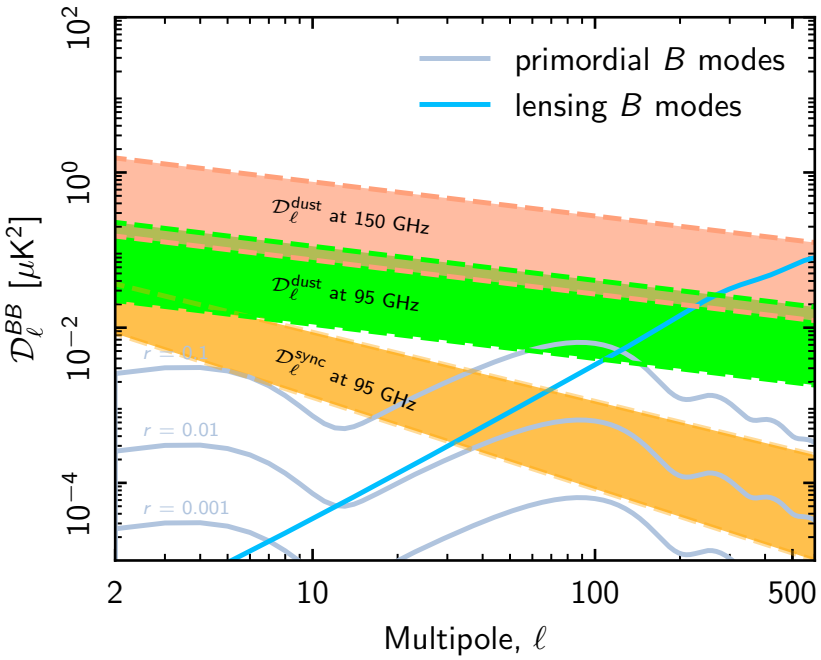

Figure 3.10: Comparison bewteen the power spectrum of synchrotron at 95 GHz (orange band), dust at 95 GHz (green band) and at 150 GHz with the one of primordial B-modes with $r = 0.1, 0.01$ and 0.001 (grey curves) and lensing B-modes (blue curve). The upper edge of the bands has been obtained from power-law fits of Planck data on the largest sky fraction considered in the analysis ($\sim 70\%$), while the lower edge comes from the smallest analyzed sky fraction ($\sim 24\%$). Note that the lower edge for synchrotron comes from the smallest sky fraction analyzed in Krachmalnicoff et al. (2018). From Planck Collaboration (2018b).

Spinning and magnetic dust

Another contribution to polarized foregrounds could come from the rotation of ~ 1 nm dust grains and molecules at GHz frequencies – the so-called *spinning dust* – possessing an electric dipole and thus emitting dipole radiation (Draine and Lazarian, 1998). Since the emission is dominated by the smallest grains – which are the easiest to spin – the spectrum will feature a peak typically around ~ 30 GHz. The polarization fraction of spinning dust is expected not to exceed $\lesssim 1\%$ (Dickinson et al., 2018) at frequencies relevant for CMB polarization experiments, making it a good candidate as the source of the Anomalous Microwave Emission (AME)[2]. Because of such a small polarization fraction, spinning dust it is not expected to represent a major polarized foreground. Nevertheless, its proper subtraction could be a necessary step for high-sensitivity future B-mode experiments searching for $r \sim 0.001$.

An additional source of contamination could reside in the magnetic dipole radiation due dust grains, ferromagnetic and ferrimagnetic materials in the interstellar medium. The spectrum of this magnetic dust emission is similar to thermal dust, and is characterized by a temperature of the order of tens of K, making difficult to disentangle it from the thermal dust emission. Contrary to spinning dust, magnetic dust could be highly polarized: theoretical studies

[2] AME is a diffuse Galactic radiation component, that cannot be explained by synchrotron, thermal-dust or free-free emission, and that has been repeatedly observed in the frequency range $\sim 10 - 60$GHz. For a review see Dickinson et al. (2018).

indicate a polarization fraction $\sim 10\% - 15\%$ (Dickinson, 2016), which could be an issue for *B*-mode searches.

Carbon Monoxide (CO) lines

The rotational transition lines of the CO molecule in our Galaxy could contaminate significantly the CMB polarization at the corresponding frequencies (Puglisi et al., 2017). Despite the moderate polarization level (between $\sim 0.5\% - 2.5\%$ (Puglisi et al., 2017)) generated by the interaction of the Galactic magnetic field and the CO molecule magnetic moment, CO lines could cause significant systematic errors in future *B*-mode searches. Thus, they should therefore carefully accounted for when choosing the bandpasses, in order to avoid the strongest lines (Dickinson, 2016).

Free-Free emission

Free electrons accelerated in the Coulomb field of ions (tipically protons), emit *free-free* radiation. The polarization fraction for this Galactic component is expected to be $\ll 1\%$ at high Galactic latitude (Dickinson, 2016), therefore it is not expected to contribute significantly to polarized foregrounds.

Point sources

Extragalactic sources, such as galaxies, can also contribute to polarized foregrounds, mainly in the infrared and radio bands. Some of the individual sources – usually called *point sources* – can be resolved and masked (Collaboration, 2016), while the rest of unresolved sources will form a polarized diffuse foreground with a few percent of polarization fraction; however, this diffuse polarized foreground can affect only small scales and should not represent a problem for *B*-mode searches (Dickinson, 2016).

Cosmic Infrared Background (CIB)

The CIB – formed by many individual galaxies – can also contribute to polarized foregrounds with a low level ($\lesssim 1\%$) of polarization: it has been shown that it does not represent a problematic foreground for *B*-mode searches at frequencies below 353 GHz (Feng and Holder, 2020).

3.2 *Beyond B-modes: PTA and laser interferometers*

This Section will be structured similarly to Section 3.1 for the CMB: after having summarized the current status and the observational per-

spectives (Sections 3.2.1 and 3.2.2), we will describe in broad terms some of the current and planned GW laser and atomic interferometers (Sections 3.2.3 and 3.2.4) and PTA surveys (Section 3.2.5), for which in Chapter 5 we will provide forecasts regarding the detection of an inflationary SGWB. Section 3.2.6 will be dedicated instead to listing the relevant sources of astrophysical foregrounds for these direct detection experiments (see also Section 5.4).

3.2.1 *The landscape of direct GW observations*

Although the existence of gravitational radiation had already been confirmed in 1982 by the measurement of the rate of orbital decay due to energy-loss in GWs in a neutron star binary (Taylor and Weisberg, 1982), the first direct observation has been performed only in 2016 by the Advanced LIGO (Harry, 2010) interferometer for a binary black-hole system (Abbott et al., 2016). Shortly after that, the first direct observation of GWs produced by a binary neutron stars system (Abbott et al., 2017) was carried out in collaboration with the Advanced Virgo interferometer (Acernese et al., 2015). With these discoveries, a new channel for astronomical observation was inaugurated, opening up, among numerous other opportunities, the possibility to observe an SGWB produced by several possible sources. In this Thesis, we will be concerned with an SGWB of inflationary origin; however, there is a plethora of physical phenomena which could in principle produce an SGWB, such as cosmic defects, first-order phase transitions in the early Universe and preheating (see Caprini and Figueroa, 2018, for a comprehensive review). On top of that, several astrophysical sources, including neutron star binaries, stellar-mass and massive black hole binaries and white dwarf binaries among others (see Christensen, 2019, for a review), can produce an SGWB of astrophysical origin. We will see in Section 3.2.6 that this astrophysical background could represent a *foreground* in searches of the primordial SGWB.

As anticipated in the introduction of this Chapter, there are at least two ways to detect an SGWB in a "direct" manner – so called in order to distinguish it from the "indirect" searches through CMB B-modes or BBN, among others methods – that is PTA and ground-based or space-borne laser (and atomic) interfometers.

For what concerns PTA, the current generation of experiments – placing upper limits on the SGWB – includes the Nanohertz Observatory for Gravitational Waves (NANOGrav) (Arzoumanian et al., 2016, 2018), the European PTA (EPTA) (Lentati et al., 2015b) and the Parkes PTA (PPTA) (Yardley et al., 2011). The next generation of PTA surveys will feature, instead the Square Kilometre Array (SKA) (Welt-

man et al., 2020), probing the nano-Hertz band ($\approx 10^{-9} - 10^{-7}$ Hz).

Ground-based laser interferometers tipically operate between a few Hertz and a few kilo-Hertz; at the moment Advanced LIGO (Harry, 2010), Advanced VIRGO (Acernese et al., 2015) and KAGRA (Somiya, 2012) are active, while the future generation will comprise the Cosmic Explorer (CE) (Reitze et al., 2019) and the Einstein Telescope (ET) (Hild et al., 2011).

Concerning observations from space, the Laser Interferometer Space Antenna (LISA) (Baker et al., 2019; Smith and Caldwell, 2019) will operate in the milli-Hertz band and is scheduled for launch in the early/mid 2030s. Furthermore, a wide array of space missions has been proposed for the 2040s, including the μAres (Sesana et al., 2019) laser interferometer for the micro-Hertz band, the Decihertz Observatory (DO) (Sedda et al., 2019) and the atomic interferometer Atomic Experiment for Dark Matter and Gravity Exploration in Space (AEDGE) (El-Neaj et al., 2019), both operating in the deci-Hertz band. We mention also the proposed Advanced Millihertz Gravitational-wave Observatory (AMIGO) (Baibhav et al., 2019) in the milli-Hertz band, which could be considered at first approximation an enhanced version of LISA.

This vast landscape of experiments is completed by two future ultra-sensitive space interferometers, the Big Bang Observer (BBO) (Crowder and Cornish, 2005b; Smith and Caldwell, 2017), the Decihertz Interferometer Gravitational wave Observatory (DECIGO) (Seto et al., 2001; Kawamura et al., 2020), both targeting the deci-Hertz band.

3.2.2 *Observational perspectives for the primordial SGWB*

We discuss here the current upper limits on the SGWB, and the perspectives of present and future observatories.

Upper limits

At the time of writing, current laser interferometers and PTA survey have not observed yet an SGWB, neither of cosmological nor of astrophysical origin. However – during their second observing run – the Advanced LIGO and Virgo collaborations have managed to put upper limits on the energy density of such a background in the $\sim 20 - 100$ Hz frequency band, corresponding to $\Omega_{GW}h^2 < 6.0 \times 10^{-8}$ at 95% C.L. for a scale-invariant background and $\Omega_{GW}h^2 < 4.8 \times 10^{-8}$ at 25 Hz for a background due to compact binaries (Abbott et al., 2019) (which, as we will see in Section 3.2.6 is expected to be a power-law with spectral index $\approx 2/3$).

Current PTA survey were able to provide upper limits in the band

$\sim 10^{-9} - 10^{-7}$ Hz as well: EPTA found $\Omega_{GW}h^2 < 1.1 \times 10^{-9}$ at a frequency 2.8 nHz (Lentati et al., 2015b); NANOGRAV found instead $\Omega_{GW}h^2 < 4.2 \times 10^{-10}$ at a frequency 3.3 nHz (Arzoumanian et al., 2016) ; finally, PPTA found $\Omega_{GW}h^2 < 2.3 \times 10^{-10}$ at a frequency 6.3 nHz (Lasky et al., 2016a).

There are several other methods that allow to search for a SGWB (see Christensen, 2019; Romano and Cornish, 2017, for reviews). This includes the Doppler tracking of spacecraft (in which the Earth and a spacecraft are considered as free test-masses), which gives a current best upper limit of $\Omega_{GW} < 0.03$ at a frequency 1.2 µHz from the Cassini data (Christensen, 2019).

We mention here also the possibility to put indirect upper limits (besides the ones provided by CMB *B*-modes), using BBN: in fact a too large GW energy density would affect the cosmic expansion rate and induce a decrease in the amount of helium produced from deuterium (see Section 1.5), changing the observed element ratios. This fact, combined with CMB and BAO observations, can be used to put a limit $\Omega_{GW} \leq 3.8 \times 10^{-6}$ at freqencies $\gtrsim 10^{-15}$ Hz (Pagano et al., 2016; Lasky et al., 2016a).

Future perspectives for an inflationary SGWB

At the moment, the most promising method for a near-future detection of an SGWB of inflationary origin is represented by the CMB *B*-mode experiments scheduled for the next decade (see Chapter 5). This is because, given the current upper limits provided by the combined Planck and BICEP2-Keck data (BICEP2 and Planck Collaborations), and assuming a standard single-field slow-roll scenario for inflation, the possibilities for detection of a primordial SGWB at solar system scales are severely limited by the almost scale-invariant nature of the Ω_{GW} spectrum (Figure 1.11), at least with detectors now available or scheduled within the next decade.

Nonetheless, there are several very compelling reasons to pursue the quest for a primordial SGWB also with direct detection experiments. Several theoretical models predict a blue-tilted or peaked primordial SGWB spectrum at higher frequencies (see Caprini and Figueroa, 2018; Guzzetti et al., 2016; Bartolo et al., 2016, and references therein), making a detection with PTA and laser interferometers frequencies feasible even for experiments planned for the next decade. We explore this possibility in Chapter 5, in the framework of the spectator axion-SU(2) inflation model.

Furthermore, in the event that a primordial SGWB, compatible with the single-field slow-roll inflation prediction, is discovered by the next-decade CMB *B*-mode experiments, this would establish a

clear goal for ultra-sensitive missions planned for the decade 2030-2040 or later, such as DECIGO and BBO.

3.2.3 *Laser interferometers*

The detection principle for laser interferometers is quite simple (see Appendix A or Romano and Cornish (2017) for a review): as a GW is passing, it changes the proper distance between the two freely moving test-masses at the ends of the arm of the interferometer, producing phase-shifts in the laser beams traveling back-and-forth along the arm. As we will compute in Appendix A (see also the review Romano and Cornish, 2017), the specific design of the interferometer is one of the factors determining its frequency response.

An SGWB signal – differently from other GW signals like transient (i.e. binary inspirals or burst events) or continuous periodic ones from pulsars – will manifest itself only as an extra source of noise in a single detector, making impossible to distinguish the two components if the signal is smaller than the instrumental noise, as typically happens for a primordial SGWB. Nonetheless, if the signal is greater or comparable to the instrumental noise, a subtraction strategy based on the different spectral shapes of the two may be possible.

However, a much more effective method has been devised in order to attempt the detection of an SGWB: the *cross-correlation* of the outputs of two or more detectors (see Section 5.3.1).

Another possible strategy for detection using a single interferometer – adopted for instance by the LISA mission – is the construction of *null channels*, that is specific combinations of the interferometer outputs that allow to measure the detector noise.

In the following, we will briefly describe the design and capabilities of each laser interferometer we will consider in Chapter 5 for our forecasts on the primordial SGWB, starting from the LISA mission.

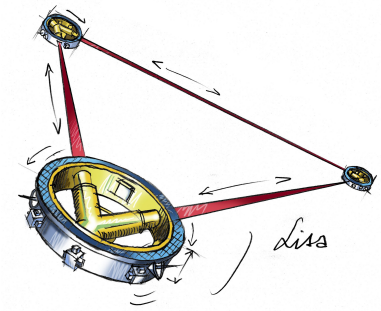

Figure 3.11: Schematic design of the LISA mission. From https://www.esa.int/Science_Exploration/Space_Science/LISA.

LISA

Low-frequency GW observations from Earth-based detectors are strongly limited, below $\sim$ 1 Hz, by the presence of seismic noise. Space missions, such as LISA and others, are therefore required to explore frequencies below this value. In particular, the LISA mission will be able to probe the band $\approx$ 0.1 mHz $-$ 0.1 Hz and search an SGWB up to $\Omega_{GW} \sim 10^{-13}$ in this band.

LISA will consist of three spacecrafts, each on hosting two test-masses, disposed in an equilateral triangle configuration with arm lenght 2.5 Gm and connected by six laser links, two traveling in opposite directions along each each arm: this is due to the fact that, because of the distance between spacecrafts, the direct reflection

typical of a Michelson interferometer is not possible, so phase-locking between the arriving and leaving laser signal has to be performed instead.

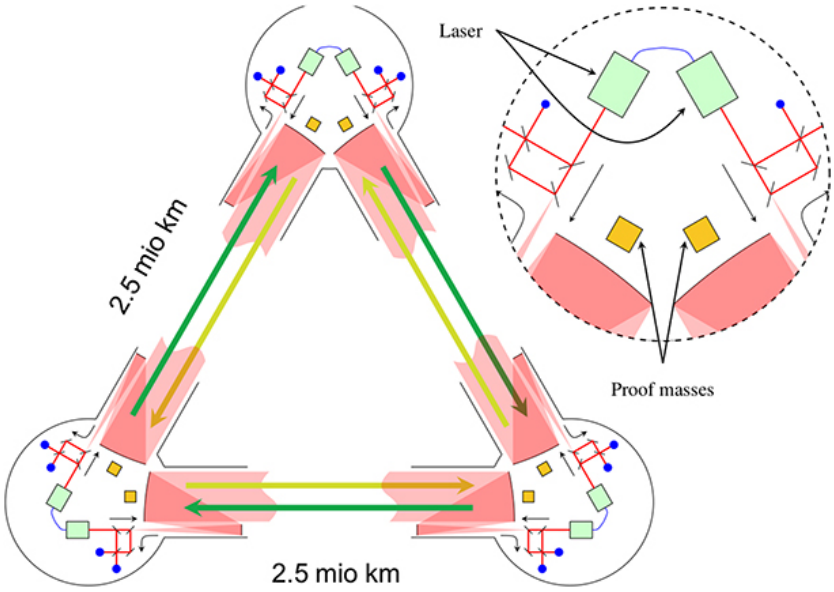

Figure 3.12: A more detailed schematic representation of the LISA mission, showing the laser links (green and yellow lines) traveling in opposite directions inside each interferometer arm of lenght 2.5 Gm and the position of test-masses and lasers inside each of the three spacecrafts. From Schuldt (2018).

As we anticipated above, this particular configuration permits the construction of the so-called Time Delay Interferometry (TDI) signals (see Appendix A), allowing to measure the instrumental noise at the output of the interferomter and thus to disentangle it from the sought-after SGWB signal, even in absence of cross-correlation with another instrument.

LISA will perform an Heliocentric orbit at a distance of about 1 AU from the Sun, trailing Earth by 20° and inclined by 60° with respect to the ecliptic (Figure 3.13).

The LISA mission is now a Phase A mission for European Space Agency (ESA) with ESA state members and NASA contributions, scheduled for launch in the early or mid 2030s (Baker et al., 2019). It is worth mentioning the extraordinary success obtained by two flight demonstrations, namely the LISA Pathfinder mission (2015-2017) and the Gravity Recovery And Climate Explorer Follow-On mission (2018-), launched in order to test the readiness of LISA's technology.

DO

DO is a proposed post-LISA mission (2035-2050) that will probe the yet unobserved deci-hertz band ($0.01 - 1\,\text{Hz}$). Among the many other goals of its rich science case, including observations of intermediate mass black holes and meausurements of the eccentricity of binary

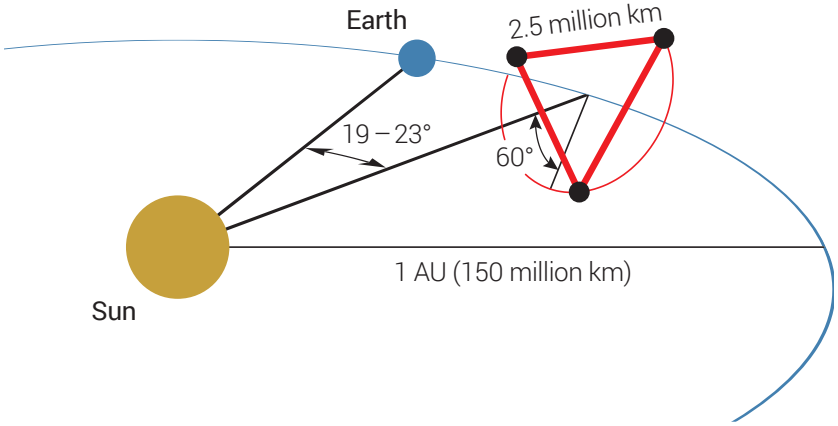

Figure 3.13: Orbit for the LISA mission. From Baker et al. (2019).

black holes, it will target a SGWB up to an amplitude $\Omega_{GW}h^2 \sim 10^{-14} - 10^{-15}$, depending on the choice of its actual design, between the two proposed alternatives: DO Optimal or DO Conservative.

Both the Optimal and Conservative options have been proposed as LISA-like missions with shorter arm lenght (10^8 m) and one order of magnitude improvement in acceleration noise with respect to LISA. However, the DO Conservative design will improveover LISA by adopting smaller wavelenght lasers (532 nm instead of 1064 nm used for LISA), higher laser power (10 W instead of 2 W) and larger diameter telescopes (1 m instead of 0.3 m). The DO Optimal design further improves over the Conservative one by using 30 W-lasers and 2 m-telescopes.

μAres

Also μAres is a proposed mission for the 2040s decade: it will probe the unexplored region μHz region ($\approx 10^{-7} - 10^{-2}$ Hz), between PTA survey and LISA. The science case for this mission is extremely rich and encompasses massive black holes physics and astrophysics, Galactic white dwarfs and binary black holes, extreme mass ration ispirals (EMRIs) among others, and also SGWBs, both of cosmological and astrophysical (Galactic and Extragalactic binary white dwarfs, massive black hole binaries, Extragalactic binary black holes and neutron stars) origin. In particular, it will target a cosmological SWGB at the level of $\Omega_{GW}h^2 \sim 6 \times 10^{-17}$ at 2×10^{-4}Hz.

The μAres mission will be composed by two identical equilateral triangle LISA-like constellations, with longer arms $L = 430 \times 10^9$ m. In this case, one of the two triangular configurations would be trailing Mars orbit within the ecliptic plane while the other would be in the same orbit but 90° tilted with respect to the ecliptic plane (Figure

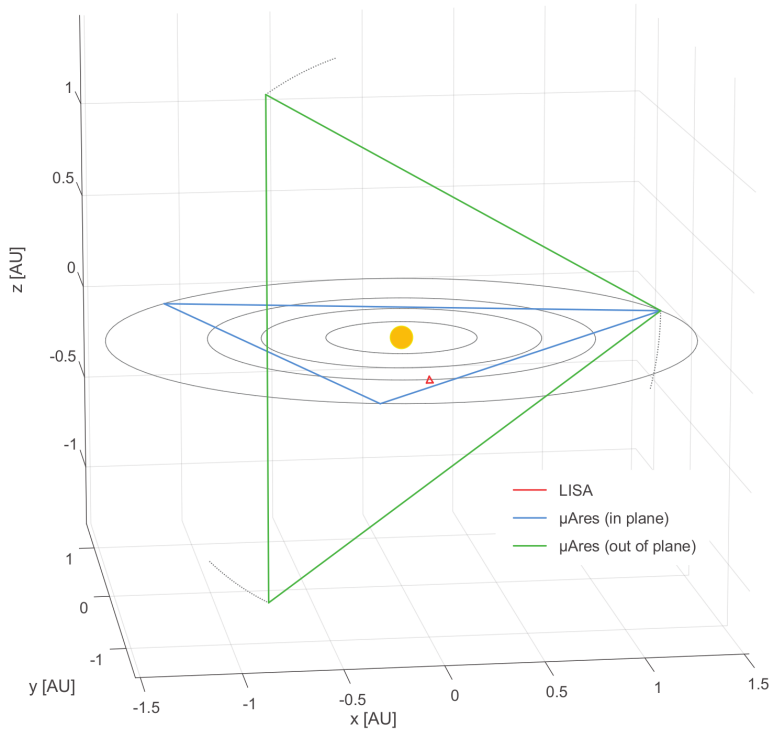

Figure 3.14: Configuration of the μAres mission. From Sesana et al. (2019).

3.14).

BBO

BBO is another proposed post-LISA space mission: it will be an ultra-sensitive experiment operating in the band $\approx 0.03 - 3\,\mathrm{Hz}$, capable of probing a primordial SGWB down to $\Omega_{GW} \sim 10^{-17}$ with minimal contamination from astrophysical foregrounds (see Sections 3.2.6 and 5.4).

BBO will be composed by four independent equilateral triangle LISA-like constellations with arms of 5×10^7 m and very powerful lasers ($\sim 500\,\mathrm{W}$) in Heliocentric orbit at 1 AU distance from the Sun (Figure 3.16): of these four, two triangular constellations will be coplanar and rotated by 180° one with respect to the other, forming the so-called *hexagram* configuration (Figure 3.15), while the other two will be on the same orbit, but ahead and behind the BBO-hexagram by 120°.

This particular configuration has two main advantages. First, the BBO-hexagram allows ultra-sensitive measurements of the SGWB by cross-correlation of the outputs of the two co-located instruments. Second, the two single interferometers grant a high angular resolu-

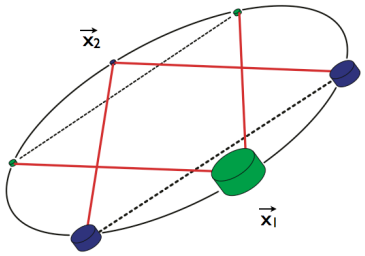

Figure 3.15: The BBO hexagram configuration. From Romano and Cornish (2017).

tion, necessary for the subtraction of the foreground generated in the BBO band by binary black holes and neutron stars (Section 3.2.6).

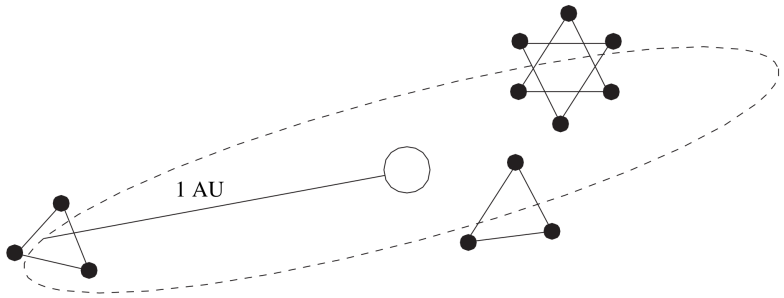

Figure 3.16: Configuration of the four BBO constellations. From Cutler and Harms (2006).

DECIGO

The concept of the proposed DECIGO mission is very similar to the BBO one: an hexagram constellation composed by two co-located triangular interferometer for ultra-sensitive SGWB searches and two other single constellations useful for compact binaries sources identification and subtraction (Figure 3.18).

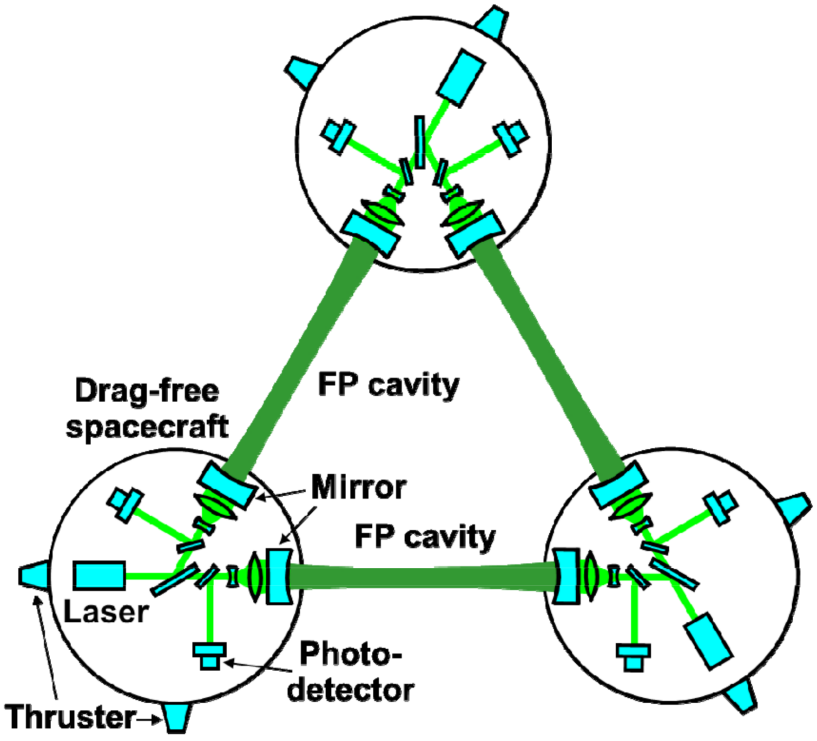

Figure 3.17: Schematic design for a single DECIGO constellation. From Kawamura et al. (2020).

In the DECIGO case, however, the arm length will be shorter (10^6 m) and it will feature *Fabry-Pérot* cavities in its arms (Figure 3.17), allowing for a much lower laser power with respect to BBO (10 W).

DECIGO will be slightly less sensitive than BBO, reaching a level $\Omega_{GW} \sim 5 \times 10^{-17}$ in the band $\approx 0.1 - 10$ Hz.

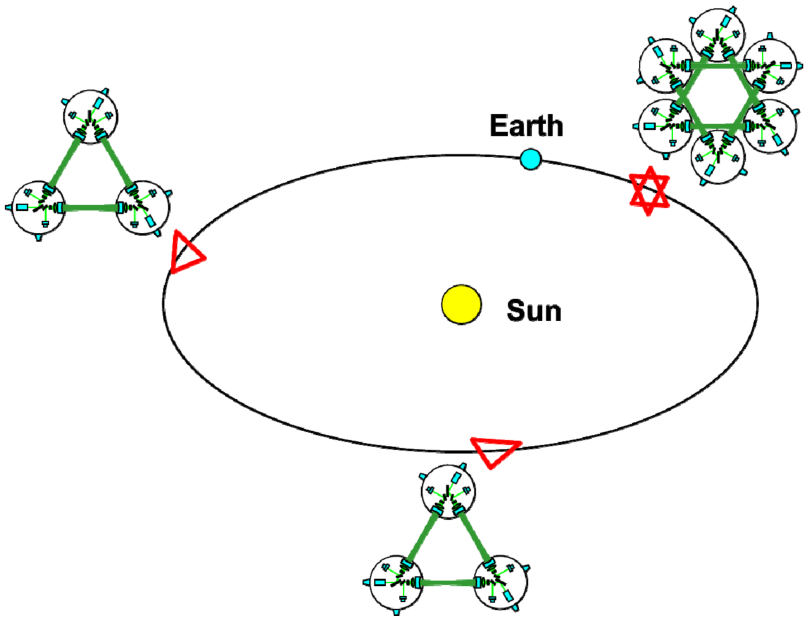

Figure 3.18: Configuration of the DECIGO mission. From Kawamura et al. (2020).

ET

As we anticipated above, the main factor limiting the sensitivity of Earth-based GW detectors at low-frequencies is the seismic noise ($f \lesssim 1$ Hz). The other major limitations are due to the test masses and suspensions thermal noise ($f \lesssim 100$ Hz) and to laser shot-noise (100 Hz $\lesssim f \lesssim 10^4$ Hz). The third generation detector design ET is expected to reduce all these noise sources, improving the sensitivity by $\sim$ one order of magnitude over the second generation ground-based interferometers (Advanced LIGO and Virgo), and reaching a value of $\Omega_{GW} \sim 10^{-12}$ for an SGWB.

The ET design we will consider in this Thesis is the so-called *xylophone* configuration Hild et al. (2011): this instrument will be composed by three detectors, each one consisting of two individual Michelson interferometers – one optimized for the low-frequency range (ET-LF) and the other for the high frequencies (ET-HF) – with angle-opening of 60° and arm lenght of 10 km, forming an equilateral triangle configuration (Figure 3.19). Only the ET-LF interferometers will be located underground, to reduce the seismic noise.

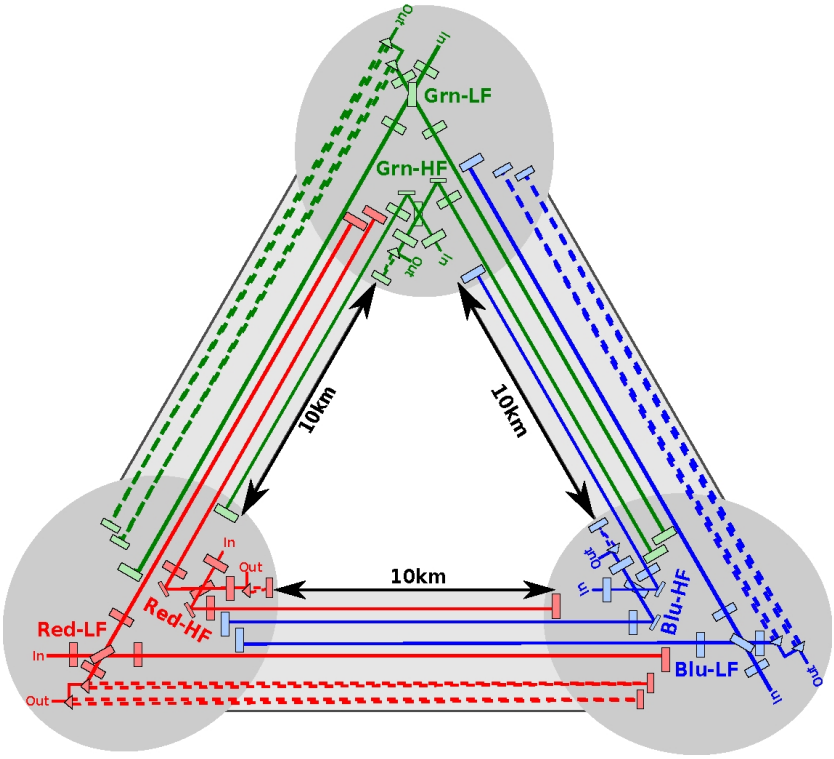

Figure 3.19: Schematic design of ET. See text for details. From Hild et al. (2011).

3.2.4 *Atomic interferometers: AEDGE*

The detection principle behind atomic interferometers, such as the AEDGE experiment, is that the passage of a GW with strain h induces a phase-shift $\Delta\varphi$ in the relative phase between cold atom clouds by changing their separation L by an amount $\delta L = hL$ (El-Neaj et al., 2019):

$$\Delta\varphi = \omega_A \times 2L, \tag{3.3}$$

where ω_A is the frequency of the atomic transition we are considering.

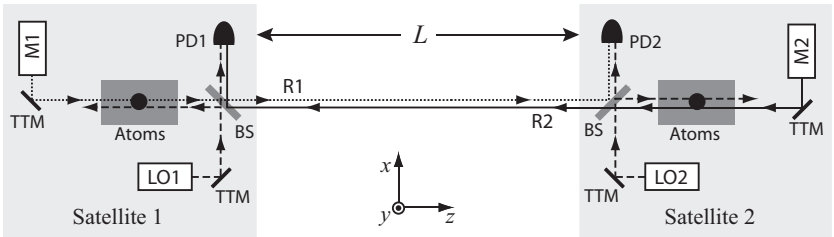

Figure 3.20: Experimental setup of the AEDGE experiment. Description in the text. From El-Neaj et al. (2019).

AEDGE is an atomic interferometer space mission proposed for the years 2035-2050: it will probe the deci-hertz band ($\approx 0.01 - 10\,\mathrm{Hz}$)

and with a sensitivity to an SGWB similar to DO Optimal ($\Omega_{GW}h^2 \sim 10^{-15}$).

The experimental setup for the AEDGE experiment is shown in Figure 3.20: the experiment is composed by two satellites that contain clouds of ultra-cold atoms (acting as test-masses), connected by two laser beams traveling along the arm L in opposite directions.

3.2.5 *PTA experiments: SKA*

Searches of an SGWB can be conducted also using PTA surveys in the frequency range $\approx 10^{-9} - 10^{-7}$ Hz. The basic principle behind these searches is that the passage of a GW produces correlated modulation in the arrival times of the radio pulses emitted by an array of Galactic pulsars with rotation period of ~ 1 ms (see Romano and Cornish, 2017, and references therein).

The observational power of PTA surveys will increase in the next decades, as the parameters on which the sensitivity of these survey to an SGWB depends (such as the timing precision, the total observations time, the number of observed pulsars in the array and the number of observations) are expected to improve.

In this Thesis, we will perform forecasts for the SKA PTA survey assuming the observation of 200 pulsars with millisecond periods and 50 ns residuals, for a period of 10 yr and an observation cadence of one every week. This setup should be reasonable for the year ~ 2040, according to Mingarelli et al. (2019), allowing for searches of an SGWB down to a level of $\Omega_{GW} \sim 10^{-14}$. However, as we will discuss later in Section 3.2.6, the PTA band is dominated by the astrophysical foreground produced by massive black hole binaries, awhich needs to be subtracted in order to detect a cosmological SGWB wit amplitude smaller than this foreground.

3.2.6 *Astrophysical foreground sources for PTA and laser interferometers*

Similarly to what happens for B-mode experiments, also direct cosmological SGWB searches could be impeded by the presence of a multi-component astrophysical foreground. Also in this case, subtraction strategies can be devised in order to attempt the detection of a primordial SGWB; we will consider the subtraction of astrophysical foregrounds in a dedicated section (Section 5.4), while here we will just briefly summarize the various sources and their importance for each of the experiments considered in the previous section.

Each GW experiment, probing a different frequency band, will be affected in a distinct way by the various astrophysical sources able to produce such a contaminating background.

We will start considering the situation of the ground-based experiment ET. The most relevant foreground in the band of these ground based experiments is expected to be the one produced by unresolved compact binaries, that is BBH, BNS and BH-NS systems. This prediction is based on the current estimates of the merging rates of these compact objects (Abbott et al., 2019) – which is still subject to large uncertainties – and yields a predicted amplitude of the BBH+BNS foreground at $f_* = 25\,\mathrm{Hz}$ of $\Omega_* = 8.9^{+12.6}_{-5.6} \times 10^{-10}$. The BBH+BNS signal is well approximated at low frequencies by the power-law

$$\Omega_{BBH+BNS}(f) = \Omega_* \left(\frac{f}{f_*}\right)^{2/3}, \tag{3.4}$$

from which it is possible to infer that this foreground will be not only a significant limiting factor at ET frequencies (Zhu et al., 2013; Sachdev et al., 2020) for the search of a cosmologically produced SGWB, but also in the LISA band (Pieroni and Barausse, 2020), as well as DO, μAres and AEDGE ones. Subtraction strategies (see for instance Pieroni and Barausse, 2020; Pan and Yang, 2019) are currently being developed to reduce the impact of this foreground.

The compact binary foreground could affect also the DECIGO and BBO bands, however, as we will see in Section 5.4, BBO should be able to resolve and subtract most of these sources, while DECIGO should be capable of substantially reducing their impact in a similar way.

Unresolved GWD are also capable of producing an astrophysical SGWB with a shape approximately given by Eq 5.32; this foreground should affect mainly the low-frequency part of the LISA band, and the bands of the other laser and atomic space interferometers. However, as we will see in Section 5.4 LISA should be able to disentangle this Galactic contribution exploiting its anisotropy and its modulation in time due to the motion of the constellation (Adams and Cornish, 2014), and similarly for the other interferometers.

The contribution of EGWD to the astrophysical foreground, differently from GWD, is expected to be fairly isotropic (with an hint of anisotropy due to the stronger signal from nearby Galaxies) and should have an amplitude about one order of magnitude smaller than it Galactic counterpart. It could be a relevant foreground for LISA and the other space interferometers, although its unique spectral shape deviating from a power-law (see Eq. 5.33) could be very useful to disentangle it from a cosmological SGWB.

Finally, we consider the unresolved MBHB astrophysical SGWB: this signal is created by the coalescence of MBHB when galaxies merge and its amplitude depends on galaxy merger rates and on the MBHB masses, which have both considerable astrophysical un-

certainties. This foreground has a typical frequency dependence $\Omega_{MBHB} \propto f^{2/3}$ for frequencies $f \lesssim 10^{-8}$ Hz, and becomes considerably steeper at higher frequencies (see Eq. 5.35): it dominates the SKA range and the band of μAres below $\lesssim 10^{-5}$ Hz.

A conservative upper limit can be derived for the MBHB foreground at PTA frequencies ($f \lesssim 10^{-8}$ Hz) (Caprini and Figueroa, 2018):

$$\Omega_{MBHB}h^2 \gtrsim 10^{-11} \left(\frac{f}{10^{-8}\text{Hz}}\right)^{2/3}. \tag{3.5}$$

Part II

Constraining the Shape of the Tensor Spectrum

4
A Principal Component Analysis of the Tensor Spectrum

This Chapter is based on the work Campeti et al. (2019b).

In this Chapter we will study how the *shape of the spectrum of primordial gravitational waves* can be constrained by the future CMB *B*-mode experiments LiteBIRD, SO and CMB-S4 (Section 3.1.2).

This study is motivated by the fact that, in addition to the standard prediction of single-field slow-roll inflation models, several other production mechanisms have been studied as possible sources of primordial B-modes; among them, massive gravity inflation (Domènech et al., 2017), open inflation (Yamauchi et al., 2011), the SU(2)-axion model (Dimastrogiovanni and Peloso, 2013; Adshead et al., 2013b; Maleknejad et al., 2013), modified gravity models with speed of gravitational waves different from light speed (Raveri et al., 2015), models of inflation with topological defects/cosmic strings (Lizarraga et al., 2014), rolling axion (Namba et al., 2016), high-scale inflation (Baumann et al., 2016), multifield inflation (Price et al., 2015) and others. In order to be able to distinguish different physical mechanisms it is necessary to be able to quantify deviations of the measured spectrum from the power-law inflationary prediction, as it is done in (Hiramatsu et al., 2018) for the first time for the reconstruction of the tensor power spectrum.

This work aims at providing a Principal Component Analysis (PCA) of the primordial tensor spectrum, similar to what has been done for scalar modes prior to the Planck mission (see Leach, 2006, and references therein). The PCA formalism allows to identify and study eigenvectors of the Fisher matrix associated to the primordial perturbation spectra, assessing the modulation in sensitivity of an experiment on the different cosmological perturbation scales, and determining where features in the tensor power spectrum can be probed more efficiently.

This technique has been applied in many different contexts, i.e. the scalar primordial power spectrum (Hu and Okamoto, 2004; Leach, 2006)), the reconstruction of the inflaton potential (Kadota et al., 2005), the process of reionization (Hu and Holder, 2003), the dark energy equation of state (Huterer and Starkman, 2003), weak lensing (Munshi and Kilbinger, 2006), the optimal binning of the primordial power spectrum (Paykari and Jaffe, 2010), the search of inflationary and reionization features in the Planck data (Obied et al., 2018) and many others.

Although with different procedure and final goals, PCA has also been applied to the tensor power spectrum in a recent work (Farhang and Vafaei Sadr, 2018). We expand these analyses and set rather different perspectives for our study, (i) by including, for the first time as a major aspect and in a coherent manner, the contribution from residual diffuse foreground contamination (Section 4.3), using the most recent techniques of foreground separation and cleaning via Maximum Likelihood Parametric Fitting implemented into the ForeGroundBuster (FGBuster) publicly available code (See `github.com/fgbuster/`

`fgbuster` and reference therein); (*ii*) by deriving robust expectations concerning the sensitivity of three forthcoming CMB probes (Sections 4.4.1 and 4.4.2) and modelling these experiments as realistically as possible (including $1/f$ noise when available); (*iii*) by investigating through a Monte Carlo Markov chain (MCMC) analysis the limitations of this technique, namely the impact of the physicality priors (which prevent the exploration of forbidden regions where the power spectrum assumes negative, and thus unphysical, values) on the derived constraints, the residual correlations between parameters and the departures from Gaussian behaviour (Sections 4.2.3 and 4.4.4).

The Chapter is organized as follows. In Section 4.1 we give the necessary definitions regarding the observational setup, the CMB power spectra and the fiducial cosmological model, and in Section 4.2 we review the general PCA algebra. In Section 4.3 we study and include the diffuse astrophysical foregrounds in our analysis, assessing the level of contamination and its role in the PCA, in Section 4.3.1 and 4.3.2, respectively. In Section 4.4 we predict and study the capability of future satellite (4.4.1) and ground-based (4.4.2) probes of constraining deviations from the inflationary CGB spectrum; in Section 4.4.3 we give explicit examples of deviations from the inflationary predictions and how PCA can measure and characterize those; Section 4.4.4 is dedicated to the study of the limitations and caveats imposed by the PCA method in the context of the tensor power spectrum. Finally, in Section 4.5 we outline our conclusions and future perspectives.

4.1 *Overview of the Observational Setup*

In this section, we briefly review the standard formalism for scalar and tensor power spectra of primordial perturbations, as well as for the angular power spectra in the CMB, and we define our fiducial cosmological model. Moreover, we define the nominal specifications of the CMB B-mode probes we will consider throughout the analysis.

According to single field, slow-roll inflationary scenario, quantum vacuum fluctuations excite cosmological scalar, vector and tensor perturbations. While vector modes decay, scalar and tensor modes in the metric stay constant and we focus on them in the following. The scalar curvature spectrum can be parametrized in the usual way as a power-law spectrum, as in Eq. 1.113, in which we set the pivot-scale k_0 to 0.002 Mpc^{-1}. No information is stored in the higher order statistics, as the vacuum fluctuations are assumed to be Gaussian distributed. The presence of matter fields during inflation changes this picture (see Agrawal et al., 2018a). Similarly, the tensor power spectrum can be written using the same standard power-law parametrization, as in Eq. 1.125, for which we choose again the pivot-scale $k_0 = 0.002\,\mathrm{Mpc}^{-1}$. We will use often the tensor-to-scalar ratio r as defined in Eq. 1.126. Currently there are only upper limits available on r, as discussed in Section 1.8.6.

The actual observables are not scalar or tensor power spectra, but the angular power spectra $C_\ell^{XX'}$ of CMB anisotropies (see Section 2.1.6), where X are generic labels for the total intensity of linear polarization. They are defined using the two-point correlation function of

the spherical harmonic coefficients $\langle a^{X*}_{\ell m} a^{X'}_{\ell' m'} \rangle = \delta_{\ell\ell'}\delta_{mm'} C^{XX'}_{\ell}$, where $X, X' \in \{T, E, B\}$, representing respectively the total intensity (T), gradient (E) and curl (B) modes of the CMB polarization (Kamionkowski et al., 1997; Seljak and Zaldarriaga, 1997) and $a^{X}_{\ell m}$ are the multipole moments of total intensity and polarization fluctuations.

We provide now the link between the observable angular power spectra and the primordial one. First of all, we remind that each angular power spectra has uncorrelated scalar and tensor contributions, that is $C^{XX',\,prim}_{\ell} = C^{XX'}_{\ell,s} + C^{XX'}_{\ell,t}$. The scalar and tensor contribution can be written in terms of the primordial power spectra as

$$C^{XX'}_{\ell,x} = \frac{2\pi}{\ell(\ell+1)} \int d\ln k \, \mathcal{P}_y(k) \, T^{X}_{\ell,y}(k) \, T^{X'}_{\ell,y}(k) \, , \tag{4.1}$$

where for the scalar case $X, X' = \{T, E\}$, $x = \{s\}$ and $y = \{\mathcal{R}\}$, while for the tensor one $X, X' = \{T, E, B\}$, $x = \{t\}$ and $y = \{T\}$. The $T^{X}_{\ell,y}$ are the scalar or tensor transfer functions; they depend on cosmological parameters as we review next, and are obtained from the solution of the Boltzmann equations. We compute them using the publicly available code CAMB (Code for Anisotropies in the Microwave Background (Lewis et al., 2000)) .

4.1.1 *Fiducial Model Adopted*

Our fiducial cosmological model is a flat ΛCDM with the six parameters fixed by the most recent observations (Planck Collaboration, 2018). We choose the best fit cosmological parameters from Table 2 in the quoted reference, obtained from the TT, TE, EE spectra and also including the large scale polarization (labeled as *low E*) and gravitational lensing. The model is made by 4 parameters expressing background quantities in a flat FLRW Universe, specifically the abundance of particles in the standard model ($\Omega_b h^2 = 0.02237$), CDM ($\Omega_c h^2 = 0.12$), reionization optical depth ($\tau = 0.0544$), amplitude of the Hubble constant today ($H_0 = 67.36$); 2 parameters define the power spectrum of scalar perturbations, namely its amplitude ($A_s = 2.1 \times 10^{-9}$), and scalar spectral index ($n_s = 0.9649$). For what concerns the tensor power spectrum, we consider three cases, corresponding to $r = 0$, $r = 0.001$ and $r = 0.01$. The value $r = 0.001$ is particularly relevant from the point of view of both observation and theory: it is close to the limit sensitivity of future B-mode probes and the prediction of the original Starobinsky model of inflation (see Planck Collaboration, 2018c, and references therein). The $r = 0.01$ case would be a strong signal within reach by the operating probes in the near future. For both models with $r > 0$, we assume a scale-invariant spectrum with tensor spectral index $n_T = 0$.

4.1.2 *Instrumental Specifications*

As we anticipated, we will consider several future CMB B-mode probes, representing the ongoing projects with ultimate sensitivity for r and n_T. The relevant parameters for us are represented by the instrumental sensitivity, usually given in μK-arcmin, the full width at half maximum (FWHM), the sky fraction considered, f_{sky}, as well as the relevant multipole range in the angular domain. As anticipated in the introduction. we will consider the LiteBIRD satellite[1] designed in order to have as primary goal the CGB observations from space (Hazumi et al., 2019). For what concerns ground probes, we consider the SO (The Simons Observatory Collaboration et al., 2018); in particular, we consider the small aperture telescopes (SATs), since they will gather most of the information on the primordial B-mode power spectrum. Finally, we also study the case of the ultimate network of ground-based probes, the CMB-S4 (Abazajian et al., 2016).[2] We report in Table 4.1 the instrumental specifications for these three experiments. The sensitivity reported is for polarization measurements. The ℓ range for LiteBIRD is given by $\ell_{min} = 2$ and $\ell_{max} = 1350$, for SO and CMB-S4 is instead $\ell_{min} = 30$ and $\ell_{max} = 4000$. The Table also resports the sky fraction f_{sky} and the delensing factor λ (defined in Section 4.1.3) employed for each experiment. For SO and CMB-S4 we additionally take into account $1/f$ noise, adopting the optimistic case of (The Simons Observatory Collaboration et al., 2018) for SO and using the specifications contained in the websites in footnote 2 for CMB-S4. For LiteBIRD, the reported specifications were taken during the Phase A1 process (Hazumi 2019, private communication) and may slightly differ from the definitive ones.

[1] See litebird.jp/eng.

[2] For CMB-S4 we also use specifications from the websites `https://www.nsf.gov/mps/ast/aaac/cmb_s4/report/CMBS4_final_report_NL.pdf` and `https://cmb-s4.org/wiki/index.php/Survey_Performance_Expectations`.

Following (Stompor et al., 2016) and (The Simons Observatory Collaboration et al., 2018), the instrumental noise model for a given experiment and a given frequency ν is

$$N_{\ell,\nu}^{XX} = \left[w_{X,\nu}^{-1} \exp\left(\ell(\ell+1) \frac{\theta_{FWHM,\nu}^2}{8 \log 2} \right) \right] \cdot \left[1 + \left(\frac{\ell}{\ell_{knee}} \right)^{\alpha_{knee}} \right], \quad (4.2)$$

where $w_{X,\nu}^{-1/2}$ is the sensitivity of the experiment (white noise level) in the frequency channel ν in μK-rad, $\theta_{FWHM,\nu}$ represents the beam size in radians and α_{knee} and ℓ_{knee} parametrize the $1/f$ noise contribution for each frequency channel. Moreover, we assume perfect polarization efficiency, so that $w_E^{-1/2} = w_B^{-1/2} = \sqrt{2} w_T^{-1/2}$.

Experiment	Frequency [GHz]	Sensitivity [μK-arcmin]	FWHM [arcmin]	ℓ_{knee}	α_{knee}
LiteBIRD ($f_{sky} = 0.6$; $\lambda = 0.8$)	40.0	36.1	69.2	n/a	n/a
	50.0	19.6	56.9		
	60.0	20.2	49.0		
	68.0	11.3	40.8		
	78.0	10.3	36.1		
	89.0	8.4	32.3		
	100.0	7.0	27.7		
	119.0	5.8	23.7		
	140.0	4.7	20.7		
	166.0	7.0	24.2		
	195.0	5.8	21.7		
	235.0	8.0	19.6		
	280.0	9.1	13.2		
	337.0	11.4	11.2		
	402.0	19.6	9.7		
SO (SATs) ($f_{sky} = 0.1$; $\lambda = 0.5$)	27.0	35.3	91.0	15	-2.4
	39.0	24.0	63.0	15	-2.4
	93.0	2.7	30.0	25	-2.6
	145.0	3.0	17.0	25	-3.0
	225.0	5.9	11.0	35	-3.0
	280.0	14.1	9.0	40	-3.0
CMBS-S4 ($f_{sky} = 0.03$; $\lambda = 0.1$)	20.0	14.0	11.0	200	-2.0
	30.0	8.7	76.6	50	-2.0
	40.0	8.2	57.5	50	-2.0
	85.0	1.6	27.0	50	-2.0
	95.0	1.3	24.2	50	-2.0
	145.0	2.0	15.9	65	-3.0
	155.0	2.0	14.8	65	-3.0
	220.0	5.2	10.7	65	-3.0
	270.0	7.1	8.5	65	-3.0

Table 4.1: Instrumental specifications for the LiteBIRD, SO and CMB-S4 experiments.

4.1.3 *Astrophysical and Instrumental Contributions to the Observed Power Spectrum*

In the following, we will use $C_\ell^{XX'}$ for the total observed power spectrum

$$C_\ell^{XX'} = C_\ell^{XX',prim} + C_\ell^{XX',noise} + \lambda C_\ell^{XX',lens} + C_\ell^{XX,fgs}\,, \tag{4.3}$$

where $C_\ell^{XX',prim}$ is the primordial angular power spectrum, $C_\ell^{XX',noise}$ is the contribution from instrumental noise (including the $1/f$ noise term and the noise degradation after component separation as we will define in Section 4.3.1), $\lambda C_\ell^{XX',lens}$ represents the lensing term and $C_\ell^{XX,fgs}$ is the residual contamination by polarized diffuse foregrounds, which will be described in detail in Section 4.3.

The contribution from gravitational lensing acts as a contaminant when estimating the primordial CMB power spectrum. This term can be modelled, thus removing the bias in the observed power spectrum. However, the associated cosmic variance will still limit the constraints, especially on B-modes. By performing the so-called delensing in the map-domain (Knox and Song, 2002; Kesden et al., 2002; Hu and Okamoto, 2002a; Smith et al., 2012) the lensing correction to the observed power spectrum and the associated cosmic variance can be suppressed. We model the result of this operation directly in the power spectrum domain, suppressing $C_\ell^{XX',lens}$ by a constant factor λ. $\lambda = 0$ means that the lensing contribution is completely removed and $\lambda = 1.0$ means that no delensing is performed. The effectiveness of delensing depends on the noise level and the resolution of of the experiment, we take $\lambda = 0.8$ for LiteBIRD (see Namikawa et al., 2016), $\lambda = 0.5$ for SO (The Simons Observatory Collaboration et al., 2018) and $\lambda = 0.1$ for CMB-S4 (see Abazajian et al., 2016). As for $C_\ell^{XX',prim}$, $C_\ell^{XX',lens}$ is evaluated with CAMB.

4.2 *Principal Component Analysis of the Tensor Power Spectrum*

In this section we briefly review the formalism of Fisher information matrix (Section 4.2.1) and the PCA (Section 4.2.2). We apply it to the tensor power spectrum and highlight the new aspects related to this context (Section 4.2.3).

4.2.1 *Fisher information matrix for tensor power spectrum*

In order to discretize the tensor power spectrum $\mathcal{P}_T$, following (Hu and Okamoto, 2004), we write

$$\mathcal{P}_T(k) = A_s \sum_i p_i W_i(\ln k)\,, \tag{4.4}$$

where W_i is the discretization window function, which we choose to be a triangle

$$W_i(\ln k) = \max\left(1 - \left|\frac{\ln k - \ln k_i}{\Delta \ln k}\right|, 0\right) , \tag{4.5}$$

and

$$\Delta \ln k = \ln k_{i+1} - \ln k_i \,, \tag{4.6}$$

is the discretization constant. In this discrete representation, the derivative of the $C_\ell^{XX'}$ with respect to the power spectrum parameters p_i becomes

$$D_{\ell i}^{XX'} = \left.\frac{\partial C_\ell^{XX'}}{\partial p_i}\right|_{\rm fid} = \frac{2\pi}{\ell(\ell+1)} A_s \int d\ln k \, T_\ell^X(k) \, T_\ell^{X'}(k) \, W_i(\ln k) \,. \tag{4.7}$$

We choose the k range $10^{-4} < k < 0.2\,\mathrm{Mpc}^{-1}$, which comfortably contain the scales to which the CMB power spectrum is sensitive to. The discretization scale is chosen to be $\Delta \ln k = 0.05$, sharper features are smeared out because of geometrical projection effects and lensing (Hu and Okamoto, 2004).

The Fisher information matrix for a Gaussian field on the sphere is (see, e.g., Tegmark, 1997)

$$F_{ij} = f_{sky} \sum_{\ell=2}^{\ell_{\rm max}} \frac{2\ell+1}{2} \mathrm{Tr}\left[\mathbf{D}_{\ell i} \mathbf{C}_\ell^{-1} \mathbf{D}_{j\ell} \mathbf{C}_\ell^{-1}\right] , \tag{4.8}$$

where we are approximating the loss of information due to the partial celestial coverage with a factor proportional to the covered sky fraction f_{sky}, $\mathbf{C}_\ell$ is the matrix

$$\mathbf{C}_\ell = \begin{pmatrix} C_\ell^{TT} & C_\ell^{TE} & 0 \\ C_\ell^{TE} & C_\ell^{EE} & 0 \\ 0 & 0 & C_\ell^{BB} \end{pmatrix} , \tag{4.9}$$

and $\mathbf{D}_{i\ell}$ is its derivative with respect to p_i.

As emphasized in (Hu and Okamoto, 2004), the lensing contribution $C_l^{XX',lens}$ contains the product between C_ℓ^{BB}, which depends on the primordial tensor power spectrum parameters, and $C_\ell^{\phi\phi}$. Therefore, when performing the derivatives with respect to the power spectrum parameters p_i in (4.7), we take into account this dependence. The lensing potential, instead, does not depend on the tensor power spectrum, so does not contribute to the $D_\ell^{XX'}$.

We address also the possible issue of degeneracies between the effect that the primordial power spectrum and the other cosmological parameters can have on the C_ℓs. In particular, following (Hu and Okamoto, 2004) and (Leach, 2006), the Fisher matrix $F_{\mu\nu}$ for both

power spectrum and cosmological parameters can be written as a block matrix

$$F_{\mu\nu} = \begin{pmatrix} F_{ij} & \mathbf{B} \\ \mathbf{B^T} & F_{ab} \end{pmatrix}, \tag{4.10}$$

where F_{ab} is the block for the cosmological parameters $\{A_s, n_S, \tau, \Omega_b h^2, \Omega_D h^2, H_0\}$, F_{ij} is the one for the power spectrum parameters and $\mathbf{B}$ contains the cross terms between power spectrum and cosmological parameters. We emphasize that r is not included in the cosmological parameters so that the primordial tensor power spectrum is entirely defined by the p_i coefficients in Eq. 4.8. We study the effect of the inclusion of r in Section 4.4.4. Inverting Eq. 4.10 we obtain the covariance matrix $C_{\mu\nu} = F^{-1}_{\mu\nu}$, whose upper diagonal block C_{ij} is the covariance matrix for the power spectrum parameters orthogonalized with respect to the cosmological parameters and the corresponding Fisher matrix would be $F^{orth}_{ij} = (C_{ij})^{-1}$. Performing a block-wise inversion of the matrix in Eq. 4.10 (see, e.g., Press et al., 1992) we get

$$F^{orth}_{ij} = F_{ij} - \mathbf{B}\, F^{-1}_{ab}\, \mathbf{B^T}, \tag{4.11}$$

where the first term is the original information content on the primordial power spectrum and the second term expresses the information loss due to the degeneracy with the cosmological parameters.

4.2.2 *Principal component analysis*

PCA (see e.g. Hu and Okamoto, 2004; Paykari and Jaffe, 2010; Munshi and Kilbinger, 2006) aims at identifying the uncorrelated variables and ranking them according to their uncertainty. In practice, since we assume the covariance matrix to be the inverse of the Fisher information, it consists in performing the singular-value decomposition

$$\mathbf{F} = \mathbf{S^T}\, \mathbf{E}\, \mathbf{S}, \tag{4.12}$$

where the rows of $\mathbf{S}$ are the eigenvectors of $\mathbf{F}$, $\mathbf{E} = diag(\mathbf{e})$ and e_i are the eigenvalues of $\mathbf{F}$ ordered from the largest to smallest. The PCA produces in this way a new set of parameters m_a – called PCA amplitudes – that are linear combinations of the original parameters p_i

$$\mathbf{m} = \mathbf{S}\, \mathbf{p}. \tag{4.13}$$

The covariance of these new parameters is $\mathbf{E}^{-1}$ and therefore they are uncorrelated and the uncertainty on their determination is given by

$$\sigma_a = e_a^{-1/2}, \tag{4.14}$$

where the first PCA amplitude m_1, corresponding to the largest eigenvalue, is the best-measured component, while the last PCA

amplitude m_n, corresponding to the smallest eigenvalue, is the worst-measured component. In summary, PCA finds a natural basis for the free parameters for a given experimental configuration and tells us the linear combinations of the original parameters that can be determined best.

Another goal of PCA is to compress the information. Suppose that we want to consider only a fixed number of linear combinations of the parameters, the first PCA amplitudes are the choice that retains the largest fraction of the total information. In many cases – which include ours – most of the information is retained in the first few PCA modes. We can determine the number of PCA modes that is worth keeping in our analysis by plotting the information fraction retained in first N modes (e.g. Figure 4.4), as we will describe in Section 4.4.

4.2.3 *PCA modes for model testing*

The $\mathcal{S}_a(k)$, with a lower then some N, can be used as a basis for the primordial tensor power spectrum. Of course, they span a subspace of all possible functions – the modes to which the given experimental configuration is sensitive to. This basis can be used to probe the detectability of specific theoretical models that predict features in the tensor power spectrum (see the introduction of this Chapter). We discuss here two approaches that we exploit and compare later in this Chapter.

We already have the Fisher uncertainty on the m_a coefficients from the construction of the PCA basis. Therefore, given a theoretical power spectrum $\mathcal{P}_{model}$, it is natural to forecast how detectable it is by first projecting it over the PCA modes

$$m_a = \int d\ln k\, \mathcal{S}_a(k)\mathcal{P}_{model}(k)\,, \tag{4.15}$$

and then evaluating the probability of getting a value higher than $\sum_{a=1}^{N}(m_a/\sigma_a)^2$ from a χ^2 distribution with N degrees of freedom. This significance forecast is both extremely fast and easy to perform because it neither involve any additional run of Boltzmann codes nor require any likelihood sampling. It is therefore particularly attractive for studying large sets of inflationary models and probing their parameters space.

This approach is essentially a Fisher estimation that has notable caveats. First, the uncertainties are lower bounds that are not guaranteed to be reached. Second, this formalism – including the way we constructed the PCA modes – is insensitive to the physicality prior $P_T > 0$: it is based on the curvature of the likelihood with respect to the PCA amplitudes but the likelihood is not differentiable around

$P_T = 0$. This is formally true also for r or each entry of the $\mathbf{p}$ vector, but the physicality prior translates into $r > 0$ and $p_i > 0$ and therefore their one-sided derivatives and curvatures are well defined.

Since this is not true for PCA amplitudes, we also consider another route to model testing. We modify the CosmoMC (Lewis and Bridle, 2002; Lewis, 2013) package for MCMC, redefining the tensor power spectrum (Leach, 2006) as

$$\mathcal{P}_T(k) = A_s \sum_{a=1}^{N} m_a \mathcal{S}_a(k)\,, \tag{4.16}$$

where the $\mathcal{S}_a$ are the same PCA modes defined in the previous approach. We then fit the full set of parameters $\{m_1,..., m_N, A_s, n_s, \tau, \Omega_b h^2, \Omega_D h^2, H_0\}$ to a given angular power spectrum assuming flat priors. Clearly, if the best fit is consistent with all the PCA amplitudes m_a being consistent with zero, no deviation from scale-invariance is detected. This approach can account for the full complexity of the posterior distribution and, in particular, the physicality prior $\mathcal{P}_T(k) > 0$.

As we anticipated in the introduction of this Chapter, several examples of theoretical models that predict features in tensor power spectrum have been studied in the literature. It is beyond the scope of this work to investigate specifically these scenarios since our focus is on the applicability and limitations of the PCA to express constraints on the tensor power spectrum. However, in Section 4.4.3, we apply this formalism to a toy-model of red-tilted spectrum.

4.3 *The role of diffuse astrophysical foregrounds*

In the estimation of the Fisher matrix we include the uncertainty due to the removal of diffuse foregrounds, in addition to the ones from instrumental noise, lensing and cosmic variance. This contribution has not been considered up to now in the PCA literature and in particular for the analysis concerning the tensor spectrum. However, it is well known that diffuse foregrounds are the predominant source of uncertainty on large scale B-mode polarization (see e.g. Planck Collaboration, 2018a, and reference therein). In this section we first explain how we model this uncertainty and then show that including foregrounds is necessary, especially when the experimental configuration provides access to the largest angular scales, including the reionization bump.

4.3.1 *Uncertainties from foreground cleaning*

Several emission mechanisms contribute to the diffuse foregrounds from our own Galaxy (see Dickinson, 2016, and references therein).

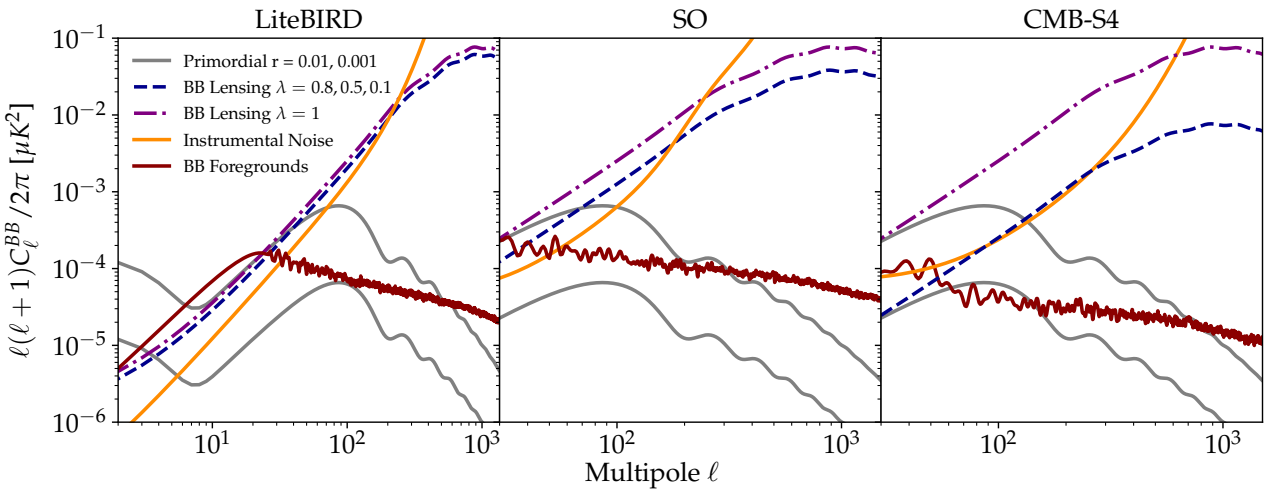

Figure 4.1: The power spectrum of foregrounds residuals for dust and synchrotron (solid red curve) and the post-component separation instrumental noise (solid orange curve) for the three experiments considered in this work, the lensing contribution $\lambda C_\ell^{XX',lens}$ with delensing factor $\lambda = 0.8$ for LiteBIRD, $\lambda = 0.5$ for SO and $\lambda = 0.1$ for CMB-S4 (dashed blue curve) and without delensing ($\lambda = 1$, dot-dashed purple curve). We also plot as a reference the primordial BB power spectrum $C_\ell^{BB,prim}$ for $r = 0.01$ (upper solid grey curve) and $r = 0.001$ (lower solid grey curve).

In our analysis we consider thermal dust and synchrotron radiation – respectively emitted by thermal emission of dust grains and cosmic ray electrons spiraling the Galactic magnetic field. They are most important contaminants to the CMB B-modes from CGB. We leave to a future work the inclusion of other contaminants of secondary importance, like spinning and magnetic dust (Draine and Lazarian, 1998; Draine and Hensley, 2013) and carbon monoxide (Greaves et al., 1999; Puglisi et al., 2017).

As we anticipated, we will exploit the publicly available code FGBuster which represents an implementation of parameter fitting in foreground estimation and removal for CMB experiments. We review here very briefly the corresponding formalism used for the computation of the uncertainties after component separation, which is based on the parametric maximum likelihood approach (Errard et al., 2011; Errard et al., 2016; Stompor et al., 2016, 2009), and is the basis of the FGBuster implementation. In the presence of multi-component emissions contributing to the signal measured on a given sky pixel p, we can write

$$\mathbf{d}_p = \mathbf{A}\mathbf{s}_p + \mathbf{n}_p, \tag{4.17}$$

where the data vector $\mathbf{d}_p$ contains the multi-frequency measurements for the sky pixel p, $\mathbf{s}_p$ is the multi-component sky signal vector (with each polarized sky component represented by an entry of the vector), $\mathbf{A}$ is the mixing matrix and $\mathbf{n}_p$ is the instrumental noise vector. The instrumental noise at each frequency is assumed known a priori to be Gaussian and uncorrelated, with variance matrix $\mathbf{N}_p$. The columns of the mixing matrix are the SEDs of the components. They are not completely determined a priori and can have free parameters – the

so-called spectral parameters β – that have to be determined from the frequency maps.

In our analysis we consider three components: CMB, thermal dust and synchrotron. We assume perfect calibration and therefore the CMB emission law has no free parameters and is constant in thermodynamic units. For the frequency dependence of the synchrotron emission, we assume its brightness temperature to be a curved power-law

$$\mathbf{A}_{sync}(\nu) = \left(\frac{\nu}{\nu_0}\right)^{\beta_s + C_s \log(\nu/\nu_0)} . \tag{4.18}$$

where ν_0 is the reference and pivot frequency of the synchrotron emission and is fixed at 70 GHz. The spectral index β_s and the curvature C_s are the free parameters. Note that, as of today, no evidence was found for the curvature (see Krachmalnicoff et al., 2018, and references therein). However, the experimental configurations that we consider will have a much higher sensitivity and therefore their results can be influenced by small departures from the standard power-law emission. For dust, we assume the standard modified black-body

$$\mathbf{A}_{dust}(\nu) = \left(\frac{\nu}{\nu_0}\right)^{\beta_d+1} \frac{e^{\frac{h\nu_0}{kT_d}} - 1}{e^{\frac{h\nu}{kT_d}} - 1}, \tag{4.19}$$

where in this case ν_0 is chosen equal to 353 GHz. β_d is the spectral index of the emissivity and T_d is the temperature of the grains, and they are both free parameters. In total, we have four free parameters. Their reference values (i.e. the "true" values that we assume in the forecast) are $\beta_s = -3.0$, $C_s = 0$, $\beta_d = 1.54$ and $T_d = 20$ K, which well represent current constraints and measurements (Planck Collaboration, 2018b).

The component separation process first estimates the non-linear parameters and then uses the estimated mixing matrix to separate CMB and foregrounds through a linear combination of the frequency maps. These two steps are shared by many component separation approaches, we refer to Stompor et al. (2009) for more details on the specific procedure that we consider. We can identify two contributions to the uncertainty of the estimated CMB map, both sourced by the instrumental noise. In the first step, the statistical uncertainty in the determination of the spectral parameters and the consequent imperfect estimation of the emission laws causes a leakage of foreground power into the CMB map – the so-called *statistical foreground residuals*. Even if the mixing matrix were perfectly recovered, in the second step the noise in the frequency maps propagates to the component maps and is referred to as *statistical noise*. These uncertainty terms add extra power to the CMB map. We forecast these

contributions following (Errard et al., 2011).

In order to estimate the statistical foregrounds residuals we first evaluate the statistical uncertainty on the spectral parameters as the inverse of their Fisher information

$$\mathbf{\Sigma}^{-1} \simeq -\mathrm{tr}\left\{\left[\frac{\partial \mathbf{A}^T}{\partial\beta}\mathbf{N}^{-1}\mathbf{A}(\mathbf{A}^T\mathbf{N}^{-1}\mathbf{A})^{-1}\mathbf{A}^T\mathbf{N}^{-1}\frac{\partial \mathbf{A}}{\partial\beta'} - \frac{\partial \mathbf{A}^T}{\partial\beta}\mathbf{N}^{-1}\frac{\partial \mathbf{A}}{\partial\beta'}\right]\sum_p \mathbf{s}_p\mathbf{s}_p^T\right\}. \tag{4.20}$$

The power spectrum of the foreground residuals is equal to

$$C_\ell^{fgs} \equiv \sum_{k,k'}\sum_{j,j'}\mathbf{\Sigma}_{kk'}\alpha_k^{0j}\alpha_{k'}^{0j'}C_\ell^{jj'}, \tag{4.21}$$

where

$$\alpha_k^{0j} \equiv -\left[(\mathbf{A}^T\mathbf{N}^{-1}\mathbf{A})^{-1}\mathbf{A}^T\mathbf{N}^{-1}\frac{\partial \mathbf{A}}{\partial\beta_k}\right]_{0j}, \tag{4.22}$$

and j and j' run over dust and synchrotron and o is the component-index of the CMB.

This estimation assumes spatially-constant spectral parameters, which is probably a too stringent assumption given the high sensitivity of the experimental configurations we consider. Therefore we suppose to fit the spectral parameters independently over patches equal to HEALPix pixels with resolution parameter $N_{side} = 8$, corresponding to an extension of about 7 degrees in the sky. The adopted value reflects the current knowledge concerning the typical angular scale of spatial variation of foreground spectral parameters (Planck Collaboration, 2018b), currently implemented in foreground models (Thorne et al., 2017). The number of patches is $n_{patch} = [12 \times f_{sky} \times N_{side}^2]$ and, assuming statistical isotropy of the foregrounds, this factor rescales upwards $\mathbf{\Sigma}$ and, consequently, C_ℓ^{fgs}. This estimation follows Errard et al. (2016) and works on scales smaller than the patch size, $\ell_{patch} \simeq 25$. On larger scales the foregrounds residuals have the shape of a white spectrum because the noise and, consequently, the foregrounds residuals in each patch are uncorrelated (see Errard and Stompor, 2018, for more details). For simplicity, we take these large scales foreground residuals to be constant and equal to the statistical residuals around $\ell = \ell_{patch}$.

As far as the statistical noise is concerned, we follow (Stompor et al., 2016) and estimate it as

$$C_\ell^{XX',noise} \equiv \left[\left(\mathbf{A}^T\left(\mathbf{N}_\ell^{XX'}\right)^{-1}\mathbf{A}\right)^{-1}\right]_{CMB\ CMB}, \tag{4.23}$$

where $\mathbf{N}_\ell^{XX'} \equiv \left(N_\ell^{XX'}\right)^{\nu\nu'} \equiv N_{\ell,\nu}^{XX'}\delta_\nu^{\nu'}$ is a matrix containing the instrumental noise for each frequency channel as we anticipated

in Eq. 5.9. Note that the term $N_{\ell,\nu}^{XX'}$ is diagonal in X, X', since the instrumental noise is uncorrelated in T, E and B.

The statistical residuals and the noise after component separation are output by FGBuster, which contains the forecast tool xForecast (Stompor et al., 2016) and relies on PySM (Thorne et al., 2017) for the simulation of the foreground emission.

We report the foreground residuals and the noise after component separation for LiteBIRD, SO and CMB-S4 in Figure 4.1. Already at this stage, we can see that the inclusion of the foreground residuals is always relevant for scales larger than a degree and is particularly important at the scales accessible from space.

4.3.2 *Impact of foreground residuals on PCA*

In order to evaluate the impact of foreground residuals, we compare the uncertainties σ_r on the tensor-to-scalar ratio obtained from the Fisher matrix F_{ab} for the cosmological parameters (Section 4.2.1) with and without the addition of foregrounds. As we can see from the values reported in Table 4.2 for the three considered experimental configurations and three values of r, a proper inclusion of the uncertainty coming from the foregrounds is most important for the LiteBIRD configuration, with an increase in σ_r by about a factor ~ 4 (assuming $r = 0$). The SO configuration is the least affected by foregrounds, being dominated by the instrumental noise contribution, with σ_r growing by a factor between 1.25 and 1.44, depending on the value of r we are assuming. CMB-S4 shows a definitely significant increase between, with the uncertainty on r taking a factor ranging between 1.25 and 2.3.

Experiment	r	σ_r	$\sigma_{r,NOFG}$	Ratio
LiteBIRD	$r = 0$	2.7×10^{-4}	6.6×10^{-5}	4.1
	$r = 0.001$	4.0×10^{-4}	2.0×10^{-4}	2.0
	$r = 0.01$	6.0×10^{-4}	4.4×10^{-4}	1.36
SO	$r = 0$	8.2×10^{-4}	5.7×10^{-4}	1.44
	$r = 0.001$	8.6×10^{-4}	6.2×10^{-4}	1.39
	$r = 0.01$	1.3×10^{-3}	1.04×10^{-3}	1.25
CMB-S4	$r = 0$	4.6×10^{-4}	2.0×10^{-4}	2.3
	$r = 0.001$	5.4×10^{-4}	3.0×10^{-4}	1.8
	$r = 0.01$	1.2×10^{-3}	9.6×10^{-4}	1.25

Table 4.2: Comparison between uncertainty on tensor-to-scalar ratio r from Fisher matrix including (σ_r) or not including ($\sigma_{r,NOFG}$) foregrounds residuals into the analysis, for three experimental configurations and three values of r. The ratio of the uncertainties on r before and after the inclusion of foregrounds is also shown.

On the basis of these evidences, we proceed by addressing the variation in the properties of PCA modes with and without foregrounds. We apply the formalism developed in Section 4.2 for deriving the PCA modes $S_a(k)$ and we restrict here to the LiteBIRD case with $r = 0$. The results are shown in Figure 4.2. For reasons which will be

explained in the next Section, the $S_a(k)$ are obtained in this case by orthogonalizing with respect to all cosmological parameters except r. Consequently, the non-oscillatory modes, typically among the first ones, catch the overall power of tensor modes and play the effective role of the parameter r itself.

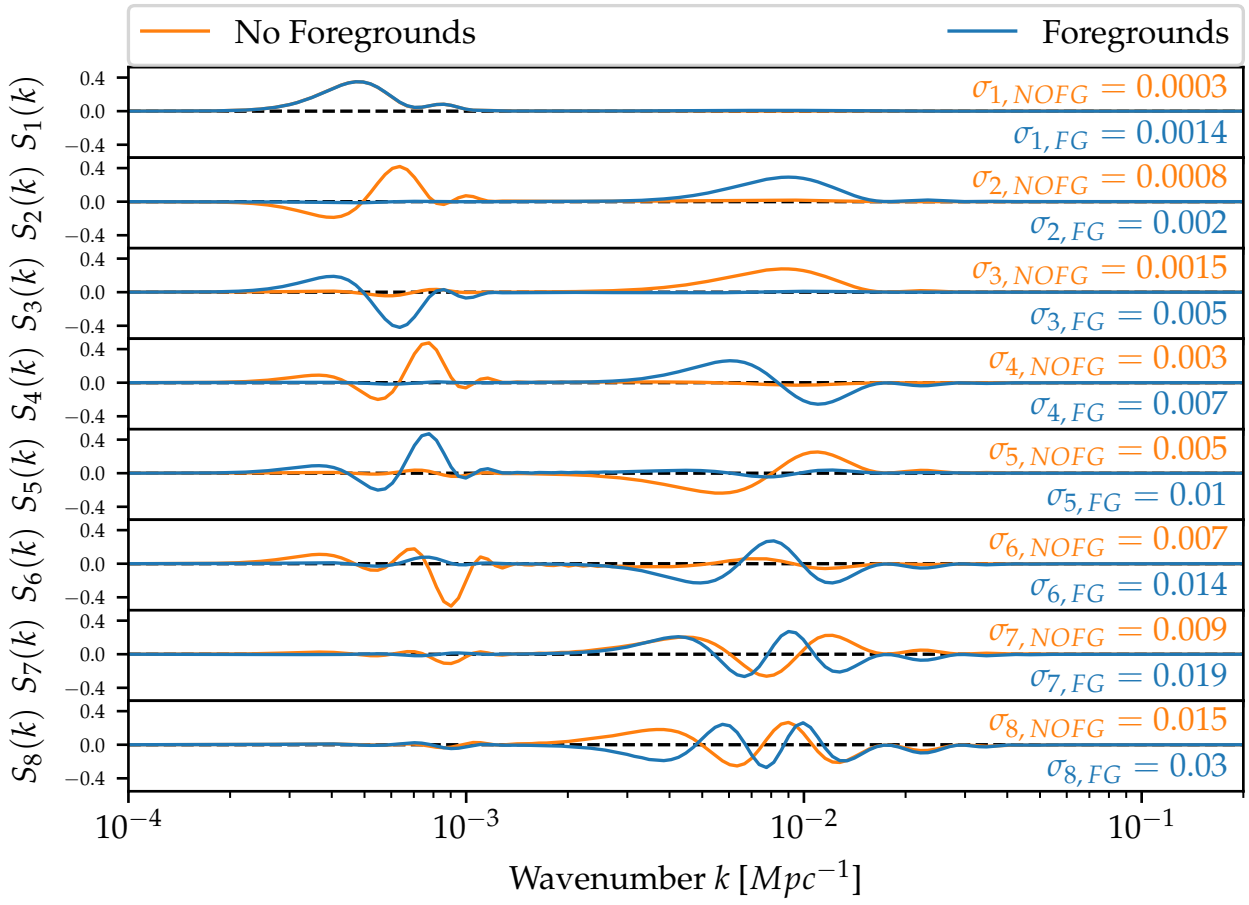

Figure 4.2: A comparison between the first eight PCA modes, obtained with LiteBIRD specifications, assuming $r = 0$ and delensing factor $\lambda = 0.8$, with (solid blue curve) and without (solid orange curve) the foregrounds residuals. The errors on the modes with (indicated as $\sigma_{a,FG}$ in blue) and without ($\sigma_{a,NOFG}$ in orange) foregrounds are also reported. Note that our results will based on the modes *with* foregrounds.

Both with and without foregrounds, we see two different positive modes that pick up power around $k \approx 6 \times 10^{-4}\text{Mpc}^{-1}$ and $k \approx 6 \times 10^{-3}\text{Mpc}^{-1}$, respectively. These are the scales contributing to the reionization and recombination bump (Hiramatsu et al., 2018). The other modes present oscillatory patterns with characteristic oscillation scales getting shorter and shorter as n increases, meaning that the experimental setup provides weaker constraints on smaller features of the primordial power spectrum. The presence of foregrounds has visible and non-negligible effects on all the PCA modes and their eigenvalues. While the positive mode related to the reionization bump is the best constrained mode both with and

without foregrounds, the one related to the recombination bump is upgraded from third to second mode when foregrounds residuals are considered, overtaking the first oscillatory pattern around $k \approx 6 \times 10^{-4}\mathrm{Mpc}^{-1}$. Note that the constraints on both modes are degraded, but the effect is more important for the latter since foreground residuals are the dominant uncertainty for the reionization peak, while they are lower than lensing and noise for the recombination peak. A closer look at the errors associated to each mode (also reported in Figure 4.2) shows how foregrounds lead to a dramatic loss of information on the reionization bump. This information is indeed carried by the foregrounds-free modes $\mathcal{S}_{1,NOFG}$ and $\mathcal{S}_{2,NOFG}$ – which corresponds to the modes $\mathcal{S}_{1,FG}$ and $\mathcal{S}_{3,FG}$. Their uncertainty grows by a factor ~ 5 (from $\sigma_{1,NOFG} = 0.0003$ to $\sigma_{1,FG} = 0.0014$) and by a factor ~ 6 (from $\sigma_{2,NOFG} = 0.0008$ to $\sigma_{3,FG} = 0.005$). In comparison, the information loss on the recombination bump is restrained: the constraint on the foreground-free mode $\mathcal{S}_{3,NOFG}$ – which corresponds to $\mathcal{S}_{2,FG}$ and carries most of the information on the recombination bump – is just $\sim 30\%$ smaller ($\sigma_{3,NOFG} = 0.0015$ instead of $\sigma_{2,FG} = 0.002$). Note that shifts of relative importance when foregrounds are introduced are also present in the other modes (see Figure 4.2) and, in all the cases, the uncertainties σ_a associated to each PCA mode S_a increase. The SO and CMB-S4 configurations do not get constraints from the reionization bump, and therefore the shape and relative importance of the PCA modes do not change when foregrounds are introduced. However, as in the LiteBIRD case, their constraints on all the modes are reduced. In the CMB-S4 case the effect of foregrounds is certainly non-negligible, with the uncertainties on the first two modes taking a factor 2.5 and 2, respectively. Concerning SO, since the instrumental noise is higher, the presence of foreground residuals is less important but still noticeable, with enhancements by a factor 1.36 on $\mathcal{S}_1$ and 1.18 on $\mathcal{S}_2$.

We conclude that the contribution of the foreground residuals definitely cannot be neglected in a PCA analysis of the primordial tensor perturbations in the context of *B*-mode experiments. The inclusion of foregrounds will therefore be the baseline for our analysis in the prosecution of this work.

4.4 *Constraining primordial tensor perturbations with PCA*

We now discuss the application of the PCA formalism described in Sections 4.2 and 4.3 to the experimental configurations we consider. As emphasized before, the application to the tensor power spectrum needs some special cares compared to the scalar power spectrum case. The reason is that in the former case the PCA basis

does not describe small deviations of a large, well constrained power spectrum. One of the most important consequences is that, if some power from primordial gravitational waves is found in the B-modes power spectrum, the relative constraints on the PCA amplitudes can be very different from the ones predicted by the PCA analysis itself (i.e. $\sigma_i < \sigma_j$ for $i < j$). In other words, the information in a power spectrum with a power contribution from tensors can be very different from the information matrix that defined the PCA basis. This is potentially problematic because the extent of the tensor contribution is not known a priori but the number of modes retained is fixed to N from the onset, discarding the information lying outside the space spanned by $\{\mathcal{S}_a \mathcal{S}_a^T\}_{a<N}$. In the scalar case we just have to choose a sufficiently high N to capture most of the Fisher information from which the $\mathcal{S}_a$ themselves where defined. In the tensor case we have to test the stability of this property with respect to a range of possible Fisher information matrices $\mathbf{F}_r$, arising from angular power spectra different from the one used for the definition of the $\mathcal{S}_a$ basis (which assumes no tensors). We can think of the sum of the eigenvalues of $\mathbf{F_r}$ as the total information about the primordial tensor power spectrum. It can be computed as $tr(\mathbf{F_r})$, without performing a Singular Value Decomposition (SVD). The Fisher information on the first N m_a coefficients, on the contrary, is equal to $\mathbf{S}_N^T \mathbf{F}_r \mathbf{S}_N$, where the matrix $\mathbf{S}_N$ contains the first N columns of $\mathbf{S}$. Therefore, when we describe the power spectrum only in terms of the first N $\mathcal{S}_a$ modes, the fraction of the total information we retain is given by

$$I(r, N) = \frac{tr\left(\mathbf{S}_N^T \mathbf{F}_r \mathbf{S}_N\right)}{tr\left(\mathbf{F}_r\right)}. \tag{4.24}$$

For $r = 0$, our parametrization of the tensor power spectrum is by construction the one that guarantees the maximum I for any value of N. For $r \neq 0$ this is no longer true, but a value of I sufficiently high means that the parametrization still capture (approximately) all of the information that our data can provide. We choose N such that I is high enough (98%) up to $r < 0.01$. Once N is fixed, the Fisher uncertainties associated with the i-th PCA mode in our basis are given by

$$\sigma_i^2 = \left(\mathbf{S}_N^T \mathbf{F}_r \mathbf{S}_N\right)^{-1}_{ii}, \tag{4.25}$$

Note that for $r \neq 0$ it is no longer guaranteed that $\sigma_i < \sigma_j$ for $i < j$ and that m_i and m_j are uncorrelated for $i \neq j$. After studying the I function and choosing the appropriate value of N, we study the PCA products for three observed CMB power spectra, computed for a scale invariant primordial power spectrum with $r = 0$, 0.01 and 0.001.

4.4.1 *Application to LiteBIRD*

The Fisher matrix for $r = 0$, which we use to define the PCA basis, is shown in Figure 4.3 and its first eigenvectors are the blue functions reported in Figure 4.2. We can recognize in the matrix the features that we highlighted in Section 4.3.2, when discussing the functions. Most of the information is concentrated in two regions, precisely the scales that contribute the most to the recombination and the reionization bumps, in accord with (Hiramatsu et al., 2018). The strong off-diagonal correlations express the fact that we are chiefly sensitive to the overall power in those regions, while we have much less information about features within them.

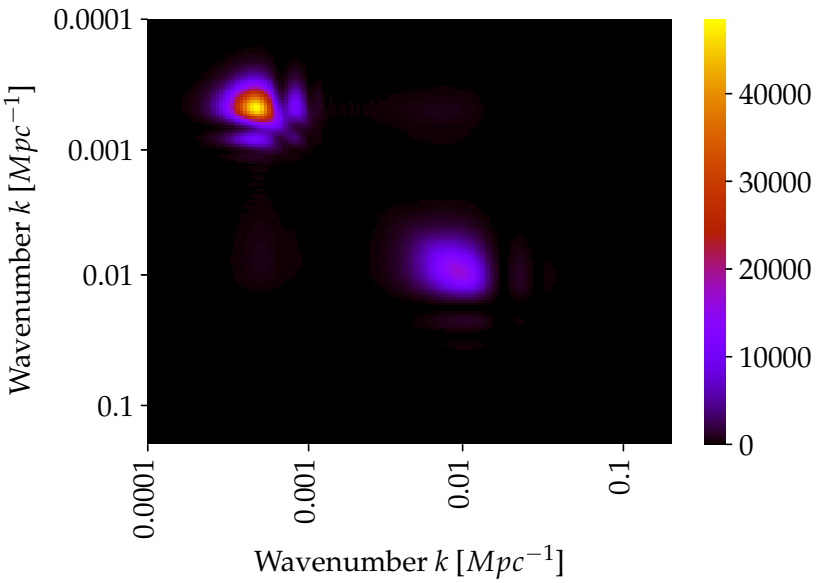

Figure 4.3: Fisher matrix for LiteBIRD, for $r = 0$ and delensing factor $\lambda = 0.8$. The color bar gives the value of the elements of the matrix, with higher value representing more information.

Figure 4.4 shows the evaluation of I over a grid of values of r and N. Considering that r axis is log-scaled, the level curves are quite vertical, meaning that the PCA basis defined for $r = 0$ is effective in capturing the information in an observation with a very different primordial power spectrum. While for $r = 0$ we need five modes in order to capture 98% of the information, we only need three more modes when $r = 0.01$. For LiteBIRD we indeed set N = 8.

In Table 4.3 we compare the uncertainties and the signal-to-noise ratio $S/N = (m_a^2/\sigma_a^2)^{1/2}$ associated to each of the modes retained for three values of r . We can see from this table that the values of σ_a for the case $r = 0$ are monotonically increasing – as expected – but those of the $r \neq 0$ cases are not. In particular, in these latter cases the second mode has smaller uncertainty than the first one. Reminding

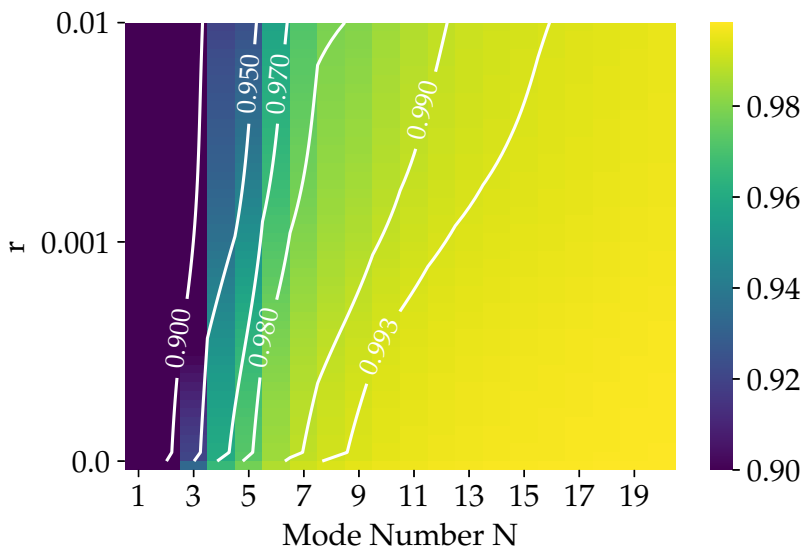

Figure 4.4: Information fraction $I(r, N)$ (Eq. 4.24) as a function of r and number of modes retained in the analysis N, using the LiteBIRD experimental configuration. The level curves of constant $I(r, N)$ for 90%, 95%, 97%, 99% and 99.3% are reported in white. To obtain this plot we generated Fisher matrices $\mathbf{F}_r$ for 50 logarithmically spaced values of r between 0.0001 and 0.01 plus the value $r = 0$.

the shape of these modes, we see that this means that as r is different from zero, we get more information from the recombination bump than from the reionization bump. This trend is also reflected in the associated S/N ratio, which is greater in the second mode than in the first for both $r = 0.001$ and $r = 0.01$. Moreover, the S/N ratio suggests that only the second mode, for both $r \neq 0$ cases, can be detected. However, one should not interpret this as a limit of PCA, but as a product of the fact that we are performing PCA over a signal simulated with a flat tensor power spectrum characterized only by its tensor-to-scalar ratio, while PCA is designed to describe power spectra with more features. We refer to Section 4.4.3 for a toy example of early universe model where the application of the PCA is more suited.

Even if we do not report the results in detail, we have also run the case with no delensing ($\lambda = 1.0$ instead of $\lambda = 0.8$) and, as expected, we see that delensing also contributes in shifting the relative importance in terms of information, from the reionization to the recombination bump.

4.4.2 *Application to SO and CMB-S4*

We now focus on the two ground based experiments, SO and CMB-S4. We consider them together because the results are similar, as we shall see. To start with, the Fisher matrices for the two configurations (shown in Figures 4.7 and 4.8) have essentially the same structure. By comparing with the LiteBIRD case (Figure 4.3) we observe that SO

Experiment	PCA mode	$r = 0$	$r = 0.001$		$r = 0.01$	
			σ_a	S/N	σ_a	S/N
LiteBIRD	1st	0.0014	0.005	1.0	0.03	2.0
	2nd	0.002	0.002	3.0	0.003	16.0
	3rd	0.005	0.01	0.09	0.06	0.14
	4th	0.007	0.007	0.13	0.009	1.02
	5th	0.01	0.019	0.14	0.09	0.3
	6th	0.014	0.014	0.17	0.02	1.2
	7th	0.019	0.019	0.02	0.02	0.2
	8th	0.03	0.03	0.08	0.04	0.6
SO	1st	0.004	0.004	1.2	0.006	8.0
	2nd	0.01	0.01	0.08	0.014	0.6
	3rd	0.019	0.019	0.14	0.03	0.9
	4th	0.03	0.03	0.006	0.04	0.05
CMB-S4	1st	0.002	0.002	2.2	0.005	9.0
	2nd	0.006	0.006	0.09	0.014	0.4
	3rd	0.01	0.01	0.3	0.02	1.4
	4th	0.014	0.019	0.005	0.03	0.03
	5th	0.02	0.02	0.14	0.04	0.7
	6th	0.03	0.03	0.04	0.05	0.2

Table 4.3: Comparison between the uncertainties from Fisher analysis for the three values of r and the three experiments considered in this work. The signal-to-noise ratio (S/N) for the two cases $r = 0.001$ and $r = 0.01$ is also reported.

and CMB-S4 are not sensitive to the scales that could be probed with the reionization bump. On the other hand, the higher resolution and delensing capability give access to some information beyond the first acoustic peak. These features are visible also in the PCA modes, as we can see in Figure 4.9.

In order to choose N and make sure that we can use our PCA basis also for observed spectra that have power in the primordial tensor power spectrum, we study $I(r, N)$. This check is passed, as Figures 4.5 and 4.6 show that the dependence on r is even weaker than in the LiteBIRD case. We therefore need fewer modes to capture 98% of the information in the whole r range and use $N = 6$ for CMB-S4 and $N = 4$ for SO. Note that the two configurations have similar I for $r = 0$ but differ for higher values of r, with the SO case being essentially r-independent. The reason is that SO has a higher noise than CMB-S4 and consequently it needs a higher signal with respect to the latter experiment to produce changes in the Fisher matrix.

The uncertainties on the PCA modes obtained for both experiments and the three different values of r are reported in Table 4.3, together with the associated S/N ratio. Thanks to the higher sensitivity, the uncertainties of CMB-S4 are essentially always half of those SO. Beyond this difference they share the same qualitative behaviour. Notably, their uncertainty in the $r = 0.001$ case essentially coincide

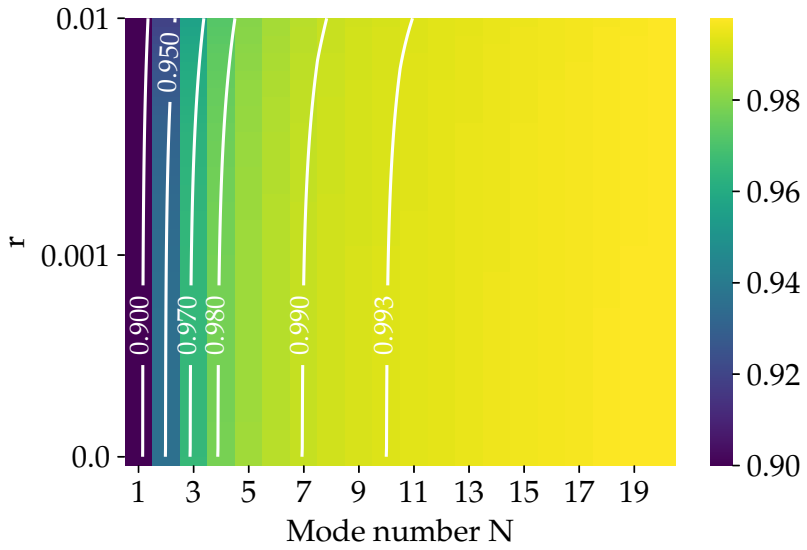

Figure 4.5: Information fraction $I(r, N)$ (Eq. 4.24) as a function of r and number of modes retained in the analysis N, using the SO experimental configurations.

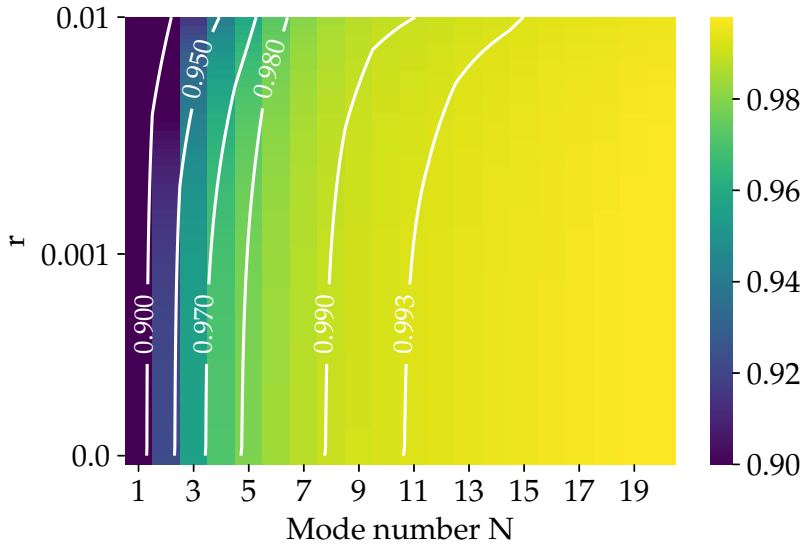

Figure 4.6: Information fraction $I(r, N)$ (Eq. 4.24) as a function of r and number of modes retained in the analysis N, using the CMB-S4 experimental configurations.

with $r = 0$.

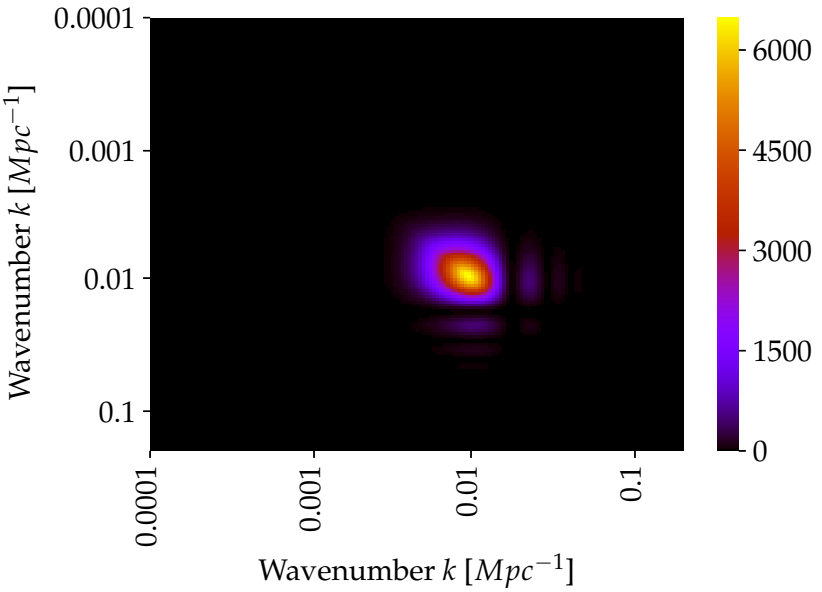

Figure 4.7: Fisher matrix for SO with $r = 0$. The color bar gives the value of the elements of the matrix.

4.4.3 *Example of application: tilted spectra from inflation*

As we discussed in Section 4.2.3, PCA can be used to detect deviation of the tensor power spectrum with respect to the fiducial case. In this section we show a very basic application of the PCA method, by applying it to data simulated using a red-tilted model of the tensor power spectrum and to the inflationary consistency relation.

Red-tilted model

We consider a model parametrized as $\mathcal{P}_T(k) = A_T(k/k_0)^{n_{T1}}$ on scales $k < k_1$ and $\mathcal{P}_T(k) = A_T$ on scales $k \geq k_1$, with $(k_1 = 0.001\ \text{Mpc}^{-1}, n_{T1} = -1)$ (Figure 4.11). This simple model has been considered also in (Hiramatsu et al., 2018) and (Farhang and Vafaei Sadr, 2018), because of its resemblance with the tensor power spectrum predicted by open inflation associated with bubble nucleation (Yamauchi et al., 2011). However, we warn the reader that our choice of the model and the parameters (k_1, n_{T1}) is not motivated by fundamental physics and is only an example of exploitation of the PCA. We leave the study of tensor power spectra from specific early universe physics to a future work. In this example we construct the PCA modes assuming the fiducial cosmology with $r = 0$ and the specifications of the LiteBIRD satellite, while the data used as input

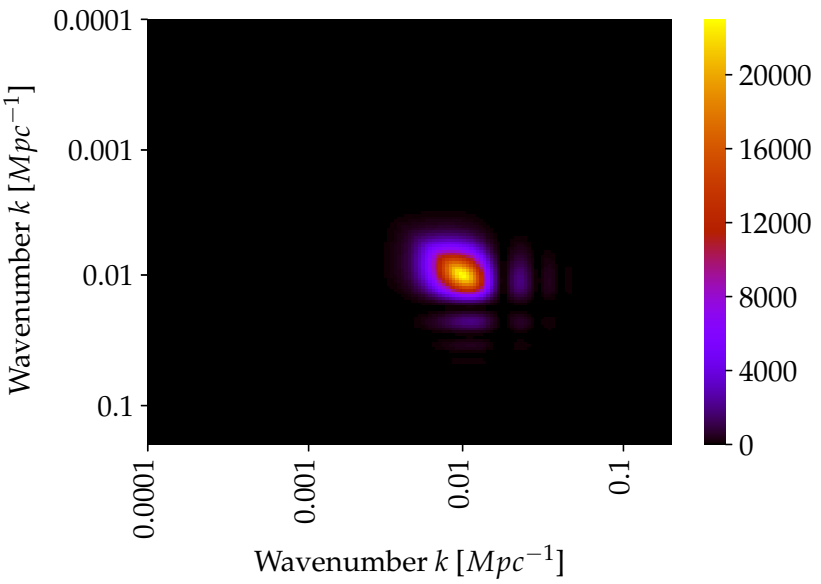

Figure 4.8: Fisher matrix for CMB-S4 with $r = 0$. The color bar gives the value of the elements of the matrix.

for the MCMC are simulated assuming the red-tilted tensor power spectrum described above with $r = 0.01$. The PCA amplitudes recovered from the MCMC for this red-tilted model are reported in Figure 4.10, and are clearly consistent with projected ones (solid orange curve), showing a characteristic trend not compatible with the fiducial scale-invariant spectrum (solid blue curve). Also the cosmological parameters are very well recovered and compatible with the input ones, therefore this application represents a success for PCA. We also compute a chi-square from the ratio of likelihoods for this red-tilted model and the fiducial scale-invariant model with $r = 0.01$, obtaining $\chi^2 \sim 8$. This value can be compared to the value $\chi^2 \sim 20$ reported in Table 3 of (Hiramatsu et al., 2018) for the same power spectrum model and a similar experimental configuration which, however, does not include foregrounds. The difference between the two values is indeed due to the addition of foregrounds, since the red-tilted model starts to differ from a scale-invariant model with $r = 0.01$ around the reionization bump scales, and, as we explained in Section 4.3.2, the constraints on these scales are strongly affected by the presence of foregrounds.

Testing inflationary consistency relation

The consistency relation, namely $n_T = -r/8$ (Planck Collaboration, 2018c), is a standard prediction of canonical single-field inflation (see Section 1.8), and its confirmation, given a detection of primordial

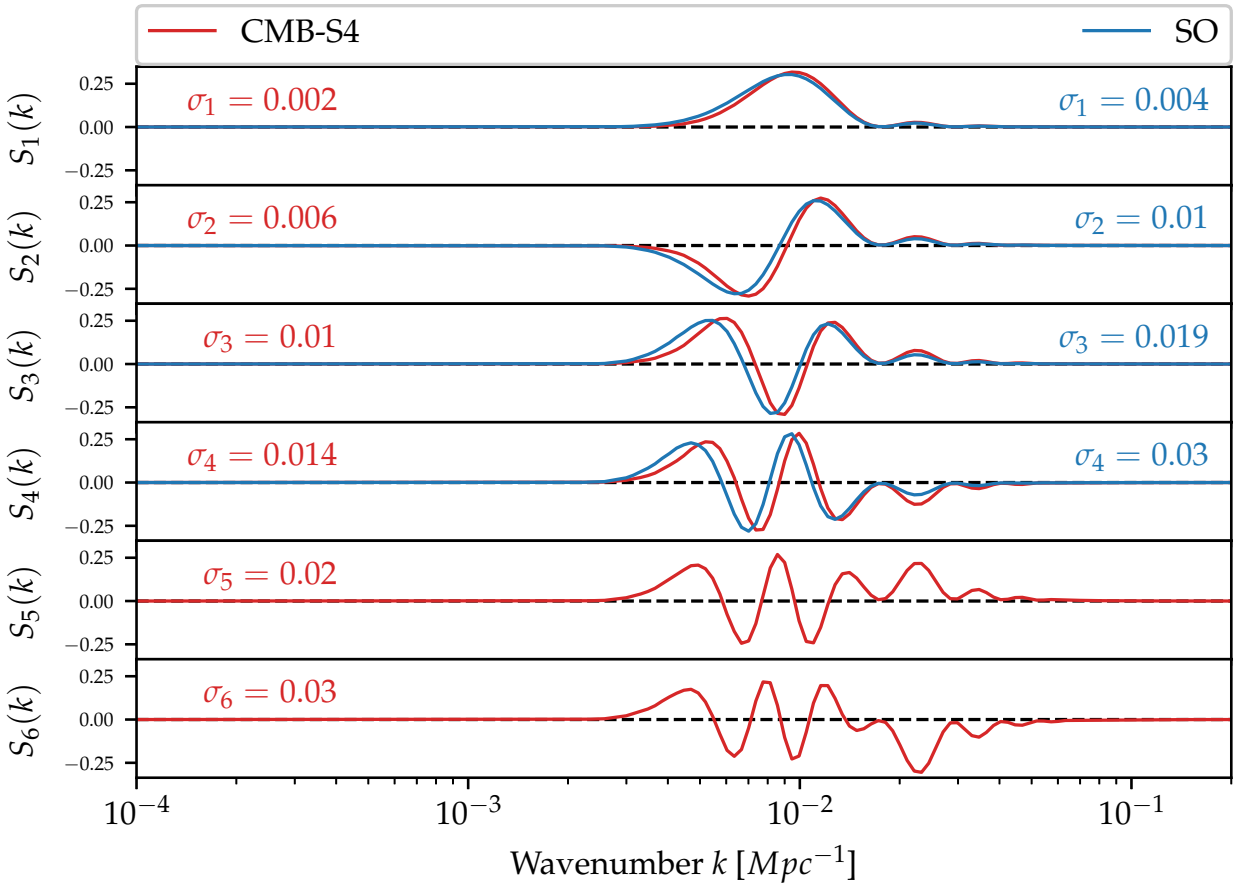

Figure 4.9: First four PCA modes for the SO (solid blue line) and first six for the CMB-S4 (solid red line) experiments with $r = 0$. We also report the uncertainties on each mode for CMB-S4 (on the left) and for SO (on the right).

gravitational waves, would be of paramount importance to determine the source of such signal. In order to test this relation, we use the PCA basis of Section 4.4.1 for LiteBIRD and the one of Section 4.4.2 for the CMB-S4 experiment, and then we project two models according to eq. (4.15), in which we assume the consistency relation (one with $r = 0.05$ and one with $r = 0.01$), on the PCA basis. We compare then the projected amplitudes of the models with $n_T = -r/8$ to the ones with $n_T = 0$, to see if the given experiment will be able to distinguish the tilt due to the consistency relation from a scale-invariant model with the same r. Unfortunately, we find that these two models are indistinguishable for LiteBIRD and CMB-S4 in both the $r = 0.05$ and $r = 0.01$ cosmologies, given that the errors σ_a on the projected amplitudes m_a are about two orders of magnitude larger than the effect of the consistency relation on a scale-invariant spectrum in the case $r = 0.01$ and about one or two orders of magnitude (depending on the specific mode) in the case $r = 0.05$ for both experiments.[3]

[3] This is in agreement with the results presented in (Abazajian et al., 2016) for CMB-S4.

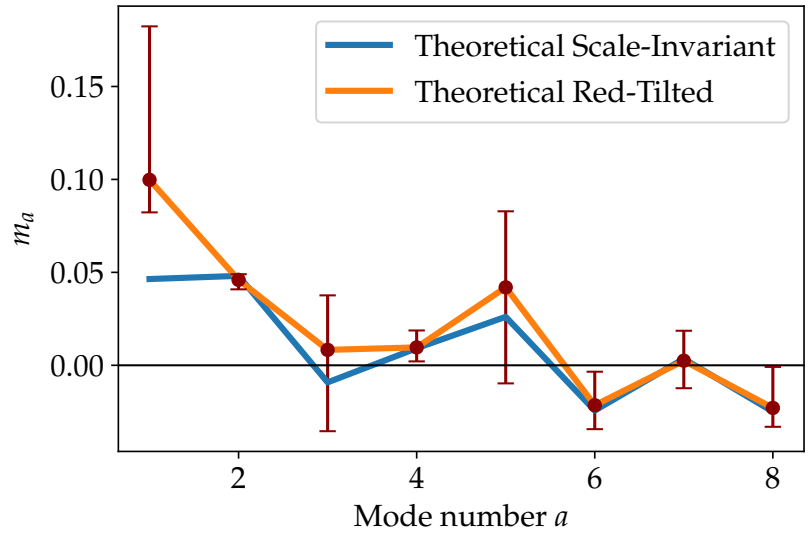

Figure 4.10: The red points represent the PCA amplitudes m_a obtained from the MCMC for the red-tilted model as a function of the mode number a, with error bars obtained from the MCMC. In orange, the theoretical red-tilted tensor power spectrum model projected onto the PCA basis through formula (4.15), in blue the theoretical scale-invariant power spectrum obtained via the same formula.

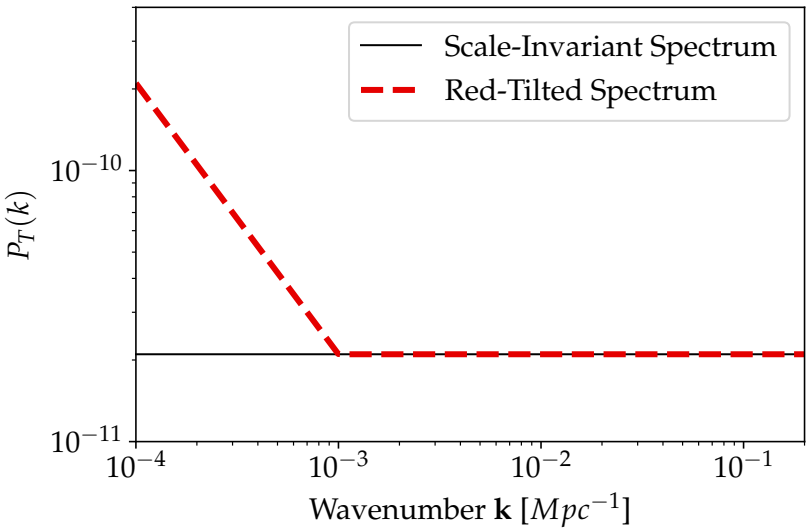

Figure 4.11: The red-tilted tensor power spectrum described in Section 4.4.3 (dashed red curve) and the scale-invariant power spectrum A_T for $r = 0.01$ (solid black line).

However, we will explore the possibility of extending this analysis in Section 5.5.3, exploiting the lever provided by space laser interferometers to test the consistency relation.

4.4.4 *Limitations of the PCA and MCMCs*

The PCA methodology we used to forecast the constraints on $\mathcal{P}_T$ is insensitive to the physicality prior $\mathcal{P}_T > 0$. In this section we discuss in detail the importance of such a prior and how it can jeopardize the validity of these Fisher estimates. While doing that, we also justify our choice of parametrizing $\mathcal{P}_T$ only as a linear combination of PCA modes, without including the popular cosmological parameter r. We indeed show that this parametrization makes the Fisher analysis marginally more robust against the physicality prior.

To start with, let us highlight briefly the consequences of including r in the parametrization of $\mathcal{P}_T$ (and in the set of cosmological parameters against which we orthogonalize the PCA modes). Clearly, we can equivalently impose that in our tensor power spectrum basis $\{\mathcal{S}_a\}$ we have $\mathcal{S}_1 = (1, ..., 1)$, so that m_1 is effectively r and the associated uncertainty is σ_r (we refer to this choice as the *basis with the constant mode* and contrast it with our *standard basis* described in Sections 4.4.1 and 4.4.2). The $\mathcal{S}_a$ functions for $a > 1$ are still PCA modes, but the orthogonality with $\mathcal{S}_1$ changes their shape. Most notably, $\mathcal{S}_1$ can be the only positive definite mode, forcing all the others to be oscillatory – as can be seen in Figure 4.12 for the LiteBIRD configuration[4]. Note also that, in this constant mode basis, the tensor spectrum used to build the PCA basis has the same value of r for which the basis is going to be used.

[4] Incidentally, we note that the orthogonalization with respect to the other six cosmological parameters $\{A_s, n_s, \tau, \Omega_b h^2, \Omega_D h^2, H_0\}$ has no effect either on the shapes or the uncertainties of the modes. The reason is that most of the information about the modes come from the BB angular power spectrum, while the one about the six ΛCDM parameters come from TT, EE and TE.

We now discuss a first visual argument showing that the Fisher estimates are very often inconsistent with the physicality prior. We run the Fisher analysis on the LiteBIRD configuration using the basis with the constant mode and two input angular power spectra, generated with $r = 0.01$ and $r = 0.001$. Assuming that the σ_a we obtain are correct, we plot in Figure 4.13 and 4.14 the 2σ range in which the modes are statistically expected to oscillate in 95% of the cases. When $r = 0.01$, for the modes up to $\mathcal{S}_4$ this range does not intersect the physicality prior. For the other modes, the intersection means that the Fisher estimate is unrealistic, as it predicts an oscillation larger than what is allowed by the physicality prior. The case $r = 0.001$, due to the lower S/N, is even more affected by the prior (Figure 4.14): the 2σ-contours intersect the negative region for all the modes beyond r.

Second, we now run actual MCMC to estimate $\{m_a\}$ and the other cosmological parameters. We consider input power spectra generated with $r = 0.01$ and $r = 0.001$, all the three experimental configurations

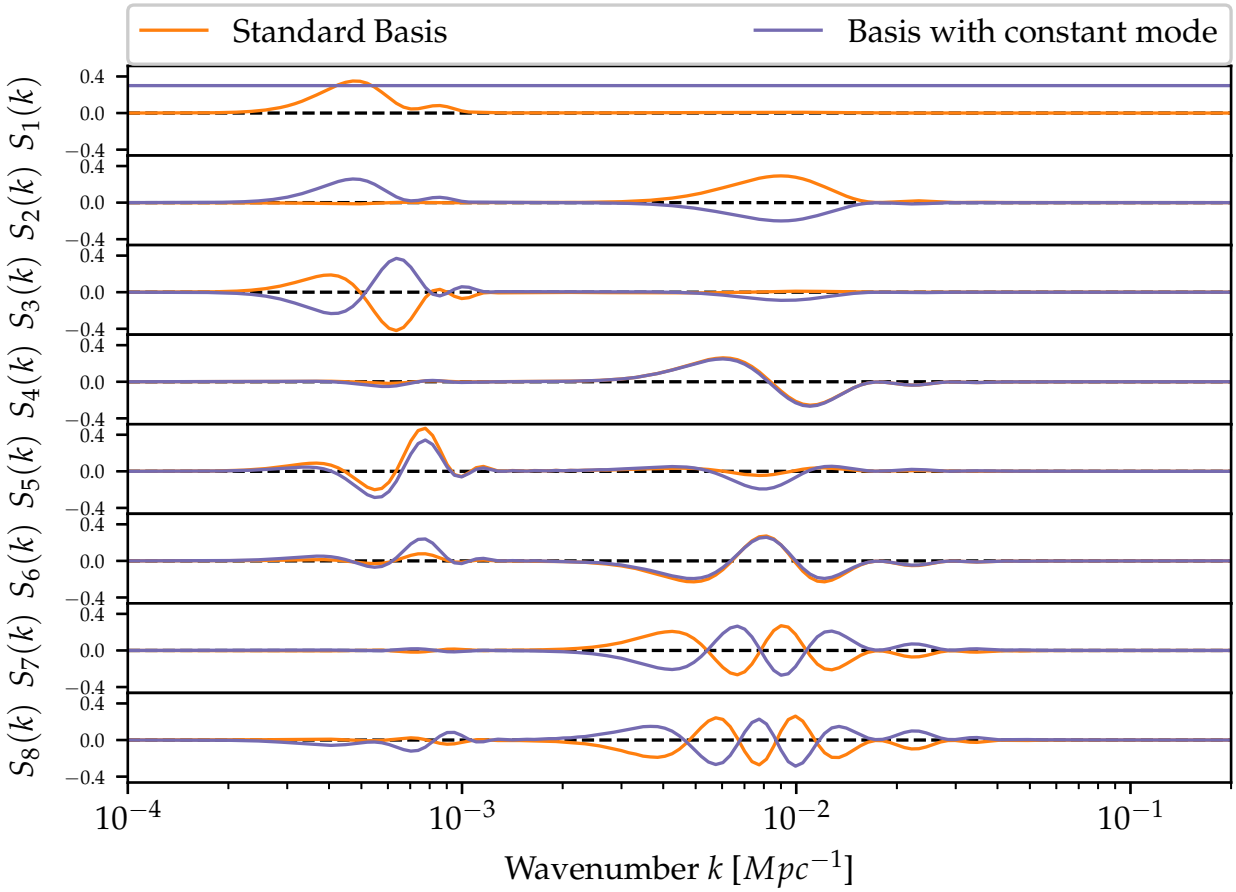

Figure 4.12: The first 8 PCA modes $\mathcal{S}_a(k)$ for the LiteBIRD experiment in the standard basis (solid orange curve) and in the constant r mode basis (solid purple curve). Note that the first mode of the constant r mode basis has been arbitrarily rescaled here to 0.3 to be shown in the same figure as the standard basis, but in reality is normalized to 1, as explained in the text.

and basis both with and without constant mode. The uncertainties derived from the MCMC estimation σ_{MCMC} have to be larger or equal to the Fisher ones σ_{Fisher}. Without the physicality prior we checked that it is indeed the case, but as we turn on the prior the constraints that it imposes on the m_a values often dominate or are comparable with those imposed by the observation, resulting in $\sigma_{Fisher} > \sigma_{MCMC}$ for most of the modes (Tables 4.4-4.6). Only very few of the highest S/N modes satisfy $\sigma_{Fisher} < \sigma_{MCMC}$ and, interestingly, in the LiteBIRD case, for $r = 0.001$, their number is two when we use our standard basis and only one when we impose a constant mode. The effect of the physicality priors is visible even more clearly in the 1D and 2D marginal distribution of the MC samples (Figures 4.15 and 4.16): the marginal distributions are strongly asymmetric, the contours have often polygonal shapes and are very different from the ones expected from the Fisher analysis (red ellipses). As it is evident from these plots, the non-Gaussianity of the contours is

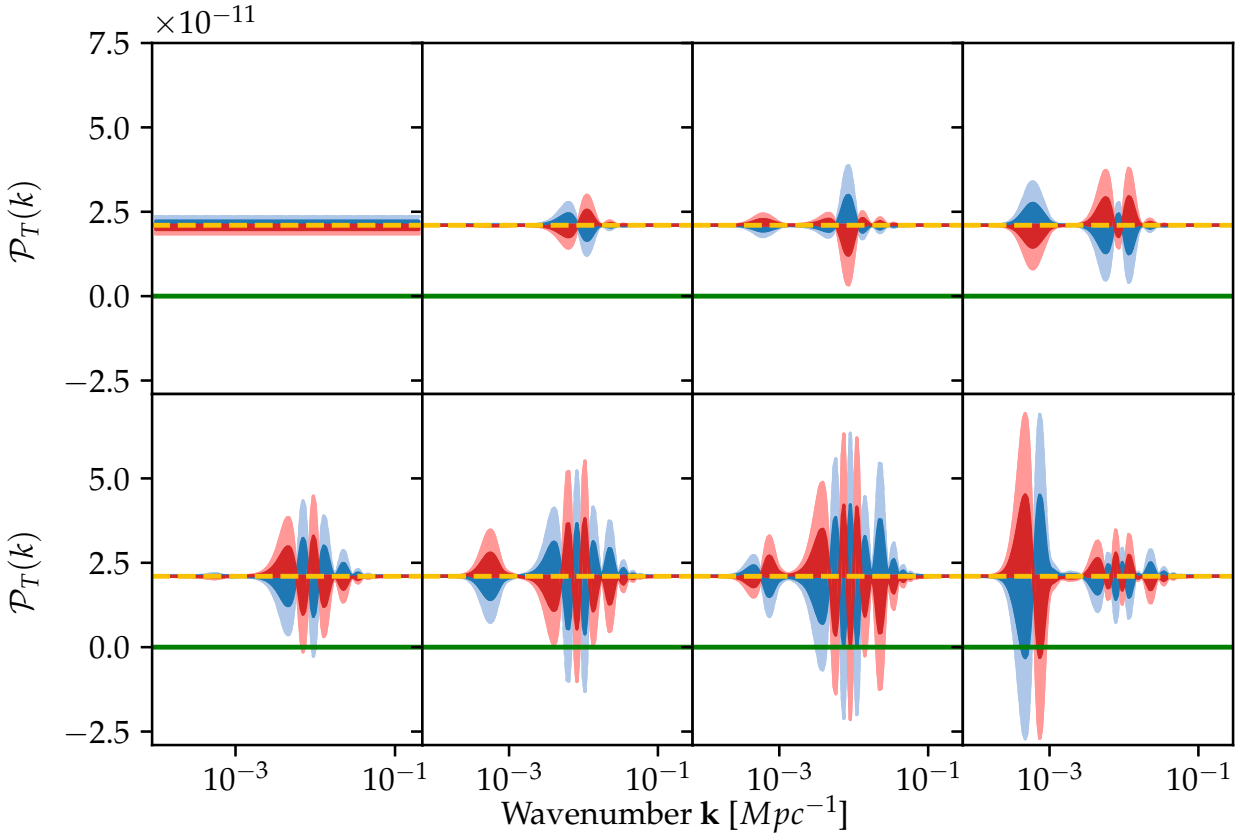

Figure 4.13: Plots of $(rA_s \pm A_s\,\sigma_{a,Fisher}\,\mathcal{S}_a(k))$ for each mode a, for the first eight PCA modes in the constant mode basis with $r = 0.01$ for LiteBIRD (dark blue for $+$ and dark red for $-$ shaded contours). The light blue (light red) shaded represents show the $+2\sigma$ (-2σ) contours and the yellow dashed line represents A_T. The top panel contains the first four modes in increasing order from left to right and the bottom panels the modes 5-8. The physicality prior is indicated with a solid green line.

such that the maxima of the marginal distributions are significantly different from the best-fit values (which of course match the input values of the parameters). As a side comment, in the LiteBIRD case and input power spectrum with $r = 0.01$, we compare our standard basis and the basis with the constant mode (only the first three modes, figure 4.17). We note that the latter case shows a m_1-m_3 correlation[5], while the former has the kind of shape we expect from uncorrelated parameters with asymmetric probability distributions. This behaviour of our basis is preferable, as the PCA should ideally yield uncorrelated parameters.

Concluding, while we can always use the PCA basis to model the primordial tensor power spectrum, the Fisher uncertainties – that we obtain as a byproduct of the PCA – are rarely accurate in absolute terms and should be used only for relative comparisons.

[5] We can understand this 2D marginal as follows. Figure 4.13 shows that $\mathcal{S}_3$ is strongly peaked in a very small k-range and, consequently, $m_a\mathcal{S}_a$ can hit the prior even for m_3 very close to zero, if they are negative. This prior effect occurs more easily when m_1 (i.e. r) is small, producing the m_1-m_3 correlation.

Experiment	PCA basis construction	Input MCMC	PCA mode	σ_{Fisher}	σ_{MCMC}
LiteBIRD	Standard basis	r=0.01	1st	0.03	0.04
			2nd	0.003	0.004
			3rd	0.06	0.03
			4th	0.009	0.009
			5th	0.09	0.04
			6th	0.02	0.014
			7th	0.02	0.014
			8th	0.04	0.014
		r=0.001	1st	0.005	0.009
			2nd	0.002	0.002
			3rd	0.01	0.008
			4th	0.007	0.004
			5th	0.019	0.01
			6th	0.014	0.004
			7th	0.019	0.003
			8th	0.03	0.003
	Constant mode basis	r = 0.01	1st (const.)	0.0006	0.0017
			2nd	0.007	0.01
			3rd	0.01	0.012
			4th	0.019	0.015
			5th	0.019	0.016
			6th	0.03	0.017
			7th	0.04	0.019
			8th	0.04	0.017
		r = 0.001	1st (const.)	0.0004	0.0005
			2nd	0.003	0.002
			3rd	0.007	0.002
			4th	0.009	0.0017
			5th	0.014	0.002
			6th	0.019	0.0016
			7th	0.019	0.002
			8th	0.03	0.002

Table 4.4: Comparison between uncertainties on the first eight PCA modes for LiteBIRD for different PCA bases and different values of r. In the first two cases we take our PCA basis produced with $r = 0$ (standard basis) and project on it the models with $r = 0.01$ (first case from the top) and $r = 0.01$ (second case from the top). In the third and fourth case from the top instead, we construct the PCA basis with a constant $r = 0.01$ and $r = 0.001$ mode, respectively, so that $m_1 = r$. The third column from the left shows the value of r chosen in the simulation used as input data for the MCMC.

Experiment	PCA basis construction	Input MCMC	PCA mode	σ_{Fisher}	σ_{MCMC}
SO	Standard basis	$r = 0.01$	1st	0.006	0.007
			2nd	0.014	0.014
			3rd	0.03	0.019
			4th	0.04	0.02
		$r = 0.001$	1st	0.004	0.004
			2nd	0.01	0.006
			3rd	0.019	0.007
			4th	0.03	0.008
	Constant mode basis	$r = 0.01$	1st (const.)	0.0013	0.002
			2nd	0.014	0.014
			3rd	0.019	0.017
			4th	0.04	0.017
		$r = 0.001$	1st (const.)	0.0009	0.0009
			2nd	0.01	0.0019
			3rd	0.019	0.002
			4th	0.03	0.0018

Table 4.5: Comparison between uncertainties on the first four PCA modes for SO for different PCA bases and different values of r.

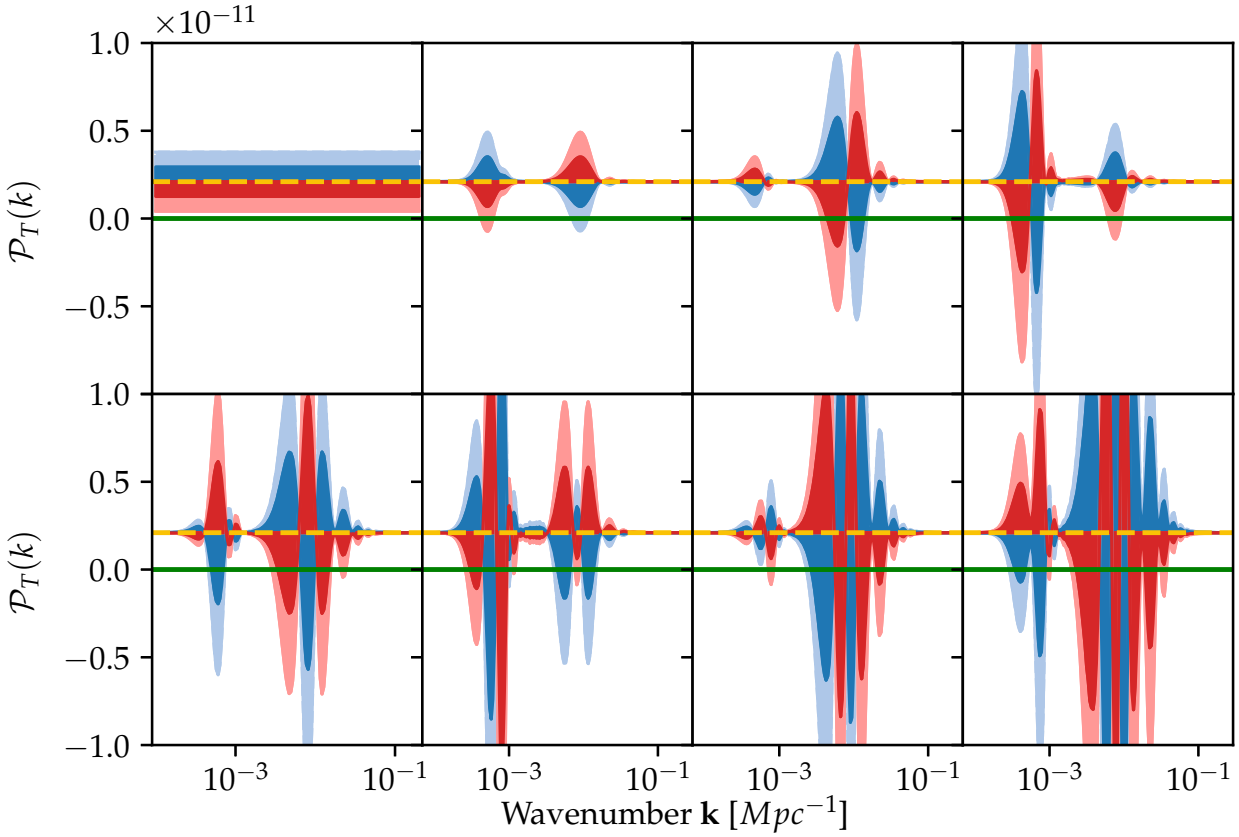

Figure 4.14: Plots of $(rA_s \pm A_s\sigma_{a,Fisher}\mathcal{S}_a(k))$ for each mode a, for the first eight PCA modes in the constant mode basis with $r = 0.001$ for LiteBIRD.

4.5 *Chapter summary*

In this Chapter, we studied the principal component analysis applied to the tensor primordial power spectrum, with the goal of investigating its capability to detect, in a model-independent way, deviations from scale-invariance through the B-modes of the CMB polarization anisotropies. The PCA technique consists in diagonalizing the Fisher matrix and taking its eigenvectors to form a basis of uncorrelated modes, called PCA modes. The modes are ranked from the best to the worst measured ones according to the inverse of the square root of the eigenvalue associated to each mode, which represents the uncertainty on that mode.

We derived constraints on the power spectrum parameters using the specifications from three future B-mode probes, namely LiteBIRD, SO and CMB-S4. We included the contributions of gravitational lensing by Large Scale Structure, instrumental noise and – most important – the residuals of diffuse foregrounds (dust and synchrotron) following a foreground cleaning procedure. We found that residuals

Experiment	PCA basis construction	Input MCMC	PCA mode	σ_{Fisher}	σ_{MCMC}
CMB-S4	Standard basis	$r = 0.01$	1st	0.005	0.008
			2nd	0.014	0.014
			3rd	0.02	0.02
			4th	0.03	0.02
			5th	0.04	0.021
			6th	0.05	0.022
		$r = 0.001$	1st	0.002	0.003
			2nd	0.006	0.004
			3rd	0.01	0.0057
			4th	0.019	0.0059
			5th	0.01	0.0061
			6th	0.03	0.006
	Constant mode basis	$r = 0.01$	1st (const.)	0.0012	0.0019
			2nd	0.01	0.014
			3rd	0.014	0.014
			4th	0.03	0.015
			5th	0.03	0.015
			6th	0.04	0.016
		$r = 0.001$	1st (const.)	0.0005	0.0005
			2nd	0.006	0.0019
			3rd	0.01	0.002
			4th	0.019	0.0017
			5th	0.019	0.0016
			6th	0.03	0.0015

Table 4.6: Comparison between uncertainties on the first six PCA modes for CMB-S4 for different PCA bases and different values of r.

have a major impact on the analysis, and, in order to have realistic signal-to-noise ratio for the experiment considered, they must be included. Indeed, depending on the experiment and the value of tensor-to-scalar ratio r considered, adding foregrounds residuals can increase even by a factor ~ 4 the uncertainty on r and on the PCA modes. Moreover, we found that the effect of foregrounds is relevant for both satellite and ground-based experiments.

Then, through the shapes of these PCA modes and the uncertainty associated to each mode, we characterized the k-range for which each of the three experiments will be most sensitive to features in the power spectrum. In particular, LiteBIRD showed peaks of sensitivity, corresponding to the reionization and the recombination bump in the B-mode spectrum, consistent with (Hiramatsu et al., 2018). Moreover, we found that the relative importance of the two peaks quickly shifts from the reionization peak to the recombination one as we probe values of r different from zero. For SO and CMB-S4, instead, the sensitivity is peaked on the recombination bump with CMB-S4 showing significantly smaller uncertainties on the first modes with respect to SO.

Throughout our discussion, we have explained how the choices we have made in constructing our basis basis try to address the obstacles to the application of the PCA to the tensor power spectrum.

Firstly, since it is still undetected, we use a reference angular power spectrum with no tensor contribution for constructing the Fisher matrix. We devised, however, a procedure to choose the number of PCA modes retained that makes the basis well suited to analyze angular power spectra with substantial tensor contributions. Second, we remove r from the parametrization of the tensor power spectrum, which is then expressed solely as a linear combination of PCA modes. We found indeed that including r makes difficult for any other mode to have Fisher predictions that are robust with respect to the physicality prior $P_T > 0$. In any case, this prior remains the main limitation to the applicability of the PCA analysis to the tensor power spectrum, as highlighted in our comparison with the MCMC analysis.

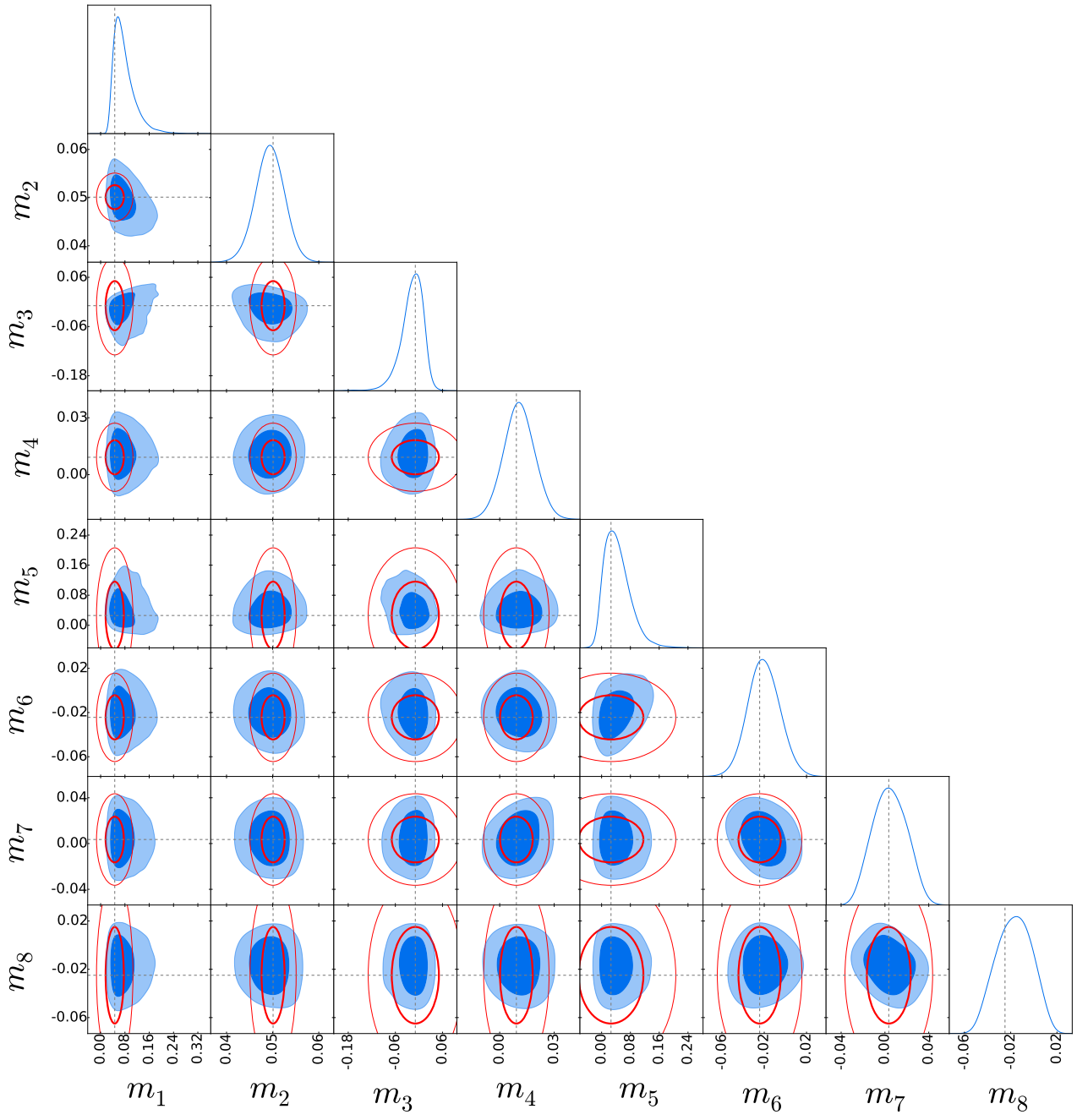

Figure 4.15: 1D and 2D marginal distributions of the first eight PCA amplitudes for the standard PCA basis for LiteBIRD, using as input for the MCMC a model with $r = 0.01$ (in blue). The contours represent 68% and 95% CL and the dashed grey line is showing the fiducial values of m_a. Also shown are the contours expected from the Fisher analysis (thick red ellipses for the 1σ errors and thin ones for 2σ).

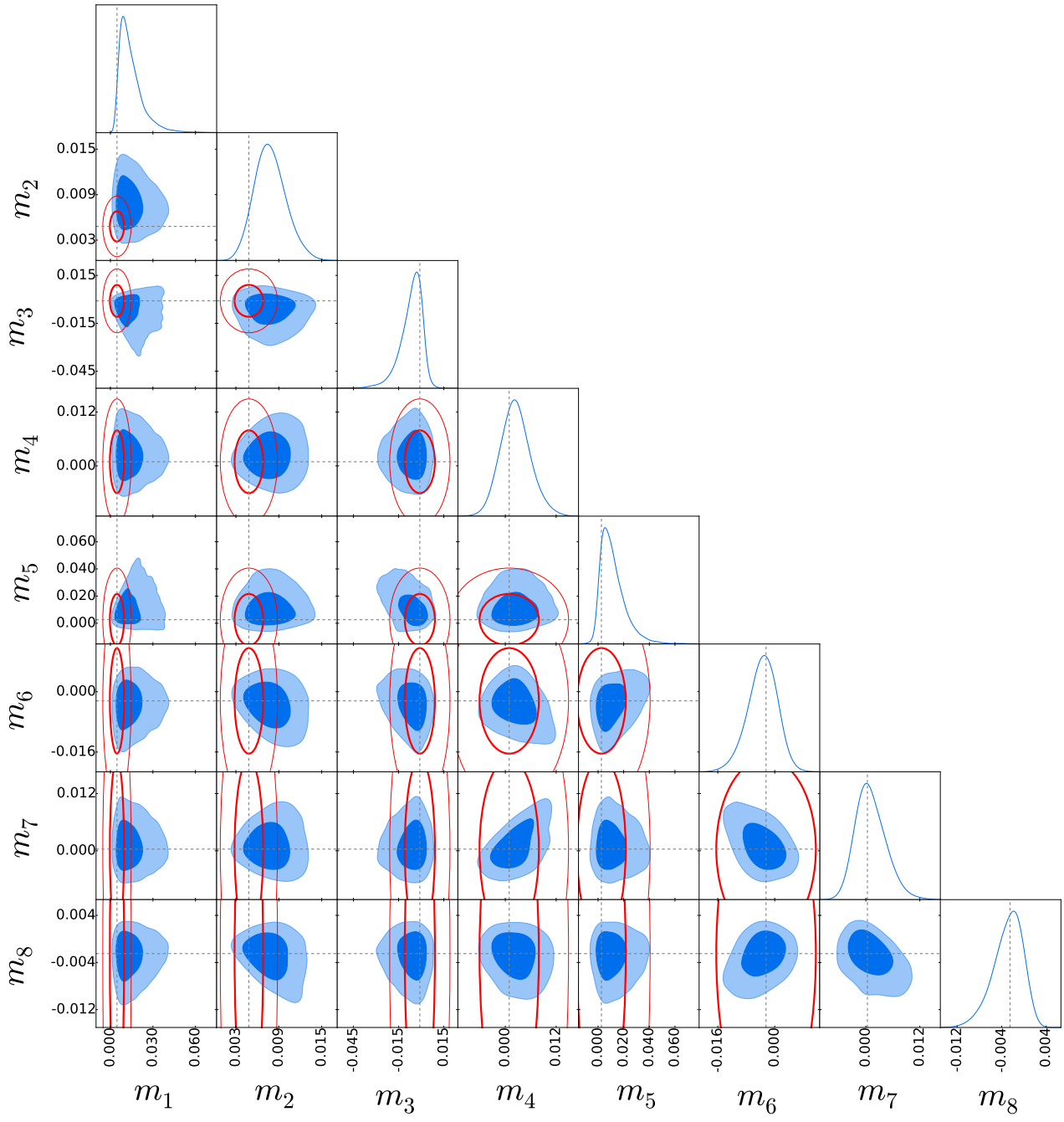

Figure 4.16: 1D and 2D marginal distributions of the first eight PCA amplitudes for the standard PCA basis for LiteBIRD, using as input for the MCMC a model with $r = 0.001$.

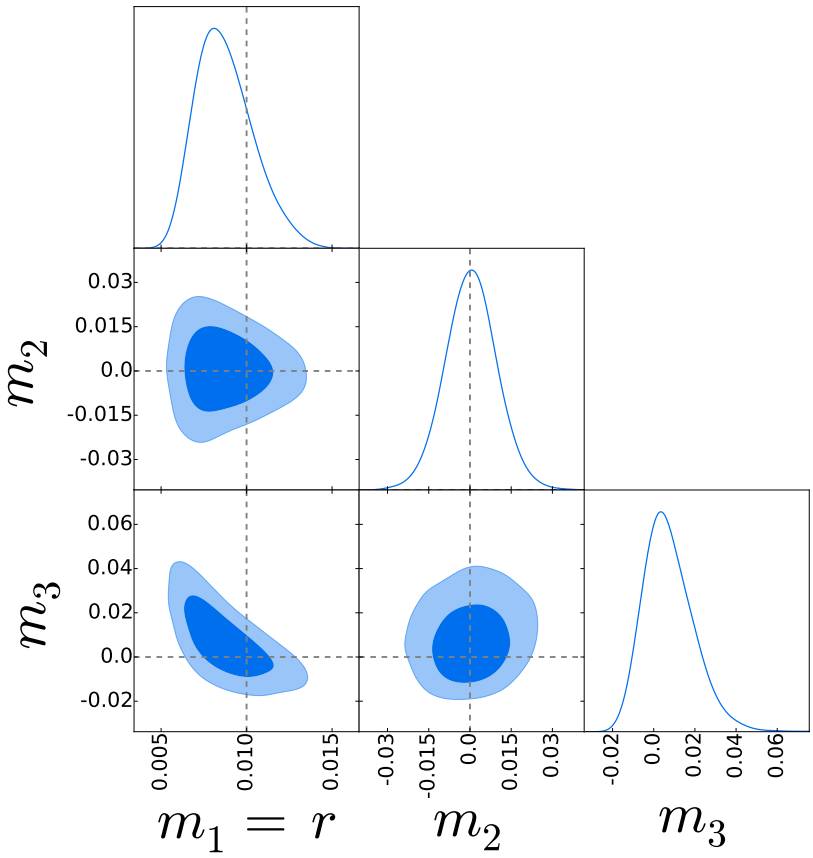

Figure 4.17: 1D and 2D marginal distributions of the first three PCA amplitudes in the constant mode basis with $r = 0.01$ for LiteBIRD. Note that in this basis the first mode has $m_1 = r$.

5
A Multi-Frequency Study of the Tensor Spectrum: Combining LiteBIRD, PTA and Laser Interferometers

This Chapter is based on the work Campeti et al. (2020).

In this Chapter we will extend the analysis of Chapter 4 and investigate the possibility of measuring the spectrum of the primordial SGWB signal using not only CMB B-mode experiments (see Section 3.1.2), but also PTA surveys (Section 3.2.5), and laser and atomic interferometers (Section 3.2.3), thus obtaining constraints across ~ 23 decades in frequency.

For the CMB and PTA experiments we consider the LiteBIRD mission and SKA, respectively. For the interferometers we consider space mission proposals including LISA, BBO, DECIGO, μAres, DO and AEDGE, as well as the ground-based ET proposal.

As we already mentioned, combining these experiments, we can measure the SGWB spectrum across 23 decades in frequency; if we also include indirect probes using the Big Bang Nucleosynthesis (BBN) and the number of relativistic degrees of freedom, the range extends to 29 decades (Lasky et al., 2016a; Adshead et al., 2020a). This combination enables a detailed characterization of the SGWB that goes beyond the simple detection of r, which will be of utmost importance to determine if the detected primordial SGWB was sourced by the quantum vacuum fluctuations in the metric tensor, as in the single-field slow-roll scenario, or from alternative scenarios that can also produce the SGWB. In this context, the possibility of SGWB production from gauge fields, both Abelian (Sorbo, 2011; Barnaby and Peloso, 2011; Barnaby et al., 2012; Cook and Sorbo, 2012, 2013; Namba et al., 2016; Shiraishi et al., 2016; Domcke et al., 2016; Özsoy, 2020) and non-Abelian (Maleknejad et al., 2013; Adshead et al., 2013b,a; Dimastrogiovanni and Peloso, 2013; Maleknejad and Sheikh-Jabbari, 2011, 2013; Maleknejad, 2016; Dimastrogiovanni et al., 2017; Obata and Soda, 2016; Adshead et al., 2016; Adshead and Sfakianakis, 2017; Agrawal et al., 2018a,b), has been investigated in the literature.

These sourced gravitational waves come with distinct observational signatures: they can be non-scale-invariant, partially chiral (circularly polarized), and strongly non-Gaussian. In this work, we focus on the first signature, i.e., the spectrum of the SGWB, which can be blue, red, or with a bump. See the above list of references for the other two signatures. Note also that the high-frequency GW produced by the gauge field during (p)reheating after inflation contributes to the effective number of relativistic degrees of freedom, which provides further constraints on the axion-U(1) models (Adshead et al., 2018, 2020a,b). Specifically, we seek to gather in one resource the expectations on the SGWB from the most promising

future experiments, covering the whole frequency range of the GW spectrum, and study how they distinguish between the single-field slow-roll prediction and the SU(2) gauge field predictions. We build on the work of Ref. Thorne et al. (2018) whose focus was on detection of chirality of the SGWB from the SU(2) gauge field (also see Ref. Domcke et al. (2020) for prospects to detect chirality of the SGWB by LISA and ET).

To this end, we try to use coherent assumptions for each experiment and, whenever possible, to derive the relevant quantities from the first principles using the latest available information in the literature. We provide therefore a quick reference for both communities of cosmologists and GW astronomers for the sensitivities of future experiments capable of detecting a SGWB, summarizing the mathematical tools needed to compute such sensitivities for both the CMB and interferometers. Finally, we show our results in a coherent manner by plotting error bars representing the uncertainty on the binned tensor power spectrum for each experiment. For example, we derive forecasts for the precision on the tensor-to-scalar ratio r and the tensor spectral index n_T, for the combination of CMB B-modes experiments and laser interferometers (LiteBIRD+LISA and LiteBIRD+BBO), using a Monte Carlo Markov Chain exploration of the full cosmological parameters space.

We differentiate our work from the previous literature in three ways. First, we provide frequency-integrated error bars from the binned sensitivity curves for all the detectors. Second, we include astrophysical foregrounds for all experiments. Finally, we use the latest and realistic CMB sensitivity curves for the LiteBIRD mission, including state-of-the-art simulations for the CMB foregrounds.

The Chapter is organized as follows. In Section 5.1 we describe the two theoretical tensor power spectrum models for which we will provide forecasts in the subsequent sections: the single-field slow-roll model and the spectator axion-SU(2) model. In Section 5.2 we discuss the experimental setup for the CMB B-mode experiment LiteBIRD, including the instrumental noise, the lensing contribution and the astrophysical foregrounds contamination. In Section 5.3 we construct the instrumental sensitivity curves for PTA experiments and interferometers, while in Section 5.4 we illustrate the effect of the astrophysical foregrounds on each experiment. Section 5.5 is dedicated to the discussion of our results concerning forecasts on the sensitivity of all the experiments for the spectator axion-SU(2) and single-field slow-roll models. We also present the updated forecasts on the tensor spectral index n_T exploiting the combination of CMB experiments and laser interferometers. We conclude in Section 5.6 with future perspectives.

5.1 *Theoretical Models of Tensor Power Spectrum*

In this Section we review the theoretical models of the primordial tensor power spectrum for which we will provide forecasts in the rest of the Chapter. We consider two possibilities in this respect: one is the nearly scale-invariant tensor power spectrum predicted in the context of the single field-slow roll inflation, while the other is the one produced by the spectator axion-SU(2) model (Dimastrogiovanni et al., 2017).

5.1.1 *Single-Field Slow-Roll Model*

As we discussed in Section 1.8, in the single-field slow-roll inflationary scenario, cosmological scalar and tensor perturbations are

produced by the quantum vacuum fluctuations. The power spectrum for the scalar perturbations is parametrized by a power-law (see Eq. 1.113) $\mathcal{P}_{\mathcal{R}}^{vac}(k) = A_S\,(k/k_0)^{n_S-1}$, where $k_0 = 0.05\,\mathrm{Mpc}^{-1}$ is the pivot-scale and the superscript *vac* indicates that it is produced by quantum vacuum fluctuations. The same applies to the tensor power spectrum (see Eq. 1.125)

$$\mathcal{P}_T^{vac}(k) = A_T \left(\frac{k}{k_0}\right)^{n_T}. \tag{5.1}$$

We also enforce the inflationary consistency relation in single-field slow-roll inflation (Lyth and Riotto, 1999), connecting the spectral index and the amplitude of the tensor spectrum as $n_T = -r/8$.

5.1.2 *Spectator Axion-SU(2) Model*

Gauge fields are ubiquitous in physics and can affect the predictions of inflation (see Maleknejad et al. (2013) for a review). In this work we consider the SGWB produced in the spectator axion-SU(2) model (Dimastrogiovanni et al., 2017) based on the "chromo-natural" inflation model (Adshead and Wyman, 2012). This model has the Lagrangian

$$\mathcal{L} = \mathcal{L}_{inflaton} + \frac{1}{2}\left(\partial_\mu\chi\right)^2 - \mu^4\left[1+\cos\left(\frac{\chi}{f}\right)\right] - \frac{1}{4}F^a_{\mu\nu}F^{a\mu\nu} + \frac{\lambda}{4f}\chi F_{\mu\nu}\tilde{F}^{a\mu\nu}, \tag{5.2}$$

where $\mathcal{L}_{inflaton}$ represents a generic inflaton sector generating the quasi-de Sitter expanding background and the curvature perturbations in agreement with the current CMB observations, χ is a pseudo-scalar axion field with a cosine-type potential, μ and f are dimensionful parameters and λ is a dimensionless coupling constant for the axion and gauge fields. The field strength tensor of the SU(2) gauge field is given by $F^a_{\mu\nu} = \partial_\mu A^a_\nu - \partial_\nu A^a_\mu - g\epsilon^{abc}A^b_\mu A^c_\nu$ with g being the gauge field self-coupling constant, and $\tilde{F}^{a\mu\nu}$ is its dual. We ignore the effect of the gravitational Chern-Simons term $R\tilde{R}$ because its effect on the SGWB is sub-dominant compared to the $F\tilde{F}$ term (Mirzagholi et al., 2020).

During inflation the SU(2) gauge field establishes a homogeneous and isotropic vacuum expectation value, $\bar{A}^b_i = a(t)Q(t)\delta^b_i$ (Maleknejad and Sheikh-Jabbari, 2011, 2013), which is an attractor solution (Maleknejad and Erfani, 2014; Domcke et al., 2019; Wolfson et al., 2020). The perturbation around this value contains scalar, vector, and tensor modes (Maleknejad and Sheikh-Jabbari, 2011, 2013), and the tensor mode linearly mixes with gravitons to produce the SGWB. In particular, the gauge field produces a chiral SGBW with either left- or right-handed circular polarization, depending on which circular polarization mode experiences a transient growth near horizon

crossing (Adshead et al., 2013b,a; Dimastrogiovanni and Peloso, 2013; Maleknejad et al., 2013).

Assuming that only left-handed polarized GWs are produced, we can write the sourced contribution to the tensor spectrum as (Thorne et al., 2018)

$$\mathcal{P}_T^{L,\,Sourced}(k) = r_* \mathcal{P}_\mathcal{R}(k) \exp\left[-\frac{1}{2\sigma^2}\ln^2\left(\frac{k}{k_p}\right)\right], \tag{5.3}$$

$$\mathcal{P}_T^{R,\,Sourced}(k) \simeq 0, \tag{5.4}$$

where $\mathcal{P}_\mathcal{R}$ is the scalar curvature perturbation power spectrum, the parameter r_*, which is the tensor-to-scalar ratio at the peak scale $k = k_p$, controls the amplitude of the tensor power spectrum, and the parameter σ controls the width of the Gaussian-shaped feature produced in the spectrum by this model. These parameters are related to the model parameters given in Eq. 5.2 (see below). This form of the tensor power spectrum is valid for the cosine potential given in Eq. 5.2 as well as for axion potentials with an inflection point (Fujita et al., 2019).

The total tensor spectrum will be the sum of the sourced and the vacuum contributions

$$\mathcal{P}_T(k, k_p, r_*, \sigma) = \mathcal{P}_T^{vac}(k) + \mathcal{P}_T^{Sourced}(k, k_p, r_*, \sigma), \tag{5.5}$$

$$\mathcal{P}_T^{Sourced}(k, k_p, r_*, \sigma) = \mathcal{P}_T^{L,\,Sourced}(k) + \mathcal{P}_T^{R,\,Sourced}(k), \tag{5.6}$$

while the contribution of the axion and SU(2) gauge fields to $\mathcal{P}_\mathcal{R}$ is negligible with respect to the vacuum one for an appropriate choice of the model parameters[1], i.e., $m_Q \equiv gQ/H \geq \sqrt{2}$ where H is the Hubble expansion rate during inflation (Dimastrogiovanni and Peloso, 2013; Dimastrogiovanni et al., 2017); thus, $\mathcal{P}_\mathcal{R}(k) = \mathcal{P}_\mathcal{R}^{vac}(k)$. The parameters $\{r_*, k_p, \sigma\}$ can be connected to the physical parameters in the model Lagrangian $\{g, \lambda, \mu, f\}$ (Thorne et al., 2018; Fujita et al., 2019). The peak wavenumber k_p corresponds to the time t_* at which χ is at the inflection point of the potential, $\chi(t_*) = \pi f/2$. The value of m_Q is given by $m_* \equiv m_Q(t_*) = (g^2\mu^4/3\lambda H^4)^{1/3}$. The other relevant dimensionless variable is $\xi_* \equiv \lambda\dot{\chi}(t_*)/(2fH) \approx m_* + m_*^{-1}$. With these variables, we can write $k/k_p = e^{H(t-t_*)}$, $\sigma^2 = (\lambda/2\xi_*)^2/[2\mathcal{G}(m_*)]$, and $\mathcal{G}(m_*) \approx 0.666 + 0.81m_* - 0.0145m_*^2 - 0.0064m_*^3$. The effective tensor-to-scalar ratio at the peak scale r_* can also be related to the model parameters, but in principle can assume any positive value, while the width of the Gaussian feature σ is bounded by the peak scale choice k_p because of the attractor behavior of the background axion field coupled to the SU(2) gauge fields.

In the rest of this work we will consider three sets of parameters:

$$\{r_*, k_p, \sigma\} = \left\{400, 10^{15}\,\mathrm{Mpc}^{-1}, 9.1\right\}, \quad \left\{0.15, 10^{11}\,\mathrm{Mpc}^{-1}, 8\right\}, \quad \left\{50, 10^{6}\,\mathrm{Mpc}^{-1}, 4.8\right\}, \tag{5.7}$$

[1] We do not include the non-linear scalar curvature perturbation induced by the gauge field. This can be very large in the original chromo-natural model in which the axion plays the role of inflaton (Papageorgiou et al., 2018; Domcke et al., 2019). This contribution in the spectator axion-SU(2) model is smaller (Agrawal et al., 2018a), but may still affect the allowed parameter space in which the sourced GW is comparable to or larger than the vacuum contribution (Papageorgiou et al., 2019). There is also a possibility of having a non-negligible contribution to the scalar sector for a very large σ parameter choice, if the energy fraction of the axion grows after inflation and the axion decays faster than the inflaton (see Thorne et al., 2018, and references therein).

and we will refer to them as *AX1*, *AX2* and *AX3* models, respectively. For all cases we will assume the vacuum contribution to the tensor-to-scalar ratio of $r_{vac} = 10^{-5}$ (Thorne et al., 2018), although this choice might be subject to backreaction of particle production of the gauge field (Maleknejad and Komatsu, 2019; Papageorgiou et al., 2019). To avoid this we can simply assume a larger value for r_{vac}, which would add the scale-invariant component to all the figures we show in this Chapter.

We chose the parameters given in Eq. 5.7 to provide representative examples for our analysis. The first set of parameters represents a tensor spectrum model that is simultaneously detectable by both CMB and laser interferometers, while still satisfying the upper bound provided by the BICEP2/Keck/Planck analysis (see the end of Section 5.1.1). The second set produces instead a spectrum that is just outside the reach of LiteBIRD and at the same time comfortably detectable by the advanced interferometers μAres, DECIGO and BBO, thanks to the large bump feature produced at $k_p = 10^{11}\text{Mpc}^{-1}$. The third parameter set produces a spectrum that peaks in the PTA experiments frequency range while still being compatible with the BICEP2/Keck/Planck upper limit in the CMB range. Thanks to the relationship between σ and k_p, which tends to flatten out the spectrum, we were able to obtain a model that is detectable by SKA and LiteBIRD, but not by space interferometers LISA, DO, AEDGE, DECIGO and the ground-based ET (Section 5.5).

In Figure 5.1 we show the tensor power spectra $\mathcal{P}_T$ as a function of the wavenumber k for the five cases considered in this work. We have checked that all models are consistent with the current CMB shortwave and second-order back-reaction (Clarke et al., 2020), indirect upper bounds (Cabass et al., 2016), PTA limits (Arzoumanian et al., 2018) and ground-based interferometers LIGO/Virgo (Abbott et al., 2019) limits.

5.1.3 *Gravitational Wave Energy Density*

A quantity commonly used in the literature to show the sensitivities of GW observatories is the fractional energy density in GWs at the present (conformal) time $\Omega_{GW}(k, \tau_0)$ (Kolb and Turner, 1990) (Eqs. 1.129-1.132).

The GW transfer function $\mathcal{T}(k, \tau)$ – needed to obtain Ω_{GW} using Eq. 1.132 – can be computed by solving numerically the wave equation (Eq. 1.115). However, this can be quite computationally expensive, especially since the GW transfer function depends on cosmological parameters and therefore we will need to compute this quantity for each point in the cosmological parameter space explored

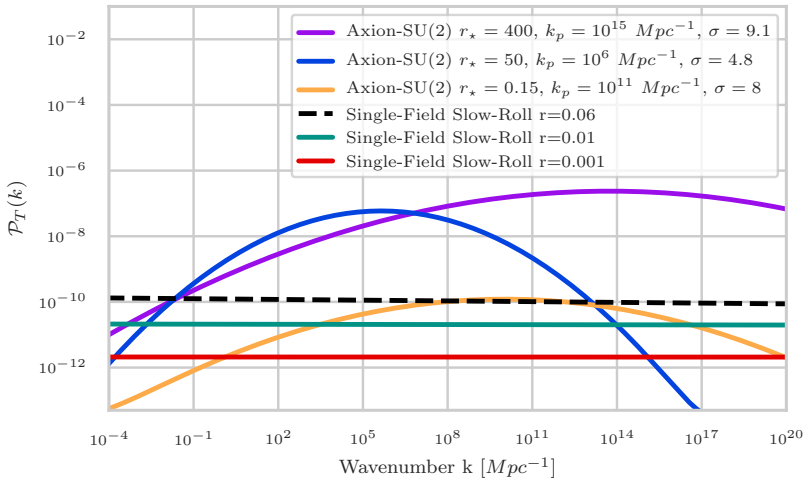

Figure 5.1: Tensor power spectra as a function of the wavenumber k for the five representative cases considered in this work, plus a standard $r = 0.06$ model representing the CMB upper bound from the BICEP2/Keck/Planck combined analysis (black dashed curve).

in the MCMC analysis of Section 5.5.3. Therefore, in the rest of this work, we will find convenient to use the approximate analytical expressions for Ω_{GW} derived in Section 1.9 (Figure 1.11), taking also into account the suppression factor due to changes in effective relativistic degrees of freedom in the early Universe described in Section 1.9.1.

5.2 *Updated Forecasts for CMB B-mode Experiments: The LiteBIRD Case*

CMB experiments are at the forefront of the search for a primordial SGWB. As we discussed in Sections 3.2.2 and 3.1.1, the current best observational bounds on the SGWB come from the CMB. Furthermore, as it will be shown in Section 5.5, they represent our best opportunity to detect a SGWB if the correct model for its production is the single-field slow-roll inflation with $r \lesssim 0.001$.

The current generation of operating CMB experiments includes BICEP2/Keck, POLARBEAR, ACT, SPT and CLASS while the next generation of experiments, planned for this decade, will comprise the Simons Array, SO, SPO and CMB-S4 on the ground-based side, and the LiteBIRD mission observing from space. In this work, we will focus on making forecasts for the LiteBIRD, which is expected to be – together with CMB-S4 – the most sensitive among the planned missions, capable of detecting a tensor-to-scalar ratio $r \lesssim 0.001$.

As we discussed in Section 2.3.2, the signature of the primordial SGWB in the B-mode polarization has two main contributions: one at very large scales (around $k \sim 6 \times 10^{-4}\,\mathrm{Mpc}^{-1}$) where the CMB

photons are re-scattered by the free electrons made available by cosmic reionization (Zaldarriaga, 1997), producing the so-called *reionization bump*, and the other at intermediate scales ($k \sim 6 \times 10^{-3}\,\mathrm{Mpc}^{-1}$) corresponding to the *recombination bump* (Hiramatsu et al., 2018). This primordial signal, however, is fainter than the contaminating signals of the secondary origin: smaller scales are dominated by the *gravitational lensing* due to the cosmological Large Scale Structure, which converts the E-mode polarization of the CMB into a secondary B-mode (Zaldarriaga and Seljak, 1998) (Section 2.4), while larger scales are contaminated by the presence of the *diffuse Galactic foregrounds* (Section 3.1.3).

In this Section we first review the formalism of CMB power spectra (Section 5.2.1). We then describe the relevant noise sources for CMB experiments, including the instrumental, the lensing and the astrophysical foreground contributions (Section 5.2.2). Finally, we review the Fisher matrix approach for computing the binned uncertainties on the tensor power spectrum for a CMB experiment (Section 5.2.3).

5.2.1 *CMB angular power spectra for the axion-SU(2) model*

We already defined the necessary formalism of the CMB angular power spectra in Section 4.1; we specialize here the expression for the angular power spectra in Eq. 4.1 to the axion-SU(2) sourced contribution to the tensor spectrum, defined in Section 5.1.2

$$C_{\ell,t}^{XX',\,Sourced} = \frac{2\pi}{\ell(\ell+1)} \int d\ln k \left[\mathcal{P}_T^{L,\,Sourced}(k) + \mathcal{P}_T^{R,\,Sourced}(k)\right](k)\, T_{\ell,T}^{X}(k)\, T_{\ell,T}^{X'}(k)\,, \tag{5.8}$$

with $XX' = \{TT, EE, TE, BB\}$. Note that the chiral tensor spectrum produced in the axion-SU(2) model also yields non-zero parity-odd cross-spectra such as TB and EB spectra, which could be used as an observational marker to distinguish it from the standard SGWB from the vacuum fluctuations (Lue et al., 1999; Saito et al., 2007; Contaldi et al., 2008). However, these cross-power spectra are difficult to detect unless $r \gtrsim 0.05$ (Thorne et al., 2018); thus, in this work we will be concerned only by the intensity of the SGWB rather than by its circular polarization, and consider only the BB spectrum in our analysis.

5.2.2 *Noise and Foregrounds for CMB Experiments*

In this work we will consider the LiteBIRD satellite and its constraining power on the SGWB. Similarly to what we did in 4.1.2, we characterize this instrument using the following parameters: the polarization sensitivity (in μK-arcmin units) at each frequency channel,

the Full Width at Half Maximum (FWHM) for the instrument beams, the observed sky fraction f_{sky} and the multipole range of the measurement. For LiteBIRD we adopt a multipole range from $\ell_{min} = 2$ to $\ell_{max} = 200$. We report all the other specifications in Table 5.1.

Experiment	Frequency [GHz]	Sensitivity [μK-arcmin]	FWHM [arcmin]
LiteBIRD ($f_{sky} = 0.6$)	40	59.29	60
	50	32.78	56
	60	25.76	48
	68	15.91	43
	78	13.10	39
	89	11.25	35
	100	7.74	29
	119	5.37	25
	140	5.65	23
	166	5.81	21
	195	6.48	20
	235	15.16	19
	280	17.98	24
	337	24.99	20
	402	49.90	17

Table 5.1: Instrumental specifications adopted for the LiteBIRD CMB experiment (LiteBIRD collaboration, private communication).

As outlined by 4.3, there are three relevant noise sources which contribute to the total observed CMB B-mode spectrum C_ℓ^{BB}: the gravitational lensing B-mode $C_\ell^{BB,lens}$, the residual contamination due to polarized diffuse foregrounds $C_\ell^{BB,fgs}$, and the post component separation noise $C_\ell^{BB,noise}$.

We model the instrumental noise (Stompor et al., 2016) at each frequency channel ν as

$$N_{\ell,\nu}^{BB} = \left[w_{B,\nu}^{-1} \exp\left(\ell(\ell+1) \frac{\theta_{FWHM,\nu}^2}{8 \ln 2} \right) \right], \tag{5.9}$$

where $w_{B,\nu}^{-1/2}$ is the white noise level (or sensitivity) in each frequency channel in μK-rad and $\theta_{FWHM,\nu}$ is the beam size in radians.

The lensing represents a contaminant of unknown amplitude when searching for a primordial signal and affects especially the smaller angular scales of the CMB B-modes. We compute $C_\ell^{BB,lens}$ using the `CAMB` code. Note that for LiteBIRD we conservatively do not consider any cleaning from the lensing contamination, i.e. a procedure called delensing (Knox and Song, 2002; Kesden et al., 2002; Hu and Okamoto, 2002a; Smith et al., 2012), corresponding to a choice of $\lambda = 1$ for the delensing parameter in Eq. 4.3. We also stress that high-resolution ground-based experiments such as CMB-S4 can

be exploited to delens LiteBIRD data to enhance its capability in reconstructing the SGWB (see Section 2.4).

On the other hand, the dominant source of noise on large scale B-mode polarization is the diffuse Galactic foregrounds (see, e.g., Planck Collaboration, 2018a, and references therein). In particular, we will consider the two main sources of foregrounds for B-mode experiments: thermal dust and the synchrotron radiation (see Section 3.1.3). We generate simulated sky maps of the polarized Galactic foreground emission using the "d1s1" sky model in the Python Sky Model (`PySM`) code (Thorne et al., 2017), and degrade them to a `HEALPIX` (Górski et al., 2005) resolution $N_{side} = 128$. We add to the simulated maps an instrumental white noise realization generated by the model in Eq. 5.9. We perform component separation for three possible spectral energy distributions (SEDs): the CMB SED, for which we assume no free parameters; the thermal dust SED, for which we take the one-component modified black-body in Eq. 4.19, and the synchrotron SED, for which we assume the curved power-law in Eq. 4.18.

We compute the contributions of residual foregrounds $C_\ell^{BB,fgs}$ and post component separation noise $C_\ell^{BB,noise}$ to the observed spectrum using the parametric maximum likelihood approach (Errard et al., 2011; Errard et al., 2016; Stompor et al., 2016, 2009) implemented in the publicly available ForeGroundBuster (`FGBuster`) code[2]. This code allows for several different choices of cleaning techniques, among which we choose the *Multi-Resolution* procedure, an evolution of the *Multi-patch* technique presented in (Errard and Stompor, 2018). While in the Multi-Patch approach we fit all the spectral parameters over independent sky patches equal to `HEALPIX` pixels with the same resolution parameter N_{side}, in the Multi-resolution approach, each of the free spectral parameters is fitted on a different `HEALPIX` grid with different resolution. The patches resolution for each parameter are gathered in the Multi-resolution vector $\mathbf{N}_{sides}$, for which we adopt the choice $\mathbf{N}_{sides} = [\beta_d, T_d, \beta_s, C_s] = [64, 8, 8, 0]$, obtained by prioritizing the characterization of dust SED over synchrotron SED and by requiring that systematic residuals are much smaller than the statistical ones (J. Errard 2019, private communication). This selection of parameters provides appropriate residuals for the current foreground modeling in LiteBIRD.

[2] See `https://github.com/fgbuster/fgbuster` and reference therein.

We average the resulting residual foregrounds plus post-component separation noise spectra over 100 noise realizations, obtaining the final spectrum in Figure 5.2 (red curve). This spectrum is roughly composed by two parts. In the angular domain, the diffuse Galactic foregrounds are usually characterized by a decaying power law with the angular multipole. Therefore, at high ℓ, the foreground contam-

ination is less relevant, and the component separation noise is the co-addition of sensitivity in multi-frequency channels corresponding to the CMB solution. On the other hand, at low and intermediate multipoles, the structure is dominated by the component separation residuals from the large scale pattern of foregrounds.

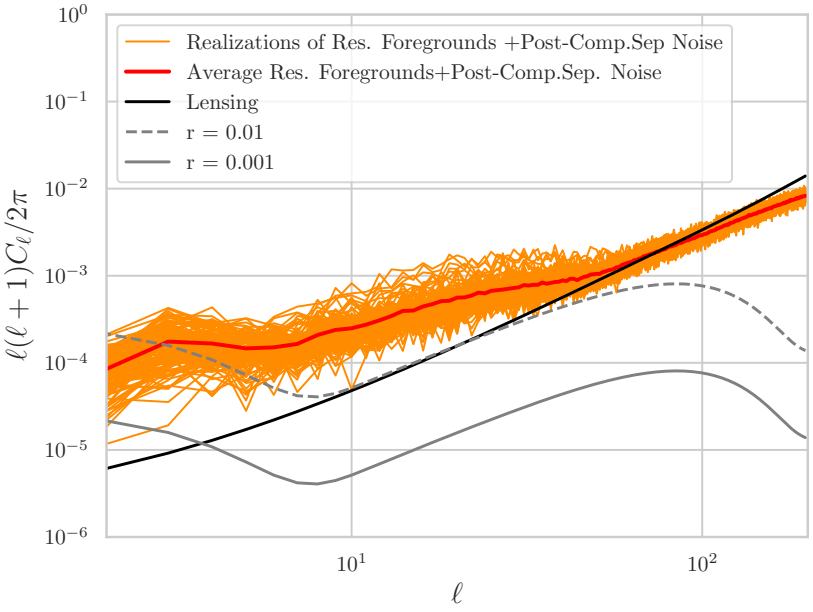

Figure 5.2: The sum of the residual foregrounds and post-component separation noise for 100 noise realizations (in orange) and their average (in red). We also show the lensing power spectrum $C_\ell^{BB,lens}$ (black solid line) and the primordial B-mode signals for $r = 0.01$ (dashed grey) and $r = 0.001$ (solid grey).

5.2.3 *Fisher Matrix for the Tensor Power Spectrum*

To compute the binned uncertainties on the tensor power spectrum for LiteBIRD, we use a Fisher matrix approach similar to the one described in Section 4.2.1 (Campeti et al., 2019a; Hiramatsu et al., 2018). The tensor power spectrum $\mathcal{P}_T$ can be discretized as in Eq. 4.4, where we choose a discretization window function W_i equal to 1 inside the i-th of the N power spectrum bins and 0 outside

$$W_i(\ln k) = \begin{cases} 1 & \text{for } k_{i-1} \leq k < k_i \text{ with } 1 \leq i \leq N \\ 0 & \text{for } k < k_{i-1} \text{ and } k > k_i \end{cases}, \tag{5.10}$$

and $\Delta \ln k = (\ln k_{i+1} - \ln k_i)$ is the width of the i-th bin. Similarly to Eq. 4.7, we can write the derivative of the C_ℓ^{BB} with respect to the power spectrum parameters p_i in a simple way:

$$D_{\ell i}^{BB} = \left.\frac{\partial C_\ell^{BB}}{\partial p_i}\right|_{\rm fid} = \frac{2\pi}{\ell(\ell+1)} A_S \int d\ln k \, T_\ell^B(k) \, T_\ell^B(k) \, W_i(\ln k) \,. \tag{5.11}$$

We choose the k range to be $10^{-4}\,\mathrm{Mpc}^{-1} < k < 1\,\mathrm{Mpc}^{-1}$ such that it contains the whole sensitivity curve of the LiteBIRD experiment. To

obtain the error bar on each power spectrum wavenumber bin, we first compute the Fisher information matrix (see, e.g., Tegmark, 1997) (see Eq. 4.8)

$$F_{ij} = f_{sky} \sum_{\ell=2}^{\ell_{\rm max}} \frac{2\ell+1}{2} \mathrm{Tr}\left[D_{\ell i}^{BB} \left(C_\ell^{BB}\right)^{-1} D_{j\ell} \left(C_\ell^{BB}\right)^{-1} \right], \tag{5.12}$$

where the factor f_{sky} takes into account the loss of modes by a partial sky coverage. We then take the diagonal of its inverse to obtain

$$\sigma^2_{PS}(k_i) = (F^{-1})_{ii}. \tag{5.13}$$

The desired binned uncertainty on Ω_{GW} is then easily obtained from Eq. 1.129

$$\sigma_{\Omega_{GW}}(k_i) = \sigma_{PS}(k_i) \cdot \frac{A_S}{12H_0^2} \left[\mathcal{T}'(k,\tau_0)\right]^2. \tag{5.14}$$

5.3 *Interferometers and PTA*

The landscape of the current and future GWs experiments is vast, characterized by their complementarity in probing the GW spectrum across a wide range of frequencies. The frequency window between $\sim 10^{-7}$ and ~ 10 Hz is expected to be observed from space through a host of funded and proposed laser interferometers, ranging from μAres (Sesana et al., 2019) in the micro-Hertz band, to LISA (Smith and Caldwell, 2019) and AMIGO (Baibhav et al., 2019) in the milli-Hertz band, to BBO (Crowder and Cornish, 2005b; Smith and Caldwell, 2017), DECIGO (Seto et al., 2001) and DO (Sedda et al., 2019) in the deci-Hertz bands. In this work we also include the recently proposed space-based atom interferometer AEDGE (El-Neaj et al., 2019), which will observe the deci-Hertz band as well. Going higher in the GW frequency ($\sim 10 - 10^3$ Hz), the next-generation ground-based detectors (CE (Reitze et al., 2019) and ET (Hild et al., 2011)), also exploiting laser interferometry, will complement the previous observations in the high-frequency part of the GW spectrum. Note however that, while ET – being composed by three interferometers disposed in an equilateral triangle configuration (see Section 3.2.3) – will be able to detect an SGWB on its own, CE – which has been proposed as a single detector with perpendicular arms – will need to be correlated in a network of other interferometers to attempt the detection of an SGWB. We will not consider further CE in the following, leaving the exploration of cross-correlation in a network of interferometers to future work.

We summarize in Table 5.3 the main instrumental characteristics and capabilities of GW observatories treated in this work, including

the experiment type, the arm lenght (L) for traditional interferometers, the total observation length (T_{obs}), the observational efficiency ϵ to compute the actual observation time $T_{eff} = \epsilon T_{obs}$, the frequency range at which the experiment is operating, and the minimum of the binned sensitivity curve with and without foregrounds.

Experiment	Type	L [m]	T_{obs} [yr]	ϵ	Freq.Range [Hz]	Ω_{GW}^{min} w/o Fgs	Ω_{GW}^{min} w/ Fgs	References
LISA	Space M.I.	2.5×10^9	4	75%	$10^{-4} - 10^{-1}$	5.9×10^{-14}	9.9×10^{-14}	Smith and Caldwell (2019)
DO Cons.	Space M.I.	10^8	4	75%	$10^{-3} - 10^{1}$	3.7×10^{-15}	2.1×10^{-14}	Sedda et al. (2019)
DO Opt.	Space M.I.	10^8	4	75%	$10^{-3} - 10^{1}$	7.1×10^{-16}	3.7×10^{-15}	Sedda et al. (2019)
μAres	Space M.I.	430×10^9	10	100%	$10^{-6} - 10^{-2}$	4.7×10^{-18}	2×10^{-17}	Sesana et al. (2019)
DECIGO	Space F.P.I.	10^6	10	100%	$10^{-4} - 10^{1}$	2×10^{-17}	9.8×10^{-17}	Kuroyanagi et al. (2015)
BBO	Space M.I.	5×10^7	10	100%	$10^{-4} - 10^{1}$	1.8×10^{-18}	1.8×10^{-18}	Crowder and Cornish (2005a)
AEDGE	Space A.I.	4.4×10^7	5	60%	$10^{-2} - 1$	4.2×10^{-16}	2.6×10^{-15}	El-Neaj et al. (2019)
ET	Ground M.I.	1×10^4	1	100%	$1 - 10^{3}$	4.5×10^{-14}	2.8×10^{-13}	Hild et al. (2011)
SKA	PTA	-	10	100%	$10^{-9} - 10^{-7}$	3.8×10^{-14}	7.4×10^{-14}	Weltman et al. (2020), Mingarelli et al. (2019)

Table 5.2:Summary of the instrumental specifications for the interferometers and PTA considered in this work. "M.I." stands for Michelson Interferometer, "F.P.I." stands for Fabry-Pérot Interferometer and "A.I." stands for Atomic Interferometer. The binning used to compute the values of Ω_{GW}^{min} is $\Delta \ln k = 1.2$.

Going lower in the frequency, PTAs will probe GWs in the $\sim 10^{-9} - 10^{-7}$ Hz region. There are several planned and ongoing PTA experiments (NANOGrav (Arzoumanian et al., 2016, 2018), EPTA (Lentati et al., 2015a), PPTA (Kerr et al., 2020; Hobbs, 2013), IPTA (Perera et al., 2019)). In this work we show the expected constraints for the most ambitious experiment of this kind, i.e., the SKA (Weltman et al., 2020).

All of the experiments listed above will target several GW sources, both stochastic and deterministic, but in the following we will be interested only in the stochastic ones, and in particular in the possibility of detecting a SGWB of the *primordial* origin. Therefore, we will

consider other SGWB sources, such as unresolved Galactic and extra-Galactic compact binaries for instance, as a *foreground* or *confusion noise* to our sought-after primordial signal.

In this Section, we will describe the formalism required to compute the sensitivity curves for the interferometers (Subsection 5.3.1), neglecting for the moment the effect of foregrounds. In fact, a detailed description of our choices concerning the astrophysical foreground contamination will be given later in Section 5.4, also analyzing how it affects the sensitivity curve for each experiment. The method used to compute the sensitivity curve for the SKA, together with a description of the impact of foregrounds for this PTA experiment, will be described instead in Section 5.4.4. To supplement these sections, in Appendix we describe the construction of the interferometers response functions (Appendix A) and the noise properties of each experiment (Appendix B).

5.3.1 *Instrumental Sensitivity Curves*

In this Section we derive the equation for the sensitivity curve of a GW laser interferometer to an homogeneous and isotropic SGWB. Three of the experiments considered in this work (μAres, DECIGO, BBO) are designed as two independent triangular interferometers, with consequently uncorrelated instrumental noises. The target of these experiments is to measure the *cross-correlation* of the outputs of the two independent detectors. Therefore, in the following we will provide formulae for both the sensitivity of a single detector (suited for LISA, DO and ET) and for the cross-correlation of two independent detectors. Our discussion follows Refs. (Smith and Caldwell, 2017; Romano and Cornish, 2017; Schmitz, 2020), and we refer to those papers for a more complete and detailed derivation. For a derivation of the sensitivity curve of a PTA experiment, which will not be reproduced here, we refer the reader to Refs. (Romano and Cornish, 2017; Hazboun et al., 2019).

A SGWB can be expanded in plane waves as

$$h_{ab}(t,\vec{x}) = \int_{-\infty}^{+\infty} df \int d^2\hat{n} \sum_{P=+,\times} \tilde{h}_P(f,\hat{n}) e^P_{ab}(\hat{n}) e^{i2\pi f(t-\hat{n}\cdot\vec{x})}, \qquad (5.15)$$

where $\tilde{h}_P$ is the amplitude of a sinusoidal plane GW, $P = +, \times$ is the linear polarization state of GW, $\hat{n}$ the GW propagation direction and e^P_{ab} the polarization tensor. In time domain, the data d_I of a detector I can be written as the sum of the signal s_I and noise n_I

$$d_I(t) = s_I(t) + n_I(t). \qquad (5.16)$$

Moving to Fourier space, the noise spectrum for a single detector is

determined by

$$\langle \tilde{n}_I(f)\tilde{n}_I^*(f')\rangle = \frac{1}{2}\delta(f-f')\mathcal{S}_n^I(f). \tag{5.17}$$

Similarly, we define the GW signal strain power spectrum S_s through the correlation of the GW Fourier modes defined in Eq. 5.15:[3]

$$\langle \tilde{h}_P(f,\hat{n})\tilde{h}^*_{P'}(f',\hat{n}')\rangle = \frac{1}{2}\delta(f-f')\frac{\delta^{(2)}(\hat{n}-\hat{n}')}{4\pi}\delta^{PP'}\mathcal{S}_s(f). \tag{5.19}$$

We can now introduce the *response function* $T_I^P(f,\hat{n})$ to describe the signal response of a detector I to a sinusoidal plane GW, which will be computed in Appendix A for several different detector configurations. Using this we write the signal response $\tilde{s}_I$ of a detector I in Fourier space as

$$\tilde{s}_I(f) = \int d^2\hat{n} \sum_{P=+,\times} T_I^P(f,\hat{n})\tilde{h}_P(f,\hat{n}), \tag{5.20}$$

with $T_I^P(f,\hat{n}) = T_I^{ab}(f,\hat{n})\, e^P_{ab}(\hat{n})e^{-i2\pi f\hat{n}\cdot\vec{x}}$.

For a network of detectors $I, J = 1, 2, ...$, we write

$$\langle \tilde{s}_I(f)\tilde{s}_J^*(f')\rangle = \frac{1}{2}\delta(f-f')\tilde{C}_{IJ}(f) = \frac{1}{2}\delta(f-f')\mathcal{R}_{IJ}(f)\mathcal{S}_s(f), \tag{5.21}$$

where $\tilde{C}_{IJ}$ is the covariance matrix of the signal response defined by

$$\tilde{C}_{IJ} = \langle \tilde{s}_I\tilde{s}_J\rangle - \langle \tilde{s}_I\rangle\langle \tilde{s}_J\rangle, \tag{5.22}$$

and $\mathcal{R}_{IJ}(f)$ is the so-called *overlap reduction function* for the detector pair IJ (Flanagan, 1993) (see also discussion in Appendix A)

$$\mathcal{R}_{IJ}(f) = \int \frac{d^2\hat{n}}{4\pi} \sum_{P=+,\times} T_I^P(f,\hat{n})T_J^{P*}(f,\hat{n}). \tag{5.23}$$

As we anticipated in Section 3.2.6, the usual approach used to measure an SGWB is to cross-correlate the outputs $d_I(t)$ and $d_J(t)$ of two detectors I and J. The cross-correlation estimator is therefore

$$\hat{X} = \int_\infty^{+\infty} df \int_\infty^{+\infty} df' \delta_T(f-f')d_I^*(f)d_J^*(f')Q(f), \tag{5.24}$$

where $Q(f)$ is a filter function and δ_T is a finite-time approximation to the Dirac delta function. The mean value for the estimator $\hat{X}$ reads then

$$\langle \hat{X}\rangle = T\int_0^\infty S_s(f)\mathcal{R}_{IJ}(f)Q(f)df, \tag{5.25}$$

where T is the mission observation time. Its variance reads instead

$$\sigma_{\hat{X}}^2 \approx \frac{T}{2}\int_0^\infty S_n^2(f)|Q(f)|^2 df. \tag{5.26}$$

[3] More generally, the covariance matrix of $\tilde{h}_P$ can be written in terms of the "GW Stokes parameters" in analogy to the electromagnetic waves (Seto, 2006)

$$\langle \tilde{h}_P(f,\hat{n})\tilde{h}^*_{P'}(f',\hat{n}')\rangle = \frac{1}{2}\delta(f-f')\frac{\delta^{(2)}(\hat{n}-\hat{n}')}{4\pi}\begin{pmatrix} I+Q & U-iV \\ U+iV & I-Q\end{pmatrix}. \tag{5.18}$$

Here, I is the Stokes I and should not be confused with the index for the detector used in the main text. Circular polarization from chiral GW due to the SU(2) gauge field would appear as the Stokes V (Thorne et al., 2018). In this work we are concerned only with the total intensity of the SGWB and ignore Q, U, or V, hence $\delta^{PP'}$ in Eq. 5.19.

It easy to show that the optimal filter maximizing the signal-to-noise ratio (hereafter SNR) for a cross-correlation measurement of a SGWB using a pair of detectors I, J, takes the form (Allen, 1996)

$$Q(f) = \frac{\mathcal{S}_s(f)}{\mathcal{S}_n^2(f)} \mathcal{R}_{IJ}^*(f), \tag{5.27}$$

from which follows (see Romano and Cornish (2017), Schmitz (2020) and references therein)

$$SNR = \frac{\langle \hat{X} \rangle}{\sqrt{\sigma_X^2}} = \left[2T \int_{f_{min}}^{f_{max}} \frac{\mathcal{R}_{IJ}^2(f) \mathcal{S}_s^2(f)}{\mathcal{S}_n^I(f) \mathcal{S}_n^J(f)} df \right]^{1/2}, \tag{5.28}$$

where $[f_{min}, f_{max}]$ is the detector pair bandwidth.

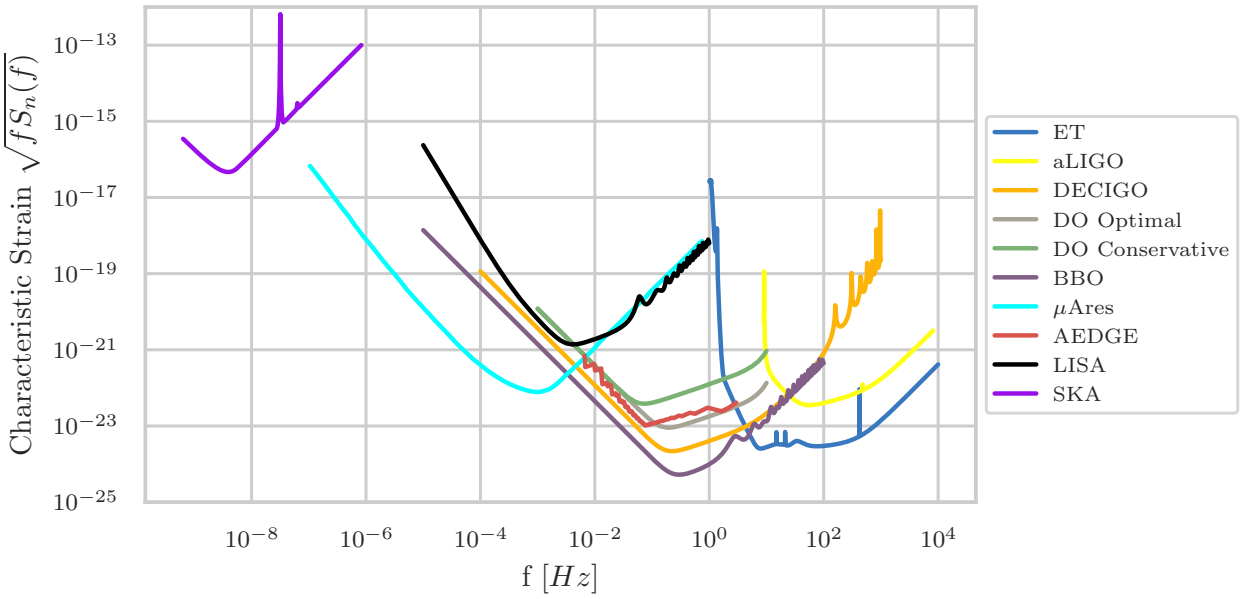

Figure 5.3: Strain sensitivity curves (without the contribution of astrophysical foregrounds discussed in Section 5.4) for all the interferometers and PTA experiments considered in this work. We also plot for reference the strain curve for the Advanced LIGO (aLIGO) experiment.

Since the GW strain power spectrum density can be related to the fractional energy density spectrum in GW as (Romano and Cornish, 2017)

$$S_s(f) = \frac{3H_0^2}{4\pi^2 f^3} \Omega_{GW}(f), \tag{5.29}$$

we can write the sensitivity curve in terms of the minimum detectable gravitational wave energy density Ω_{GW} with the desired SNR in a frequency bin Δf as (Smith and Caldwell, 2017)

$$\Omega_{GW}^{min}(f_i) = \left[n_{det} T \int_{f_i - \Delta f/2}^{f_i + \Delta f/2} \left(\frac{3H_0^2}{4\pi^2} \right)^2 \sum_{J>I} \frac{\mathcal{R}_{IJ}^2(f)}{f^6 \mathcal{S}_n^I(f) \mathcal{S}_n^J(f)} df \right]^{-1/2}, \tag{5.30}$$

for a network of n_{det} detectors $I, J = 1, 2....$

Another useful quantity, which is common in the literature, is the strain spectral sensitivity $\mathcal{S}_h$ for the detector network, defined as

$$\mathcal{S}_h = \left(\sum_{J>I} \frac{\mathcal{R}^2_{IJ}(f)}{\mathcal{S}^I_n(f)\mathcal{S}^J_n(f)} \right)^{-1/2} . \tag{5.31}$$

In Appendices A and B, we give details on our computations for the overlap reduction function $\mathcal{R}_{IJ}(f)$ and the noise spectrum $\mathcal{S}_n(f)$ for each experiment, respectively. In Figure 5.3 we show the strain sensitivity curves for all the interferometers and PTA experiments considered in this work.

5.4 *Astrophysical foregrounds for interferometers and PTA*

We proceed now to describe the main sources of astrophysical foregrounds considered in this work: we first provide approximate analytical fitting formulas for each component; then we introduce a new filter function capable of maximizing the SNR expression including foregrounds (eventually mitigating them with external information) and describe our foreground cleaning strategy on a case-by-case basis.

5.4.1 *Approximate analytical fits for the foreground sources*

As we anticipated in Section 3.2.6, the main sources of astrophysical foregrounds for laser and atomic interferometers are represented by the unresolved populations of *Galactic* and *Extragalactic white dwarfs*, as well as unresolved *stellar mass compact binaries*, such as *black hole*, *neutron star* and *black hole - neutron star binaries*. At PTA frequencies the dominant foreground is expected to be the one due to the coalescence of *Massive Black Hole Binaries* (MBHB). This latter foreground could be of importance also for the μAres interferometer, at frequencies below $\sim 10^{-5}$ Hz.

We now describe the model adopted for each of the foreground contributions mentioned above, starting with the GWD confusion noise. Following Refs. (Cornish and Robson, 2017; Robson et al., 2019), we parametrize it as

$$\mathcal{S}^{gal}_{fg}(f) = A f^{-7/3} e^{-f^{\alpha}+\beta f \sin \kappa f} [1 + \tanh(\gamma(f_k - f))] \, \mathrm{Hz}^{-1}, \tag{5.32}$$

where $A = 9 \times 10^{-45}$ and the parameters α, β, κ, γ and f_k are reported in Table 1 of Ref. (Robson et al., 2019). These parameters vary according to the total mission observation time, hence the amount of cleaning that is possible to perform on the data.

On the other hand, the contribution to the SGWB of the EGWD binaries can be analytically approximated as (Nishizawa et al., 2012)

$$\mathcal{S}_{fg}^{exgal}(f) = 4.2\times10^{-47}\left(\frac{f}{1\,\mathrm{Hz}}\right)^{-7/3}\exp\left(-2\left(\frac{f}{5\times10^{-2}\mathrm{Hz}}\right)^{2}\right)\mathrm{Hz}^{-1}. \tag{5.33}$$

The contribution of unresolved BBH and BNS, as we anticipated in Section 3.2.6, can be approximately expressed at interferometers frequencies by a power-law (see Eq. 3.4)

$$\mathcal{S}_{fg}^{BBH+BNS}(f) = \frac{3H_0^2}{4\pi^2 f^3}\Omega_*\left(\frac{f}{f_*}\right)^{2/3}, \tag{5.34}$$

where we assume for the amplitude of the BBH+BNS foreground a value of $\Omega_* = 8.9\times10^{-10}$ at $f_* = 25\,\mathrm{Hz}$, which is the best estimate according to the current measured merging rates of these compact objects (Abbott et al., 2019).

As for the unresolved MBHB foreground at SKA and μAres frequencies, we use the analytical model given in (Sesana et al., 2008)

$$S_{fg}^{MBHB}(f) = \frac{h_0^2}{f}\left(\frac{f}{f_0}\right)^{-4/3}\left(1+\frac{f}{f_0}\right)^{2\gamma}, \tag{5.35}$$

where the parameters h_0, f_0 and γ are determined by the particular astrophysical model assumed for the MBHB system. The shape and amplitude of the MBHB foreground can vary greatly according to the theoretical model considered and, in particular, to the eccentricity of the binary system. However, just for the purpose of showing an indicative level for this foreground, we adopt the VHMhopk model (Lodato and Natarajan, 2006), with parameters $h_0 = 0.69\times10^{-15}$, $f_0 = 4.27\times10^{-8}$ Hz and $\gamma = -1.08$, which are consistent with the current upper limits from the 11-year NANOGrav data set (Arzoumanian et al., 2018).

5.4.2 *A new filter for foreground mitigation*

In this Section, we will describe a possible strategy for the mitigation of astrophysical foreground, introducing in particular a new filter $Q(f)$ maximizing the noise-only SNR (Eq. 5.28), but also the SNR including foregrounds, taking also into account the possibility of mitigation by using external information on the foregrounds provided by other experiments.

Specifically, we consider the possibility of a *multi-band* cleaning strategy for the BBH+BNS foreground in the space interferometers bands: it has been shown in the works of Pieroni and Barausse (2020) and Pan and Yang (2019) that it is indeed possible to use the

information on the BBH+BNS populations gathered by ground-based experiments – such as Advanced LIGO/Virgo or the future ET and CE detectors – to remove to a certain degree this foreground contamination from the band of space-borne interferometers like LISA.

In the following, we will assume to *know the foreground* $S_{fg}^{BBH+BNS}$ *up to a fractional uncertainty on its amplitude* σ_{fg}. In this case, the cross-correlation estimator $\hat{X}$ (defined in 5.24 will contain also the foreground contribution – which we denote by S_{fg} in the following, dropping the superscript $BBH + BNS$ for notational simplicity – besides the primordial one (S_s):

$$\langle \hat{X} \rangle = T \int_0^\infty [S_s(f) + S_{fg}(f)] \mathcal{R}_{IJ}(f) Q(f) df. \tag{5.36}$$

Thus, we define the following cross-correlation estimator of the primordial signal S_s

$$\hat{Y} = \hat{X} - T \int_0^\infty S_{fg}(f) \mathcal{R}_{IJ}(f) Q(f) df, \tag{5.37}$$

and we can write the associated SNR as (Pan and Yang, 2019)

$$SNR_{\hat{Y}} = \frac{\mu}{\sqrt{\sigma_{instr}^2 + \sigma_{sys}^2}} \tag{5.38}$$

where μ is the mean value of the primordial signal $S_s(f)$,

$$\mu = T \int_0^\infty S_s(f) \mathcal{R}_{IJ}(f) Q(f) df, \tag{5.39}$$

σ_{instr} is the statistical uncertainty due to detector noise

$$\sigma_{instr}^2 \approx \frac{T}{2} \int_0^\infty S_n^2(f) |Q(f)|^2 df, \tag{5.40}$$

and σ_{sys} is the systematic bias due to the limited accuracy of the foreground measurement

$$\sigma_{sys}^2 = \sigma_{fg}^2 \left(T \int_0^\infty S_{fg}(f) \mathcal{R}_{IJ}(f) Q(f) df \right)^2. \tag{5.41}$$

We will show in Appendix C (Poletti D. *in preparation*) – in a similar way to the fact that the filter $Q(f)$ in Eq. 5.27 maximizes the foreground-less SNR (Eq. 5.28) – that the filter

$$Q(f) = \frac{S_s R_{IJ}^*}{S_n^2} - 2T \frac{I_{s \times fg}}{\sigma_{fg}^{-2} + 2T\, I_{fg \times fg}} \frac{S_{fg} R_{IJ}^*}{S_n^2}, \tag{5.42}$$

where

$$I_{s \times fg} = \int \frac{S_s(f) S_{fg}(f)}{S_n^2} |\mathcal{R}_{IJ}|^2(f) df, \tag{5.43}$$

and

$$I_{fg\times fg} = \int \frac{S_{fg}^2(f)}{S_n^2} |\mathcal{R}_{IJ}|^2(f) df, \tag{5.44}$$

maximizes the SNR in Eq. 5.38, taking into account the presence of foregrounds.

Note that, if we know the spectral shape of the foreground but we do not have any external constraint σ_{fg} on its amplitude, we can still apply Eqs. 5.38 and 5.42 in the limit $\sigma_{fg} \to \infty$ (and $T > 0$): in this case the filter has zero response to the foreground template and this corresponds to subtracting the foregrounds by only exploiting its spectral dependence.

Moreover, the SNR 5.38 and the filter 5.42 can obviously be applied to whatever foreground with known spectral shape, not only to the $BBH + BNS$ foreground.

Finally, we note that an expression for the binned sensitivity curve in terms of the minimum detectable GW energy density can be easily obtained in an analogous way to Eq. 5.30 also in the case with foregrounds.

5.4.3 *Foreground cleaning strategy*

We discuss now, on a case-by-case basis, our treatment of the contamination of the astrophysical foregrounds when attempting a detection of the primordial SGWB for each of the experiments considered in this work, starting with LISA.

LISA

As evident from Figure 5.4, the WD binaries constitute one of the most relevant confusion noise source in the LISA band, at frequencies $f \lesssim 5\,\mathrm{mHz}$. However, it has been shown in Adams and Cornish (2014) that this foreground can be subtracted almost completely by exploiting its anisotropy and its time-modulation due to the motion of LISA's constellation (see also Pieroni and Barausse, 2020). In this work, therefore, we will optimistically assume that the GWD foreground can be perfectly subtracted.

The EGWD foreground could also be relevant in the LISA band, in particular between $f \gtrsim 5\,\mathrm{mHz}$ and $f \sim 0.2\,\mathrm{Hz}$, beyond which it starts to deviate from a power-law behavior. Differently from the GWD one, this foreground is expected to be almost isotropic, with a hint of anisotropy due to the stronger signal by nearby galaxies which may be used to favor the subtraction. Moreover, its unique spectral shape could also help in separating and subtracting this contaminant from the primordial signal. As shown in Pan and Yang (2019), the impact of this foreground on the SNR is secondary with respect to

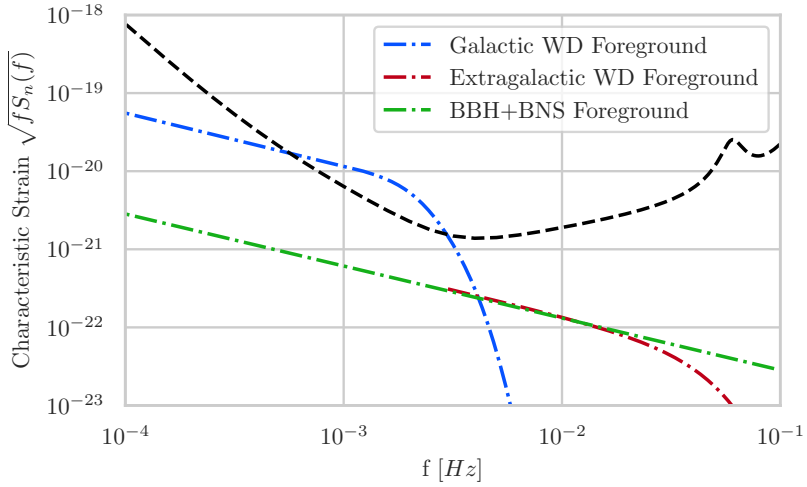

Figure 5.4: Characteristic strain noise curve for LISA (dashed black). The foregrounds due to the GWD after removal of resolved sources (dot-dashed blue), the $BBH + BNS$ foreground (dot-dashed green) and the EGWD contribution (dot-dashed red) are also shown.

the BBH+BNS foreground, as we will discuss below. This happens because the spectral shape of the EGWD foreground can be predicted very accurately at lower frequencies, thus the uncertainty on these frequencies – where LISA is more sensitive – is very small and slightly growing at higher frequencies. Therefore, we will optimistically assume that the EGWD foreground can be perfectly subtracted for our purposes.

The main foreground in the LISA band is represented by the unresolved BBH+BNS populations. Differently from the GWD and EGWD foreground – which cannot be subtracted using ground-based experiments, since WD binaries never enter their bands – we exploit a multi-band cleaning technique for the BBH and BNS foreground. We adopt a value $\sigma_{fg} = 0.1$ for the fractional uncertainty on the foreground amplitude, justified by the analysis of Pieroni and Barausse (2020), involving multi-band cleaning with Advanced LIGO and Virgo. A value $\sigma_{fg} = 1.3 \times 10^{-2}$ can also be reached using a network of three CE detectors located in Australia, China and US (Pan and Yang, 2019). Furthermore, the level $\sigma_{fg} \sim 10^{-3}$ could be reached using external information provided by ET (M. Pieroni, A. Ricciardone e E. Barausse in preparation).

DO Optimal and Conservative

The DO interferometer, both in its Optimal and Conservative incarnations, suffers mainly from the presence of the BBH and BNS foreground (Figure 5.5). The contribution from GWD is almost irrelevant in both designs, as it affects only the very low-frequency part of both sensitivity curves. The same holds for the AEDGE experi-

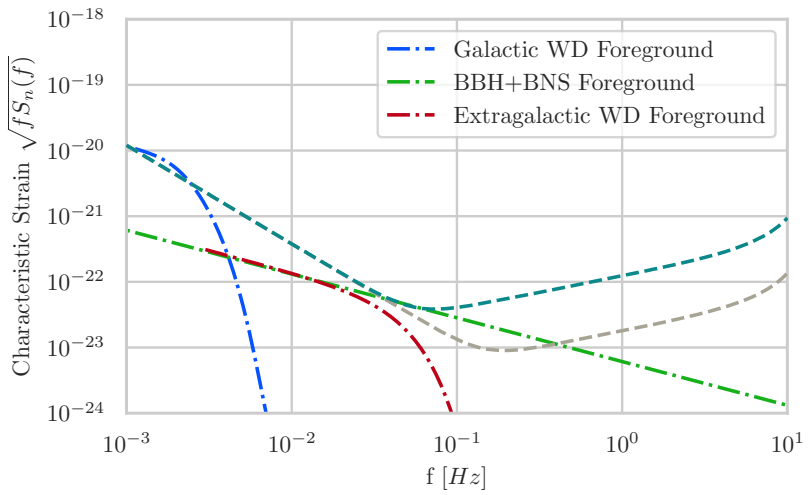

Figure 5.5: Characteristic strain noise curve for DO Optimal (dashed grey) and DO Conservative (dashed dark green). The foregrounds due to the GWD (dot-dashed blue), the $BBH + BNS$ foreground (dot-dashed green) and the EGWD contribution (dot-dashed red) are also shown.

ment (Figure 5.6), since it has similar sensitivity and frequency range to DO Optimal (Figure 5.3). For DO (Optimal and Conservative) and AEDGE, we make the same foreground cleaning assumption described above for LISA.

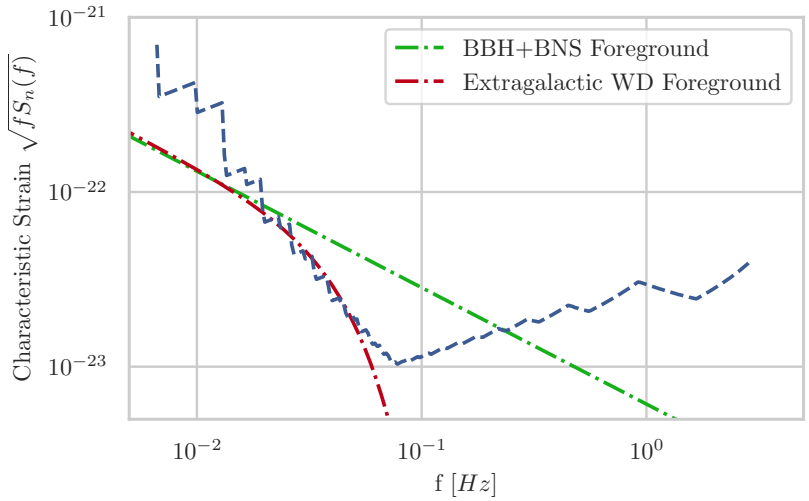

Figure 5.6: Characteristic strain noise curve for AEDGE (dashed blue). The relevant foregrounds are the $BBH + BNS$ (dot-dashed green) and the EGWD binaries (dot-dashed red).

DECIGO and BBO

As for DECIGO and BBO, the BBH+BNS foreground constitutes the main contaminant in their bands (Figures 5.7 and 5.8). BBH and BNS can be individually resolved and subtracted by these two ultra-sensitive interferometers (see Section 3.2.6), leaving a residual

foreground with amplitude a factor $\sim 5 \times 10^{-3}$ smaller than the original one in the DECIGO case (see Nishizawa et al. (2012); Yagi and Seto (2011) and references therein), while BBO should be capable instead of resolving all compact binaries in its band, thanks to its deeper sensitivity, which allows to fully subtract them (Cutler and Harms, 2006; Nishizawa et al., 2012).

Despite the subtraction of resolved sources, the BBH+BNS foreground remains a strong limiting factor for DECIGO: it has been suggested in the past that an improvement of a factor ~ 2 or ~ 3 in sensitivity should be enough to fully resolve and subtract this foreground (Nishizawa et al., 2012). In alternative to this sensitivity boost, we also try to consider the possibility of a multi-band cleaning for DECIGO using ET, corresponding to $\sigma_{fg} \sim 10^{-3}$; however, in this case the sensitivity does not improve significantly with respect to the case in which we only use the spectral dependence to subtract the foreground. We conclude that in order to fully restore the SGWB detection power of DECIGO, we need at least a value $\sigma_{fg} \sim 10^{-6}$, which is at the moment outside of the reach of external ground-based experiments.

The EGWD confusion noise is expected to contribute mostly in DECIGO's and BBO's bands in the range $10^{-3} - 10^{-1}$ Hz. As we discussed in LISA's case, potentially this foreground could be subtracted in a very efficient way using its unique spectral dependence, and moreover its contribution is expected to drop very steeply beyond $f \sim 0.2\,\mathrm{Hz}$, thus not limiting the maximum sensitivity of DECIGO and BBO. For these reasons, we neglect it in the following analysis.

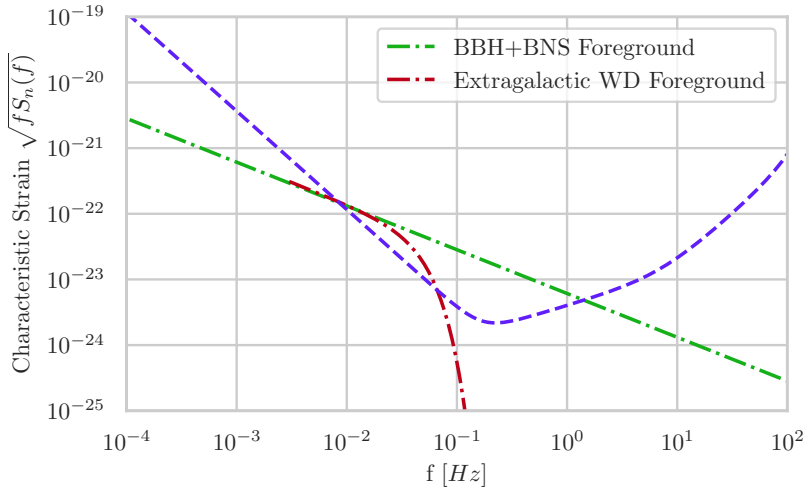

Figure 5.7: Characteristic strain noise curve for DECIGO (dashed orange). The relevant foregrounds are the EGWD (dot-dashed red) and the $BBH + BNS$ foreground (dot-dashed green).

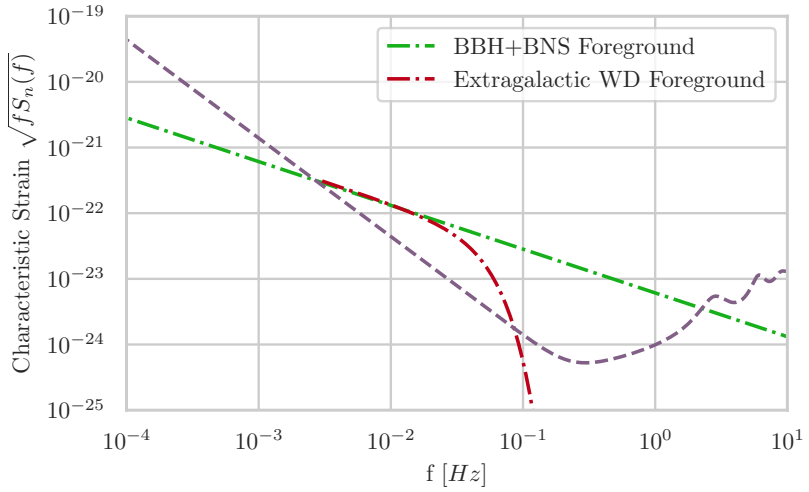

Figure 5.8: Characteristic strain noise curve for BBO (dashed orange). The relevant foregrounds are the EGWD (dot-dashed red) and the $BBH + BNS$ foreground (dot-dashed green).

μAres

The sensitivity curve of μAres appears to be strongly affected by the Galactic WD foreground in almost all the experiment bandwidth (Figure 5.9). However, we assume that a subtraction strategy, exploiting its anisotropy and time-modulation similarly to LISA's case Adams and Cornish (2014), can be applied also to μAres, perfectly subtracting this contaminant. The EGWD foreground, on the other hand, should be of little importance for μAres, and we neglect it in the following.

The BBH+BNS foreground is also very relevant in the μAres band, therefore we adopt a multi-band cleaning approach as in LISA's case: for the AX1 model, a value $\sigma_{fg} = 0.1$ is enough to obtain multiple detections over μAres band, while for the other SGWB models we also show results for $\sigma_{fg} = 10^{-3}$ (in conjunction with third-generation detector ET). However, even the latter value for σ_{fg} it is not enough to detect some SGWB models (see for instance the standard $r = 0.01$ case in Figure 5.24): we conclude that to restore the full "sensitivity bucket" of μAres, we need at least a value $\sigma_{fg} \sim 10^{-5}$, which is not foreseen at the moment using for proposed third-generation ground-based detectors.

In addition to the usual three foreground components we described above, the coalescence of MBHB could produce an unresolved foreground between $\sim 10^{-7}$ and $\sim 10^{-5}$ Hz (dot-dashed purple curve). The actual contribution of MBHB strongly depends on the model of galaxy merger rates during cosmological evolution and on the typical BH masses involved, which have both considerable astrophysical uncertainties. One possibility could be of using LISA to

detect every MBHB merger during mission time as resolved sources, constructing then a model for the MBHB population at μAres frequencies (Bonetti et al., 2019). Again, the capability of LISA of detecting all MBHB mergers in the Universe depends on the actual MBHB astrophysical scenario. We neglect this foreground, since, according to current predictions, this foreground should not affect the most sensitive bins in the μAres sensitivity curve for the detection of an SGWB, thus making our results robust against its inclusion.

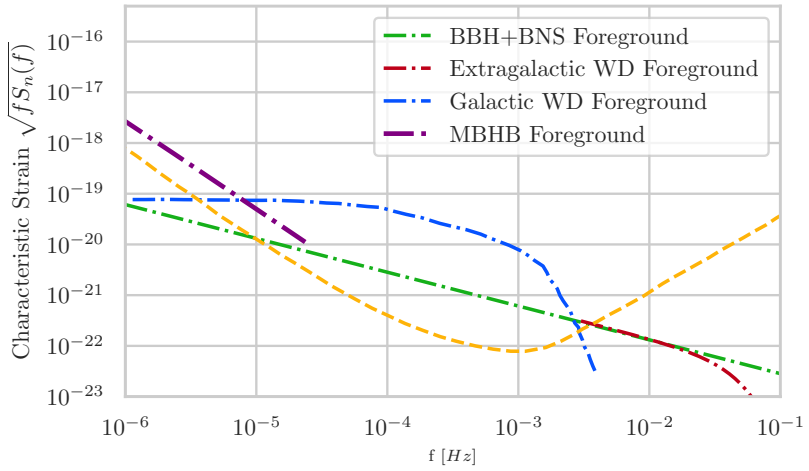

Figure 5.9: Characteristic strain noise curve for μAres (dashed orange). The relevant foregrounds are the $BBH + BNS$ (dot-dashed green), the EGWD binaries (dot-dashed red) and the unresolved MBHB (dot-dashed purple).

ET

Concerning the ground-based ET, the dominant source of the confusion noise in this frequency band is represented by BBH and BNS (Figure 5.10). The BBH contribution can be remarkably reduced by individually resolving sources, leaving a residual with amplitude a factor $\sim$ 200 smaller than the initial foreground, while the BNS and BH-NS contributions are more strenuous and can be reduced only by a factor $\sim$ 2 and $\sim$ 10, respectively (Zhu et al., 2013). The total $BBH + BNS$ foreground will be reduced by an overall factor of $\sim$ 3 (Zhu et al., 2013), thus still constituting an important limiting factor when attempting a detection of the primordial SGWB. We adopt in this case the $\sigma_{fg} \to \infty$ limit in our filter for ET, corresponding to subtraction using only the spectral dependence of this foreground.

5.4.4 SKA

For SKA we optimistically include only the white noise component in the noise budget; however, we note that the so-called "red noise" component due to pulsar timing noise (Hazboun et al., 2019) could

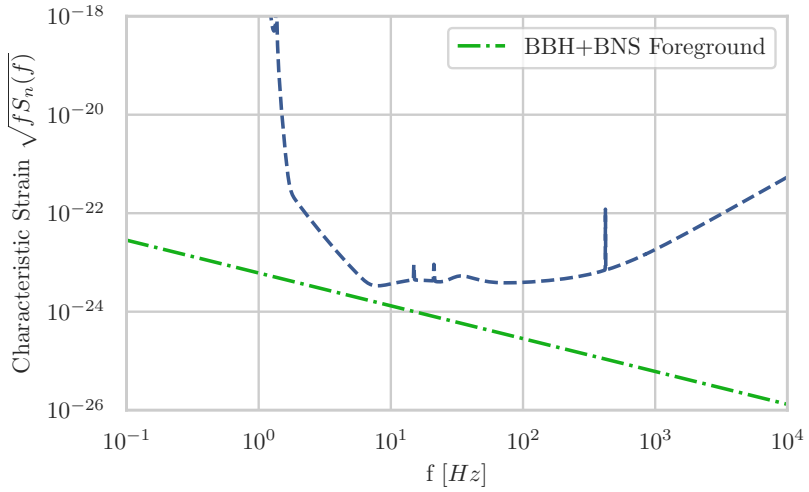

Figure 5.10: Characteristic strain curves for ET (dahsed blue). The relevant foreground for this experiment, namely due the $BBH + BNS$ populations, is shown as a dot-dashed green line.

be present in the data, raising considerably the noise level in the lower frequency part of the PTA sensitivity curves. We use the the codes `hasasia`[4] (Hazboun et al., 2019) and `gwent`[5] to compute the sensitivity to the SGWB, choosing for the pulsars an rms timing residual of $\sigma_t = 50$ ns, an observing time $T = 10$ yr, a number of pulsars $N_p = 200$ and an average observation cadence of 1 per week (Mingarelli et al., 2019).

[4] https://hasasia.readthedocs.io/en/latest/index.html

[5] https://gwent.readthedocs.io/en/latest/index.html

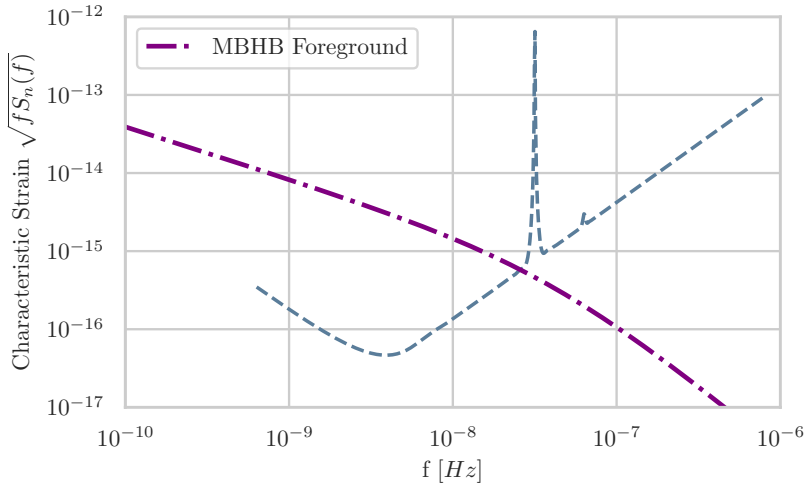

Figure 5.11: Characteristic strain curves for SKA (dashed blue). The relevant foreground for this experiment, namely the unresolved MBHB noise, is shown as a dot-dashed purple line.

As for the foreground, Figure 5.11 shows that the most sensitive part of the SKA bandwidth will be limited by the presence of the MBHB astrophysical foreground. We adopt, in this case, a subtraction strategy based on the spectral shape of this contaminant, using the

limit $\sigma_{fg} \to \infty$ in the SNR and filter expressions in Eqs. 5.38 and 5.42, respectively.

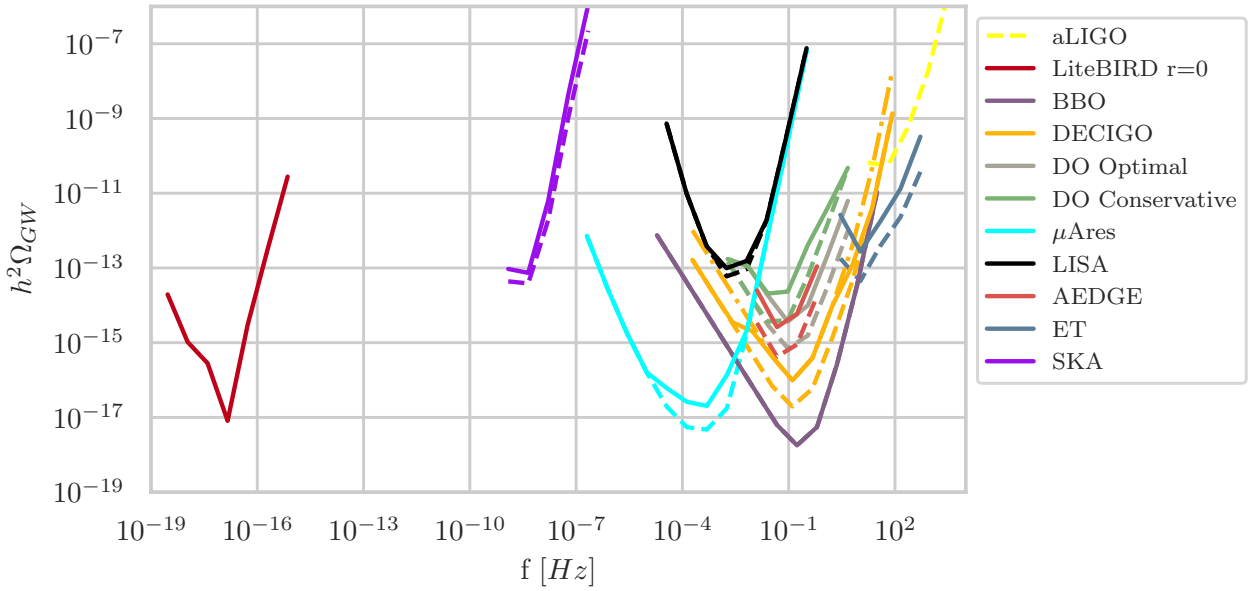

Figure 5.12: Sensitivity curves on the energy density of gravitational waves Ω_{GW} with (solid and dot-dashed lines) and without (dashed lines) the contribution of the astrophysical foregrounds for all the experiments considered in this work, obtained with a logarithmic binning in wavenumber with $\Delta \ln k = 1.2$. Note that we assume a value $\sigma_{fg} = 0.1$ for LISA, DO Optimal and Conservative for the case with foregrounds (see Section 5.4), while for μAres we choose $\sigma_{fg} = 10^{-3}$. For DECIGO we show two sensitivity curves with foregrounds: the dot-dashed one assumes subtraction using only the spectral dependence of the foreground (that is by taking the filter 5.42 in the limit $\sigma_{fg} \to \infty$), while the dashed one assumes multi-band cleaning with $\sigma_{fg} = 10^{-3}$. BBO, on the other side, should be able to resolve and fully subtract all compact binaries in its band. We also plot for reference the sensitivity curve for the aLIGO experiment without the astrophysical foregrounds.

5.5 *Results*

In this Section we present the forecasts for CMB, PTA and interferometers, described respectively in Sections 5.2 and 5.3. We will first show the binned sensitivity curves obtained for LiteBIRD, SKA, and all the interferometers (Section 5.5.1). Then, in Section 5.5.2 we will proceed to show the error bars for each experiment and each of the five example tensor power spectrum models described in Section 5.1.

5.5.1 *Binned Ω_{GW} Sensitivity Curves*

We calculate the binned sensitivity curves to the gravitational wave energy density Ω_{GW} using Eq. 5.14 for the LiteBIRD CMB experiment and Eq. 5.30 for all the interferometers and PTA experiments (and its equivalent when taking the foregrounds into account, see for details Section 5.4). We plot them in Figure 5.12, choosing $\Delta \ln k = 1.2$ as the power spectrum discretization scale. The solid and dashed lines show the sensitivities obtained with and without the foregrounds, respectively. The sensitivity of a CMB experiment to Ω_{GW}, as computed in Section 5.2.3, depends on the fiducial tensor power spectrum used to compute the C_ℓ in the Fisher matrix given in Eq. 5.12; thus,

the sensitivity of LiteBIRD (in red) is computed for $r = 0$ – that is without including cosmic variance – for consistency with what is done for the interferometers.

We find that the best sensitivity of LiteBIRD (including foregrounds) at frequencies $f \sim 10^{-17}$ Hz is similar to those of the most advanced among the interferometers, namely μAres at $f \sim 10^{-3}$ Hz, DECIGO and BBO at $f \sim 10^{-1}$ Hz. However, when plotting error bars on the model predictions in the next sub-Section, we find that the shape of the GW spectrum is very different for CMB and interferometer frequencies. It has a rising spectrum towards the CMB frequency after the transition between the matter and radiation dominated eras, while for the single-field slow-roll model it rapidly flattens out at higher frequencies, making a detection challenging for interferometers. The situation changes dramatically for some parameter choices of the axion-SU(2) model, which can produce a strongly blue-tilted signal easily detectable at interferometer frequencies (Thorne et al., 2018).

Figure 5.12 also highlights the fact that the frequency window between $\sim 10^{-16} - 10^{-9}$ Hz is devoid of any experiment. The constraints on the SGWB intensity in this range come only from indirect limits, such as the BBN, second-order back-reaction and CMB shortwave calculations (Clarke et al., 2020).

Concerning the effect of the foregrounds, we find significant impacts in the frequency range $\approx 1 - 10^3$ Hz due to unresolved BBH and BNS, mainly limiting the sensitivity of ET. Also the DO and AEDGE experiments seem to be still affected for a fractional uncertanty on the amplitude of the BBH+BNS foreground at the level $\sigma_{fg} = 0.1$. However, this does not prevent detection of the AX1 model at high significance in multiple bins for these three experiments, as we will see in the following. Moreover, in order to detect primordial SGWB signals with lesser SNR than the AX1 model, it will possible to further decrease σ_{fg} to the $\sim 1.3 \times 10^{-2}$ level using external information from third generation ground-based experiments such as CE (see Pan and Yang (2019) and Section 5.4), or even to the $\sim 10^{-3}$ level using ET (M. Pieroni, A. Ricciardone e E. Barausse in preparation).

Note that the LiteBIRD sensitivity always includes the foregrounds.

5.5.2 *Error bars for the spectator Axion-SU(2) models*

Next, we calculate the 1σ error bars on Ω_{GW} for five models of the primordial tensor spectrum. Of these, three are the AX1, AX2 and AX3 models defined in Section 5.1.2 (see Eq. 5.7), while the other two

are single-field slow-roll ones with $r = 0.01$, 0.001 and $n_T = -r/8$. In this Section we discuss the results for the former models, while in the next Section 5.5.3 we discuss the latter.

In Figure 5.13, we show the results for LiteBIRD, SKA, LISA and ET. The light and dark shaded areas show the error bars for the AX1 model with and without the astrophysical foregrounds included in our calculation (see discussion in Section 5.4). We always take the foregrounds into account for the LiteBIRD CMB satellite, as explained in Section 5.2.2.

For what concerns the AX1 model, we tuned its parameter set to have simultaneous detections in the CMB, PTA and interferometers ranges, while still being consistent with the BICEP2/Keck/Planck upper bound at CMB scales (the dashed pink curve in Figure 5.13).

By observing closely the CMB part of the spectrum, the LiteBIRD error bars clearly show two peaks of sensitivity corresponding to the reionization bump (second bin from the left) and the recombination bump (fourth and fifth bins from the left), as we anticipated in Section 5.2. Both these bumps corresponds to detections of this model (Figure green error bars in 5.13).

For the space-borne interferometer LISA, we adopt a multi-band cleaning of the BBH+BNS foreground, exploiting external information from Advanced LIGO/Virgo, which provide $\sigma_{fg} = 0.1$, as we discussed in Section 5.4: this allows detection in two bins either with or without foregrounds (blue error bars in Figure 5.13).

The ground-based ET (purple error bars in Figure 5.13) shows detections only in the absence of the foreground. We have tried to tune the axion-SU(2) parameter set to have detections also from ground in the presence of the foreground, but were not successful due to the attractor behavior of the theory and the CMB upper bounds, as explained in Section 5.1.2.

On the other hand, SKA shows remarkably two detections in the foreground-less case and one in the case with foregrounds for this model, confirming PTA surveys as a useful instrument to characterize exotic SGWB models with bump- or peak-like features in their frequency range (see also Garcia-Bellido et al. (2016)).

In Figures 5.14–5.16, we show the expected error bars for the AX1 model for the other interferometers. We show the error bars only for the experiments that can give a detection (without the foregrounds contamination) in at least one bin. Therefore, we show DO Conservative, DO optimal and AEDGE only for the AX1 model, which has the strongest signal in the frequency range favorable to them. We do not show them for the other models because they would not be able to have a detection in at least one bin. However, we make an exception for DECIGO and BBO and do not show their error bars for the AX1

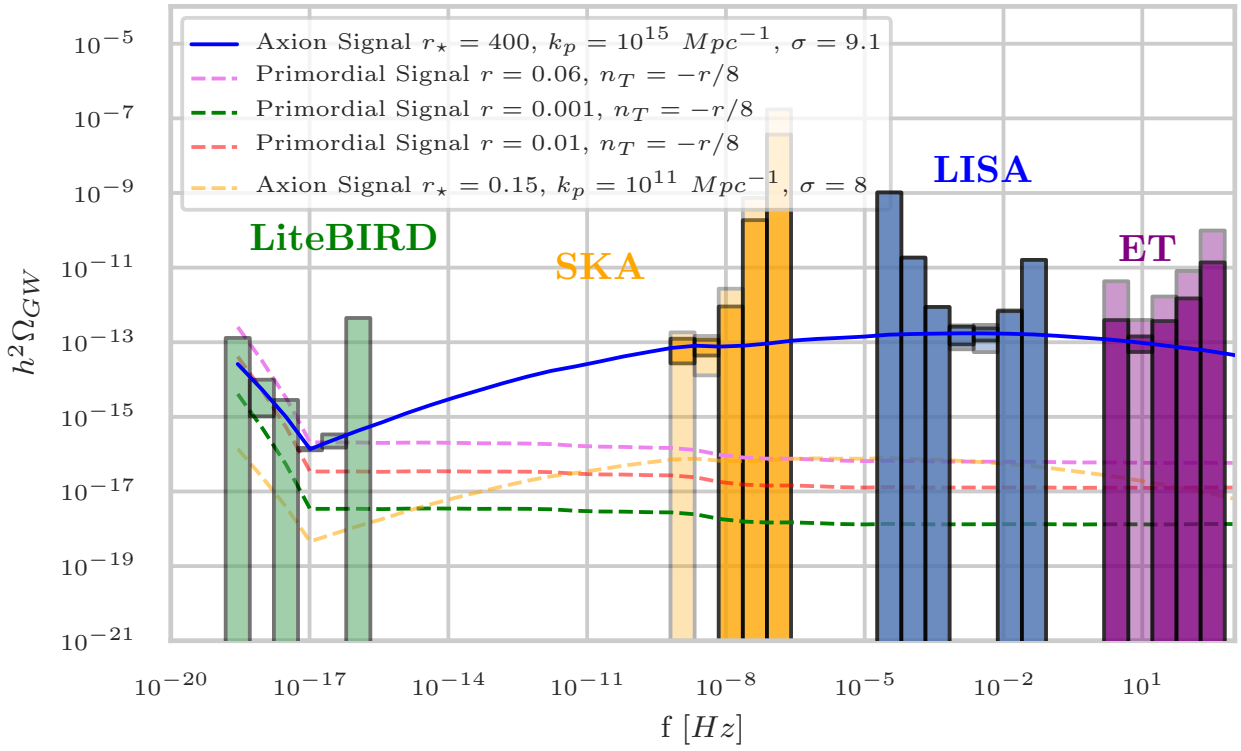

Figure 5.13: Expected 1σ error bars on Ω_{GW} for the AX1 model (the solid blue line) for the LiteBIRD (green), SKA (orange), LISA (blue), and ET (purple). We show the constraints with and without the astrophysical foregrounds in the light and dark shared areas, respectively. We use the logarithmic binning in wavenumber with $\Delta \ln k = 1.2$. We also show for comparison the other tensor spectrum models adopted in this work (dashed lines), including the BICEP2/Keck/Planck upper bound $r = 0.06$.

model despite excellent prospects for the detection, since these experiments are so sensitive that the error bars would be for the most part invisible, similarly to what happens for the μAres experiment.

Figures 5.14 and 5.15 show that the error bars for the DO Conservative and Optimal designs are similar for this particular model, with the less-sensitive Conservative setup having two detections missing with respect to the Optimal case in the last two bins. In both cases, the foreground contamination appears to have a small impact. Figure 5.16 shows the error bars for the AEDGE atomic interferometer: this detector shows a similar sensitivity to the DO Optimal design, with the latter being slightly less sensitive while covering a wider frequency range.

The error bars on the AX1 model for the μAres mission are shown in Figure 5.17. The foreground contamination plays a minor role in this very high SNR case, and μAres is capable of detecting this model across an impressive range of frequencies $\sim 10^{-6} - 10^{-2}$ Hz, even for a value as high as $\sigma_{fg} = 0.1$ for the BBH+BNS multi-band foreground cleaning, as provided by Advanced LIGO/Virgo.

Next, we show the error bars for the AX2 model. This set was specifically tuned to show the capability of the axion-SU(2) to pro-

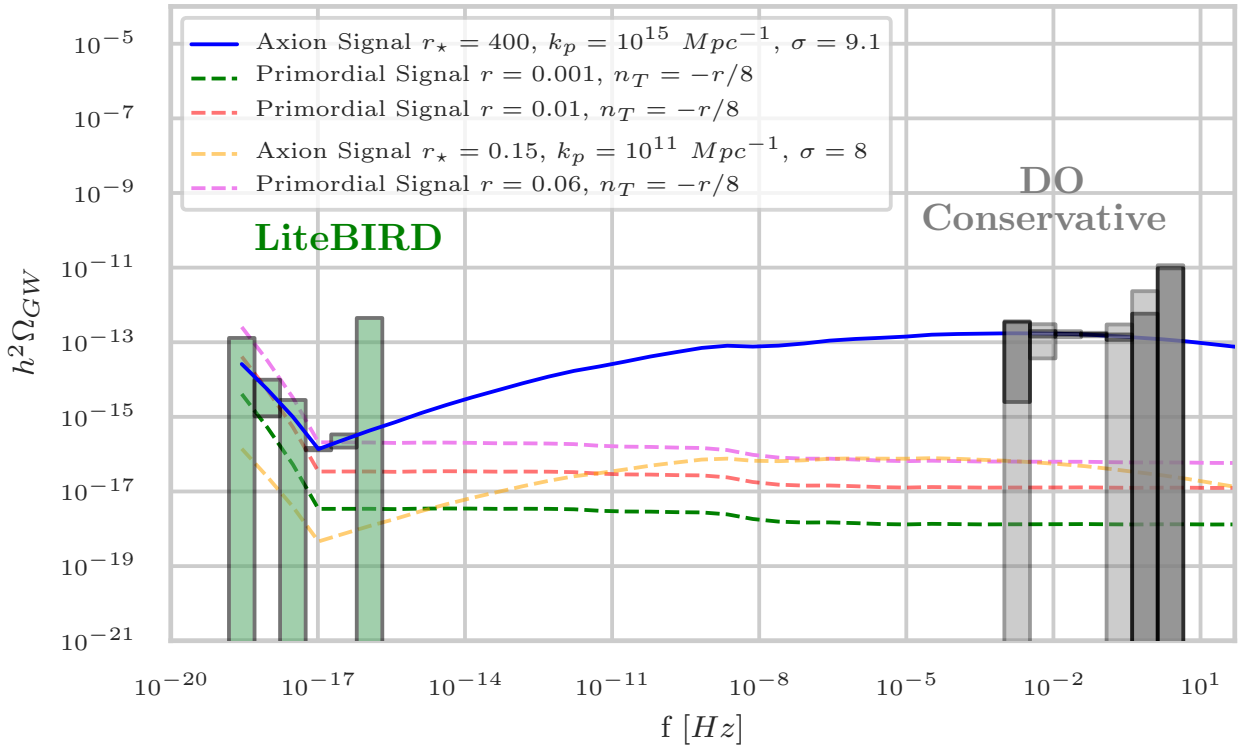

Figure 5.14: Same as Figure 5.13 but for the DO Conservative.

duce a signal out of the reach of LiteBIRD while being detectable in the interferometer bands. For this case we use a larger bin size, $\Delta \ln k = 2.0$. In Figures 5.18, 5.19 and 5.20, we show the results for this model for μAres, DECIGO and BBO, respectively. Concerning the BBH+BNS foreground cleaning, we adopt for μAres a value $\sigma_{fg} \sim 10^{-3}$, which is enough to have high-significance detections in three bins in the case with foregrounds. For DECIGO we show instead two different options for the foreground treatment: the very light shaded error bars represent the case in which we only use the spectral dependence to subtract the foreground, while the light shaded error bars assume instead multi-band cleaning with $\sigma_{fg} \sim 10^{-3}$. The dark shaded error bars show, as always, the case without foregrounds. In this case, we see that the addition of foregrounds for DECIGO does not allow any detection, while we have a detection at high significance in one bin in the case without foregrounds contamination.

BBO, on the other hand, should be able to resolve and subtract all compact sources (see Discussion in Section 5.4): because of this, the error bars for BBO with and without foregrounds are the same, showing detections of the AX2 model at high-significance in three

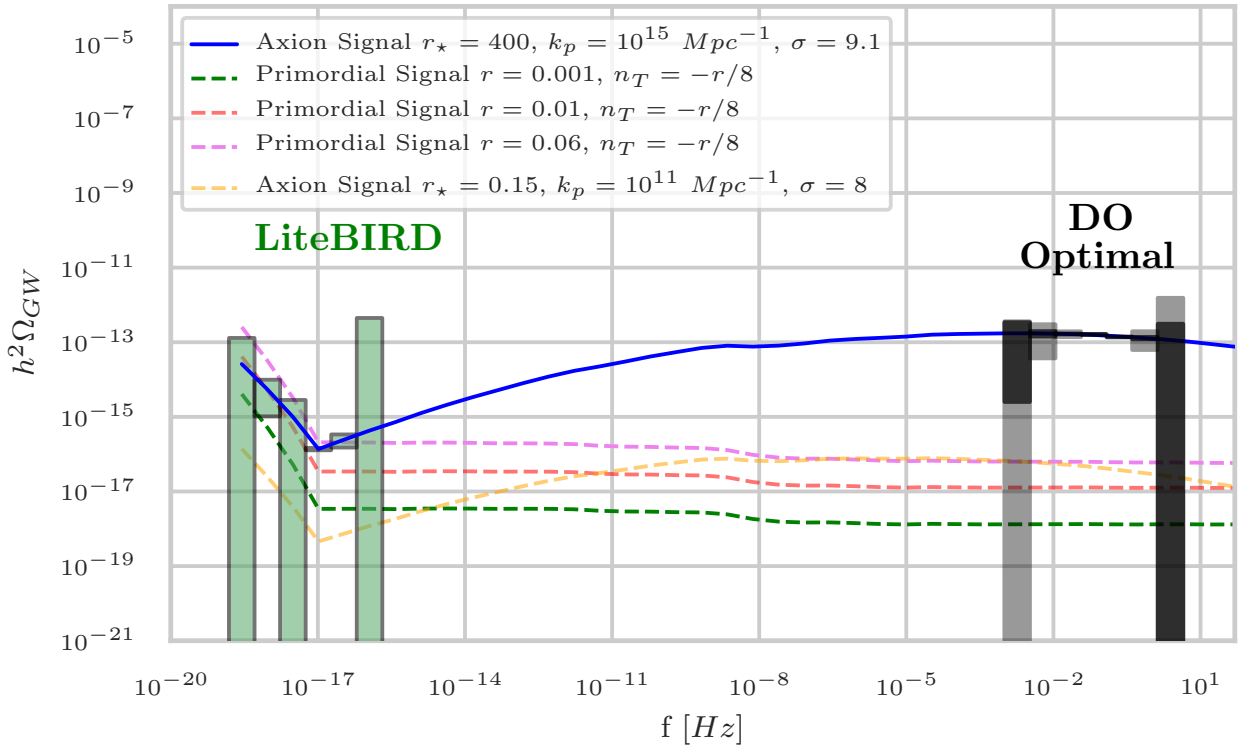

Figure 5.15: Same as Figure 5.13 but for the DO Optimal.

bins.

We have explored the possibility of having an axion-SU(2) tensor spectrum peaked in the PTA frequency range with the AX3 model, producing a signal detectable by SKA and LiteBIRD – while still complying with the BICEP2/Keck/Planck upper bound on CMB scales – but outside the reach of LISA and ET (even without the foreground contamination, see Figure 5.21). This behavior of the tensor spectrum can be obtained thanks to the attractor nature of the axion-SU(2) model, which poses a minimum value for the Gaussian width of the spectrum bump σ for a given peak scale k_p (see Section 5.1.2). Although we do not show error bars for other experiments, we checked that the AX3 model is also not detectable by DO, AEDGE and DECIGO, while μAres and BBO can detect it at high significance in three bins, even when accounting for foregrounds.

5.5.3 *Error bars on single-field slow-roll models and combined constraints on n_T*

We consider now the two single-field slow-roll models with $r = 0.01$ and 0.001, both with $n_T = -r/8$. We choose a bin size of $\Delta \ln k = 2.0$.

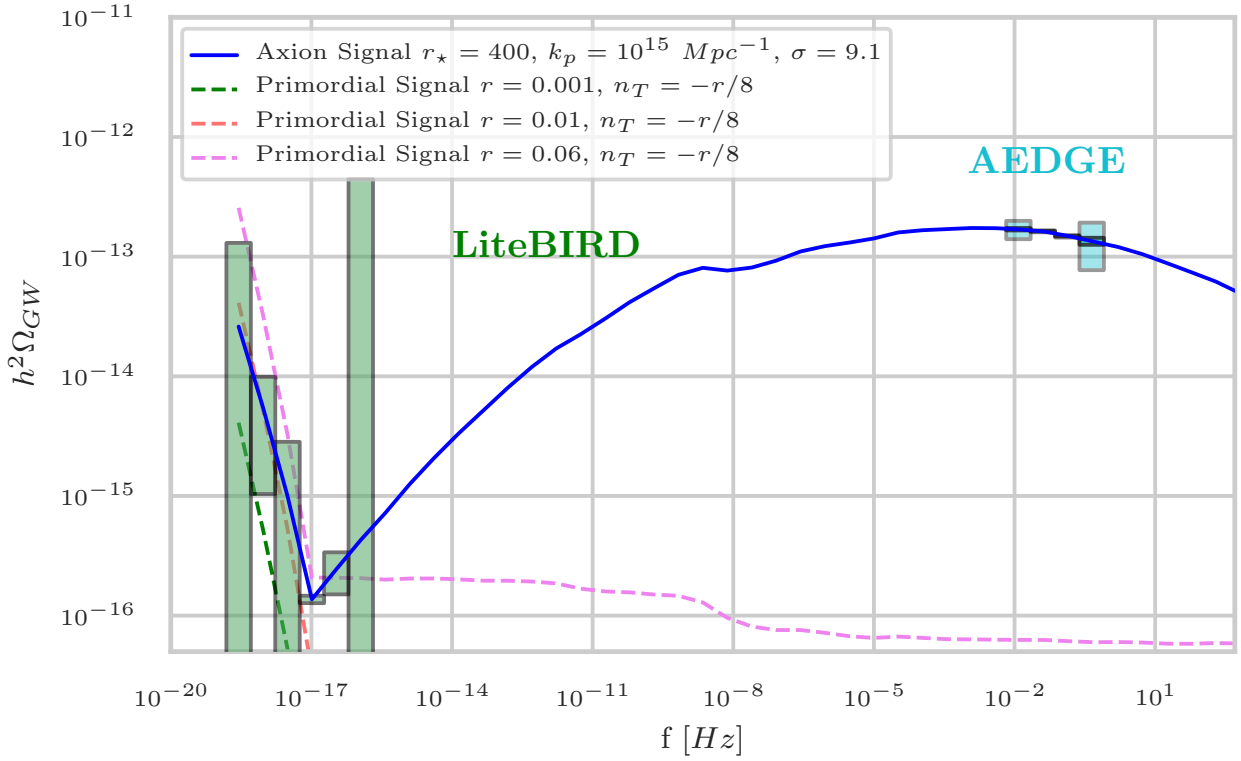

Figure 5.16: Same as Figure 5.13 but for the AEDGE. Note a different scale for the vertical axis.

The model with the larger $r = 0.01$ is easily detected by LiteBIRD in multiple bins. On interferometric scales, it can be detected in two bins by BBO (Figure 5.23), while μAres can detect this model only without foregrounds (Figure 5.24), and DECIGO, in its standard design, cannot detect this model even without foregrounds (Figure 5.22).

To have a detection in at least one bin for the lower $r = 0.001$, we try increasing the binning scale to $\Delta \ln k = 4.0$. This model is detected by LiteBIRD on the CMB side, however not even BBO, the most sensitive among the considered experiments, can detect it on the side of interferometers (Figure 5.25). The SNR remains smaller than 1 even considering a single bin enclosing the whole BBO band.

With the extremely high sensitivity of BBO at frequencies $\sim$ 16 orders of magnitude larger than the CMB, one can create a significant lever-arm, providing interesting constraints on the spectrum tilt n_T. The path of multi-frequency measurements of the primordial tensor spectrum has been explored in the past, in the context of forecasts (see for instance Smith et al., 2006, for the combination of Planck/CMBPol and DECIGO/BBO), as well as of the analysis of

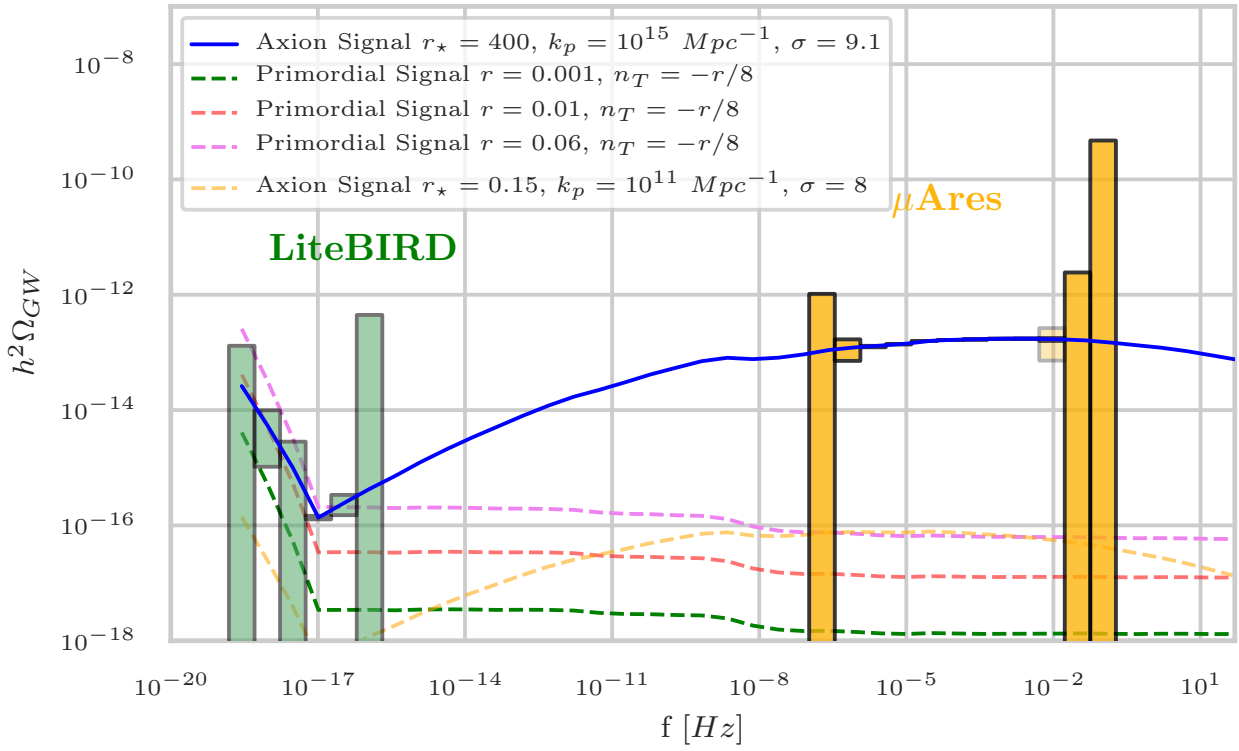

Figure 5.17: Same as Figure 5.13 but for the μAres. Note a different scale for the vertical axis.

available datasets, combining for instance the Planck, BICEP2/Keck, PPTA and LIGO data (Meerburg et al., 2015), and adding SPTPol (Lasky et al., 2016b) or COrE and other indirect constraints (Cabass et al., 2016) to the previous datasets.

Here, we update the forecasts on the tensor power spectrum amplitude r and the tilt n_T from the combination of CMB and laser interferometers, considering in particular the two configurations LiteBIRD+LISA and LiteBIRD+BBO. We take into account foregrounds for all experiments. We bin the LISA and BBO sensitivity curves with $\Delta \ln k = 2.0$ and 4.0, respectively. We explore the full cosmological parameters space including $\{A_S, n_S, \tau, \Omega_b h^2, \Omega_c h^2, H_0, r, n_T\}$ via the Monte Carlo Markov Chain (MCMC). We modify the `MontePython` MCMC package (Audren et al., 2013; Brinckmann and Lesgourgues, 2018) by adding a Gaussian likelihood for the interferometers (Mandic et al., 2012)

$$\mathcal{L}(\hat{\Omega}_i, \sigma_i | \vec{\theta}) \propto \exp\left[\frac{1}{2}\sum_i \frac{(\hat{\Omega}_i - \Omega_M(f_i;\vec{\theta}))^2}{\sigma_i^2}\right], \tag{5.45}$$

where $\Omega_M(f|\vec{\theta})$ is the proposed model as a function of frequency f and model parameters $\vec{\theta}$, $\hat{\Omega}_i$ the fiducial model in the frequency bin

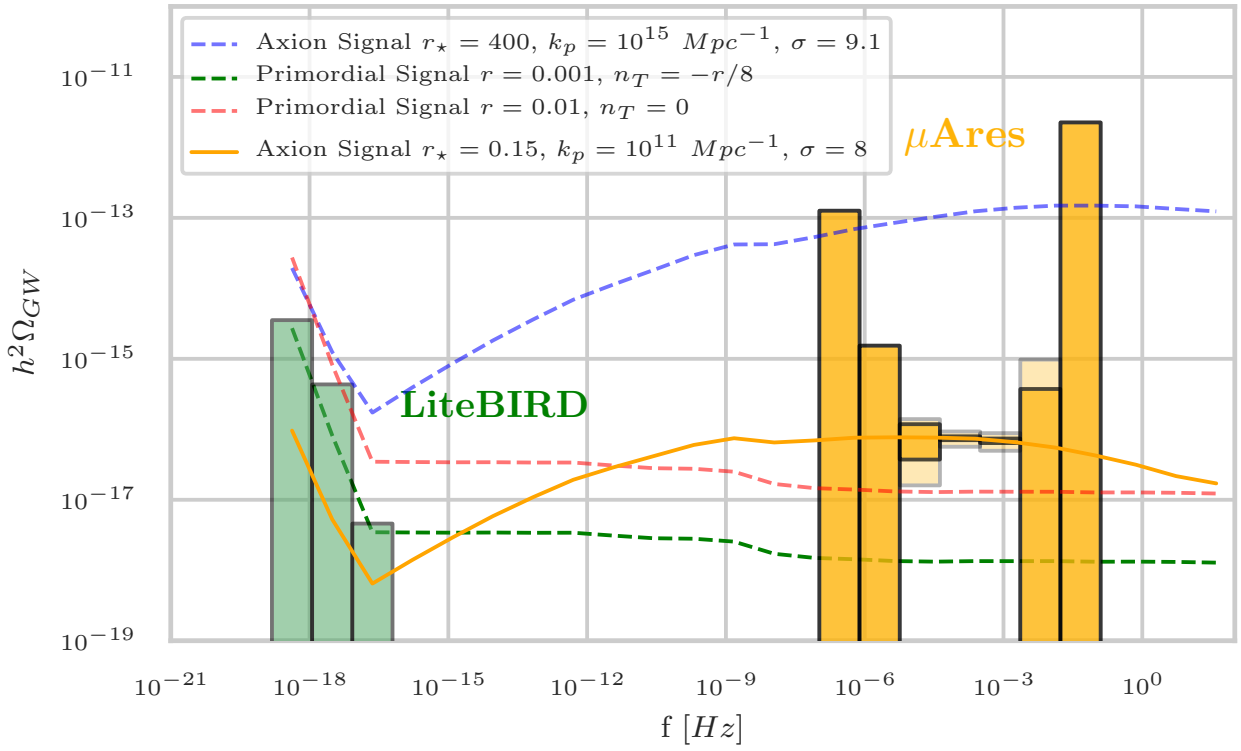

Figure 5.18: Expected 1σ error bars on Ω_{GW} for the AX2 model (the solid orange line) for the LiteBIRD (green) and μAres (orange). We show the constraints with and without the astrophysical foregrounds in the light and dark shaded areas, respectively. Note that the error bars with foregrounds are computed assuming a multi-band cleaning with $\sigma_{fg} \sim 10^{-3}$. We use the logarithmic binning in wavenumber with $\Delta \ln k = 2.0$. We also show for comparison the other tensor spectrum models adopted in this work (dashed lines).

f_i and σ_i^2 its variance in the same bin. For the CMB, we adopt instead the standard Gaussian likelihood (Perotto et al., 2006), with noise and foregrounds C_ℓ spectra determined from the LiteBIRD specifications (see Section 5.2.2).

We adopt for the fiducial model $r = 0.01$ and $n_T = -r/8$ given by the inflationary consistency relation, while the values for the other cosmological parameters are taken from Ref. (Planck Collaboration, 2018). We show in Figure 5.26 the $1D$ and $2D$ marginal distributions of the n_S, r and n_T parameters for four possible observational configurations: (i) constraints from LiteBIRD alone (red contours); (ii) constraints from LiteBIRD and LISA (grey contours), (iii) constraints from LiteBIRD and BBO (blue contours); and (iv) constraints from LiteBIRD and BBO assuming the fiducial signal in the LiteBIRD range but no signal in the BBO range, that is $\hat{\Omega}_i = 0$ in every bin f_i (orange contours). This configuration is chosen to quantify possible deviations from the consistency relation in the eventuality of a detection at $\sim 5\sigma$ by LiteBIRD, but no detection in BBO.

For (i) we recover the following best-fitting parameters with 1σ uncertainties: $n_S = 0.9665^{+0.017}_{-0.018}$, $r = 0.013^{+0.003}_{-0.006}$ and $n_T = 0.09^{+0.18}_{-0.20}$; thus, a test of the consistency relation is out of discussion using the

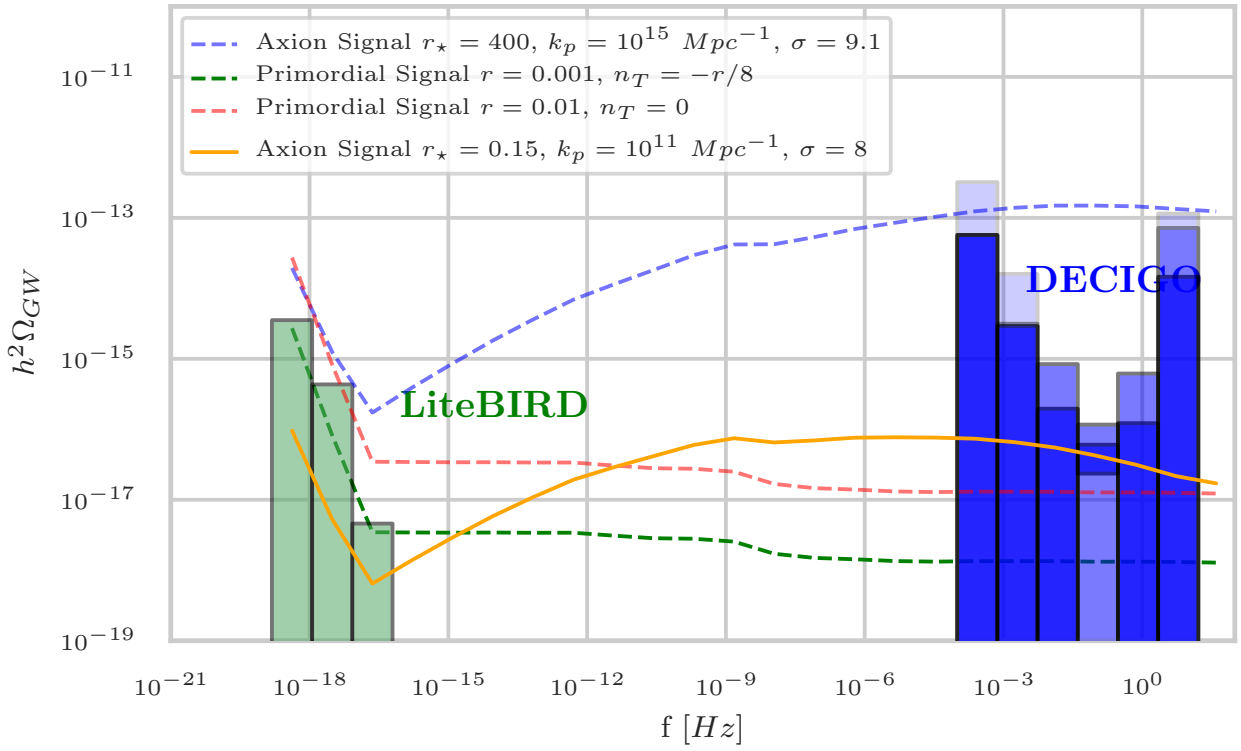

Figure 5.19: Same as Figure 5.18 but for the DECIGO. Note that we show two different cases for the error bars with foregrounds: the very light shaded areas correspond to the case in which we we only use the spectral dependence to subtract the foreground, while the light shaded error bars assume instead multi-band cleaning with $\sigma_{fg} \sim 10^{-3}$.

CMB alone: only extreme deviations from the consistency relation (e.g., axion-SU(2) models) can be detected in this case.

For (ii) the addition of LISA impacts mainly the error on n_T by limiting the range of allowed blue-tilted models, but this is still not enough to distinguish the consistency relation from the scale-invariant case. In this case the recovered parameters are $n_S = 0.9669 \pm 0.017$, $r = 0.0109 \pm 0.003$ and $n_T = 0.026^{+0.18}_{-0.10}$. The further inclusion of the ground-based interferometer ET jointly with LISA does not improve significantly the constraints with respect to LISA alone because of the large foreground contamination affecting this experiment.

For (iii) the effect of adding BBO is evident in Figure 5.26: the constraints on r and n_T become significantly tighter and also the maxima of the marginal distributions for the recovered parameters are very close to their fiducial values. Using the LiteBIRD+BBO configuration, we recover the following parameters: $n_S = 0.9649^{+0.016}_{-0.017}$, $r = 0.0100 \pm 0.0011$ and $n_T = -0.00125^{+0.011}_{-0.007}$. Also in this case, however, the error on the tensor spectral index, although remarkably smaller than the LiteBIRD only case, does not allow to distinguish the consistency relation from a scale-invariant case.

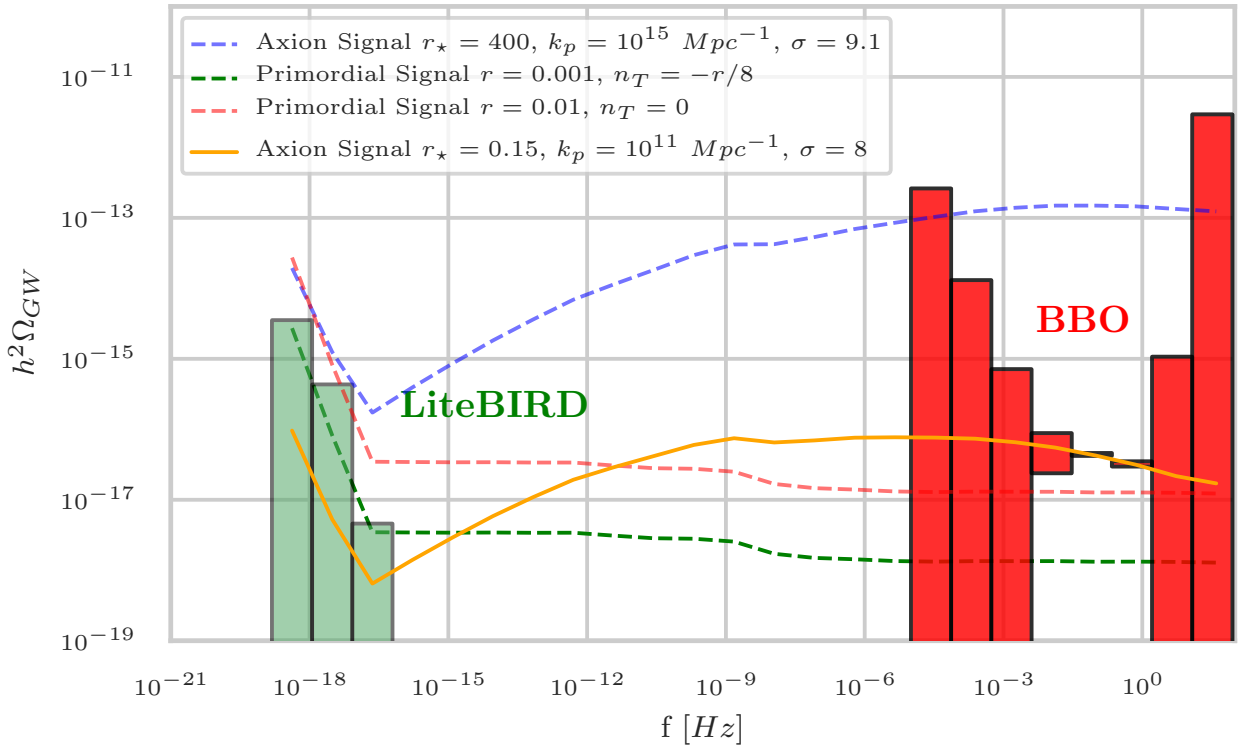

Figure 5.20: Same as Figure 5.18 but for the BBO.

For (iv) we recover $n_S = 0.96559^{+0.018}_{-0.016}$, $r = 0.0076^{+0.0017}_{-0.0016}$ and $n_T = -0.15^{+0.12}_{-0.05}$. As it can be argued from Figure 5.26, the recovered tensor-to-scalar ratio shows a bias: this is because, to have an undetectable signal at interferometers scales, the spectrum must have a large red tilt, so large that it affects also the CMB scales. Therefore, even in the absence of a consistency relation detection, if we do not detect a signal in BBO, the red tilt in the power-law model of tensor power spectrum has to be so large that we can detect its departure from the single-field slow-roll consistency relation.

5.6 *Chapter summary*

We have calculated in this Chapter the sensitivities of CMB, PTA, and interferometers for SGWB from the primordial GW across 23 decades in frequency. Not only we do provide the sensitivity curves for the GW energy density parameter Ω_{GW} (Figure 5.12) as commonly done in the literature, but also we provide the binned 1σ error bars on the model predictions for Ω_{GW} from two representative classes of sources of the primordial SGWB: the quantum vacuum fluctuation in the metric tensor (i.e., the homogeneous solution of Einstein's equation)

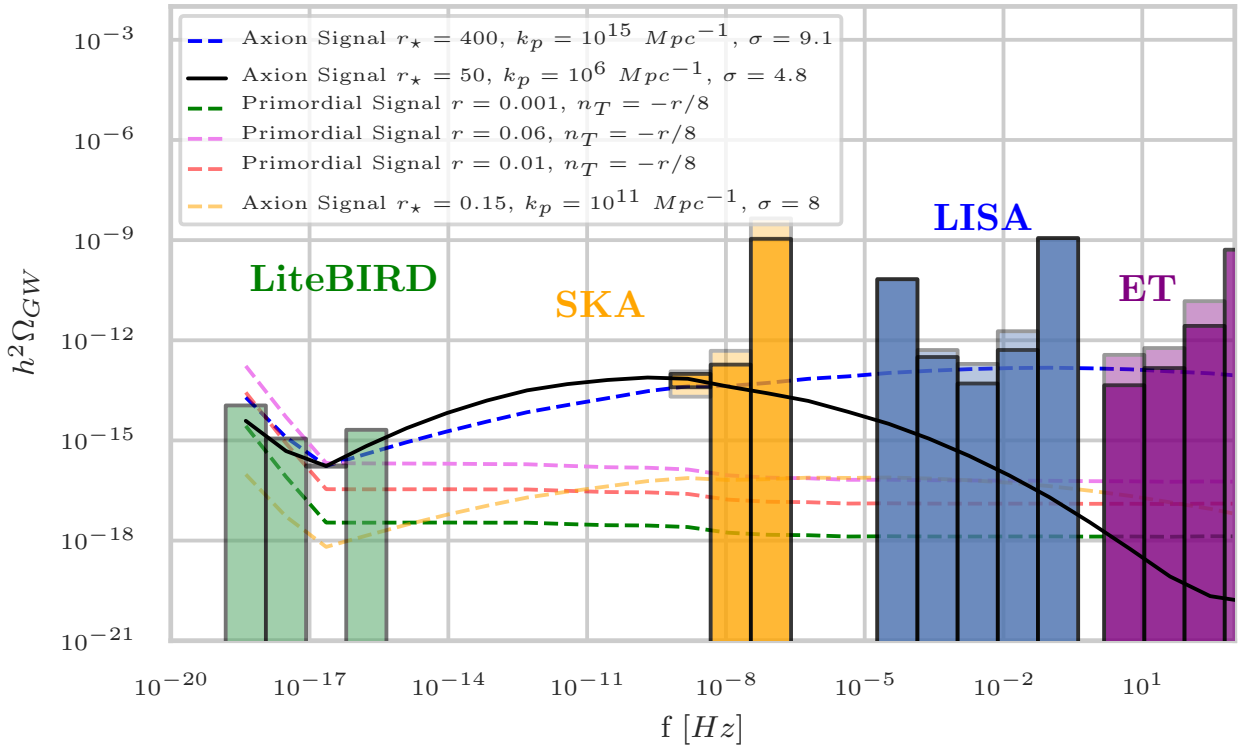

Figure 5.21: Same as Figure 5.13 but for the AX3 model, with a logarithmic binning of $\Delta \ln k = 2.0$.

from single-field slow-roll inflation models with $r = 0.01$ and 0.001 and the tensor tilt given by the consistency relation $n_T = -r/8$, and the source-induced primordial GW from the spectator axion-SU(2) model (i.e., from the stress energy tensor in the right hand side of Einstein's equation).

For CMB and PTA we considered the most ambitious future experiments LiteBIRD and SKA, respectively, while for interferometers we considered a host of funded and proposed space (LISA, μAres, DO, AEDGE, DECIGO, BBO) and ground-based (ET) GW observatories covering a wide range of frequencies from 10^{-7} to 10^{3} Hz. We took into account the instrumental noise, the response functions, and most importantly the contamination of the astrophysical foregrounds in the forecasts. We have presented all the details in our computation with homogeneous assumptions for all experiments in one place, which should provide convenient resources for the experiments in search of the primordial SGWB.

We showed that it is possible to tune the axion-SU(2) model parameters to have detections with high significance in multiple frequency bins in the CMB, PTA and space interferometers frequency ranges, even when accounting for the foreground contamination

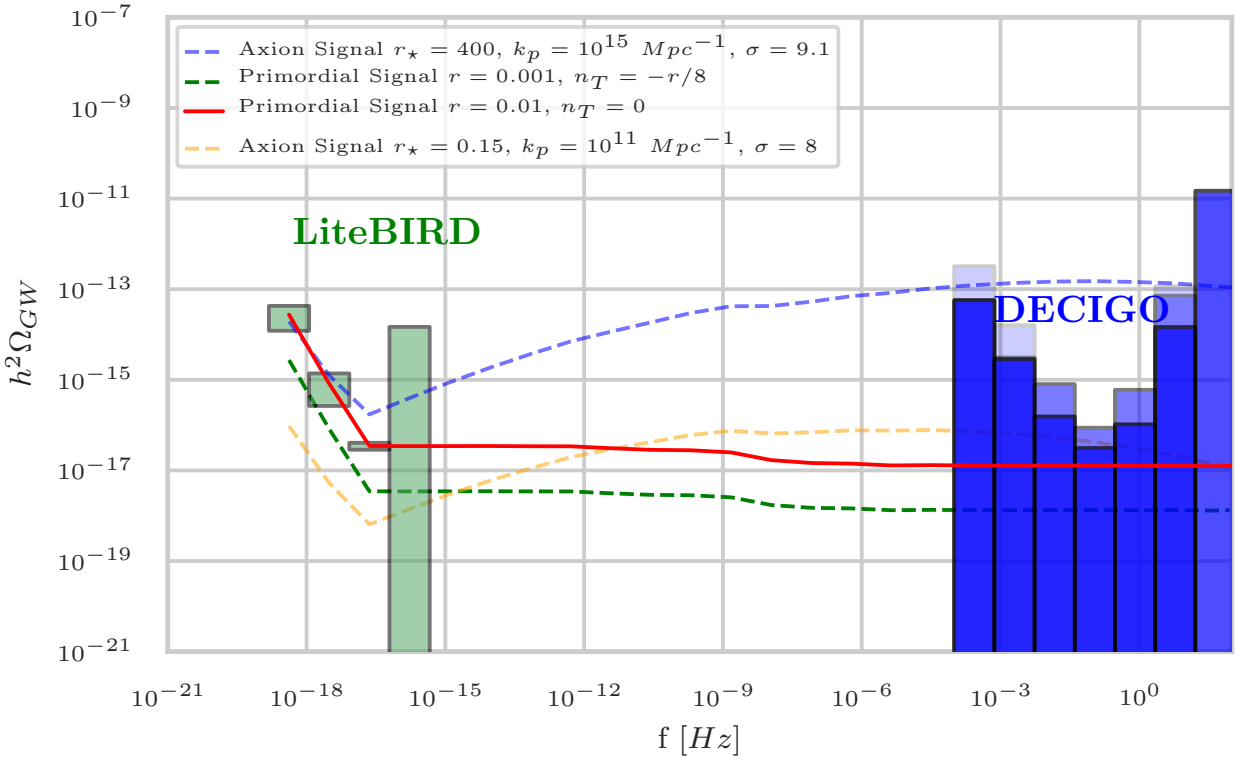

Figure 5.22: Expected 1σ error bars on Ω_{GW} for the single-field slow-roll model with $r = 0.01$ and $n_T = -r/8$ (the solid red line) for the LiteBIRD (green) and DECIGO (blue). Dark shaded areas correspond to error bars without foregrounds. Concerning error bars with foregrounds, we show two different cases: the very light shaded areas correspond to the case in which we only use the spectral dependence to subtract the foreground, while the light shaded error bars assume instead multi-band cleaning with $\sigma_{fg} \sim 10^{-3}$. We use the logarithmic binning in wavenumber with $\Delta \ln k = 2.0$. We also show for comparison the other tensor spectrum models adopted in this work (dashed lines).

(Figures 5.13-5.17), while remaining consistent with all current upper limits. We also showed that the parameters of the axion-SU(2) model can be chosen in such a way that the signal is out of reach for CMB experiments, while being detectable by the most sensitive space interferometers, i.e., μAres, DECIGO and BBO (Figures 5.18-5.20). Conversely, the model parameters can be tuned in order to obtain a signal detectable by CMB and PTA experiments, while remaining outside the reach of space-borne interferometers LISA, DO, AEDGE and DECIGO and the ground-based one, ET (5.21). This motivates the search of a signal in a multi-frequency approach, such as the one we adopted in this work: for a complete characterization of the primordial SGWB, it is necessary to cover all three CMB, PTA and interferometers ranges.

On the other hand, the situation is different for future ground-based interferometers, for which the current estimates for the foreground contamination prevent detections of the axion-SU(2) model. It is indeed difficult to obtain a tensor spectrum detectable by the ET experiment when taking into account foregrounds while still complying with the BICEP2/Keck/Planck upper bound on CMB scales (Figure

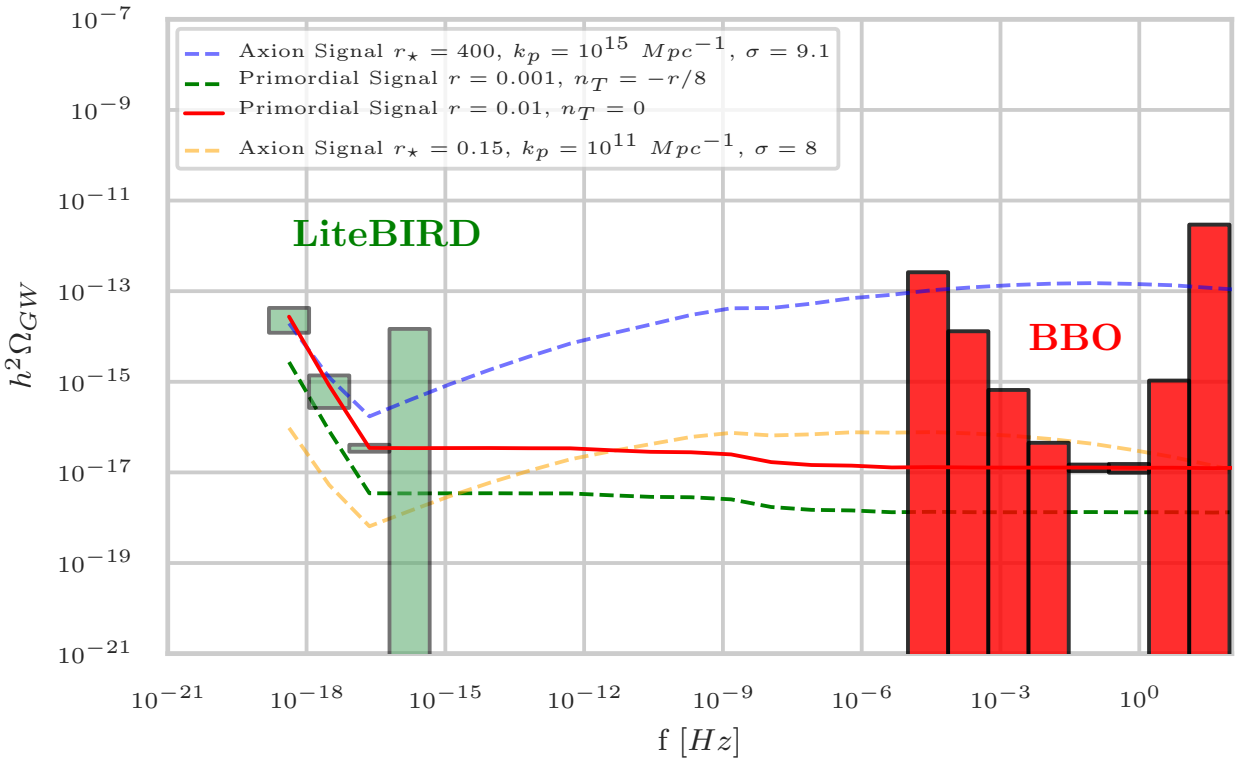

Figure 5.23: Same as Figure 5.22 but for the BBO.

5.13). This is due to the attractor behavior of the axion-SU(2) model, posing an upper limit on the width of the spectrum bump for a given peak scale k_p.

For what concerns the single-field slow-roll power spectrum, we showed that the $r = 0.01$ model can be detected comfortably and simultaneously by LiteBIRD, by BBO (Figures 5.23, by μAres (but only in the case without foregrounds, see Figure 5.24), but not by DECIGO in its standard design (Figure 5.22). We also found that the lower tensor-to-scalar ratio $r = 0.001$ can be detected only by LiteBIRD, while not even the ultra-sensitive BBO can detect such a signal on the interferometers side (Figure 5.25).

Finally, we presented updated constraints on r and n_T combining LiteBIRD with LISA and LiteBIRD with BBO, to leverage on the scale dependence of the tensor spectrum. We conclude that distinguishing the single-field slow-roll consistency relation from the scale-invariant case remains out of reach even for LiteBIRD+BBO. However, if we detect tensors in the CMB but not in BBO, we would detect a significant deviation from the consistency relation in the context of the power-law primordial spectrum.

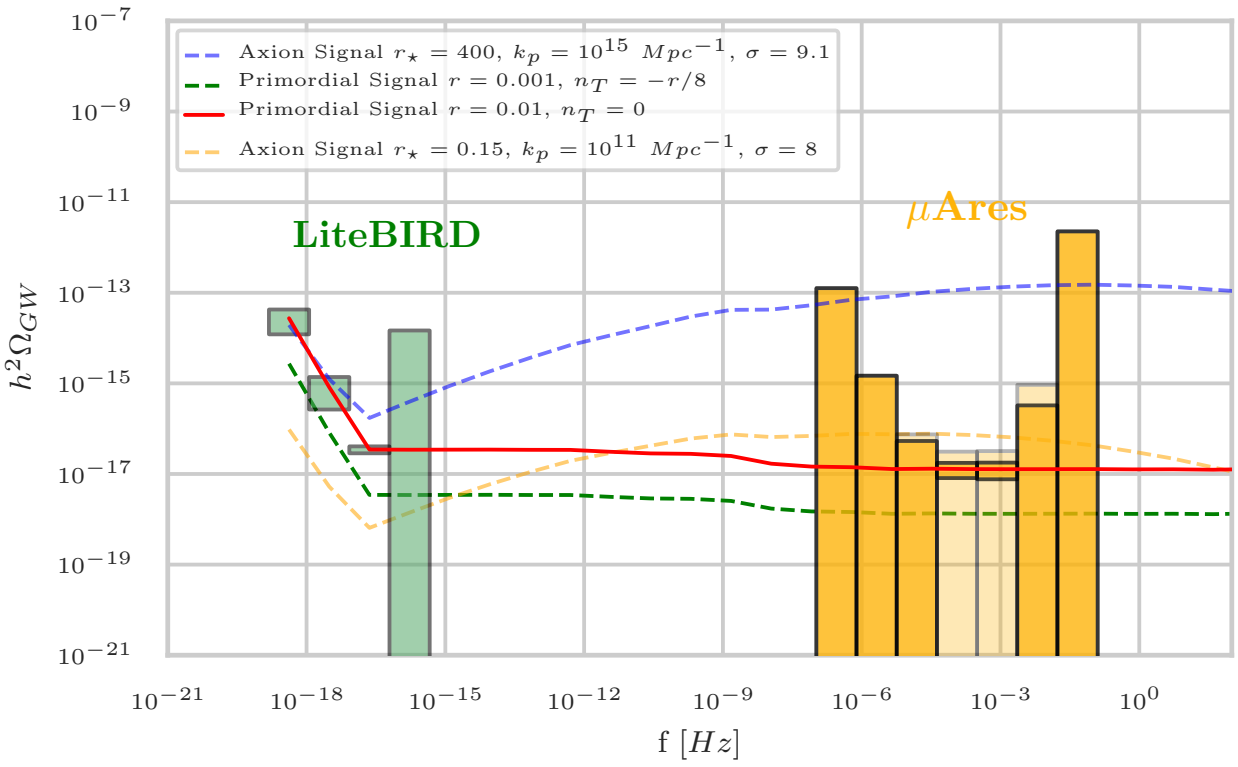

Figure 5.24: Same as Figure 5.22 but for the μAres. Note that the error bars with foregrounds are computed assuming a multi-band cleaning with $\sigma_{fg} \sim 10^{-3}$.

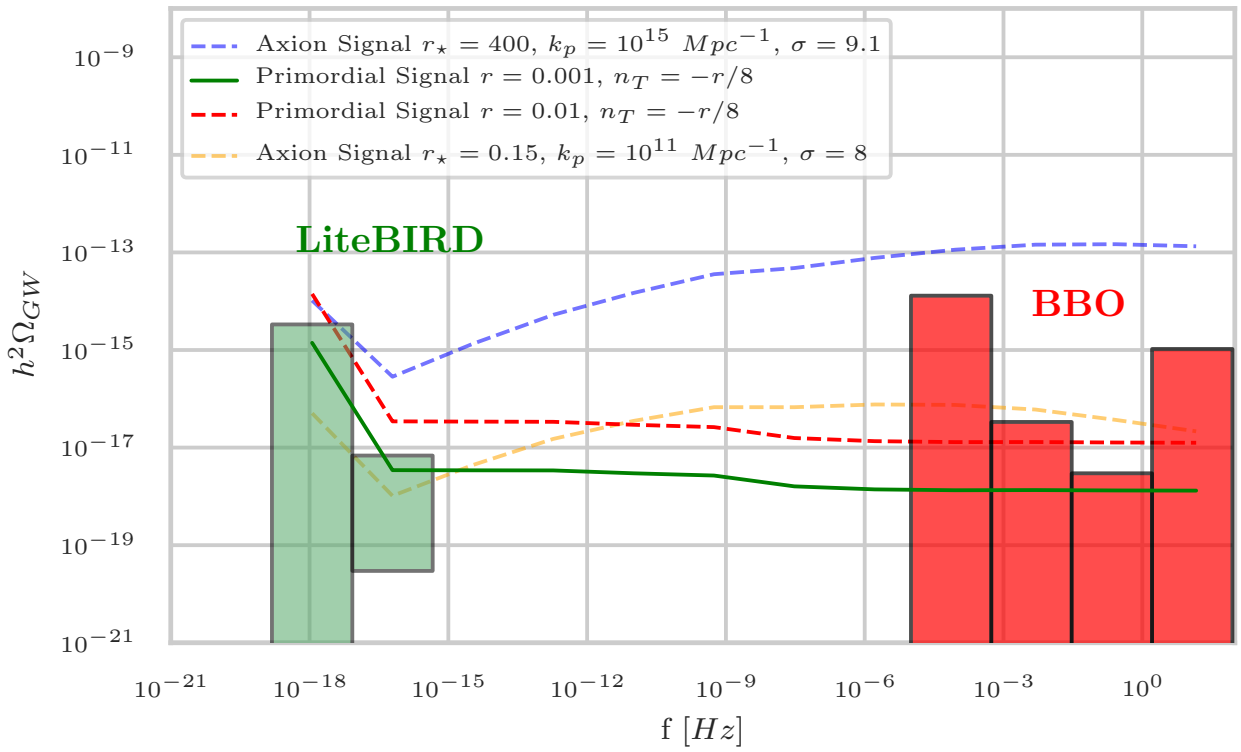

Figure 5.25: Same as Figure 5.23 but for $r = 0.001$ with a logarithmic binning of $\Delta \ln k = 4.0$.

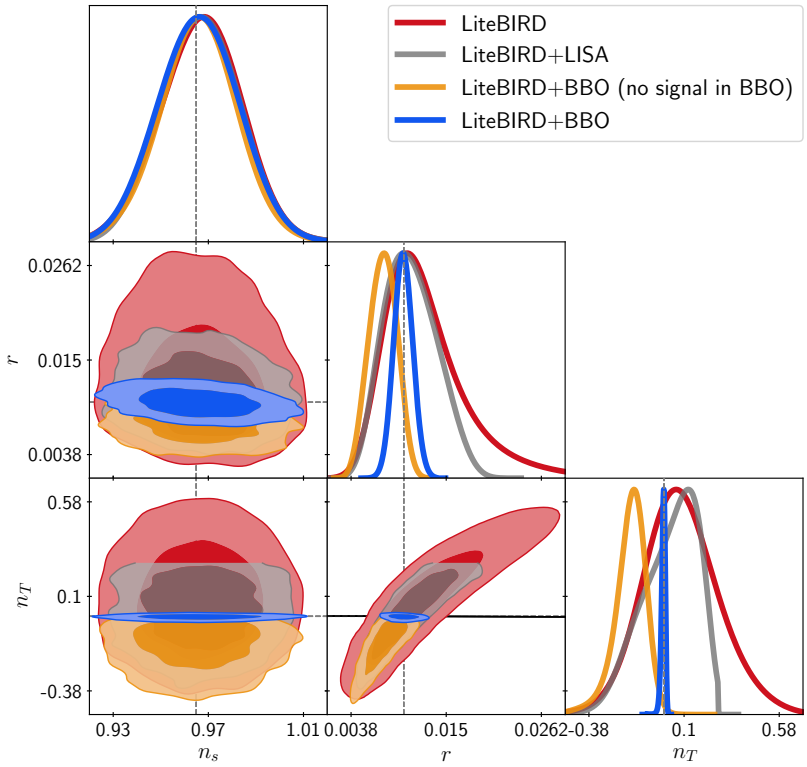

Figure 5.26: 1D and 2D marginal distributions of the n_S, r and n_T parameters for four possible observational configurations: LiteBIRD alone (red contours), LiteBIRD+LISA (grey), LiteBIRD+BBO (blue), and LiteBIRD+BBO assuming the fiducial signal in the LiteBIRD range but no signal in the BBO range (orange). The contours show the 68% and 95% CL, the dashed lines show the fiducial parameters, and the solid black line shows the consistency relation.

6
Conclusions and prospects

The primordial SGWB is a window on quantum gravitational effects at extreme energies, probing the boundaries of our current knowledge of quantum mechanichs and Gravity. This sought-after signal contains, indeed, a unique wealth of information on the very early Universe physics and could allow us to probe energy scales unreachable by terrestrial particle colliders.

Because of the major impact that this discovery would have on cosmology, we want to assess what is the ultimate information we can get on this signal. To do so, in this Thesis, we studied the possibility of obtaining precision measurements on the shape of the spectrum of the primordial GWs, taking two main steps while pursuing this major goal:

1. first, we develop a *model-independent treatment for characterizing the shape of the primordial tensor power spectrum, including an unprecedented level of realism in our analyses which reflects the current knowledge concerning present and future CMB B-mode experiments*;

2. second, we provide *forecasted constraints across* $\sim$ 23 *decades in frequency on the shape of the primordial tensor spectrum* considering all the probes and all configurations, especially the ultimate and most ambitious *CMB B-mode probes, space-borne and ground-based interferometers and PTA surveys*.

In addition to the ultimate experiments, we also consider those operating now or imminently, with the purpose of showing how our knowledge of physics and our targets will change depending on the progresses of observations.

For the same reason, we particularly refine our analyses for CMB *B*-mode experiments: as highlighted by our work, they currently represent the most promising channel for near future detection, and therefore they will be of the utmost importance in shaping the future of SGWB observations.

The first step in our study has been assessing the potential of future B-mode experiments in constraining the shape of the SWGB spectrum: we applied PCA to the tensor primordial power spectrum and investigated the capability of three future CMB B-mode experiments (namely LiteBIRD, SO and CMB-S4) to detect deviations from scale-invariance in a model-independent way (see Chapter 4 and the work in Campeti et al. (2019b)).

In order to be as realistic as possible, our forecasts included the contributions of gravitational lensing, instrumental noise and – for the first time in this type of literature – the astrophysical foreground residuals due to Galactic thermal dust and synchrotron emissions. We found that residuals undoubtedly have a substantial effect on the uncertainty on r and on the PCA modes, are relevant for both satellite and ground-based experiments, and cannot be neglected in any treatment which aspires to be realistic.

Studying the PCA modes and their associated uncertainty, we characterized the wavenumber-range for which each of the three experiments will be most sensitive to features in the power spectrum: the SO and CMB-S4 sensitivities peak around the recombination bump, while LiteBIRD proved to be sensitive also to the reionization bump.

In the construction of the PCA basis, we used a reference angular power spectrum with no tensor contribution, since r is still undetected: therefore, we had to implement a technique to chose the number of PCA modes to retain in our basis, in order to properly represent cases with nonzero tensor contributions. Moreover, we removed the tensor-to-scalar ratio r from the parametrization of the tensor power spectrum, expressing the latter exclusively as a linear combination of PCA modes.

We found, by comparing our Fisher and MCMC predictions on the PCA modes uncertainties, that the main limitation when applying PCA to the tensor power spectrum is represented by the physicality prior on P_T, that is the condition that it must be positive definite. In this respect, we also found that including r in the tensor power spectrum parametrization worsen the impact of the physicality prior on the PCA modes, hence our choice of parametrizing the spectrum solely as a linear combination of PCA modes.

We provided also two examples of application of PCA to primordial GWs. We first apply it to a red-tilted toy model of tensor spectrum, resulting in a successful performance of the PCA formalism, and then we use it to test the inflationary consistency for an $r = 0.05$ and an $r = 0.01$ model, with the expected result that neither LiteBIRD nor CMB-S4 will be able to test this relation even in the $r = 0.05$ case.

The second step of our study was to extend the analysis by including, beside B-mode probes, the constraining power on the shape of the SWGB of GW laser and atomic interferometers and PTA surveys (see Chapter 5 and the work in Campeti et al. (2020)).

We provided sensitivity curves for the GW energy density parameter Ω_{GW} with binned 1σ error bars on the model predictions for two models of primordial SGWB: the standard single-field slow-roll inflation model and the spectator axion-SU(2) model.

We performed our forecasts for a wide array of experiments: we chose as representative of future CMB B-mode probes the LiteBIRD satellite mission, for PTA the SKA survey, and for interferometers we considered the proposed space missions LISA, μAres, DO, AEDGE, DECIGO, BBO and ground-based observatory ET.

While in the literature the astrophysical foreground contribution is often overlooked, in favor of a more simplified and sometimes too optimistic approach, we included them in our analysis for each of the considered experiments, using the state-of-the-art simulations for the LiteBIRD foregrounds and approximate analytical fitting formulas for interferometers and PTA. Furthermore, we introduced and applied into our pipeline a new filter $Q(f)$ for direct detection experiments, maximizing the SNR ratio with and without foregrounds.

We get the most comprehensive picture of the status of SGWB observations, by considering a variety of scenarios: concerning the axion-SU(2) model, we found that its parameters can be tuned in order to obtain a signal with simultaneous detections at high significance in multiple bins in the CMB, PTA and space interferometers frequency ranges, even when accounting for the foreground contamination, while remaining consistent with all current upper limits. We also found that another choice of parameters can produce a signal unreachable by CMB experiments and, at the same time, detectable by the most sensitive space interferometers. Similarly, an appropriate tuning of the model parameters can produce a signal detectable by CMB and PTA experiments, but not by most of the space-borne and the ground-based detectors. We conclude that a complete characterization of the primordial SGWB requires extensive frequency coverage, such as the one provided by the combination of CMB, PTA and interferometers.

The single-field slow-roll power spectrum with $r = 0.01$, on the other hand, can only be detected by LiteBIRD, BBO and μAres (but only in the case without foregrounds). Moreover, the $r = 0.001$ can be detected only by LiteBIRD among all the experiments considered in this work: the CMB remains therefore the most powerful tool for detection within the framework of the single-field slow-roll scenario.

We also updated the constraints on r and n_T parameters for the

standard single field slow-roll scenario with $r = 0.01$: we combine LiteBIRD with LISA and LiteBIRD with BBO, fully exploiting to lever arm created by the scale dependence of the tensor spectrum. We extended then the test of the consistency relation previously performed using the PCA technique solely for CMB experiments: we include in this case the space interferometers LISA and BBO in addition to LiteBIRD. This analysis showed that, although distinguishing the single-field slow-roll consistency relation from the scale-invariant case is not achievable even with the powerful combination of LiteBIRD and BBO, if we detect tensors in the CMB but not in BBO, we would detect a deviation from the consistency relation.

We consider now the future perspectives of our work, starting with the possibilities offered by our model-independent analysis of the tensor spectrum. From a theoretical point of view, we stress that the PCA formalism can be applied to any scenario of Early Universe to quantify possible departures from the simplest inflationary scenarios, as we do in a toy example of a red-tilted model. Moreover, this model-independent formalism could be applied in a systematic exploration of the models present in the literature, in order to quickly assess the detectability by future CMB experiments of the features in the tensor power spectrum introduced by each specific model.

From the observational perspective, our analysis highlighted the complementarity of ultimate B-mode experiments over the next decade, probing large scales interested by the reionization power in the B-modes, uniquely accessed from space (LiteBIRD), and smaller ones from ground based probes (SO, CMB-S4), jointly looking at the degree scales, where the signal from cosmological gravitational waves is imprinted at recombination. The high level of complementarity between ground-based and satellite CMB experiments in terms of their multipole range and capability to detect information on the primordial universe physics, is currently a subject of interest in the literature (see 3.1.2 and references therein). There is indeed the possibility of creating a synergy between them: we could exploit the extended frequency coverage of LiteBIRD to remove foregrounds from the data of CMB-S4, obtaining high resolution CMB data, and then profit from the small scales coverage and delensing capabilities of CMB-S4 to clean the lensing contamination from LiteBIRD data.

As we discussed above, the constraints on the SGWB obtained from the CMB alone can be significantly improved by adding information from several other probes in different frequency intervals. Moreover, our results concerning the extensions of the analysis to the PTA and interferometers ranges could have a significant impact on the way we think about future measurements. In fact, if the primordial SGWB is discovered during the next decade by ground-based

CMB observatories or LiteBIRD, characterizing the power spectrum beyond the value of r and testing chirality and Gaussianity would be of utmost importance for deciphering the origin of the SGWB. If the discovered SGWB were found to be nearly scale-invariant, parity even and Gaussian, it would set a target for the DECIGO and BBO to test the prediction of single-field slow-roll inflation models. On the other hand, if the SGWB were found to be blue-tilted, chiral or non-Gaussian, it would give excellent prospects for direct detection by LISA in the 2030s as well as by other proposed post-LISA direct detection experiments at any frequencies, opening up a new window to particle physics during inflation.

Concerning future work, a direct extension would be to apply the PCA formalism to the extensive landscape of experiments described in Chapter 5, thus characterizing the frequency ranges – across ~ 23 decades – in which the combination of CMB and direct detection experiments would be more sensitive to features in the tensor power spectrum. Also in this case a systematic exploration of the parameter space could be performed, just as in the CMB-only case.

The problem of foreground cleaning for direct detection experiments is also a very relevant subject on which further research is needed: as we approach the launch date of LISA, more realistic assessment of the performance of interferometers under the effect of astrophysical SGWB foregrounds is needed. In this regard, the foreground treatment and cleaning strategy we adopted for interferometers and PTA, can be improved in some ways, although this is neither an easy nor a quick task: we could use full simulations to produce the foregrounds contributions instead of approximate fitting formulas, and develop foreground cleaning algorithms (such as the one in Pieroni and Barausse, 2020), adapting them to each of the considered experiments configurations. We could also improve the realism of some assumptions in our foreground treatment: for instance, the possibility of subtracting the GWD and EGWD should be assessed with detailed simulations and calculations from first principles for each of the considered experiment configurations (Adams and Cornish, 2014).

On a final note, my involvement as a member of the LiteBIRD collaboration has also been one of the driving forces behind some of the analyses presented in this work: our results, as we outlined throughout this Thesis, strengthen the scientific case for this ultra-sensitive future B-mode mission.

Part III

Appendices

A
Interferometers Designs and Response Functions

A necessary ingredient to compute the sensitivity curve of a GW direct SGWB experiment (Eq. 5.30) is the *overlap reduction function* $\mathcal{R}_{IJ}(f)$ of the detector pair IJ (Eq. 5.23) (Flanagan, 1993), which is computed from the *response function* $T_I(f, \hat{n})$ of each of the detector involved in the cross-correlation (Eq. 5.20). We summarize here the formalism necessary to compute it, following Ref. (Smith and Caldwell, 2017) to which we refer the reader for further details.

The overlap reduction function depends on the design of the detector and the combination of laser signals from the interferometer arms that we choose to form at the detector output. The response of space interferometers can also depend on time because of the orbital motion of the spacecrafts composing the detector; however, for simplicity we ignore this dependence.

Let us start by considering the response of a single arm of the interferometer, from which we build the response of the full detector. The physical principle behind the detection of GWs in a laser interferometer is simple: the passage of GWs changes the proper distance between two freely moving test-masses at the opposite ends of an interferometer arm, causing phase-shifts in the laser beams which are traveling back-and-forth in each arm. It can be shown (Smith and Caldwell, 2017) that the phase change due to light traveling from the test-mass i to the test-mass j along a single interferometer arm is

$$\Delta\varphi_{ij}(t) = \int_{-\infty}^{+\infty} df \int d^2\hat{n} \sum_{P=+,\times} \tilde{h}_P(f, \hat{n}) e^{i2\pi f t_i} e^P_{ab}(\hat{n}) T^{ab}(\hat{l}_{ij} \cdot \hat{n}, f), \tag{A.1}$$

where L is the arm length, the test-masses i and j are located at $\vec{x}_i$ and $\vec{x}_j + L\hat{l}_{ij}$, respectively, t_i is the time at which light left the mass i, t is the time of arrival at the mass j and T^{ab} is the single-arm response

function given by

$$T^{ab}(\hat{l}\cdot\hat{n},f) = \hat{l}^a\hat{l}^b\,\mathcal{T}(\hat{l}\cdot\hat{n},f)\,e^{-i2\pi\hat{n}\cdot\vec{x}_i}, \tag{A.2}$$

$$\mathcal{T}(\hat{l}\cdot\hat{n},f) = \frac{1}{2}\,\mathrm{sinc}\left[\frac{f}{2f^*}(1-\hat{l}\cdot\hat{n})\right]e^{i\frac{f}{2f^*}(1-\hat{l}\cdot\hat{n})}, \tag{A.3}$$

where $f^* = 1/(2\pi L)$. To measure the SGWB it is necessary to correlate the phase differences from different arms or paths around the interferometer. For example, we write the correlation between the $i \to j$ and the $k \to l$ paths as

$$\langle \Delta\tilde{\varphi}_{ij}(f)\Delta\tilde{\varphi}^*_{kl}(f')\rangle = \frac{1}{2}\delta(f-f')\mathcal{R}_{ij,kl}(f)\mathcal{S}_s(f), \tag{A.4}$$

where $\mathcal{R}_{ij,kl}$ is the overlap reduction function defined in Eq. 5.23, which we rewrite in this case as

$$\mathcal{R}_{ij,kl}(f) = \int \frac{d^2\hat{n}}{4\pi} T^{ab}(\hat{l}_{ij}\cdot\hat{n},f)\,T^{ab*}(\hat{l}_{kl}\cdot\hat{n},f). \tag{A.5}$$

To build the detector responses for the experiments we consider in this work, we start from the simplest design adopted for the LISA mission. The current proposal for LISA showcases three spacecrafts, each occupying a vertex $\vec{x}_i$ with $i = A, B, C$ of an equilateral triangle ABC of side $L = 2.5 \times 10^9$ m; laser beams (six in total) travel back and forth along each of the triangle sides. We compute the response function for LISA using the standard Time-Delay Interferometry (TDI) signals. In this particular case (Smith and Caldwell, 2019), the interferometer response function at the detector vertex A reads

$$T^{ab}_{ABC}(\hat{n},f) = \frac{1}{2}e^{-i2\pi f\hat{n}\cdot\vec{x}_A}\left[(\hat{l}_{AB}\otimes\hat{l}_{AB})\mathcal{T}(\hat{l}_{AB}\cdot\hat{n},f) - (\hat{l}_{AC}\otimes\hat{l}_{AC})\mathcal{T}(\hat{l}_{AC}\cdot\hat{n},f)\right], \tag{A.6}$$

$$\mathcal{T}(\hat{l}\cdot\hat{n},f) = \frac{1}{2}W(f,f^*)\left(\mathrm{sinc}\left[\frac{f}{2f^*}(1-\hat{l}\cdot\hat{n})\right]e^{-i\frac{f}{2f^*}(3+\hat{l}\cdot\hat{n})} + \mathrm{sinc}\left[\frac{f}{2f^*}(1+\hat{l}\cdot\hat{n})\right]e^{-i\frac{f}{2f^*}(1+\hat{l}\cdot\hat{n})}\right), \tag{A.7}$$

where $W(f,f^*) = 1$ for the Michelson signals and $W(f,f^*) = 1-e^{-2if/f^*}$ for the TDI signals we are interested in. Specifically, the TDI A and E modes overlap reduction function[1] for LISA (the blue curve in Figure A.1) will be

$$\mathcal{R}_{A,E} = \mathcal{R}_{ABC,\,ABC} - \mathcal{R}_{ABC,\,BCA}, \tag{A.8}$$

where $\mathcal{R}_{ABC,\,ABC}$ is the response for the auto-correlation at the vertex A and $\mathcal{R}_{ABC,\,BCA}$ is the one for the cross-correlation between the signals at the vertices A and B (Smith and Caldwell, 2019).

We use TDI signals to compute the overlap reduction function also for DO (green curve in Figure A.1), which has been proposed as a LISA-like interferometer with shorter arms of lenght $L = 10^8$ m.

[1] The three TDI signals are constructed by diagonalizing the signal covariance matrix and are named the A, E and T modes. Note that Eq. A.8 is valid only for the A and E TDI modes, which are the most sensitive to the SGWB, while the T mode is much less sensitive and is used instead to remove noise from the A and E modes (Smith and Caldwell, 2019).

Differently from the LISA and DO detectors, BBO will feature six spacecrafts forming two independent triangular LISA-like interferometers ABC and $A'B'C'$ with sides $L = 5 \times 10^7$ m. The two interferometers will be co-planar with one being rotated by 180° with respect to the other, creating the so-called "hexagram" configuration.

In this case, it is convenient to introduce another signal combination that we can form from the Michelson signals $s_{mich,A}(t)$ and $s_{mich,C}(t)$ at the vertices A and C of one interferometer, respectively (Smith and Caldwell, 2017)

$$s_X(t) = s_{mich,A}(t) + 2s_{mich,C}(t). \tag{A.9}$$

The detector response function for the Michelson signal $s_{mich,A}(t)$ at the vertex A takes the form in Eq. A.6, while the one for the $s_X(t)$ signal combination is given by

$$T^{ab}_X(\hat{n}, f) = T^{ab}_{ABC}(\hat{n}, f) + 2T^{ab}_{CAB}(\hat{n}, f), \tag{A.10}$$

and for both responses the transfer function $\mathcal{T}(\hat{l} \cdot \hat{n}, f)$ is given by Eq. A.7 with $W(f, f^*) = 1$.

Now, to compute the overlap reduction function for the BBO hexagram configuration, we cross-correlate the Michelson signal $s_{mich,A}$ at the vertex A on the interferometer ABC and the combination $s_{X'}(t) = s_{mich,A'}(t) + 2s_{mich,C'}(t)$ on the other interferometer $A'B'C'$ (Smith and Caldwell, 2017) (the black curve in Figure A.1). As shown in (Smith and Caldwell, 2017), it is convenient then to correlate the Michelson signal $s_{mich,A}(t)$ with the signal combination $s^{'}_X(t)$, because the total noises for these two signals will be uncorrelated over the frequencies at which space-based interferometers are typically most sensitive. The final overlap reduction function for this signal combination (Smith and Caldwell, 2017) will be

$$\mathcal{R}_{Hexagram} = \mathcal{R}_{ABC,\,ABC} + \mathcal{R}_{X',X'} + 2\mathcal{R}_{ABC,\,X'}. \tag{A.11}$$

The DECIGO design is similar to the BBO, with two independent triangular interferometers with arms $L = 10^6$ m disposed in the hexagram configuration. Unlike BBO, however, the current DECIGO design envisages *Fabry-Pérot* (hereafter FP) interferometers; the response function at the vertex A (Kudoh et al., 2006) becomes therefore

$$T^{ab}_{FP}(\hat{n}, f) = \frac{1}{2} e^{-i2\pi f \hat{n}\cdot\vec{x}_A} \left[(\hat{l}_{AB} \otimes \hat{l}_{AB}) - (\hat{l}_{AC} \otimes \hat{l}_{AC}) \right], \tag{A.12}$$

and – similarly to what we do for BBO – we cross-correlate it with the response at the vertex A' on the second interferometer, obtaining the overlap reduction function depicted in the orange curve in Figure A.1.

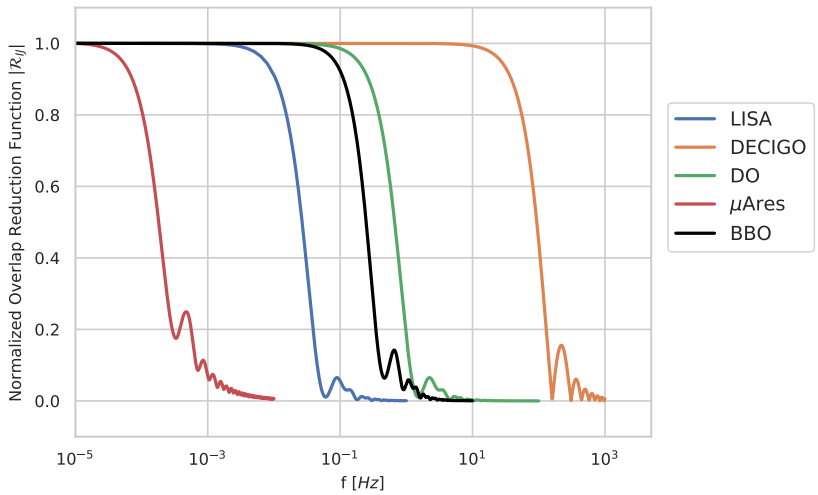

Figure A.1: Absolute value of the overlap reduction functions $|\mathcal{R}_{IJ}|$ normalized to 1, computed for the interferometers LISA, DECIGO, DO, BBO, μAres and CE.

The μAres experiment will be composed, similarly to DECIGO and BBO, by two identical triangular LISA-like constellations with arms $L = 430 \times 10^9$ m. However, in this case one of the two triangular interferometer would be trailing Mars orbit within the ecliptic plane while the other would be in the same orbit but 90 degrees tilted with respect to the ecliptic plane (Sesana et al., 2019). In order to compute the overlap reduction function for μAres, we adopt again the same method employed for BBO, taking into account the design differences. We show the resulting curve in the purple line in Figure A.1.

Finally, we take into consideration the ET ground-based experiment. The current proposal consists of a network of three interferometers with arm opening of 60 degrees, arranged in a such a way to form an equilateral triangle. For the ET experiment there is no need to compute the overlap reduction function, since the strain sensitivity curves (as defined in Eq. 5.31) are publicly available[2].

[2] http://www.et-gw.eu/index.php/etsensitivities

B
Interferometers Noise Models

To compute the sensitivity curve in Eq. 5.30 we need not only the overlap reduction function, but also the *noise power spectral density* $\mathcal{S}_n(f)$ for each detector (Eq. 5.17). Let us start from the LISA mission. Following Ref. (Smith and Caldwell, 2019), we use the noise models reported in the LISA Science Requirements Document[1]: the two main noise sources are acceleration noise and optical metrology noise, with spectra

[1] https://www.cosmos.esa.int/web/lisa/lisa-documents

$$\mathcal{S}_{acc}^{LISA}(f) = \frac{\left(\sqrt{(\delta a)^2}/L\right)^2}{(2\pi f)^4}\left(1+(f_1/f)^2\right)\,\mathrm{Hz}^{-1}, \tag{B.1}$$

$$\mathcal{S}_{opt}^{LISA} = \left(\sqrt{(\delta x)^2}/L\right)^2\,\mathrm{Hz}^{-1}, \tag{B.2}$$

where $\sqrt{(\delta a)^2} = 3\times10^{-15}\,\mathrm{m\,s^{-2}}$ and $\sqrt{(\delta x)^2} = 1.5\times10^{-11}\,\mathrm{m}$ are the rms amplitudes for acceleration and optical metrology noise, respectively, and $f_1 = 0.4\,\mathrm{mHz}$. The noise spectra for the TDI A and E signals that we used to compute the response function for LISA in Appendix **??** are

$$\mathcal{S}_n^{A,E}(f) = |W(f,f^*)|^2\left[(4+2\cos(f/f^*))\mathcal{S}_{opt}^{LISA} + 8(1+\cos(f/f^*)) + \cos^2(f/f^*)\mathcal{S}_{acc}^{LISA}(f)\right]. \tag{B.3}$$

Combining the A and E modes, we reduce the noise power by a factor $\sqrt{2}$ to obtain (Smith and Caldwell, 2019)

$$\mathcal{S}_h^{LISA} = \left[\left(\frac{\mathcal{R}_A}{\mathcal{S}_n^A}\right)^2 + \left(\frac{\mathcal{R}_E}{\mathcal{S}_n^E}\right)^2\right]^{-1/2}. \tag{B.4}$$

For BBO (Crowder and Cornish, 2005a) we use

$$\mathcal{S}_{acc}^{BBO}(f) = 2.3\times10^{-52}(1\,\mathrm{Hz}/f)^4\,\mathrm{Hz}^{-1}, \tag{B.5}$$

$$\mathcal{S}_{opt}^{BBO} = 8\times10^{-50}\,\mathrm{Hz}^{-1}, \tag{B.6}$$

and the noise model for one of the two identical triangular interferometers proposed in (Smith and Caldwell, 2017)

$$S_n^{BBO} = \frac{5}{2}\left[\mathcal{S}_{opt}^{BBO}(f) + 2\mathcal{S}_{acc}^{BBO}(f)(1+\cos^2(f/f^*))\right]. \tag{B.7}$$

For DECIGO we use the noise model (Kuroyanagi et al., 2015):

$$\mathcal{S}_n^{DECIGO} = \mathcal{S}_{shot}^{DECIGO}(f) + \mathcal{S}_{rad}^{DECIGO}(f) + \mathcal{S}_{acc}^{DECIGO}(f), \tag{B.8}$$

with shot noise, radiation pressure noise and acceleration noise given by

$$\mathcal{S}_{shot}^{DECIGO}(f) = \frac{\hbar\pi\lambda}{P_{eff}}\left(\frac{1}{4fL}\right)^2\left[1+\left(\frac{f}{f^*}\right)^2\right], \tag{B.9}$$

$$\mathcal{S}_{rad}^{DECIGO}(f) = \frac{\hbar P}{\pi\lambda}\left(\frac{16F}{ML}\right)^2\left(\frac{1}{2\pi f}\right)^4\left[1+\left(\frac{f}{f^*}\right)^2\right]^{-1}, \tag{B.10}$$

$$\mathcal{S}_{acc}^{DECIGO}(f) = \frac{\hbar P}{\pi\lambda}\left(\frac{16F}{3ML}\right)^2\left(\frac{1}{2\pi f}\right)^4, \tag{B.11}$$

where $P = 10\,\mathrm{W}$ is the laser output power, $\lambda = 532\,\mathrm{nm}$ is the laser wavelenght, $M = 100\,\mathrm{kg}$ is the mirror mass, $R = 0.5\,\mathrm{m}$ is the mirror radius, $F = 10.18$ is the FP cavity finesse and $P_{eff} = 6.68\,\mathrm{W}$ is the effective laser output power.

For DO we use the noise curves shown in Ref. (Sedda et al., 2019) and kindly provided by Christopher Berry. Also for μAres we use the noise curves kindly provided by Alberto Sesana, as shown in Ref. (Sesana et al., 2019). For AEDGE we use the strain sensitivity curve shown in Ref. (El-Neaj et al., 2019) and kindly provided by the AEDGE collaboration. For ET we use the strain sensitivity curve available from Ref. (Hild et al., 2011) (see also website in footnote 2).

C
Derivation of a new filter for foreground mitigation

We will demonstrate in this Appendix that the new filter $Q(f)$ (Eq. 5.42) we introduced in Section 5.4.2 maximizes the noise-only SNR (Eq. 5.28) and also $SNR_{\hat{Y}}$ (Eq. 5.38), which takes foregrounds into account (Poletti D. *in preparation*).

We first simplify the notation by defining the dot product:

$$A \cdot B = \int_{-\infty}^{+\infty} df A^*(f) B(f) S_n^2. \tag{C.1}$$

We also define for convenience the following quantities (dropping all the f dependences)

$$P = \frac{2 S_s R_{IJ}}{S_n^2} \quad \text{and} \quad F = \frac{2 S_{fg} R_{IJ}}{S_n^2}. \tag{C.2}$$

With this notation, we can rewrite the square of Eq. 5.38 as

$$SNR_{\hat{Y}}^2 = \frac{(Q \cdot P)^2}{(Q \cdot Q) + \sigma_{fg}^2 (Q \cdot F)^2}. \tag{C.3}$$

Note that:

1. $SNR_{\hat{Y}}$ does not depend on the normalization of Q;
2. if $P \propto F$ (i.e. the foregrounds and the primordial signal have the same shape), maximizing $SNR_{\hat{Y}}$ or the noise-only SNR (Eq. 5.28) is equivalent;
3. thanks to point 1 above, instead of maximizing the whole fraction appearing on the right-hand side of Eq. C.3, we can just minimize its denominator under the constraint that its numerator is constant.

   The Lagrangian therefore reads:

$$\mathcal{L}(Q, \lambda) = (Q \cdot Q) + \sigma_{fg}^2 (Q \cdot F)^2 + \lambda (Q \cdot P + const.); \tag{C.4}$$

note that the function is strictly convex: local minima are also global. Let's look for them:

$$\nabla_Q \mathcal{L}(Q, \lambda) = 2Q + 2\sigma_{fg}^2 (Q \cdot F)F + \lambda P = 0. \tag{C.5}$$

We now make the ansatz $Q \propto P - xF$ and see if this is a solution for some x,

$$xF - \sigma_{fg}^2 (Q \cdot F)F \propto P. \tag{C.6}$$

Assuming that F is not parallel to P, we can rewrite this last equation as

$$x - \sigma_{fg}^2 (P \cdot F - xF \cdot F) = 0, \tag{C.7}$$

leading to

$$x = \frac{P \cdot F}{\sigma^{-2} + F \cdot F}. \tag{C.8}$$

Noting that the Hessian is $2 + \sigma_{fg}^2 FF^T$, which is positive defined, the expression

$$Q \propto P - \frac{P \cdot F}{\sigma^{-2} + F \cdot F} F \tag{C.9}$$

is a (global) minimum and therefore maximizes $SNR_{\hat{Y}}$. Spelling out this last equation for Q in terms of the quantities S_s, S_n, S_{fg} and R_{IJ} we get the expression for the filter reported in Eq. 5.42.

Bibliography

K. N. Abazajian, P. Adshead, Z. Ahmed, S. W. Allen, D. Alonso, K. S. Arnold, C. Baccigalupi, J. G. Bartlett, N. Battaglia, B. A. Benson, C. A. Bischoff, J. Borrill, V. Buza, E. Calabrese, R. Caldwell, J. E. Carlstrom, C. L. Chang, T. M. Crawford, F.-Y. Cyr-Racine, F. De Bernardis, T. de Haan, S. di Serego Alighieri, J. Dunkley, C. Dvorkin, J. Errard, G. Fabbian, S. Feeney, S. Ferraro, J. P. Filippini, R. Flauger, G. M. Fuller, V. Gluscevic, D. Green, D. Grin, E. Grohs, J. W. Henning, J. C. Hill, R. Hlozek, G. Holder, W. Holzapfel, W. Hu, K. M. Huffenberger, R. Keskitalo, L. Knox, A. Kosowsky, J. Kovac, E. D. Kovetz, C.-L. Kuo, A. Kusaka, M. Le Jeune, A. T. Lee, M. Lilley, M. Loverde, M. S. Madhavacheril, A. Mantz, J. Marsh, D. J. E. andz McMahon, P. D. Meerburg, J. Meyers, A. D. Miller, J. B. Munoz, H. N. Nguyen, M. D. Niemack, M. Peloso, J. Peloton, L. Pogosian, C. Pryke, M. Raveri, C. L. Reichardt, G. Rocha, A. Rotti, E. Schaan, M. M. Schmittfull, D. Scott, N. Sehgal, S. Shandera, B. D. Sherwin, T. L. Smith, L. Sorbo, G. D. Starkman, K. T. Story, A. van Engelen, J. D. Vieira, S. Watson, N. Whitehorn, and W. L. Kimmy Wu. CMB-S4 Science Book, First Edition. *arXiv e-prints*, October 2016.

Kevork Abazajian et al. CMB-S4 Decadal Survey APC White Paper. *Bull. Am. Astron. Soc.*, 51(7):209, 2019a. DOI: 10.2172/1556957.

Kevork Abazajian et al. CMB-S4 Science Case, Reference Design, and Project Plan. 7 2019b.

B. P. Abbott, R. Abbott, T. D. Abbott, M. R. Abernathy, F. Acernese, K. Ackley, S. W. Ballmer, J. C. Barayoga, S. E. Barclay, B. C. Barish, D. Barker, LIGO Scientific Collaboration, and Virgo Collaboration. Observation of Gravitational Waves from a Binary Black Hole Merger. *Phys. Rev. Lett.*, 116(6):061102, February 2016. DOI: 10.1103/PhysRevLett.116.061102.

B. P. Abbott, R. Abbott, T. D. Abbott, F. Acernese, K. Ackley, C. Adams, T. Adams, P. Addesso, R. X. Adhikari, V. B. Adya, C. Affeldt, M. Afrough, B. Agarwal, M. Agathos, K. Agatsuma, N. Aggarwal, O. D. Aguiar, L. Aiello, A. Ain, P. Ajith, B. Allen,

G. Allen, LIGO Scientific Collaboration, and Virgo Collaboration. GW170817: Observation of Gravitational Waves from a Binary Neutron Star Inspiral. *Phys. Rev. Lett.*, 119(16):161101, October 2017. DOI: 10.1103/PhysRevLett.119.161101.

B.P. Abbott et al. Search for the isotropic stochastic background using data from Advanced LIGO's second observing run. *Phys. Rev. D*, 100 (6):061101, 2019. DOI: 10.1103/PhysRevD.100.061101.

T.M.C. Abbott et al. Dark Energy Survey Year 1 Results: A Precise Ho Estimate from DES Y1, BAO, and D/H Data. *Mon. Not. Roy. Astron. Soc.*, 480(3):3879–3888, 2018. DOI: 10.1093/mnras/sty1939.

Maximilian H. Abitbol, J. Colin Hill, and Jens Chluba. Measuring the Hubble constant from the cooling of the CMB monopole. 10 2019. DOI: 10.3847/1538-4357/ab7b70.

F. Acernese et al. Advanced Virgo: a second-generation interferometric gravitational wave detector. *Class. Quant. Grav.*, 32(2):024001, 2015. DOI: 10.1088/0264-9381/32/2/024001.

Matthew R. Adams and Neil J. Cornish. Detecting a stochastic gravitational wave background in the presence of a galactic foreground and instrument noise. *Phys. Rev.*, 89(2):022001, January 2014. DOI: 10.1103/PhysRevD.89.022001.

G. Addamo et al. The large scale polarization explorer (LSPE) for CMB measurements: performance forecast. 8 2020.

P. A. R. Ade et al. Detection of *B*-Mode Polarization at Degree Angular Scales by BICEP2. *Phys. Rev. Lett.*, 112(24):241101, 2014. DOI: 10.1103/PhysRevLett.112.241101.

P.A.R. Ade et al. Improved Constraints on Cosmology and Foregrounds from BICEP2 and Keck Array Cosmic Microwave Background Data with Inclusion of 95 GHz Band. *Phys. Rev. Lett.*, 116: 031302, 2016a. DOI: 10.1103/PhysRevLett.116.031302.

P.A.R. Ade et al. BICEP2 / Keck Array VIII: Measurement of gravitational lensing from large-scale B-mode polarization. *Astrophys. J.*, 833(2):228, 2016b. DOI: 10.3847/1538-4357/833/2/228.

P. Adshead and M. Wyman. Chromo-Natural Inflation: Natural inflation on a steep potential with classical non-Abelian gauge fields. *Phys. Rev. Lett.*, 108:261302, 2012. DOI: 10.1103/PhysRevLett.108.261302.

P. Adshead, E. Martinec, and M. Wyman. Perturbations in Chromo-Natural Inflation. *JHEP*, 09:087, 2013a. DOI: 10.1007/JHEP09(2013)087.

Peter Adshead and Evangelos I. Sfakianakis. Higgsed Gauge-flation. *JHEP*, 08:130, 2017. DOI: 10.1007/JHEP08(2017)130.

Peter Adshead, Emil Martinec, and Mark Wyman. Gauge fields and inflation: Chiral gravitational waves, fluctuations, and the Lyth bound. *Phys. Rev.*, D88(2):021302, 2013b. DOI: 10.1103/PhysRevD.88.021302.

Peter Adshead, Emil Martinec, Evangelos I. Sfakianakis, and Mark Wyman. Higgsed Chromo-Natural Inflation. *JHEP*, 12:137, 2016. DOI: 10.1007/JHEP12(2016)137.

Peter Adshead, John T. Giblin, and Zachary J. Weiner. Gravitational waves from gauge preheating. *Phys. Rev.*, D98(4):043525, 2018. DOI: 10.1103/PhysRevD.98.043525.

Peter Adshead, John T. Giblin, Mauro Pieroni, and Zachary J. Weiner. Constraining axion inflation with gravitational waves across 29 decades in frequency. *Phys. Rev. Lett.*, 124(17):171301, 2020a. DOI: 10.1103/PhysRevLett.124.171301.

Peter Adshead, John T. Giblin, Mauro Pieroni, and Zachary J. Weiner. Constraining axion inflation with gravitational waves from preheating. *Phys. Rev.*, D101(8):083534, 2020b. DOI: 10.1103/PhysRevD.101.083534.

Aniket Agrawal, Tomohiro Fujita, and Eiichiro Komatsu. Large tensor non-Gaussianity from axion-gauge field dynamics. *Phys. Rev.*, D97 (10):103526, 2018a. DOI: 10.1103/PhysRevD.97.103526.

Aniket Agrawal, Tomohiro Fujita, and Eiichiro Komatsu. Tensor Non-Gaussianity from Axion-Gauge-Fields Dynamics : Parameter Search. *JCAP*, 1806(06):027, 2018b. DOI: 10.1088/1475-7516/2018/06/027.

Rouzbeh Allahverdi, Robert Brandenberger, Francis-Yan Cyr-Racine, and Anupam Mazumdar. Reheating in Inflationary Cosmology: Theory and Applications. *Annual Review of Nuclear and Particle Science*, 60:27–51, November 2010. DOI: 10.1146/annurev.nucl.012809.104511.

Bruce Allen. The Stochastic gravity wave background: Sources and detection. In *Les Houches School of Physics: Astrophysical Sources of Gravitational Radiation*, pages 373–417, 4 1996.

Luca Amendola and Shinji Tsujikawa. *Dark Energy*. 2015.

Luca Amendola, Stephen Appleby, Anastasios Avgoustidis, David Bacon, Tessa Baker, Marco Baldi, Nicola Bartolo, Alain Blanchard, Camille Bonvin, Stefano Borgani, Enzo Branchini, Clare Burrage,

Stefano Camera, Carmelita Carbone, Luciano Casarini, Mark Cropper, Claudia de Rham, Jörg P. Dietrich, Cinzia Di Porto, Ruth Durrer, Anne Ealet, Pedro G. Ferreira, Fabio Finelli, Juan García-Bellido, Tommaso Giannantonio, Luigi Guzzo, Alan Heavens, Lavinia Heisenberg, Catherine Heymans, Henk Hoekstra, Lukas Hollenstein, Rory Holmes, Zhiqi Hwang, Knud Jahnke, Thomas D. Kitching, Tomi Koivisto, Martin Kunz, Giuseppe La Vacca, Eric Linder, Marisa March, Valerio Marra, Carlos Martins, Elisabetta Majerotto, Dida Markovic, David Marsh, Federico Marulli, Richard Massey, Yannick Mellier, Francesco Montanari, David F. Mota, Nelson J. Nunes, Will Percival, Valeria Pettorino, Cristiano Porciani, Claudia Quercellini, Justin Read, Massimiliano Rinaldi, Domenico Sapone, Ignacy Sawicki, Roberto Scaramella, Constantinos Skordis, Fergus Simpson, Andy Taylor, Shaun Thomas, Roberto Trotta, Licia Verde, Filippo Vernizzi, Adrian Vollmer, Yun Wang, Jochen Weller, and Tom Zlosnik. Cosmology and fundamental physics with the Euclid satellite. *Living Reviews in Relativity*, 21(1):2, April 2018. DOI: 10.1007/s41114-017-0010-3.

Giorgio Arcadi, MaÃ■ra Dutra, Pradipta Ghosh, Manfred Lindner, Yann Mambrini, Mathias Pierre, Stefano Profumo, and Farinaldo S. Queiroz. The waning of the WIMP? A review of models, searches, and constraints. *Eur. Phys. J. C*, 78(3):203, 2018. DOI: 10.1140/epjc/s10052-018-5662-y.

C. Armendariz-Picon, T. Damour, and Viatcheslav F. Mukhanov. k - inflation. *Phys. Lett. B*, 458:209–218, 1999. DOI: 10.1016/S0370-2693(99)00603-6.

Z. Arzoumanian et al. The NANOGrav Nine-year Data Set: Limits on the Isotropic Stochastic Gravitational Wave Background. *Astrophys. J.*, 821(1):13, 2016. DOI: 10.3847/0004-637X/821/1/13.

Z. Arzoumanian et al. The NANOGrav 11-year Data Set: Pulsar-timing Constraints On The Stochastic Gravitational-wave Background. *Astrophys. J.*, 859(1):47, 2018. DOI: 10.3847/1538-4357/aabd3b.

Benjamin Audren, Julien Lesgourgues, Karim Benabed, and Simon Prunet. Conservative Constraints on Early Cosmology: an illustration of the Monte Python cosmological parameter inference code. *JCAP*, 1302:001, 2013. DOI: 10.1088/1475-7516/2013/02/001.

Vishal Baibhav et al. Probing the Nature of Black Holes: Deep in the mHz Gravitational-Wave Sky. 8 2019.

John Baker, Jillian Bellovary, Peter L. Bender, Emanuele Berti, Robert Caldwell, Jordan Camp, John W. Conklin, Neil Cornish,

Curt Cutler, Ryan DeRosa, Michael Eracleous, Elizabeth C. Ferrara, Samuel Francis, Martin Hewitson, Kelly Holley-Bockelmann, Ann Hornschemeier, Craig Hogan, Brittany Kamai, Bernard J. Kelly, Joey Shapiro Key, Shane L. Larson, Jeff Livas, Sridhar Manthripragada, Kirk McKenzie, Sean T. McWilliams, Guido Mueller, Priyamvada Natarajan, Kenji Numata, Norman Rioux, Shannon R. Sankar, Jeremy Schnittman, David Shoemaker, Deirdre Shoemaker, Jacob Slutsky, Robert Spero, Robin Stebbins, Ira Thorpe, Michele Vallisneri, Brent Ware, Peter Wass, Anthony Yu, and John Ziemer. The Laser Interferometer Space Antenna: Unveiling the Millihertz Gravitational Wave Sky. *arXiv e-prints*, art. arXiv:1907.06482, July 2019.

James M. Bardeen. Gauge-invariant cosmological perturbations. *Phys. Rev.*, 22(8):1882–1905, October 1980. DOI: 10.1103/PhysRevD.22.1882.

N. Barnaby and M. Peloso. Large Nongaussianity in Axion Inflation. *Phys. Rev. Lett.*, 106:181301, 2011. DOI: 10.1103/PhysRevLett.106.181301.

N. Barnaby, J. Moxon, R. Namba, M. Peloso, G. Shiu, and P. Zhou. Gravity waves and non-Gaussian features from particle production in a sector gravitationally coupled to the inflaton. *Phys. Rev.*, D86: 103508, 2012. DOI: 10.1103/PhysRevD.86.103508.

Matthias Bartelmann and Peter Schneider. Weak gravitational lensing. *Phys. Rept.*, 340:291–472, 2001. DOI: 10.1016/S0370-1573(00)00082-X.

N. Bartolo, S. Matarrese, and A. Riotto. Adiabatic and isocurvature perturbations from inflation: Power spectra and consistency relations. *Phys. Rev.*, 64(12):123504, December 2001. DOI: 10.1103/PhysRevD.64.123504.

Nicola Bartolo, Chiara Caprini, Valerie Domcke, Daniel G. Figueroa, Juan Garcia-Bellido, Maria Chiara Guzzetti, Michele Liguori, Sabino Matarrese, Marco Peloso, Antoine Petiteau, Angelo Ricciardone, Mairi Sakellariadou, Lorenzo Sorbo, and Gianmassimo Tasinato. Science with the space-based interferometer LISA. IV: probing inflation with gravitational waves. *JCAP*, 2016(12):026, December 2016. DOI: 10.1088/1475-7516/2016/12/026.

Daniel Baumann. TASI Lectures on Primordial Cosmology. *arXiv e-prints*, art. arXiv:1807.03098, July 2018.

Daniel Baumann, Hayden Lee, and Guilherme L. Pimentel. High-Scale Inflation and the Tensor Tilt. *JHEP*, 01:101, 2016. DOI: 10.1007/JHEP01(2016)101.

R. Bernabei et al. 2 New Model independent Results From the First Six Full Annual Cycles of DAMA/LIBRA–Phase2. *Bled Workshops Phys.*, 19(2):27–57, 2018.

BICEP2 and Planck Collaborations.

BICEP2 Collaboration. BICEP2 / Keck Array x: Constraints on Primordial Gravitational Waves using Planck, WMAP, and New BICEP2/Keck Observations through the 2015 Season. *Phys. Rev. Lett.*, 121:221301, 2018. DOI: 10.1103/PhysRevLett.121.221301.

Diego Blas, Julien Lesgourgues, and Thomas Tram. The Cosmic Linear Anisotropy Solving System (CLASS) II: Approximation schemes. *JCAP*, 07:034, 2011. DOI: 10.1088/1475-7516/2011/07/034.

Matteo Bonetti, Alberto Sesana, Francesco Haardt, Enrico Barausse, and Monica Colpi. Post-Newtonian evolution of massive black hole triplets in galactic nuclei –IV. Implications for LISA. *Mon. Not. Roy. Astron. Soc.*, 486(3):4044–4060, 2019. DOI: 10.1093/mnras/stz903.

Lotfi Boubekeur and David. H. Lyth. Hilltop inflation. *JCAP*, 07:010, 2005. DOI: 10.1088/1475-7516/2005/07/010.

Latham A. Boyle, Paul J. Steinhardt, and Neil Turok. Cosmic gravitational-wave background in a cyclic universe. *Phys. Rev.*, 69(12): 127302, June 2004. DOI: 10.1103/PhysRevD.69.127302.

Robert H. Brandenberger, Ali Nayeri, Subodh P. Patil, and Cumrun Vafa. Tensor Modes from a Primordial Hagedorn Phase of String Cosmology. *Phys. Rev. Lett.*, 98(23):231302, June 2007. DOI: 10.1103/PhysRevLett.98.231302.

Thejs Brinckmann and Julien Lesgourgues. MontePython 3: boosted MCMC sampler and other features. 2018.

Martin Bucher. Physics of the cosmic microwave background anisotropy. *Int. J. Mod. Phys. D*, 24(02):1530004, 2015. DOI: 10.1142/S0218271815300049.

Christian T. Byrnes and David Wands. Curvature and isocurvature perturbations from two-field inflation in a slow-roll expansion. *Phys. Rev.*, 74(4):043529, August 2006. DOI: 10.1103/PhysRevD.74.043529.

Giovanni Cabass, Luca Pagano, Laura Salvati, Martina Gerbino, Elena Giusarma, and Alessandro Melchiorri. Updated Constraints and Forecasts on Primordial Tensor Modes. *Phys. Rev. D*, 93(6):063508, 2016. DOI: 10.1103/PhysRevD.93.063508.

Paolo Cabella and Marc Kamionkowski. Theory of Cosmic Microwave Background Polarization. *arXiv e-prints*, art. astro-ph/0403392, March 2004.

Erminia Calabrese et al. Cosmological parameters from pre-planck cosmic microwave background measurements. *Phys. Rev. D*, 87(10): 103012, 2013. DOI: 10.1103/PhysRevD.87.103012.

Paolo Campeti, Davide Poletti, and Carlo Baccigalupi. Principal component analysis of the primordial tensor power spectrum. *JCAP*, 1909(09):055, 2019a. DOI: 10.1088/1475-7516/2019/09/055.

Paolo Campeti, Davide Poletti, and Carlo Baccigalupi. Principal component analysis of the primordial tensor power spectrum. *JCAP*, 09:055, 2019b. DOI: 10.1088/1475-7516/2019/09/055.

Paolo Campeti, Eiichiro Komatsu, Davide Poletti, and Carlo Baccigalupi. Measuring the spectrum of primordial gravitational waves with CMB, PTA and Laser Interferometers. 7 2020.

Chiara Caprini and Daniel G. Figueroa. Cosmological backgrounds of gravitational waves. *Classical and Quantum Gravity*, 35(16):163001, August 2018. DOI: 10.1088/1361-6382/aac608.

John E. Carlstrom, Gilbert P. Holder, and Erik D. Reese. Cosmology with the Sunyaev-Zel'dovich Effect. *Annual Review of Astronomy and Astrophysics*, 40:643–680, January 2002. DOI: 10.1146/annurev.astro.40.060401.093803.

Sean M. Carroll. *Spacetime and Geometry*. Cambridge University Press, 7 2019. ISBN 978-0-8053-8732-2, 978-1-108-48839-6, 978-1-108-77555-7.

Julien Carron and Antony Lewis. Maximum a posteriori CMB lensing reconstruction. *Phys. Rev. D*, 96(6):063510, 2017. DOI: 10.1103/PhysRevD.96.063510.

Anthony Challinor and Antony Lewis. Lensed CMB power spectra from all-sky correlation functions. *Phys. Rev.*, D71:103010, 2005. DOI: 10.1103/PhysRevD.71.103010.

Khalil Chamcham, Joseph Silk, John D. Barrow, and Simon Saunders. *The Philosophy of Cosmology*. 2017.

Subrahmanyan Chandrasekhar. *Radiative transfer*. 1960.

Michel Chevallier and David Polarski. Accelerating Universes with Scaling Dark Matter. *International Journal of Modern Physics D*, 10(2): 213–223, January 2001. DOI: 10.1142/S0218271801000822.

J. Chluba and R. A. Sunyaev. The evolution of CMB spectral distortions in the early Universe. *Mon. Not. Roy. Astron. Soc.*, 419(2): 1294–1314, January 2012. DOI: 10.1111/j.1365-2966.2011.19786.x.

Steve K. Choi et al. The Atacama Cosmology Telescope: A Measurement of the Cosmic Microwave Background Power Spectra at 98 and 150 GHz. 7 2020.

Nelson Christensen. Stochastic Gravitational Wave Backgrounds. *Rept. Prog. Phys.*, 82(1):016903, 2019. DOI: 10.1088/1361-6633/aae6b5.

Thomas J. Clarke, Edmund J. Copeland, and Adam Moss. Constraints on primordial gravitational waves from the Cosmic Microwave Background. 4 2020.

Chris Clarkson. Establishing homogeneity of the universe in the shadow of dark energy. *Comptes Rendus Physique*, 13:682–718, 2012. DOI: 10.1016/j.crhy.2012.04.005.

Planck Collaboration. Planck 2015 results. XXVI. The Second Planck Catalogue of Compact Sources. *Astron. Astrophys.*, 594:A26, September 2016. DOI: 10.1051/0004-6361/201526914.

Carlo R. Contaldi, Joao Magueijo, and Lee Smolin. Anomalous CMB polarization and gravitational chirality. *Phys. Rev. Lett.*, 101:141101, 2008. DOI: 10.1103/PhysRevLett.101.141101.

J. L. Cook and L. Sorbo. Particle production during inflation and gravitational waves detectable by ground-based interferometers. *Phys. Rev.*, D85:023534, 2012. DOI: 10.1103/PhysRevD.86.069901, 10.1103/PhysRevD.85.023534. [Erratum: Phys. Rev.D86,069901(2012)].

J. L. Cook and L. Sorbo. An inflationary model with small scalar and large tensor nongaussianities. *JCAP*, 1311:047, 2013. DOI: 10.1088/1475-7516/2013/11/047.

Pier-Stefano Corasaniti, Tommaso Giannantonio, and Alessandro Melchiorri. Constraining dark energy with cross-correlated CMB and large scale structure data. *Phys. Rev.*, 71(12):123521, June 2005. DOI: 10.1103/PhysRevD.71.123521.

Neil Cornish and Travis Robson. Galactic binary science with the new LISA design. *J. Phys. Conf. Ser.*, 840(1):012024, 2017. DOI: 10.1088/1742-6596/840/1/012024.

Paolo Creminelli, Guido D'Amico, Jorge Noreña, and Filippo Vernizzi. The effective theory of quintessence: the w < -1 side unveiled. *JCAP*, 2009(2):018, February 2009. DOI: 10.1088/1475-7516/2009/02/018.

Jeff Crowder and Neil J. Cornish. Beyond LISA: Exploring future gravitational wave missions. *Phys. Rev. D*, 72:083005, 2005a. DOI: 10.1103/PhysRevD.72.083005.

Jeff Crowder and Neil J. Cornish. Beyond LISA: Exploring future gravitational wave missions. *Phys. Rev. D*, 72:083005, 2005b. DOI: 10.1103/PhysRevD.72.083005.

C. Cutler and J. Harms. BBO and the neutron-star-binary subtraction problem. *Phys. Rev. D*, 73:042001, 2006. DOI: 10.1103/PhysRevD.73.042001.

Sumit Dahal et al. The CLASS 150/220 GHz Polarimeter Array: Design, Assembly, and Characterization. *J. Low. Temp. Phys.*, 199(1-2): 289–297, 2020. DOI: 10.1007/s10909-019-02317-0.

Sudeep Das, Thibaut Louis, Michael R. Nolta, Graeme E. Addison, Elia S. Battistelli, J. Richard Bond, Erminia Calabrese, Devin Crichton, Mark J. Devlin, Simon Dicker, Joanna Dunkley, Rolando Dünner, Joseph W. Fowler, Megan Gralla, Amir Hajian, Mark Halpern, Matthew Hasselfield, Matt Hilton, Adam D. Hincks, Renée Hlozek, Kevin M. Huffenberger, John P. Hughes, Kent D. Irwin, Arthur Kosowsky, Robert H. Lupton, Tobias A. Marriage, Danica Marsden, Felipe Menanteau, Kavilan Moodley, Michael D. Niemack, Lyman A. Page, Bruce Partridge, Erik D. Reese, Benjamin L. Schmitt, Neelima Sehgal, Blake D. Sherwin, Jonathan L. Sievers, David N. Spergel, Suzanne T. Staggs, Daniel S. Swetz, Eric R. Switzer, Robert Thornton, Hy Trac, and Ed Wollack. The Atacama Cosmology Telescope: temperature and gravitational lensing power spectrum measurements from three seasons of data. *JCAP*, 2014(4):014, April 2014. DOI: 10.1088/1475-7516/2014/04/014.

Chiara Di Paolo and Paolo Salucci. *Fundamental properties of the dark and the luminous matter from Low Surface Brightness discs*. PhD thesis, 2020.

R. H. Dicke, P. J. E. Peebles, P. G. Roll, and D. T. Wilkinson. Cosmic Black-Body Radiation. *Astrophys. J.*, 142:414–419, July 1965. DOI: 10.1086/148306.

Clive Dickinson. CMB foregrounds - A brief review. In *Proceedings, 51st Rencontres de Moriond, Cosmology session: La Thuile, Italy, March 19-26, 2016*, pages 53–62, 2016.

Clive Dickinson, Y. Ali-Haïmoud, A. Barr, E. S. Battistelli, A. Bell, L. Bernstein, S. Casassus, K. Cleary, B. T. Draine, R. Génova-Santos, S. E. Harper, B. Hensley, J. Hill-Valler, Thiem Hoang, F. P. Israel, L. Jew, A. Lazarian, J. P. Leahy, J. Leech, C. H. López-Caraballo,

I. McDonald, E. J. Murphy, T. Onaka, R. Paladini, M. W. Peel, Y. Perrott, F. Poidevin, A. C. S. Readhead, J. A. Rubiño-Martín, A. C. Taylor, C. T. Tibbs, M. Todorović, and Matias Vidal. The State-of-Play of Anomalous Microwave Emission (AME) research. *New Astronomy Reviews*, 80:1–28, February 2018. DOI: 10.1016/j.newar.2018.02.001.

P. Diego-Palazuelos, P. Vielva, E. Martínez-González, and R. B. Barreiro. Comparison of delensing methodologies and assessment of the delensing capabilities of future experiments. *arXiv e-prints*, art. arXiv:2006.12935, June 2020.

Emanuela Dimastrogiovanni and Marco Peloso. Stability analysis of chromo-natural inflation and possible evasion of Lyth's bound. *Phys. Rev.*, D87(10):103501, 2013. DOI: 10.1103/PhysRevD.87.103501.

Emanuela Dimastrogiovanni, Matteo Fasiello, and Tomohiro Fujita. Primordial Gravitational Waves from Axion-Gauge Fields Dynamics. *JCAP*, 01:019, 2017. DOI: 10.1088/1475-7516/2017/01/019.

Scott Dodelson. *Modern Cosmology*. Academic Press, Amsterdam, 2003. ISBN 978-0-12-219141-1.

Valerie Domcke, Mauro Pieroni, and Pierre BinÃl'truy. Primordial gravitational waves for universality classes of pseudoscalar inflation. *JCAP*, 06:031, 2016. DOI: 10.1088/1475-7516/2016/06/031.

Valerie Domcke, Ben Mares, Francesco Muia, and Mauro Pieroni. Emerging chromo-natural inflation. *JCAP*, 04:034, 2019. DOI: 10.1088/1475-7516/2019/04/034.

Valerie Domcke, Juan García-Bellido, Marco Peloso, Mauro Pieroni, Angelo Ricciardone, Lorenzo Sorbo, and Gianmassimo Tasinato. Measuring the net circular polarization of the stochastic gravitational wave background with interferometers. *JCAP*, 2020(5):028, May 2020. DOI: 10.1088/1475-7516/2020/05/028.

G. Domènech, T. Hiramatsu, C. Lin, M. Sasaki, M. Shiraishi, and Y. Wang. CMB scale dependent non-Gaussianity from massive gravity during inflation. *JCAP*, 5:034, May 2017. DOI: 10.1088/1475-7516/2017/05/034.

B. T. Draine and B. Hensley. Magnetic Nanoparticles in the Interstellar Medium: Emission Spectrum and Polarization. *Astrophys. J.*, 765: 159, March 2013. DOI: 10.1088/0004-637X/765/2/159.

B. T. Draine and A. Lazarian. Electric Dipole Radiation from Spinning Dust Grains. *Astrophys. J.*, 508:157–179, November 1998. DOI: 10.1086/306387.

G.R. Dvali, Q. Shafi, and Robert K. Schaefer. Large scale structure and supersymmetric inflation without fine tuning. *Phys. Rev. Lett.*, 73: 1886–1889, 1994. DOI: 10.1103/PhysRevLett.73.1886.

Yousef Abou El-Neaj et al. AEDGE: Atomic Experiment for Dark Matter and Gravity Exploration in Space. 2019.

George F. R. Ellis. Issues in the Philosophy of Cosmology. *arXiv e-prints*, art. astro-ph/0602280, February 2006.

George F. R. Ellis, Roy Maartens, and Malcolm A. H. MacCallum. *Relativistic Cosmology*. Cambridge University Press, 2012.

J. Errard and R. Stompor. Characterizing bias on large scale CMB B-modes after galactic foregrounds cleaning. *arXiv e-prints*, November 2018.

J. Errard, F. Stivoli, and R. Stompor. Framework for performance forecasting and optimization of CMB B-mode observations in presence of astrophysical foregrounds. *Phys. Rev.*, D84:063005, 2011. DOI: 10.1103/PhysRevD.84.063005, 10.1103/PhysRevD.84.069907.

J. Errard, S. M. Feeney, H. V. Peiris, and A. H. Jaffe. Robust forecasts on fundamental physics from the foreground-obscured, gravitationally-lensed CMB polarization. *JCAP*, 3:052, March 2016. DOI: 10.1088/1475-7516/2016/03/052.

M. Farhang and A. Vafaei Sadr. Eigen-reconstruction of Perturbations to the Primordial Tensor Power Spectrum. *arXiv e-prints*, October 2018.

Farida Farsian, Nicoletta Krachmalnicoff, and Carlo Baccigalupi. Foreground model recognition through Neural Networks for CMB B-mode observations. *JCAP*, 07:017, 2020. DOI: 10.1088/1475-7516/2020/07/017.

Chang Feng and Gilbert Holder. Polarization of the Cosmic Infrared Background Fluctuations. *Astrophys. J.*, 897(2):140, 2020. DOI: 10.3847/1538-4357/ab9013.

Sergio Ferrara, Renata Kallosh, Andrei Linde, and Massimo Porrati. Minimal Supergravity Models of Inflation. *Phys. Rev. D*, 88(8):085038, 2013. DOI: 10.1103/PhysRevD.88.085038.

D. J. Fixsen, E. S. Cheng, J. M. Gales, J. C. Mather, R. A. Shafer, and E. L. Wright. The Cosmic Microwave Background Spectrum from the Full COBE FIRAS Data Set. *Astrophys. J.*, 473:576, December 1996a. DOI: 10.1086/178173.

D. J. Fixsen, E. S. Cheng, J. M. Gales, J. C. Mather, R. A. Shafer, and E. L. Wright. The Cosmic Microwave Background Spectrum from the Full COBE FIRAS Data Set. *Astrophys. J.*, 473:576, December 1996b. DOI: 10.1086/178173.

D.J. Fixsen. The Temperature of the Cosmic Microwave Background. *Astrophys. J.*, 707:916–920, 2009. DOI: 10.1088/0004-637X/707/2/916.

Eanna E. Flanagan. The Sensitivity of the laser interferometer gravitational wave observatory (LIGO) to a stochastic background, and its dependence on the detector orientations. *Phys. Rev. D*, 48: 2389–2407, 1993. DOI: 10.1103/PhysRevD.48.2389.

Wendy L. Freedman et al. The Carnegie-Chicago Hubble Program. VIII. An Independent Determination of the Hubble Constant Based on the Tip of the Red Giant Branch. 7 2019. DOI: 10.3847/1538-4357/ab2f73.

Katherine Freese, Joshua A. Frieman, and Angela V. Olinto. Natural inflation with pseudo - Nambu-Goldstone bosons. *Phys. Rev. Lett.*, 65: 3233–3236, 1990. DOI: 10.1103/PhysRevLett.65.3233.

Tomohiro Fujita, Evangelos I. Sfakianakis, and Maresuke Shiraishi. Tensor Spectra Templates for Axion-Gauge Fields Dynamics during Inflation. *JCAP*, 05:057, 2019. DOI: 10.1088/1475-7516/2019/05/057.

Nicholas Galitzki, Aamir Ali, Kam S. Arnold, Peter C. Ashton, Jason E. Austermann, Carlo Baccigalupi, Taylor Baildon, Darcy Barron, James A. Beall, Shawn Beckman, Sarah Marie M. Bruno, Sean Bryan, Paolo G. Calisse, Grace E. Chesmore, Yuji Chinone, Steve K. Choi, Gabriele Coppi, Kevin D. Crowley, Kevin T. Crowley, Ari Cukierman, Mark J. Devlin, Simon Dicker, Bradley Dober, Shannon M. Duff, Jo Dunkley, Giulio Fabbian, Patricio A. Gallardo, Martina Gerbino, Neil Goeckner-Wald, Joseph E. Golec, Jon E. Gudmundsson, Erin E. Healy, Shawn Henderson, Charles A. Hill, Gene C. Hilton, Shuay-Pwu Patty Ho, Logan A. Howe, Johannes Hubmayr, Oliver Jeong, Brian Keating, Brian J. Koopman, Kenji Kiuchi, Akito Kusaka, Jacob Lashner, Adrian T. Lee, Yaqiong Li, Michele Limon, Marius Lungu, Frederick Matsuda, Philip D. Mauskopf, Andrew J. May, Nialh McCallum, Jeff McMahon, Federico Nati, Michael D. Niemack, John L. Orlowski-Scherer, Stephen C. Parshley, Lucio Piccirillo, Mayuri Sathyanarayana Rao, Christopher Raum, Maria Salatino, Joseph S. Seibert, Carlos Sierra, Max Silva-Feaver, Sara M. Simon, Suzanne T. Staggs, Jason R. Stevens, Aritoki Suzuki, Grant Teply, Robert Thornton, Calvin Tsai, Joel N. Ullom, Eve M. Vavagiakis, Michael R. Vissers, Benjamin Westbrook, Edward J. Wollack, Zhilei Xu, and Ningfeng

Zhu. The Simons Observatory: instrument overview. In *Millimeter, Submillimeter, and Far-Infrared Detectors and Instrumentation for Astronomy IX*, volume 10708 of *Society of Photo-Optical Instrumentation Engineers (SPIE) Conference Series*, page 1070804, July 2018. DOI: 10.1117/12.2312985.

Juan Garcia-Bellido, Marco Peloso, and Caner Unal. Gravitational waves at interferometer scales and primordial black holes in axion inflation. *JCAP*, 12:031, 2016. DOI: 10.1088/1475-7516/2016/12/031.

Jaume Garriga and V. F. Mukhanov. Perturbations in k-inflation. *Physics Letters B*, 458(2-3):219–225, July 1999. DOI: 10.1016/S0370-2693(99)00602-4.

M. Gasperini and G. Veneziano. Pre-big-bang in string cosmology. *Astroparticle Physics*, 1(3):317–339, July 1993. DOI: 10.1016/0927-6505(93)90017-8.

J. N. Goldberg, A. J. Macfarlane, E. T. Newman, F. Rohrlich, and E. C. G. Sudarshan. Spin-s Spherical Harmonics and ð. *Journal of Mathematical Physics*, 8(11):2155–2161, November 1967. DOI: 10.1063/1.1705135.

K. M. Górski, E. Hivon, A. J. Banday, B. D. Wandelt, F. K. Hansen, M. Reinecke, and M. Bartelmann. HEALPix: A Framework for High-Resolution Discretization and Fast Analysis of Data Distributed on the Sphere. *Astrophys. J.*, 622:759–771, April 2005. DOI: 10.1086/427976.

J. S. Greaves, W. S. Holland, P. Friberg, and W. R. F. Dent. Polarized co emission from molecular clouds. *Astrophys. J.*, 512:L139, 1999. DOI: 10.1086/311888.

Alan H. Guth. The Inflationary Universe: A Possible Solution to the Horizon and Flatness Problems. *Adv. Ser. Astrophys. Cosmol.*, 3: 139–148, 1987. DOI: 10.1103/PhysRevD.23.347.

M. C. Guzzetti, N. Bartolo, M. Liguori, and S. Matarrese. Gravitational waves from inflation. *Nuovo Cimento Rivista Serie*, 39(9):399–495, August 2016. DOI: 10.1393/ncr/i2016-10127-1.

D. Hanson et al. Detection of B-mode Polarization in the Cosmic Microwave Background with Data from the South Pole Telescope. *Phys. Rev. Lett.*, 111(14):141301, 2013. DOI: 10.1103/PhysRevLett.111.141301.

Edward R. Harrison. *Cosmology: the Science of the Universe*. Cambridge University Press, 2000.

Gregory M. Harry. Advanced LIGO: The next generation of gravitational wave detectors. *Class. Quant. Grav.*, 27:084006, 2010. DOI: 10.1088/0264-9381/27/8/084006.

Jeffrey S. Hazboun, Joseph D. Romano, and Tristan L. Smith. Realistic sensitivity curves for pulsar timing arrays. *Phys. Rev. D*, 100(10): 104028, 2019. DOI: 10.1103/PhysRevD.100.104028.

M. Hazumi et al. LiteBIRD: A Satellite for the Studies of B-Mode Polarization and Inflation from Cosmic Background Radiation Detection. *J. Low. Temp. Phys.*, 194(5-6):443–452, 2019. DOI: 10.1007/s10909-019-02150-5.

J.W. Henning et al. Measurements of the Temperature and E-Mode Polarization of the CMB from 500 Square Degrees of SPTpol Data. *Astrophys. J.*, 852(2):97, 2018. DOI: 10.3847/1538-4357/aa9ff4.

S. Hild et al. Sensitivity Studies for Third-Generation Gravitational Wave Observatories. *Class. Quant. Grav.*, 28:094013, 2011. DOI: 10.1088/0264-9381/28/9/094013.

G. Hinshaw et al. Nine-Year Wilkinson Microwave Anisotropy Probe (WMAP) Observations: Cosmological Parameter Results. *Astrophys. J. Suppl.*, 208:19, 2013. DOI: 10.1088/0067-0049/208/2/19.

Takashi Hiramatsu, Eiichiro Komatsu, Masashi Hazumi, and Misao Sasaki. Reconstruction of primordial tensor power spectra from B-mode polarization of the cosmic microwave background. *Phys. Rev.*, D97(12):123511, 2018. DOI: 10.1103/PhysRevD.97.123511.

Christopher M. Hirata and Uroš Seljak. Reconstruction of lensing from the cosmic microwave background polarization. *Phys. Rev.*, 68 (8):083002, October 2003. DOI: 10.1103/PhysRevD.68.083002.

G. Hobbs. The Parkes Pulsar Timing Array. *Class. Quant. Grav.*, 30: 224007, 2013. DOI: 10.1088/0264-9381/30/22/224007.

W. Hu and T. Okamoto. Mass Reconstruction with Cosmic Microwave Background Polarization. *Astrophys. J.*, 574:566–574, August 2002a. DOI: 10.1086/341110.

Wayne Hu. Wandering in the Background: A CMB Explorer. *arXiv e-prints*, art. astro-ph/9508126, August 1995.

Wayne Hu. Weak lensing of the CMB: A harmonic approach. *Phys. Rev. D*, 62:043007, 2000. DOI: 10.1103/PhysRevD.62.043007.

Wayne Hu and Scott Dodelson. Cosmic Microwave Background Anisotropies. *Annual Review of Astronomy and Astrophysics*, 40:171–216, January 2002. DOI: 10.1146/annurev.astro.40.060401.093926.

Wayne Hu and Gilbert P. Holder. Model - independent reionization observables in the CMB. *Phys. Rev.*, D68:023001, 2003. DOI: 10.1103/PhysRevD.68.023001.

Wayne Hu and Takemi Okamoto. Mass Reconstruction with Cosmic Microwave Background Polarization. *Astrophys. J.*, 574(2):566–574, August 2002b. DOI: 10.1086/341110.

Wayne Hu and Takemi Okamoto. Principal power of the CMB. *Phys. Rev.*, D69:043004, 2004. DOI: 10.1103/PhysRevD.69.043004.

Wayne Hu and Naoshi Sugiyama. Anisotropies in the Cosmic Microwave Background: an Analytic Approach. *Astrophys. J.*, 444:489, May 1995. DOI: 10.1086/175624.

Caroline D. Huang, Adam G. Riess, Wenlong Yuan, Lucas M. Macri, Nadia L. Zakamska, Stefano Casertano, Patricia A. Whitelock, Samantha L. Hoffmann, Alexei V. Filippenko, and Daniel Scolnic. Hubble Space Telescope Observations of Mira Variables in the Type Ia Supernova Host NGC 1559: An Alternative Candle to Measure the Hubble Constant. 8 2019. DOI: 10.3847/1538-4357/ab5dbd.

Edwin Hubble. A Relation between Distance and Radial Velocity among Extra-Galactic Nebulae. *Proceedings of the National Academy of Science*, 15(3):168–173, March 1929. DOI: 10.1073/pnas.15.3.168.

Dragan Huterer and Glenn Starkman. Parameterization of dark-energy properties: A Principal-component approach. *Phys. Rev. Lett.*, 90:031301, 2003. DOI: 10.1103/PhysRevLett.90.031301.

Mustapha Ishak. Testing general relativity in cosmology. *Living Reviews in Relativity*, 22(1):1, December 2019. DOI: 10.1007/s41114-018-0017-4.

Raul Jimenez, Andrea Cimatti, Licia Verde, Michele Moresco, and Benjamin Wandelt. The local and distant Universe: stellar ages and H_0. *JCAP*, 2019(3):043, March 2019. DOI: 10.1088/1475-7516/2019/03/043.

B. J. T. Jones and R. F. G. Wyse. The ionisation of the primeval plasma at the time of recombination. *Astron. Astrophys.*, 149(1): 144–150, August 1985.

Kenji Kadota, Scott Dodelson, Wayne Hu, and Ewan D. Stewart. Precision of inflaton potential reconstruction from CMB using the general slow-roll approximation. *Phys. Rev.*, D72:023510, 2005. DOI: 10.1103/PhysRevD.72.023510.

Renata Kallosh, Andrei Linde, and Diederik Roest. Superconformal Inflationary α-Attractors. *JHEP*, 11:198, 2013. DOI: 10.1007/JHEP11(2013)198.

Marc Kamionkowski and Ely D. Kovetz. The Quest for B Modes from Inflationary Gravitational Waves. *Ann. Rev. Astron. Astrophys.*, 54: 227–269, 2016. DOI: 10.1146/annurev-astro-081915-023433.

Marc Kamionkowski, Arthur Kosowsky, and Albert Stebbins. Statistics of cosmic microwave background polarization. *Phys. Rev.*, D55: 7368–7388, 1997. DOI: 10.1103/PhysRevD.55.7368.

Kirit S. Karkare. Delensing Degree-Scale *B*-Mode Polarization with High-Redshift Line Intensity Mapping. *Phys. Rev. D*, 100(4):043529, 2019. DOI: 10.1103/PhysRevD.100.043529.

Seiji Kawamura, Masaki Ando, Naoki Seto, Shuichi Sato, Mitsuru Musha, Isao Kawano, Jun'ichi Yokoyama, Takahiro Tanaka, Kunihito Ioka, Tomotada Akutsu, Takeshi Takashima, Kazuhiro Agatsuma, Akito Araya, Naoki Aritomi, Hideki Asada, Takeshi Chiba, Satoshi Eguchi, Motohiro Enoki, Masa-Katsu Fujimoto, Ryuichi Fujita, Toshifumi Futamase, Tomohiro Harada, Kazuhiro Hayama, Yoshiaki Himemoto, Takashi Hiramatsu, Feng-Lei Hong, Mizuhiko Hosokawa, Kiyotomo Ichiki, Satoshi Ikari, Hideki Ishihara, Tomohiro Ishikawa, Yousuke Itoh, Takahiro Ito, Shoki Iwaguchi, Kiwamu Izumi, Nobuyuki Kanda, Shinya Kanemura, Fumiko Kawazoe, Shiho Kobayashi, Kazunori Kohri, Yasufumi Kojima, Keiko Kokeyama, Kei Kotake, Sachiko Kuroyanagi, Kei-ichi Maeda, Shuhei Matsushita, Yuta Michimura, Taigen Morimoto, Shinji Mukohyama, Koji Nagano, Shigeo Nagano, Takeo Naito, Kouji Nakamura, Takashi Nakamura, Hiroyuki Nakano, Kenichi Nakao, Shinichi Nakasuka, Yoshinori Nakayama, Kazuhiro Nakazawa, Atsushi Nishizawa, Masashi Ohkawa, Kenichi Oohara, Norichika Sago, Motoyuki Saijo, Masaaki Sakagami, Shin-ichiro Sakai, Takashi Sato, Masaru Shibata, Hisaaki Shinkai, Ayaka Shoda, Kentaro Somiya, Hajime Sotani, Ryutaro Takahashi, Hirotaka Takahashi, Takamori Akiteru, Keisuke Taniguchi, Atsushi Taruya, Kimio Tsubono, Shinji Tsujikawa, Akitoshi Ueda, Ken-ichi Ueda, Izumi Watanabe, Kent Yagi, Rika Yamada, Shuichiro Yokoyama, Chul-Moon Yoo, and Zong-Hong Zhu. Current status of space gravitational wave antenna DECIGO and B-DECIGO. *arXiv e-prints*, art. arXiv:2006.13545, June 2020.

M. Kerr et al. The Parkes Pulsar Timing Array Project: Second data release. 3 2020.

Michael Kesden, Asantha Cooray, and Marc Kamionkowski. Separation of gravitational wave and cosmic shear contributions to cosmic microwave background polarization. *Phys. Rev. Lett.*, 89:011304, 2002. DOI: 10.1103/PhysRevLett.89.011304.

Lloyd Knox and Marius Millea. Hubble constant hunter's guide. *Phys. Rev. D*, 101(4):043533, 2020. DOI: 10.1103/PhysRevD.101.043533.

Lloyd Knox and Yong-Seon Song. A Limit on the detectability of the energy scale of inflation. *Phys. Rev. Lett.*, 89:011303, 2002. DOI: 10.1103/PhysRevLett.89.011303.

Tsutomu Kobayashi, Masahide Yamaguchi, and Jun'Ichi Yokoyama. Inflation Driven by the Galileon Field. *Phys. Rev. Lett.*, 105(23):231302, December 2010. DOI: 10.1103/PhysRevLett.105.231302.

Hideo Kodama and Misao Sasaki. Cosmological Perturbation Theory. *Prog. Theor. Phys. Suppl.*, 78:1–166, 1984. DOI: 10.1143/PTPS.78.1.

Edward W. Kolb and Michael S. Turner. *The Early Universe*. Addison-Wesley, 1990. ISBN 978-0-201-62674-2.

A. Kosowsky. Cosmic microwave background polarization. *Annals of Physics*, 246(1):49–85, February 1996. DOI: 10.1006/aphy.1996.0020.

Arpine Kozmanyan, Hervé Bourdin, Pasquale Mazzotta, Elena Rasia, and Mauro Sereno. Deriving the Hubble constant using Planck and XMM-Newton observations of galaxy clusters. *Astron. Astrophys.*, 621:A34, January 2019. DOI: 10.1051/0004-6361/201833879.

N. Krachmalnicoff et al. S-PASS view of polarized Galactic synchrotron at 2.3 GHz as a contaminant to CMB observations. *Astron. Astrophys.*, 618:A166, 2018. DOI: 10.1051/0004-6361/201832768.

Hideaki Kudoh, Atsushi Taruya, Takashi Hiramatsu, and Yoshiaki Himemoto. Detecting a gravitational-wave background with next-generation space interferometers. *Phys. Rev.*, D73:064006, 2006. DOI: 10.1103/PhysRevD.73.064006.

Sachiko Kuroyanagi, Kazunori Nakayama, and Jun'ichi Yokoyama. Prospects of determination of reheating temperature after inflation by DECIGO. *PTEP*, 2015(1):013E02, 2015. DOI: 10.1093/ptep/ptu176.

Paul D. Lasky et al. Gravitational-wave cosmology across 29 decades in frequency. *Phys. Rev. X*, 6(1):011035, 2016a. DOI: 10.1103/PhysRevX.6.011035.

Paul D. Lasky et al. Gravitational-wave cosmology across 29 decades in frequency. *Phys. Rev. X*, 6(1):011035, 2016b. DOI: 10.1103/PhysRevX.6.011035.

R. Laureijs, J. Amiaux, S. Arduini, J. L. Augueres, J. Brinchmann, R. Cole, M. Cropper, C. Dabin, L. Duvet, A. Ealet, B. Garilli, P. Gondoin, L. Guzzo, J. Hoar, H. Hoekstra, R. Holmes, T. Kitching, T. Maciaszek, Y. Mellier, F. Pasian, W. Percival, J. Rhodes, G. Saavedra Criado, M. Sauvage, R. Scaramella, L. Valenziano, S. Warren, R. Bender, F. Castander, A. Cimatti, O. Le Fèvre, H. Kurki-Suonio, M. Levi, P. Lilje, G. Meylan, R. Nichol, K. Pedersen, V. Popa, R. Rebolo Lopez, H. W. Rix, H. Rottgering, W. Zeilinger, F. Grupp, P. Hudelot, R. Massey, M. Meneghetti, L. Miller, S. Paltani, S. Paulin-Henriksson, S. Pires, C. Saxton, T. Schrabback, G. Seidel, J. Walsh, N. Aghanim, L. Amendola, J. Bartlett, C. Baccigalupi, J. P. Beaulieu, K. Benabed, J. G. Cuby, D. Elbaz, P. Fosalba, G. Gavazzi, A. Helmi, I. Hook, M. Irwin, J. P. Kneib, M. Kunz, F. Mannucci, L. Moscardini, C. Tao, R. Teyssier, J. Weller, G. Zamorani, M. R. Zapatero Osorio, O. Boulade, J. J. Foumond, A. Di Giorgio, P. Guttridge, A. James, M. Kemp, J. Martignac, A. Spencer, D. Walton, T. Blümchen, C. Bonoli, F. Bortoletto, C. Cerna, L. Corcione, C. Fabron, K. Jahnke, S. Ligori, F. Madrid, L. Martin, G. Morgante, T. Pamplona, E. Prieto, M. Riva, R. Toledo, M. Trifoglio, F. Zerbi, F. Abdalla, M. Douspis, C. Grenet, S. Borgani, R. Bouwens, F. Courbin, J. M. Delouis, P. Dubath, A. Fontana, M. Frailis, A. Grazian, J. Koppenhöfer, O. Mansutti, M. Melchior, M. Mignoli, J. Mohr, C. Neissner, K. Noddle, M. Poncet, M. Scodeggio, S. Serrano, N. Shane, J. L. Starck, C. Surace, A. Taylor, G. Verdoes-Kleijn, C. Vuerli, O. R. Williams, A. Zacchei, B. Altieri, I. Escudero Sanz, R. Kohley, T. Oosterbroek, P. Astier, D. Bacon, S. Bardelli, C. Baugh, F. Bellagamba, C. Benoist, D. Bianchi, A. Biviano, E. Branchini, C. Carbone, V. Cardone, D. Clements, S. Colombi, C. Conselice, G. Cresci, N. Deacon, J. Dunlop, C. Fedeli, F. Fontanot, P. Franzetti, C. Giocoli, J. Garcia-Bellido, J. Gow, A. Heavens, P. Hewett, C. Heymans, A. Holland, Z. Huang, O. Ilbert, B. Joachimi, E. Jennins, E. Kerins, A. Kiessling, D. Kirk, R. Kotak, O. Krause, O. Lahav, F. van Leeuwen, J. Lesgourgues, M. Lombardi, M. Magliocchetti, K. Maguire, E. Majerotto, R. Maoli, F. Marulli, S. Maurogordato, H. McCracken, R. McLure, A. Melchiorri, A. Merson, M. Moresco, M. Nonino, P. Norberg, J. Peacock, R. Pello, M. Penny, V. Pettorino, C. Di Porto, L. Pozzetti, C. Quercellini, M. Radovich, A. Rassat, N. Roche, S. Ronayette, E. Rossetti, B. Sartoris, P. Schneider, E. Semboloni, S. Serjeant, F. Simpson, C. Skordis, G. Smadja, S. Smartt, P. Spano, S. Spiro, M. Sullivan, A. Tilquin, R. Trotta, L. Verde, Y. Wang, G. Williger, G. Zhao, J. Zoubian, and E. Zucca. Euclid Definition Study Report. *arXiv e-prints*, art. arXiv:1110.3193, October 2011.

Samuel M. Leach. Measuring the primordial power spectrum:

Principal component analysis of the cosmic microwave background. *Mon. Not. Roy. Astron. Soc.*, 372:646–654, 2006. DOI: 10.1111/j.1365-2966.2006.10842.x.

Adrian Lee, Maximilian H. Abitbol, Shunsuke Adachi, Peter Ade, James Aguirre, Zeeshan Ahmed, Simone Aiola, Aamir Ali, David Alonso, Marcelo A. Alvarez, Kam Arnold, Peter Ashton, Zachary Atkins, Jason Austermann, Humna Awan, Carlo Baccigalupi, Taylor Baildon, Anton Baleato Lizancos, Darcy Barron, Nick Battaglia, Richard Battye, Eric Baxter, Andrew Bazarko, James A. Beall, Rachel Bean, Dominic Beck, Shawn Beckman, Benjamin Beringue, Tanay Bhandarkar, Sanah Bhimani, Federico Bianchini, Steven Boada, David Boettger, Boris Bolliet, J. Richard Bond, Julian Borrill, Michael L. Brown, Sarah Marie Bruno, Sean Bryan, Erminia Calabrese, Victoria Calafut, Paolo Calisse, Julien Carron, Fred. M. Carl, Juan Cayuso, Anthony Challinor, Grace Chesmore, Yuji Chinone, Jens Chluba, Hsiao-Mei Sherry Cho, Steve Choi, Susan Clark, Philip Clarke, Carlo Contaldi, Gabriele Coppi, Nicholas F. Cothard, Kevin Coughlin, Will Coulton, Devin Crichton, Kevin D. Crowley, Kevin T. Crowley, Ari Cukierman, John M. D'Ewart, Rolando Dünner, Tijmen de Haan, Mark Devlin, Simon Dicker, Bradley Dober, Cody J. Duell, Shannon Duff, Adri Duivenvoorden, Jo Dunkley, Hamza El Bouhargani, Josquin Errard, Giulio Fabbian, Stephen Feeney, James Fergusson, Simone Ferraro, Pedro Fluxa, Katherine Freese, Josef C. Frisch, Andrei Frolov, George Fuller, Nicholas Galitzki, Patricio A. Gallardo, Jose Tomas Galvez Ghersi, Jiansong Gao, Eric Gawiser, Martina Gerbino, Vera Gluscevic, Neil Goeckner-Wald, Joseph Golec, Sam Gordon, Megan Gralla, Daniel Green, Arpi Grigorian, John Groh, Chris Groppi, Yilun Guan, Jon E. Gudmundsson, Mark Halpern, Dongwon Han, Peter Hargrave, Kathleen Harrington, Masaya Hasegawa, Matthew Hasselfield, Makoto Hattori, Victor Haynes, Masashi Hazumi, Erin Healy, Shawn W. Henderson, Brandon Hensley, Carlos Hervias-Caimapo, Charles A. Hill, J. Colin Hill, Gene Hilton, Matt Hilton, Adam D. Hincks, Gary Hinshaw, Renee Hložek, Shirley Ho, Shuay-Pwu Patty Ho, Thuong D. Hoang, Jonathan Hoh, Selim C. Hotinli, Zhiqi Huang, Johannes Hubmayr, Kevin Huffenberger, John P. Hughes, Anna Ijjas, Margaret Ikape, Kent Irwin, Andrew H. Jaffe, Bhuvnesh Jain, Oliver Jeong, Matthew Johnson, Daisuke Kaneko, Ethan D. Karpel, Nobuhiko Katayama, Brian Keating, Reijo Keskitalo, Theodore Kisner, Kenji Kiuchi, Jeff Klein, Kenda Knowles, Anna Kofman, Brian Koopman, Arthur Kosowsky, Nicoletta Krachmalnicoff, Akito Kusaka, Paul La Plante, Jacob Lashner, Adrian Lee, Eunseong Lee, Antony Lewis, Yaqiong Li, Zack Li, Michele Limon, Eric Linder, Jia Liu, Carlos Lopez-

Caraballo, Thibaut Louis, Marius Lungu, Mathew Madhavacheril, Daisy Mak, Felipe Maldonado, Hamdi Mani, Ben Mates, Frederick Matsuda, Loïc Maurin, Phil Mauskopf, Andrew May, Nialh McCallum, Heather McCarrick, Chris McKenney, Jeff McMahon, P. Daniel Meerburg, James Mertens, Joel Meyers, Amber Miller, Mark Mirmelstein, Kavilan Moodley, Jenna Moore, Moritz Munchmeyer, Charles Munson, Masaaki Murata, Sigurd Naess, Toshiya Namikawa, Federico Nati, Martin Navaroli, Laura Newburgh, Ho Nam Nguyen, Andrina Nicola, Mike Niemack, Haruki Nishino, Yume Nishinomiya, John Orlowski-Scherer, Luca Pagano, Bruce Partridge, Francesca Perrotta, Phumlani Phakathi, Lucio Piccirillo, Elena Pierpaoli, Giampaolo Pisano, Davide Poletti, Roberto Puddu, Giuseppe Puglisi, Chris Raum, Christian L. Reichardt, Mathieu Remazeilles, Yoel Rephaeli, Dominik Riechers, Felipe Rojas, Aditya Rotti, Anirban Roy, Sharon Sadeh, Yuki Sakurai, Maria Salatino, Mayuri Sathyanarayana Rao, Lauren Saunders, Emmanuel Schaan, Marcel Schmittfull, Neelima Sehgal, Joseph Seibert, Uros Seljak, Paul Shellard, Blake Sherwin, Meir Shimon, Carlos Sierra, Jonathan Sievers, Cristobal Sifon, Precious Sikhosana, Maximiliano Silva-Feaver, Sara M. Simon, Adrian Sinclair, Kendrick Smith, Wuhyun Sohn, Rita Sonka, David Spergel, Jacob Spisak, Suzanne T. Staggs, George Stein, Jason R. Stevens, Radek Stompor, Aritoki Suzuki, Osamu Tajima, Satoru Takakura, Grant Teply, Daniel B. Thomas, Ben Thorne, Robert Thornton, Hy Trac, Jesse Treu, Calvin Tsai, Carole Tucker, Joel Ullom, Sunny Vagnozzi, Alexander van Engelen, Jeff Van Lanen, Daniel D. Van Winkle, Eve M. Vavagiakis, Clara Vergès, Michael Vissers, Kasey Wagoner, Samantha Walker, Yuhan Wang, Jon Ward, Ben Westbrook, Nathan Whitehorn, Jason Williams, Joel Williams, Edward Wollack, Zhilei Xu, Siavash Yasini, Edward Young, Byeonghee Yu, Cyndia Yu, Fernando Zago, Mario Zannoni, Hezi Zhang, Kaiwen Zheng, Ningfeng Zhu, and Andrea Zonca. The Simons Observatory. In *Bulletin of the American Astronomical Society*, volume 51, page 147, September 2019.

L. Lentati et al. European Pulsar Timing Array Limits On An Isotropic Stochastic Gravitational-Wave Background. *Mon. Not. Roy. Astron. Soc.*, 453(3):2576–2598, 2015a. DOI: 10.1093/mnras/stv1538.

L. Lentati et al. European Pulsar Timing Array Limits On An Isotropic Stochastic Gravitational-Wave Background. *Mon. Not. Roy. Astron. Soc.*, 453(3):2576–2598, 2015b. DOI: 10.1093/mnras/stv1538.

A. Lewis, A. Challinor, and A. Lasenby. Efficient Computation of Cosmic Microwave Background Anisotropies in Closed Friedmann-Robertson-Walker Models. *Astrophys. J.*, 538:473–476, August 2000. DOI: 10.1086/309179.

Antony Lewis. Efficient sampling of fast and slow cosmological parameters. *Phys. Rev.*, D87(10):103529, 2013. DOI: 10.1103/PhysRevD.87.103529.

Antony Lewis and Sarah Bridle. Cosmological parameters from CMB and other data: A Monte Carlo approach. *Phys. Rev.*, D66:103511, 2002. DOI: 10.1103/PhysRevD.66.103511.

E. M. Lifshitz. On the gravitational stability of the expanding universe. *Zhurnal Eksperimentalnoi i Teoreticheskoi Fiziki*, 16:587–602, January 1946.

Eric V. Linder. Exploring the Expansion History of the Universe. *Phys. Rev. Lett.*, 90(9):091301, March 2003. DOI: 10.1103/PhysRevLett.90.091301.

Joanes Lizarraga, Jon Urrestilla, David Daverio, Mark Hindmarsh, Martin Kunz, and Andrew R. Liddle. Constraining topological defects with temperature and polarization anisotropies. *Phys. Rev.*, D90(10):103504, 2014. DOI: 10.1103/PhysRevD.90.103504.

Giuseppe Lodato and Priya Natarajan. Supermassive black hole formation during the assembly of pre-galactic discs. *Mon. Not. Roy. Astron. Soc.*, 371:1813–1823, 2006. DOI: 10.1111/j.1365-2966.2006.10801.x.

T. Louis, E. Grace, M. Hasselfield, M. Lungu, L. Maurin, G. E. Addison, P. A. R. Ade, S. Aiola, R. Allison, M. Amiri, E. Angile, N. Battaglia, J. A. Beall, F. de Bernardis, J. R. Bond, J. Britton, E. Calabrese, H.-m. Cho, S. K. Choi, K. Coughlin, D. Crichton, K. Crowley, R. Datta, M. J. Devlin, S. R. Dicker, J. Dunkley, R. Dünner, S. Ferraro, A. E. Fox, P. Gallardo, M. Gralla, M. Halpern, S. Henderson, J. C. Hill, G. C. Hilton, M. Hilton, A. D. Hincks, R. Hlozek, S. P. P. Ho, Z. Huang, J. Hubmayr, K. M. Huffenberger, J. P. Hughes, L. Infante, K. Irwin, S. Muya Kasanda, J. Klein, B. Koopman, A. Kosowsky, D. Li, M. Madhavacheril, T. A. Marriage, J. McMahon, F. Menanteau, K. Moodley, C. Munson, S. Naess, F. Nati, L. Newburgh, J. Nibarger, M. D. Niemack, M. R. Nolta, C. Nuñez, L. A. Page, C. Pappas, B. Partridge, F. Rojas, E. Schaan, B. L. Schmitt, N. Sehgal, B. D. Sherwin, J. Sievers, S. Simon, D. N. Spergel, S. T. Staggs, E. R. Switzer, R. Thornton, H. Trac, J. Treu, C. Tucker, A. Van Engelen, J. T. Ward, and E. J. Wollack. The Atacama Cosmology Telescope: two-season ACTPol spectra and parameters. *JCAP*, 6:031, June 2017. DOI: 10.1088/1475-7516/2017/06/031.

Thibaut Louis et al. The Atacama Cosmology Telescope: Two-Season ACTPol Spectra and Parameters. *JCAP*, 06:031, 2017. DOI: 10.1088/1475-7516/2017/06/031.

Kaloian D. Lozanov. Lectures on Reheating after Inflation. *arXiv e-prints*, art. arXiv:1907.04402, July 2019.

Arthur Lue, Li-Min Wang, and Marc Kamionkowski. Cosmological signature of new parity violating interactions. *Phys. Rev. Lett.*, 83: 1506–1509, 1999. DOI: 10.1103/PhysRevLett.83.1506.

Jean-Pierre Luminet. The Status of Cosmic Topology after Planck Data. *Universe*, 2(1):1, January 2016. DOI: 10.3390/universe2010001.

David H. Lyth and Antonio Riotto. Particle physics models of inflation and the cosmological density perturbation. *Phys. Rept.*, 314: 1–146, 1999. DOI: 10.1016/S0370-1573(98)00128-8.

Michele Maggiore. *Gravitational Waves. Vol. 2: Astrophysics and Cosmology*. Oxford University Press, 3 2018. ISBN 978-0-19-857089-9.

A. Maleknejad. Axion Inflation with an SU(2) Gauge Field: Detectable Chiral Gravity Waves. *JHEP*, 07:104, 2016. DOI: 10.1007/JHEP07(2016)104.

A. Maleknejad and E. Komatsu. Production and Backreaction of Spin-2 Particles of $SU(2)$ Gauge Field during Inflation. *JHEP*, 05:174, 2019. DOI: 10.1007/JHEP05(2019)174.

A. Maleknejad and M. M. Sheikh-Jabbari. Gauge-flation: Inflation From Non-Abelian Gauge Fields. *Phys. Lett.*, B723:224–228, 2013. DOI: 10.1016/j.physletb.2013.05.001.

A. Maleknejad and M.M. Sheikh-Jabbari. Non-Abelian Gauge Field Inflation. *Phys. Rev. D*, 84:043515, 2011. DOI: 10.1103/PhysRevD.84.043515.

A. Maleknejad, M. M. Sheikh-Jabbari, and J. Soda. Gauge Fields and Inflation. *Phys. Rept.*, 528:161–261, 2013. DOI: 10.1016/j.physrep.2013.03.003.

A. Maleknejad, M. M. Sheikh-Jabbari, and J. Soda. Gauge fields and inflation. *Phys. Rept.*, 528(4):161–261, July 2013. DOI: 10.1016/j.physrep.2013.03.003.

Azadeh Maleknejad and E. Erfani. Chromo-Natural Model in Anisotropic Background. *JCAP*, 03:016, 2014. DOI: 10.1088/1475-7516/2014/03/016.

V. Mandic, E. Thrane, S. Giampanis, and T. Regimbau. Parameter Estimation in Searches for the Stochastic Gravitational-Wave Background. *Phys. Rev. Lett.*, 109:171102, 2012. DOI: 10.1103/PhysRevLett.109.171102.

A. Manzotti. Future cosmic microwave background delensing with galaxy surveys. *Phys. Rev.*, 97(4):043527, February 2018. DOI: 10.1103/PhysRevD.97.043527.

A. Manzotti et al. CMB Polarization B-mode Delensing with SPTpol and Herschel. *Astrophys. J.*, 846(1):45, 2017. DOI: 10.3847/1538-4357/aa82bb.

P. Daniel Meerburg, RenÃľe Hloˇzek, Boryana Hadzhiyska, and Joel Meyers. Multiwavelength constraints on the inflationary consistency relation. *Phys. Rev. D*, 91(10):103505, 2015. DOI: 10.1103/PhysRevD.91.103505.

Chiara M.F. Mingarelli, Stephen R. Taylor, B.S. Sathyaprakash, and Will M. Farr. Understanding $\Omega_{\rm gw}(f)$ in Gravitational Wave Experiments. 11 2019.

Leila Mirzagholi, Eiichiro Komatsu, Kaloian D. Lozanov, and Yuki Watanabe. Effects of Gravitational Chern-Simons during Axion-SU(2) Inflation. *JCAP*, 06:024, 2020. DOI: 10.1088/1475-7516/2020/06/024.

Viatcheslav Mukhanov. *Physical Foundations of Cosmology*. 2005. DOI: 10.2277/0521563984.

Dipak Munshi and Martin Kilbinger. Principal component analysis of weak lensing surveys. *Astron. Astrophys.*, 452:63, 2006. DOI: 10.1051/0004-6361:20054586.

R. Namba, M. Peloso, M. Shiraishi, L. Sorbo, and C. Unal. Scale-dependent gravitational waves from a rolling axion. *JCAP*, 1:041, January 2016. DOI: 10.1088/1475-7516/2016/01/041.

R. Namba, M. Peloso, M. Shiraishi, L. Sorbo, and C. Unal. Scale-dependent gravitational waves from a rolling axion. *JCAP*, 1601(01): 041, 2016. DOI: 10.1088/1475-7516/2016/01/041.

Toshiya Namikawa, Daisuke Yamauchi, Blake Sherwin, and Ryo Nagata. Delensing Cosmic Microwave Background B-modes with the Square Kilometre Array Radio Continuum Survey. *Phys. Rev.*, D93 (4):043527, 2016. DOI: 10.1103/PhysRevD.93.043527.

Atsushi Nishizawa, Kent Yagi, Atsushi Taruya, and Takahiro Tanaka. Cosmology with space-based gravitational-wave detectors — dark energy and primordial gravitational waves —. *Phys. Rev.*, D85:044047, 2012. DOI: 10.1103/PhysRevD.85.044047.

I. Obata and J. Soda. Chiral primordial gravitational waves from dilaton induced delayed chromonatural inflation. *Phys. Rev.*, D93(12): 123502, 2016. DOI: 10.1103/PhysRevD.93.123502.

Georges Obied, Cora Dvorkin, Chen Heinrich, Wayne Hu, and V. Miranda. Inflationary versus reionization features from *Planck* 2015 data. *Phys. Rev.*, D98(4):043518, 2018. DOI: 10.1103/PhysRevD.98.043518.

Ogan Özsoy. Gravitational Waves from a Rolling Axion Monodromy. *arXiv e-prints*, art. arXiv:2005.10280, May 2020.

Luca Pagano, Laura Salvati, and Alessandro Melchiorri. New constraints on primordial gravitational waves from Planck 2015. *Phys. Lett. B*, 760:823–825, 2016. DOI: 10.1016/j.physletb.2016.07.078.

Zhen Pan and Huan Yang. Probing Primordial Stochastic Gravitational Wave Background with Multi-band Astrophysical Foreground Cleaning. 10 2019.

Alexandros Papageorgiou, Marco Peloso, and Caner Unal. Nonlinear perturbations from the coupling of the inflaton to a non-Abelian gauge field, with a focus on Chromo-Natural Inflation. *JCAP*, 09:030, 2018. DOI: 10.1088/1475-7516/2018/09/030.

Alexandros Papageorgiou, Marco Peloso, and Caner Unal. Nonlinear perturbations from axion-gauge fields dynamics during inflation. *JCAP*, 07:004, 2019. DOI: 10.1088/1475-7516/2019/07/004.

P. Paykari and A. H. Jaffe. Optimal Binning of the Primordial Power Spectrum. *Astrophys. J.*, 711:1–12, March 2010. DOI: 10.1088/0004-637X/711/1/1.

P. J. E. Peebles. Recombination of the Primeval Plasma. *Astrophys. J.*, 153:1, July 1968. DOI: 10.1086/149628.

A. A. Penzias and R. W. Wilson. A Measurement of Excess Antenna Temperature at 4080 Mc/s. *Astrophys. J.*, 142:419–421, July 1965. DOI: 10.1086/148307.

B.B.P. Perera et al. The International Pulsar Timing Array: Second data release. *Mon. Not. Roy. Astron. Soc.*, 490(4):4666–4687, 2019. DOI: 10.1093/mnras/stz2857.

S. Perlmutter, G. Aldering, G. Goldhaber, R. A. Knop, P. Nugent, P. G. Castro, S. Deustua, S. Fabbro, A. Goobar, D. E. Groom, I. M. Hook, A. G. Kim, M. Y. Kim, J. C. Lee, N. J. Nunes, R. Pain, C. R. Pennypacker, R. Quimby, C. Lidman, R. S. Ellis, M. Irwin, R. G. McMahon, P. Ruiz-Lapuente, N. Walton, B. Schaefer, B. J. Boyle, A. V. Filippenko, T. Matheson, A. S. Fruchter, N. Panagia, H. J. M. Newberg, W. J. Couch, and The Supernova Cosmology Project. Measurements of Ω and Λ from 42 High-Redshift Supernovae. *Astrophys. J.*, 517(2):565–586, June 1999. DOI: 10.1086/307221.

Laurence Perotto, Julien Lesgourgues, Steen Hannestad, Huitzu Tu, and Yvonne Y.Y. Wong. Probing cosmological parameters with the CMB: Forecasts from full Monte Carlo simulations. *JCAP*, 10:013, 2006. DOI: 10.1088/1475-7516/2006/10/013.

Patrick Peter and Jean-Philippe Uzan. *Primordial Cosmology*. Oxford Graduate Texts. Oxford University Press, 2 2013. ISBN 978-0-19-966515-0, 978-0-19-920991-0.

Mauro Pieroni and Enrico Barausse. Foreground cleaning and template-free stochastic background extraction for LISA. 4 2020.

Planck Collaboration. Planck 2013 results. XXII. Constraints on inflation. *Astron. Astrophys.*, 571:A22, 2014. DOI: 10.1051/0004-6361/201321569.

Planck Collaboration. Planck 2015 results - XVIII. Background geometry and topology of the Universe. *Astron. Astrophys.*, 594:A18, 2016a. DOI: 10.1051/0004-6361/201525829.

Planck Collaboration. Planck 2015 results. XIV. Dark energy and modified gravity. *Astron. Astrophys.*, 594:A14, September 2016b. DOI: 10.1051/0004-6361/201525814.

Planck Collaboration. Planck intermediate results. XLI. A map of lensing-induced B-modes. *Astron. Astrophys.*, 596:A102, 2016. DOI: 10.1051/0004-6361/201527932.

Planck Collaboration. Planck 2015 results. XX. Constraints on inflation. *Astron. Astrophys.*, 594:A20, 2016. DOI: 10.1051/0004-6361/201525898.

Planck Collaboration. Planck 2018 results. VI. Cosmological parameters. 2018.

Planck Collaboration. Planck 2018 results. IV. Diffuse component separation. 2018a.

Planck Collaboration. Planck 2018 results. XI. Polarized dust foregrounds. 2018b.

Planck Collaboration. Planck 2018 results. X. Constraints on inflation. 2018c.

Planck Collaboration. Planck 2018 results. I. Overview and the cosmological legacy of Planck. *arXiv e-prints*, art. arXiv:1807.06205, July 2018d.

Planck Collaboration. Planck 2018 results. VIII. Gravitational lensing. 7 2018e.

Planck Collaboration. Planck 2018 results. IX. Constraints on primordial non-Gaussianity. 5 2019.

POLARBEAR Collaboration. A Measurement of the Cosmic Microwave Background B-Mode Polarization Power Spectrum at Sub-Degree Scales with POLARBEAR. *Astrophys. J.*, 794(2):171, 2014. DOI: 10.1088/0004-637X/794/2/171.

POLARBEAR Collaboration. Measurement of the Cosmic Microwave Background Polarization Lensing Power Spectrum from Two Years of POLARBEAR Data. *Astrophys. J.*, 893(1):85, April 2020. DOI: 10.3847/1538-4357/ab7e29.

POLARBEAR Collaboration, P. A. R. Ade, et al. A Measurement of the Cosmic Microwave Background B-mode Polarization Power Spectrum at Subdegree Scales from Two Years of polarbear Data. *Astrophys. J.*, 848:121, October 2017. DOI: 10.3847/1538-4357/aa8e9f.

A. G. Polnarev. Polarization and Anisotropy Induced in the Microwave Background by Cosmological Gravitational Waves. *Sov. Astron.*,, 29:607–613, December 1985.

Maxim Pospelov and Josef Pradler. Big Bang Nucleosynthesis as a Probe of New Physics. *Annual Review of Nuclear and Particle Science*, 60:539–568, November 2010. DOI: 10.1146/annurev.nucl.012809.104521.

William H. Press, Saul A. Teukolsky, William T. Vetterling, and Brian P. Flannery. *Numerical Recipes in C: The Art of Scientific Computing*. Cambridge, UK: Univ. Pr., 1992.

Layne C. Price, Hiranya V. Peiris, Jonathan Frazer, and Richard Easther. Gravitational wave consistency relations for multifield inflation. *Phys. Rev. Lett.*, 114(3):031301, 2015. DOI: 10.1103/PhysRevLett.114.031301.

Giuseppe Puglisi, Giulio Fabbian, and Carlo Baccigalupi. A 3D model for carbon monoxide molecular line emission as a potential cosmic microwave background polarization contaminant. *Mon. Not. Roy. Astron. Soc.*, 469(3):2982–2996, 2017. DOI: 10.1093/mnras/stx1029.

Marco Raveri, Carlo Baccigalupi, Alessandra Silvestri, and Shuang-Yong Zhou. Measuring the speed of cosmological gravitational waves. *Phys. Rev.*, D91(6):061501, 2015. DOI: 10.1103/PhysRevD.91.061501.

M. J. Reid, J. A. Braatz, J. J. Condon, K. Y. Lo, C. Y. Kuo, C. M. V. Impellizzeri, and C. Henkel. The Megamaser Cosmology Project. IV. A Direct Measurement of the Hubble Constant from UGC

3789. *Astrophys. J.*, 767(2):154, April 2013. DOI: 10.1088/0004-637X/767/2/154.

David Reitze et al. Cosmic Explorer: The U.S. Contribution to Gravitational-Wave Astronomy beyond LIGO. *Bull. Am. Astron. Soc.*, 51:035, 7 2019.

Adam G. Riess, Alexei V. Filippenko, Peter Challis, Alejandro Clocchiatti, Alan Diercks, Peter M. Garnavich, Ron L. Gilliland, Craig J. Hogan, Saurabh Jha, Robert P. Kirshner, B. Leibundgut, M. M. Phillips, David Reiss, Brian P. Schmidt, Robert A. Schommer, R. Chris Smith, J. Spyromilio, Christopher Stubbs, Nicholas B. Suntzeff, and John Tonry. Observational Evidence from Supernovae for an Accelerating Universe and a Cosmological Constant. *Astron. J.*, 116(3):1009–1038, September 1998. DOI: 10.1086/300499.

Adam G. Riess, Stefano Casertano, Wenlong Yuan, Lucas M. Macri, and Dan Scolnic. Large Magellanic Cloud Cepheid Standards Provide a 1% Foundation for the Determination of the Hubble Constant and Stronger Evidence for Physics beyond ΛCDM. *Astrophys. J.*, 876(1): 85, 2019. DOI: 10.3847/1538-4357/ab1422.

Travis Robson, Neil J. Cornish, and Chang Liu. The construction and use of LISA sensitivity curves. *Class. Quant. Grav.*, 36(10):105011, 2019. DOI: 10.1088/1361-6382/ab1101.

Joseph D. Romano and Neil J. Cornish. Detection methods for stochastic gravitational-wave backgrounds: a unified treatment. *Living Rev. Rel.*, 20(1):2, 2017. DOI: 10.1007/s41114-017-0004-1.

George B. Rybicki and Alan P. Lightman. *Radiative Processes in Astrophysics*. 1986.

Surabhi Sachdev, Tania Regimbau, and B. S. Sathyaprakash. Subtracting compact binary foreground sources to reveal primordial gravitational-wave backgrounds. 2020.

Ken'ichi Saikawa and Satoshi Shirai. Primordial gravitational waves, precisely: the role of thermodynamics in the Standard Model. *JCAP*, 2018(5):035, May 2018. DOI: 10.1088/1475-7516/2018/05/035.

Shun Saito, Kiyotomo Ichiki, and Atsushi Taruya. Probing polarization states of primordial gravitational waves with cosmic microwave background anisotropies. *JCAP*, 2007(9):002, September 2007. DOI: 10.1088/1475-7516/2007/09/002.

A.D. Sakharov. Violation of CP Invariance, C asymmetry, and baryon asymmetry of the universe. *Sov. Phys. Usp.*, 34(5):392–393, 1991. DOI: 10.1070/PU1991v034n05ABEH002497.

Kai Schmitz. New Sensitivity Curves for Gravitational-Wave Experiments. 2020.

Thilo Schuldt. *Laser interferometry for high resolution metrology in space*. IOP Publishing Ltd 2018, 2018. ISBN 978-0-7503-1578-4.

Manuel Arca Sedda et al. The Missing Link in Gravitational-Wave Astronomy: Discoveries Waiting in the Decihertz Range. 2019.

Uros Seljak and Matias Zaldarriaga. Signature of gravity waves in polarization of the microwave background. *Phys. Rev. Lett.*, 78: 2054–2057, 1997. DOI: 10.1103/PhysRevLett.78.2054.

Alberto Sesana, Alberto Vecchio, and Carlo Nicola Colacino. The stochastic gravitational-wave background from massive black hole binary systems: implications for observations with Pulsar Timing Arrays. *Mon. Not. Roy. Astron. Soc.*, 390:192, 2008. DOI: 10.1111/j.1365-2966.2008.13682.x.

Alberto Sesana et al. Unveiling the Gravitational Universe at μ-Hz Frequencies. 2019.

Naoki Seto. Prospects for direct detection of circular polarization of gravitational-wave background. *Phys. Rev. Lett.*, 97:151101, 2006. DOI: 10.1103/PhysRevLett.97.151101.

Naoki Seto, Seiji Kawamura, and Takashi Nakamura. Possibility of direct measurement of the acceleration of the universe using 0.1-Hz band laser interferometer gravitational wave antenna in space. *Phys. Rev. Lett.*, 87:221103, 2001. DOI: 10.1103/PhysRevLett.87.221103.

A. J. Shajib, S. Birrer, T. Treu, A. Agnello, E. J. Buckley-Geer, J. H. H. Chan, L. Christensen, C. Lemon, H. Lin, M. Millon, J. Poh, C. E. Rusu, D. Sluse, C. Spiniello, G. C. F. Chen, T. Collett, F. Courbin, C. D. Fassnacht, J. Frieman, A. Galan, D. Gilman, A. More, T. Anguita, M. W. Auger, V. Bonvin, R. McMahon, G. Meylan, K. C. Wong, T. M. C. Abbott, J. Annis, S. Avila, K. Bechtol, D. Brooks, D. Brout, D. L. Burke, A. Carnero Rosell, M. Carrasco Kind, J. Carretero, F. J. Castander, M. Costanzi, L. N. da Costa, J. De Vicente, S. Desai, J. P. Dietrich, P. Doel, A. Drlica-Wagner, A. E. Evrard, D. A. Finley, B. Flaugher, P. Fosalba, J. García-Bellido, D. W. Gerdes, D. Gruen, R. A. Gruendl, J. Gschwend, G. Gutierrez, D. L. Hollowood, K. Honscheid, D. Huterer, D. J. James, T. Jeltema, E. Krause, N. Kuropatkin, T. S. Li, M. Lima, N. MacCrann, M. A. G. Maia, J. L. Marshall, P. Melchior, R. Miquel, R. L. C. Ogando, A. Palmese, F. Paz-Chinchón, A. A. Plazas, A. K. Romer, A. Roodman, M. Sako, E. Sanchez, B. Santiago, V. Scarpine, M. Schubnell, D. Scolnic, S. Serrano, I. Sevilla-Noarbe, M. Smith, M. Soares-Santos, E. Suchyta,

G. Tarle, D. Thomas, A. R. Walker, and Y. Zhang. STRIDES: a 3.9 per cent measurement of the Hubble constant from the strong lens system DES J0408-5354. *Mon. Not. Roy. Astron. Soc.*, 494(4):6072–6102, March 2020. DOI: 10.1093/mnras/staa828.

Blake D. Sherwin et al. Two-season Atacama Cosmology Telescope polarimeter lensing power spectrum. *Phys. Rev. D*, 95(12):123529, 2017. DOI: 10.1103/PhysRevD.95.123529.

M. Shiraishi, C. Hikage, R. Namba, T. Namikawa, and M. Hazumi. Testing statistics of the CMB B -mode polarization toward unambiguously establishing quantum fluctuation of the vacuum. *Phys. Rev.*, D94(4):043506, 2016. DOI: 10.1103/PhysRevD.94.043506.

G. Simard et al. Constraints on Cosmological Parameters from the Angular Power Spectrum of a Combined 2500 deg^2 SPT-SZ and Planck Gravitational Lensing Map. *Astrophys. J.*, 860(2):137, 2018. DOI: 10.3847/1538-4357/aac264.

K. M. Smith, D. Hanson, M. LoVerde, C. M. Hirata, and O. Zahn. Delensing CMB polarization with external datasets. *JCAP*, 6:014, June 2012. DOI: 10.1088/1475-7516/2012/06/014.

Tristan L. Smith and Robert Caldwell. Sensitivity to a Frequency-Dependent Circular Polarization in an Isotropic Stochastic Gravitational Wave Background. *Phys. Rev.*, D95(4):044036, 2017. DOI: 10.1103/PhysRevD.95.044036.

Tristan L. Smith and Robert Caldwell. LISA for Cosmologists: Calculating the Signal-to-Noise Ratio for Stochastic and Deterministic Sources. *Phys. Rev.*, D100(10):104055, 2019. DOI: 10.1103/PhysRevD.100.104055.

Tristan L. Smith, Hiranya V. Peiris, and Asantha Cooray. Deciphering inflation with gravitational waves: cosmic microwave background polarization vs. direct detection with laser interferometers. *Phys. Rev. D*, 73:123503, 2006. DOI: 10.1103/PhysRevD.73.123503.

G. F. Smoot, C. L. Bennett, A. Kogut, E. L. Wright, J. Aymon, N. W. Boggess, E. S. Cheng, G. de Amici, S. Gulkis, M. G. Hauser, G. Hinshaw, P. D. Jackson, M. Janssen, E. Kaita, T. Kelsall, P. Keegstra, C. Lineweaver, K. Loewenstein, P. Lubin, J. Mather, S. S. Meyer, S. H. Moseley, T. Murdock, L. Rokke, R. F. Silverberg, L. Tenorio, R. Weiss, and D. T. Wilkinson. Structure in the COBE Differential Microwave Radiometer First-Year Maps. *Astrophys. J.*, 396:L1, September 1992. DOI: 10.1086/186504.

Kentaro Somiya. Detector configuration of KAGRA: The Japanese cryogenic gravitational-wave detector. *Class. Quant. Grav.*, 29:124007, 2012. DOI: 10.1088/0264-9381/29/12/124007.

L. Sorbo. Parity violation in the Cosmic Microwave Background from a pseudoscalar inflaton. *JCAP*, 1106:003, 2011. DOI: 10.1088/1475-7516/2011/06/003.

Alexei A. Starobinsky. Spectrum of relict gravitational radiation and the early state of the universe. *JETP Lett.*, 30:682–685, 1979.

R. Stompor, Samuel M. Leach, F. Stivoli, and C. Baccigalupi. Maximum Likelihood algorithm for parametric component separation in CMB experiments. *Mon. Not. Roy. Astron. Soc.*, 392:216, 2009. DOI: 10.1111/j.1365-2966.2008.14023.x.

Radek Stompor, Josquin Errard, and Davide Poletti. Forecasting performance of CMB experiments in the presence of complex foreground contaminations. *Phys. Rev.*, D94(8):083526, 2016. DOI: 10.1103/PhysRevD.94.083526.

H. Sugai, P. A. R. Ade, Y. Akiba, D. Alonso, K. Arnold, J. Aumont, J. Austermann, C. Baccigalupi, A. J. Banday, R. Banerji, R. B. Barreiro, S. Basak, J. Beall, S. Beckman, M. Bersanelli, J. Borrill, F. Boulanger, M. L. Brown, M. Bucher, A. Buzzelli, E. Calabrese, F. J. Casas, A. Challinor, V. Chan, Y. Chinone, J. F. Cliche, F. Columbro, A. Cukierman, D. Curtis, P. Danto, P. de Bernardis, T. de Haan, M. De Petris, C. Dickinson, M. Dobbs, T. Dotani, L. Duband, A. Ducout, S. Duff, A. Duivenvoorden, J. M. Duval, K. Ebisawa, T. Elleflot, H. Enokida, H. K. Eriksen, J. Errard, T. Essinger-Hileman, F. Finelli, R. Flauger, C. Franceschet, U. Fuskeland , K. Ganga, J. R. Gao, R. Génova-Santos, T. Ghigna, A. Gomez, M. L. Gradziel, J. Grain, F. Grupp, A. Gruppuso, J. E. Gudmundsson, N. W. Halverson, P. Hargrave, T. Hasebe, M. Hasegawa, M. Hattori, M. Hazumi, S. Henrot-Versille, D. Herranz, C. Hill, G. Hilton, Y. Hirota, E. Hivon, R. Hlozek, D. T. Hoang, J. Hubmayr, K. Ichiki, T. Iida, H. Imada, K. Ishimura, H. Ishino, G. C. Jaehnig, M. Jones, T. Kaga, S. Kashima, Y. Kataoka, N. Katayama, T. Kawasaki, R. Keskitalo, A. Kibayashi, T. Kikuchi, K. Kimura, T. Kisner, Y. Kobayashi, N. Kogiso, A. Kogut, K. Kohri, E. Komatsu, K. Komatsu, K. Konishi, N. Krachmalnicoff, C. L. Kuo, N. Kurinsky, A. Kushino, M. Kuwata-Gonokami, L. Lamagna, M. Lattanzi, A. T. Lee, E. Linder, B. Maffei, D. Maino, M. Maki, A. Mangilli, E. Martínez-González, S. Masi, R. Mathon, T. Matsumura, A. Mennella, M. Migliaccio, Y. Minami, K. Mistuda, D. Molinari, L. Montier,

G. Morgante, B. Mot, Y. Murata, J. A. Murphy, M. Nagai, R. Nagata, S. Nakamura, T. Namikawa, P. Natoli, S. Nerval, T. Nishibori, H. Nishino, Y. Nomura, F. Noviello, C. O'Sullivan, H. Ochi, H. Ogawa, H. Ogawa, H. Ohsaki, I. Ohta, N. Okada, N. Okada, L. Pagano, A. Paiella, D. Paoletti, G. Patanchon, F. Piacentini, G. Pisano, G. Polenta, D. Poletti, T. Prouvé, G. Puglisi, D. Rambaud, C. Raum, S. Realini, M. Remazeilles, G. Roudil, J. A. Rubiño-Martín, M. Russell, H. Sakurai, Y. Sakurai, M. Sandri, G. Savini, D. Scott, Y. Sekimoto, B. D. Sherwin, K. Shinozaki, M. Shiraishi, P. Shirron, G. Signorelli, G. Smecher, P. Spizzi, S. L. Stever, R. Stompor, S. Sugiyama, A. Suzuki, J. Suzuki, E. Switzer, R. Takaku, H. Takakura, S. Takakura, Y. Takeda, A. Taylor, E. Taylor, Y. Terao, K. L. Thompson, B. Thorne, M. Tomasi, H. Tomida, N. Trappe, M. Tristram, M. Tsuji, M. Tsujimoto, C. Tucker, J. Ullom, S. Uozumi, S. Utsunomiya, J. Van Lanen, G. Vermeulen, P. Vielva, F. Villa, M. Vissers, N. Vittorio, F. Voisin, I. Walker, N. Watanabe, I. Wehus, J. Weller, B. Westbrook, B. Winter, E. Wollack, R. Yamamoto, N. Y. Yamasaki, M. Yanagisawa, T. Yoshida, J. Yumoto, M. Zannoni, and A. Zonca. Updated Design of the CMB Polarization Experiment Satellite LiteBIRD. *Journal of Low Temperature Physics*, 199(3-4):1107–1117, January 2020. DOI: 10.1007/s10909-019-02329-w.

A. Suzuki et al. The POLARBEAR-2 and the Simons Array Experiment. *J. Low. Temp. Phys.*, 184(3-4):805–810, 2016. DOI: 10.1007/s10909-015-1425-4.

A. Tartari et al. QUBIC: A Fizeau Interferometer Targeting Primordial B-Modes. *J. Low Temp. Phys.*, 184(3-4):739–745, 2016. DOI: 10.1007/s10909-015-1398-3.

Hiroyuki Tashiro. CMB spectral distortions and energy release in the early universe. *Progress of Theoretical and Experimental Physics*, 2014(6): 06B107, June 2014. DOI: 10.1093/ptep/ptu066.

J. H. Taylor and J. M. Weisberg. A new test of general relativity - Gravitational radiation and the binary pulsar PSR 1913+16. *Astrophys. J.*, 253:908–920, February 1982. DOI: 10.1086/159690.

Max Tegmark. How to measure CMB power spectra without losing information. *Phys. Rev.*, D55:5895–5907, 1997. DOI: 10.1103/PhysRevD.55.5895.

The BICEP/Keck Collaboration, :, P. A. R. Ade, et al. Measurements of Degree-Scale B-mode Polarization with the BICEP/Keck Experiments at South Pole. *arXiv e-prints*, July 2018.

The LIGO Scientific Collaboration, the Virgo Collaboration, B. P. Abbott, R. Abbott, T. D. Abbott, S. Abraham, F. Acernese, K. Ackley,

C. Adams, R. X. Adhikari, V. B. Adya, and J. Zweizig. A gravitational-wave measurement of the Hubble constant following the second observing run of Advanced LIGO and Virgo. *arXiv e-prints*, art. arXiv:1908.06060, August 2019.

The Simons Observatory Collaboration, P. Ade, J. Aguirre, Z. Ahmed, S. Aiola, A. Ali, D. Alonso, M. A. Alvarez, K. Arnold, P. Ashton, and et al. The Simons Observatory: Science goals and forecasts. *arXiv e-prints*, August 2018.

Ben Thorne, Jo Dunkley, David Alonso, and Sigurd Naess. The Python Sky Model: software for simulating the Galactic microwave sky. *Mon. Not. Roy. Astron. Soc.*, 469(3):2821–2833, 2017. DOI: 10.1093/mnras/stx949.

Ben Thorne, Tomohiro Fujita, Masashi Hazumi, Nobuhiko Katayama, Eiichiro Komatsu, and Maresuke Shiraishi. Finding the chiral gravitational wave background of an axion-SU(2) inflationary model using CMB observations and laser interferometers. *Phys. Rev. D*, 97(4):043506, 2018. DOI: 10.1103/PhysRevD.97.043506.

A. van Engelen, R. Keisler, O. Zahn, K. A. Aird, B. A. Benson, L. E. Bleem, J. E. Carlstrom, C. L. Chang, H. M. Cho, T. M. Crawford, A. T. Crites, T. de Haan, M. A. Dobbs, J. Dudley, E. M. George, N. W. Halverson, G. P. Holder, W. L. Holzapfel, S. Hoover, Z. Hou, J. D. Hrubes, M. Joy, L. Knox, A. T. Lee, E. M. Leitch, M. Lueker, D. Luong-Van, J. J. McMahon, J. Mehl, S. S. Meyer, M. Millea, J. J. Mohr, T. E. Montroy, T. Natoli, S. Padin, T. Plagge, C. Pryke, C. L. Reichardt, J. E. Ruhl, J. T. Sayre, K. K. Schaffer, L. Shaw, E. Shirokoff, H. G. Spieler, Z. Staniszewski, A. A. Stark, K. Story, K. Vanderlinde, J. D. Vieira, and R. Williamson. A Measurement of Gravitational Lensing of the Microwave Background Using South Pole Telescope Data. *Astrophys. J.*, 756(2):142, September 2012. DOI: 10.1088/0004-637X/756/2/142.

P. Vielva, E. Martínez-González, and M. Tucci. Cross-correlation of the cosmic microwave background and radio galaxies in real, harmonic and wavelet spaces: detection of the integrated Sachs-Wolfe effect and dark energy constraints. *Mon. Not. Roy. Astron. Soc.*, 365(3):891–901, January 2006. DOI: 10.1111/j.1365-2966.2005.09764.x.

David Wands, Nicola Bartolo, Sabino Matarrese, and Antonio Riotto. Observational test of two-field inflation. *Phys. Rev.*, 66(4):043520, August 2002. DOI: 10.1103/PhysRevD.66.043520.

Yuki Watanabe and Eiichiro Komatsu. Improved Calculation of the Primordial Gravitational Wave Spectrum in the Standard Model. *Phys. Rev.*, D73:123515, 2006. DOI: 10.1103/PhysRevD.73.123515.

Steven Weinberg. *Cosmology*. 9 2008. ISBN 978-0-19-852682-7.

A. Weltman et al. Fundamental Physics with the Square Kilometre Array. *Publ. Astron. Soc. Austral.*, 37:e002, 2020. DOI: 10.1017/pasa.2019.42.

Ira Wolfson, Azadeh Maleknejad, and Eiichiro Komatsu. How attractive is the isotropic attractor solution of axion-SU(2) inflation? 3 2020.

Kenneth C. Wong, Sherry H. Suyu, Geoff C. F. Chen, Cristian E. Rusu, Martin Millon, Dominique Sluse, Vivien Bonvin, Christopher D. Fassnacht, Stefan Taubenberger, Matthew W. Auger, Simon Birrer, James H. H. Chan, Frederic Courbin, Stefan Hilbert, Olga Tihhonova, Tommaso Treu, Adriano Agnello, Xuheng Ding, Inh Jee, Eiichiro Komatsu, Anowar J. Shajib, Alessandro Sonnenfeld, Roger D. Bland ford, Léon V. E. Koopmans, Philip J. Marshall, and Georges Meylan. HoLiCOW XIII. A 2.4% measurement of H_0 from lensed quasars: 5.3σ tension between early and late-Universe probes. *Mon. Not. Roy. Astron. Soc.*, June 2020. DOI: 10.1093/mnras/stz3094.

W. L. K. Wu, L. M. Mocanu, P. A. R. Ade, A. J. Anderson, J. E. Austermann, J. S. Avva, J. A. Beall, A. N. Bender, B. A. Benson, F. Bianchini, L. E. Bleem, J. E. Carlstrom, C. L. Chang, H. C. Chiang, R. Citron, C. Corbett Moran, T. M. Crawford, A. T. Crites, T. de Haan, M. A. Dobbs, W. Everett, J. Gallicchio, E. M. George, A. Gilbert, N. Gupta, N. W. Halverson, N. Harrington, J. W. Henning, G. C. Hilton, G. P. Holder, W. L. Holzapfel, Z. Hou, J. D. Hrubes, N. Huang, J. Hubmayr, K. D. Irwin, L. Knox, A. T. Lee, D. Li, A. Lowitz, A. Manzotti, J. J. McMahon, S. S. Meyer, M. Millea, J. Montgomery, A. Nadolski, T. Natoli, J. P. Nibarger, G. I. Noble, V. Novosad, Y. Omori, S. Padin, S. Patil, C. Pryke, C. L. Reichardt, J. E. Ruhl, B. R. Saliwanchik, J. T. Sayre, K. K. Schaffer, C. Sievers, G. Simard, G. Smecher, A. A. Stark, K. T. Story, C. Tucker, K. Vanderlinde, T. Veach, J. D. Vieira, G. Wang, N. Whitehorn, and V. Yefremenko. A Measurement of the Cosmic Microwave Background Lensing Potential and Power Spectrum from 500 deg^2 of SPTpol Temperature and Polarization Data. *Astrophys. J.*, 884(1):70, October 2019. DOI: 10.3847/1538-4357/ab4186.

Kent Yagi and Naoki Seto. Detector configuration of DECIGO/BBO and identification of cosmological neutron-star binaries. *Phys. Rev. D*, 83:044011, 2011. DOI: 10.1103/PhysRevD.83.044011. [Erratum: Phys.Rev.D 95, 109901 (2017)].

Daisuke Yamauchi, Andrei Linde, Atsushi Naruko, Misao Sasaki, and Takahiro Tanaka. Open inflation in the landscape. *Phys. Rev.*, D84:043513, 2011. DOI: 10.1103/PhysRevD.84.043513.

D.R.B. Yardley et al. On detection of the stochastic gravitational-wave background using the Parkes pulsar timing array. *Mon. Not. Roy. Astron. Soc.*, 414:1777, 2011. DOI: 10.1111/j.1365-2966.2011.18517.x.

Matias Zaldarriaga. Polarization of the microwave background in reionized models. *Phys. Rev. D*, 55:1822–1829, 1997. DOI: 10.1103/PhysRevD.55.1822.

Matias Zaldarriaga and Uros Seljak. Gravitational lensing effect on cosmic microwave background polarization. *Phys. Rev. D*, 58:023003, 1998. DOI: 10.1103/PhysRevD.58.023003.

Xing-Jiang Zhu, Eric J. Howell, David G. Blair, and Zong-Hong Zhu. On the gravitational wave background from compact binary coalescences in the band of ground-based interferometers. *Mon. Not. Roy. Astron. Soc.*, 431(1):882–899, 2013. DOI: 10.1093/mnras/stt207.